New modelling applications for Helmholtz soliton theory: from single interfaces to waveguide arrays

Emily McCOY

Materials and Physics Research Centre,

University of Salford, Salford, UK

Submitted in Partial Fulfillment of the Requirements

of the Degree of Doctor of Philosophy, June 2014

Contents

List of figures

Acknowledgments

Carrying out research and especially writing it up can be a solitary experience but it has been made much more bearable by the support of a number of people, mentioned here in no particular order.

Firstly, fellow PhD students who have always offered advice and a friendly ear: in particular Chris Bostock and Helen Christie. My time at Salford has been enriched by being part of the Science Team and so I thank all of those involved in its establishment and running.

Suggestions provided by audiences at a number of conferences including Photon 12 and the Complexity Science Conference gave useful food for thought and I hope to have acted upon them accordingly.

Advice given at internal evaluations by various members of the Salford Physics department, including from Graham McDonald, Dan Bull, Stanko Tomić and Ian Morrison, was gratefully received.

Finally on the academic front, I thank my supervisor, James Christian, who gave constant support in the first two years of the PhD and then allowed me ever more freedom during the rest of my time. He provided sound advice, talked through difficulties in the derivation of equations, guided me in the use of MATLAB, and gave me the confidence (and a less than gentle push!) to go to many more conferences than I otherwise would have done. He has also read and commented extensively on drafts of various chapters. It goes without saying that any errors that remain are mine.

Outside of work, I thank my parents who have been supportive and encouraging even though they have very little understanding about what it is I am doing and why I am doing it. James Murphy's family have always made me feel welcome and treated me with kindness and shown great pride in me. But my final thanks must go to James himself, who has been a source of comfort, love and assistance from the outset. He has helped me in so many ways that it would be foolhardy to attempt to list them. I hope this thesis makes up for the last few months of stress and tension!

Abstract

This thesis details an exploration of the behaviour of spatial optical solitons (self-collimated, self-stabilising light beams) interacting with the interface between classes of nonlinear dielectric materials.

Chapter 1 gives the theoretical background to the thesis by introducing the soliton concept, material interfaces and the Helmholtz model.

The second chapter discusses the reflection and refraction characteristics of soliton beams incident on the planar boundary between dissimilar cubic-quintic materials. The deployment of Helmholtz soliton theory allows for the simultaneous consideration of: (i) arbitrary angles of incidence, reflection and refraction (relative to the interface), and (ii) finite beam waists (as opposed to infinitely-wide plane waves). Despite an abundance of literature concerning solitons at interfaces, there appears to be no published research addressing refraction in the presence of cubic-quintic optical nonlinearity (and certainly none in arbitrary-angle contexts). Excellent agreement is generally found between theoretical predictions from a generalised Snell's law and results from extensive computer simulations.

In Chapter 3, these novel analyses have been complemented by further investigations into other fundamental aspects of optical refraction, namely Goos-Hänchen shifts and critical angle prediction. Both aspects are the first of their kind in the cubic-quintic regime.

The fourth chapter considers surface wave propagation along the interface between two dissimilar power-law materials; this research has already contributed to a published peer reviewed paper [J. M. Christian *et al.*, "Helmholtz bright spatial solitons and surface waves at power-law optical interfaces," Journal of Atomic, Molecular & Optical Physics **2012** (2012), art. no. 137967]. The chapter also expands upon that paper by giving a more detailed account of surface wave stability properties.

Chapter 5 provides an in-depth computational study into beam propagation in coupled waveguide arrays (materials whose refractive index is periodically patterned) and there appears to be a link between the beam's critical angle and the depth of the modulation of the array.

The thesis concludes with a summary of findings and suggestions surrounding the implications of this novel research.

1. Introduction

This thesis explores the behaviour of Helmholtz solitons (self-collimating, self-stabilising beams of light) at a variety of material boundaries.

The research in that which follows has only been possible because of the nature of the materials considered – they are all nonlinear optical materials. This means that the polarisation (dipole moment per unit volume) of the materials depends on the field strength of the applied optical field (this is discussed further in section 2.1.1 and see [1] for more information). This in turn means that the refractive index of the medium is dependent on the intensity of the beam propagating through it, and it is this key feature which leads to the existence of optical solitons and the Kerr effect, see section 1.1 for further discussion of this. Solitons are ubiquitous in nature [2, 3], this means that wherever an object or material has an intensity dependent refractive index, solitons can exist.

The materials which have been investigated in the following chapters include; cubic-quintic (examples of which include semiconductors AlGaAs [4], doped glasses CdS_xSe_{1-x} [5, 6], the polydiacetylene para-toluene sulfonate or 'PTS' π-conjugated polymer [7-9], chalcogenide glass Ag-As-Se [10-12], and transparent optical materials [13]), power-law (a more generalised example of a Kerr material, have been shown to exist in semiconductors, InSb [14] and GaAs/GaAlAs [15], doped filter glasses CdS_xSe_{1-x} [16] and liquid crystals such as MBBA [17]) and coupled-waveguide arrays (example of solitons in materials with CWA properties include long proteins [18], 1d ionic crystals [19] and electrical lattices [20]).

This thesis marries analytical and numerical approaches in the investigation of soliton behaviour at nonlinear interfaces – an area of optics which still remains relatively under investigated. The study is important in that it will give us a better understanding of the properties of solitons and the materials through which they travel in advance of their further use in optical technologies [21-31]. This work means that we can identify potential pitfalls in the development of such technologies, including data transfer and all optical switching [3] without the need for more extensive (and costly) physical experiments.

This study is also novel in that it calls for the use of the nonlinear Helmholtz approach to modelling soliton behaviour. Using the Helmholtz equation over the nonlinear Schrödinger equation as has been done elsewhere [32-43], provides more robust results

and gives the opportunity to explore soliton properties when they propagate at arbitrary angles - the advantages of Helmholtz soliton theory will be given in 1.3.

1.1 Spatial optical solitons

Spatial optical solitons are beams of laser light that can propagate in nonlinear optical materials, as mentioned, a material whose refractive index has a local intensity-dependent contribution. They are self-collimating, i.e. they evolve with a stationary intensity profile and uniform phase fronts, and self-stabilising in that they are robust against perturbations. These two key properties mean that solitons could be used to carry bits of data in future optical devices [21-31].

The self-focusing (and self-defocusing) of continuous wave (CW) beams in a bulk nonlinear medium has been the subject of a number of earlier studies [2, 44, 45]. A spatial soliton is formed when an equilibrium point is found between the nonlinear effects of the medium and the diffractive effects of the beam. This is highlighted in the figure below:

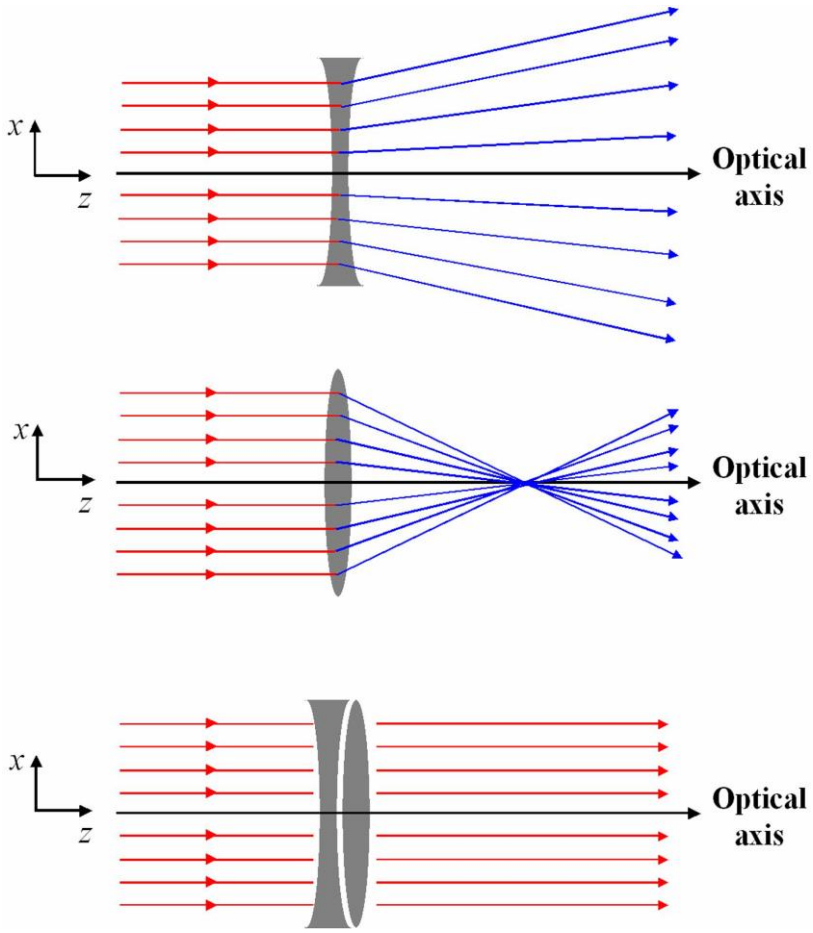

Figure 1 Showing how the equilibrium point between the focusing of the material and the diffraction of the beam lead to a spatial soliton.

The formation of a soliton is possible in a nonlinear medium (such as a Kerr type material) because of the intensity dependence of the medium's refractive index. This acts like a lens, causing the beam to focus, overcoming its natural tendency to diffract. This system is a result of its own optical waveguide since the light is confined ('trapped') to the high-index region because of the balance created by the conditions found in the system[46]. Before this response was discovered, this type of waveguide phenomenon was frequently purposely created in linear systems. This was done by introducing an increasing refractive index in the transverse region occupied by the beam [46].

The work in this thesis explores the behaviour of beams created by the self-focusing of continuous wave beams, i.e. bright spatial solitons. While properties of beams created by self-defocusing (dark solitons) are certainly of interest (see here [35, 38, 43]) the exploration of their behaviour in nonlinear systems is beyond the scope of this thesis.

1.2 Geometries: single- and multi-interface problems

The work in this thesis is based on two different types of interfaces. The first introduced are single interfaces, which appear in chapters 2, 3 and 4. The single interface is a result of two adjoining dissimilar materials, that is, two materials with uniform nonlinear refractive index are either side of the interface. Interfaces of this type have been investigated in the past [36, 40, 41, 43, 47-50], and a variety of interface phenomenon seen at them, including Goos-Hänchen shifts [36, 42, 47] and surface waves [36, 51, 52]. In chapter 5, the interface investigated is a multi-interface [53-55], which means that the first material is similar to those discussed above, however, the second medium is a coupled waveguide array. The beam propagating from medium 1 to medium 2 will experience multiple changes in waveguide, hence multi-interface. Figure 2 highlights these two situations below:

Figure 2 Showing the difference between single- and multi-interface problems.

1.3 The role of Helmholtz modelling

Undoubtedly the most popular method of modelling the propagation of spatial solitons is the nonlinear Schrödinger (NLS) equation. This type of modelling is exhibited [47-50, 56] and explained [1] in many publications, despite its inherent disadvantages. The NLS equation is not the only way to model beams of this nature; the nonlinear Helmholtz (NLH) approach, while remaining less commonly used, is developing a reputation of producing more reliable and less restrictive results.

The NLH equation, first used for modelling solitons in [34], has been used extensively in a variety of soliton based investigations [32, 34, 36, 37, 39-43]. The intrinsic advantages of the NLH equation over the NLS equation are numerous and have led to its use in this study. These advantages will be set out here.

All studies exploring soliton behaviour which use the NLS as their governing equation require the implementation of paraxial approximations [47, 48]. Such a modelling approach leads to a number of physical limitations implicit in the governing equation, and restricts the general validity of conclusions that may be drawn about the refraction properties of nonlinear beams. The NLS equation forces the assumption of the following three criteria:

i. the width of the beam is broad in comparison to the carrier wavelength;

ii. the beam is of moderate intensity;

iii. the beam must propagate very close to the reference direction.

In this research programme, Helmholtz soliton theory has been deployed to relax the third restriction: broad beams of moderate intensity may now propagate at *arbitrary angles of incidence, reflection and refraction with respect to the interface*. This intrinsic advantage of the NLH equation allows for a study of wider scope, and one which more accurately reflects the actual properties of solitons in the physical world, and theoretical and computational models need to account for this. The following section explains how we can reach the nonlinear Helmholtz governing equation from first principles.

1.4 Nonlinear Maxwell's equations

As has been identified, the use of Helmholtz soliton theory has intrinsic advantage over other approaches. In this section, it will be shown how to arrive at the nonlinear Helmholtz equation used throughout this thesis from first principles.

For a dielectric medium where $\tilde{\mathbf{B}} = \mu\tilde{\mathbf{H}}$, Maxwell's equations may be written as:

$$\nabla \times \tilde{\mathbf{B}} = \mu \frac{\partial \tilde{\mathbf{D}}}{\partial t}, \tag{1.1}$$

$$\nabla \cdot \tilde{\mathbf{D}} = 0, \tag{1.2}$$

$$\nabla \times \tilde{\mathbf{E}} = -\frac{\partial \tilde{\mathbf{B}}}{\partial t}, \tag{1.3}$$

$$\nabla \cdot \tilde{\mathbf{B}} = 0, \tag{1.4}$$

where $\tilde{\mathbf{E}}$ is the electric field vector, $\tilde{\mathbf{B}}$ is the magnetic field vector, $\tilde{\mathbf{D}}$ is the electric displacement vector, $\tilde{\mathbf{H}}$ is the magnetic field strength vector, μ is the permeability of free space and t is time. In deriving a wave equation for the dielectric field, $\tilde{\mathbf{E}}$ and $\tilde{\mathbf{B}}$ are decoupled as a first step. This can be achieved by taking the curl of equation (1.3) and substituting (1.1):

$$\nabla\times\left(\nabla\times\tilde{\mathbf{E}}\right)=\nabla\times\left(\frac{\partial\tilde{\mathbf{B}}}{\partial t}\right), \tag{1.5}$$

which leads to

$$\nabla\times\left(\nabla\times\tilde{\mathbf{E}}\right)=\mu\frac{\partial^2\tilde{\mathbf{D}}}{\partial t^2}, \tag{1.6}$$

Now using an operator identity from vector calculus, namely

$$\nabla\times\left(\nabla\times\tilde{\mathbf{E}}\right)=\nabla\left(\nabla\cdot\tilde{\mathbf{E}}\right)-\nabla^2\tilde{\mathbf{E}}, \tag{1.7}$$

it follows that equation (1.6) becomes

$$-\nabla^2\tilde{\mathbf{E}}=-\mu\frac{\partial^2\tilde{\mathbf{D}}}{\partial t^2}. \tag{1.8}$$

The next step is to simplify the left hand side of equation (1.8) by replacing the $\nabla\cdot\tilde{\mathbf{E}}$ term with the constitutive relation that connects $\tilde{\mathbf{D}}$ to $\tilde{\mathbf{E}}$ through the polarisation, $\tilde{\mathbf{P}}$ (and the associated susceptibility tensors, χ). Consider the general definitions:

$$\tilde{\mathbf{D}}\equiv\varepsilon_0\tilde{\mathbf{E}}+\tilde{\mathbf{P}}, \tag{1.9}$$

$$\tilde{\mathbf{P}}\equiv\tilde{\mathbf{P}}^{\mathrm{L}}+\tilde{\mathbf{P}}^{\mathrm{NL}}, \tag{1.10}$$

where $\tilde{\mathbf{P}}^{\mathrm{L}}$ and $\tilde{\mathbf{P}}^{\mathrm{NL}}$ are the linear and nonlinear polarisation vectors, respectively and ε_0 is the permittivity of free space. When the linear response of the medium is isotropic, $\tilde{\mathbf{P}}^{\mathrm{L}}=\varepsilon_0\chi^{(1)}\tilde{\mathbf{E}}$, $\tilde{\mathbf{D}}=\varepsilon\tilde{\mathbf{E}}+\tilde{\mathbf{P}}^{\mathrm{NL}}$ and $\varepsilon=\varepsilon_0\varepsilon_r$, where $\varepsilon_r\equiv1+\chi^{(1)}$ and $\chi^{(1)}$ is the linear susceptability. In nonlinear optics, the nonlinear optical response can often be described by expressing the polarisation as a power series in the electric field strength:

$$\tilde{\mathbf{P}}=\varepsilon_0\left[\chi^{(1)}\tilde{\mathbf{E}}(t)+\chi^{(2)}\tilde{\mathbf{E}}^2(t)+\chi^{(3)}\tilde{\mathbf{E}}^3(t)+\chi^{(4)}\tilde{\mathbf{E}}^4(t)+\chi^{(5)}\tilde{\mathbf{E}}^5(t)\right]. \tag{1.11}$$

where the second- and fourth-order polarisation terms only occur in noncentrosymmetric crystals (crystals that do not display inversion symmetry) and therefore vanish in the materials considered in this thesis [1]. By combining this constitutive relation with equation (1.2) it follows that:

$$\nabla \cdot \tilde{\mathbf{E}} = -\frac{1}{\varepsilon}\tilde{\mathbf{E}} \cdot \nabla \varepsilon - \frac{1}{\varepsilon}\nabla \cdot \tilde{\mathbf{P}}^{\mathrm{NL}}. \tag{1.12}$$

Hence, even when the linear dielectric properties of a host medium are uniform i.e. where gradients $\nabla\varepsilon$ are zero, the divergence $\nabla \cdot \tilde{\mathbf{E}}$ is generally non-vanishing. To proceed a homogeneous linear medium is assumed, so that $\nabla\varepsilon = 0$. Then by substituting equation (1.12) into equation, it obtains that:

$$\nabla\left(-\frac{1}{\varepsilon}\nabla \cdot \tilde{\mathbf{P}}^{\mathrm{NL}}\right) - \nabla^2\tilde{\mathbf{E}} = \mu\varepsilon\frac{\partial^2\tilde{\mathbf{E}}}{\partial t^2} - \mu\frac{\partial^2\tilde{\mathbf{P}}^{\mathrm{NL}}}{\partial t^2}, \tag{1.13}$$

which leads to

$$\varepsilon\mu\frac{\partial^2\tilde{\mathbf{E}}}{\partial t^2} - \nabla^2\tilde{\mathbf{E}} = \frac{1}{\varepsilon}\nabla\left(\nabla \cdot \tilde{\mathbf{P}}^{\mathrm{NL}}\right) - \mu\frac{\partial^2\tilde{\mathbf{P}}^{\mathrm{NL}}}{\partial t^2}. \tag{1.14}$$

By assuming the carrier wave has

$$\tilde{\mathbf{E}}(x,z,t) = \mathbf{E}(x,z)\exp(-i\omega t) + \mathbf{E}^*(x,z)\exp(+i\omega t), \tag{1.15}$$

where equation (1.15) is the continuous wave solution and ω is the angular frequency. The nonlinear polarisation is

$$\tilde{\mathbf{P}}^{\mathrm{NL}}(x,z,t) = \mathbf{P}^{\mathrm{NL}}(x,z)\exp(-i\omega t) + \mathbf{P}^{\mathrm{NL}}{}^*(x,z)\exp(+i\omega t), \tag{1.16}$$

then equation (1.14) becomes

$$-\mu\omega^2\varepsilon(\tilde{\mathbf{E}}) - \nabla^2\tilde{\mathbf{E}} = \frac{1}{\varepsilon}\nabla\left(\nabla \cdot \tilde{\mathbf{P}}^{\mathrm{NL}}\right) + \mu\omega^2(\tilde{\mathbf{P}}^{\mathrm{NL}}). \tag{1.17}$$

If $\tilde{\mathbf{E}}$ is linearly polarised in the *y* direction and propagates along the *z* direction, and if, therefore, the $\nabla \cdot \left(\nabla \cdot \tilde{\mathbf{P}}^{NL}\right)$ term is neglected, it emerges that

$$\frac{\partial^2 E}{\partial z^2} + \frac{\partial^2 E}{\partial x^2} + \frac{\omega^2}{c^2}n_j^2(E)E = 0. \tag{1.18}$$

Where $n_{(j)}$ is the general refractive index (including linear and nonlinear effects). Equation (1.18) is the nonlinear Helmholtz equation, which is the starting point to the analysis of all the research in the following chapters.

An assumption is made that the nonlinearities are nonresonant. Whilst this assumption excludes the consideration of some nonlinear effects, such as frequency doubling, these effects are not relevant to the work done in this thesis [57-59]; the effects of interest are described by equations discussed in section 2.2.

1.5 Thesis outline

In order to methodically describe and explain bright soliton behaviour at a variety of interfaces, the thesis will be structured as follows.

Chapter 2 discusses the reflection and refraction characteristics of soliton beams incident on the planar boundary between dissimilar cubic-quintic materials. The deployment of Helmholtz soliton theory allows for the simultaneous consideration of: (i) arbitrary angles of incidence, reflection and refraction (relative to the interface), and (ii) finite beam waists (as opposed to infinitely-wide plane waves). Despite an abundance of literature concerning solitons at interfaces, there appears to be no published research addressing refraction in the presence of cubic-quintic optical nonlinearity (and certainly none in arbitrary-angle contexts). Excellent agreement is generally found between theoretical predictions from a generalised Snell's law and results from extensive computer simulations.

In Chapter 3, these novel analyses have been complemented by further investigations into other fundamental aspects of optical refraction, namely Goos-Hänchen shifts and critical angle prediction. Both aspects are the first of their kind in the cubic-quintic regime.

The fourth chapter considers surface wave propagation along the interface between two dissimilar power-law materials; this research has already contributed to a published peer reviewed paper [36]. The chapter also expands upon that paper by giving a more detailed account of surface wave stability properties.

Chapter 5 provides an in-depth computational study into beam propagation in coupled waveguide arrays (materials whose refractive index is periodically patterned) and there appears to be a link between the beam's critical angle and the depth of the modulation of the array.

The thesis concludes with a summary of findings and suggestions surrounding the implications of this novel research.

1.6 References

1. R.W. Boyd, *Nonlinear Optics* 1992, London: Academic Press.
2. Z. Chen, M. Segev, and D.N. Christodoulides *Optical spatial solitons: historical overview and recent advances*. Reports on Progress in Physics, 2012. **75**, DOI: 086401.
3. Y.S. Kivshar and G.I. Stegeman, *Spatial Optical Soliton Guiding Light for Future Technonogies.* Optics & Photonics News, 2002. **13**(2): p. 59-63.
4. S. Tanev and D.I. Pushkarov, *Solitary wave propagation and bistability in the normal dispersion region of highly nonlinear optical fibres and waveguides.* Optics Communications, 1997. **141**(5-6): p. 322-328.
5. L.H. Acioli, A.S.L. Gomes, J.M. Hickmann, and C.B.d. Araujo, *Femtosecond dynamics of semiconductor-doped glasses using a new source of incoherent light.* Applied Physics Letters, 1990. **56**(23): p. 2279-2281.
6. P. Roussignol, D. Ricard, J. Lukasik, and C. Flytzanis, *New results on optical phase conjugation in semiconductor-doped glasses.* Journal of the Optical Society of America B, 1987. **4**(1): p. 5-13.
7. B.L. Lawrence and G.I. Stegeman, *Two-dimensional bright spatial solitons stable over limited intensities and ring formation in polydiacetylene para-toluene sulfonate.* Optics Letters, 1998. **23**(8): p. 591-593.
8. B.L. Lawrence, M. Cha, W.E. Torruellas, G.I. Stegeman, S. Etemad, G. Baker, and F. Kajzar, *Measurement of the complex nonlinear refractive index of single crystal p-toluene sulfonate at 1064 nm.* Applied Physics Letters, 1994. **64**(21): p. 2773-2775.
9. B.L. Lawrence, W.E. Torruellas, M. Cha, M.L. Sundheimer, G.I. Stegeman, J. Meth, S. Etemad, and G. Baker, *Identification and Role of Two-Photon Excited States in a π-Conjugated Polymer.* Physical Review Letters, 1994. **73**(4): p. 597-600.
10. G. Boudebs, S. Cherukulappurath, H. Leblond, J. Troles, F. Smektala, and F. Sanchez, *Experimental and theoretical study of higher-order nonlinearities in chalcogenide glasses.* Optics Communications, 2003. **219**(1-6): p. 427-433.
11. F. Smektala, C. Quemard, V. Couderc, and A. Barthélémy, *Non-linear optical properties of chalcogenide glasses measured by Z-scan.* Journal of Non-Crystalline Solids, 2000. **274**(1-3): p. 232-237.
12. K. Ogusu, J. Yamasaki, S. Maeda, M. Kitao, and M. Minakata, *Linear and nonlinear optical properties of Ag-As-Se chalcogenide glasses for all-optical switching.* Optics Letters, 2004. **29**(3): p. 265-267.
13. C. Zhan, D. Zhang, D. Zhu, D. Wang, Y. Li, D. Li, Z. Lu, L. Zhao, and Y. Nie, *Third- and fifth-order optical nonlinearities in a new stilbazolium derivative.* Journal of the Optical Society of America B, 2002. **19**(3): p. 369-375.
14. J. Mathew, A. Kar, N. Heckenburg, and I. Galbraith, *Time resolved self-defocusing in InSb at room temperature.* IEEE Journal of Quantum Electronics, 1985. **21**(1): p. 94-99.
15. D.S. Chemla, D.A.B. Miller, and P.W. Smith, *Nonlinear optical properties of GaAs/GaAlAs multiple quantum well material: phenomena and applications.* Optical Engineering, 1985. **24**(4): p. 556-564.
16. S.S. Yao, C. Karaguleff, A. Gabel, C. Fortenberry, C.T. Seaton, and G.I. Stegeman, *Ultrafast carrier and grating lifetimes in semiconductor-doped glasses.* Applied Physics Letters, 1985. **46**(9): p. 801-803.
17. D. Mihalache, M. Bertolotti, and C. Sibilia, *Nonlinear wave propagation in planar structures.* Progress in Optics, 1989. **27**(1): p. 229-313.
18. A.S. Davydov, *Solitons in molecular systems.* Physica Scripta, 1979. **20**(3-4): p. 387-394.
19. T. Holstein, *Studies of polaron motion.* Annals of Physics, 1959. **8**(1): p. 325-343.
20. P. Marquié, J.M. Bilbault, and M. Remoissenet, *Observation of nonlinear localized modes in an electrical lattice.* Physical Review E, 1995. **51**(6): p. 6127-6133.
21. G.S. McDonald and W.J. Firth, *All-optical switching in a nonlinear resonator.* Journal of Modern Optics, 1990. **37**(4): p. 613-626.
22. G.S. McDonald and W.J. Firth, *Spatial solitary-wave optical memory.* Journal of the Optical Society of America B, 1990. **7**(7): p. 1328-1335.
23. G.S. McDonald and W.J. Firth, *Switching dynamics of spatial solitary wave pixels.* Journal of the Optical Society of America B, 1993. **10**(6): p. 1081-1089.
24. M. Brambilla, L.A. Lugiato, F. Prati, L. Spinelli, and W.J. Firth, *Spatial Soliton Pixels in Semiconductor Devices.* Physical Review Letters, 1997. **79**(11): p. 2042-2045.
25. W.J. Firth and G.K. Harkness, *Cavity solitons.* Asian Journal of Physics, 1998. **7**(3): p. 665-677.

26. W.J. Firth and A.J. Scroggie, *Optical Bullet Holes: Robust Controllable Localized States of a Nonlinear Cavity*. Physical Review Letters, 1996. **76**(10): p. 1623-1626.
27. L. Spinelli and M. Brambilla, *Signal amplification by means of cavity solitons in semiconductor microcavities.* European Physics Journal D, 1999. **6**(1): p. 523-532.
28. L. Spinelli, G. Tissoni, M. Brambilla, F. Prati, and L.A. Lugiato, *Spatial solitons in semiconductor microcavities.* Physical Review A, 1998. **58**(3): p. 2542-2559.
29. G. Tissoni, L. Spinelli, M. Brambilla, T. Maggipinto, M. Perrini, and L.A. Lugiato, *Cavity solitons in passive bulk semiconductor Microcavities. I. Microscopic and modulational instabilities.* Journal of the Optical Society of America B, 1999. **16**(11): p. 2083-2094.
30. G. Tissoni, L. Spinelli, M. Brambilla, T. Maggipinto, I.M. Perrini, and L.A. Lugiato, *Cavity solitons in passive bulk semiconductor microcavities. II. Dynamical properties and control.* Journal of the Optical Society of America B, 1999. **16**(11): p. 2095-2105.
31. L.A. Lugiato, L. Spinelli, G. Tissoni, and M. Brambilla, *Modulational instabilities and cavity solitons in semiconductor microcavities.* Journal of Optics B - Quantum Semiconductors, 1999. **1**(1): p. 43-51.
32. P. Chamorro-Posada, G.S. McDonald, and G.H.C. New, *Propagation Properties of Nonparaxial Spatial Solitons.* Journal of Modern Optics, 2000. **47**(11): p. 1877-1886.
33. P. Chamorro-Posada, G.S. McDonald, and G.H.C. New, *Non-paraxial beam propagation methods.* Optics Communications, 2001. **192**(1–2): p. 1-12.
34. P. Chamorro-Posada, G.S. McDonald, and G.H.C. New, *Non-paraxial solitons.* Journal of Modern Optics, 1998. **45**(6): p. 1111-1121.
35. P. Chamorro-Posada and G.S. McDonald, *Helmholtz Dark Solitons.* Optics Letters, 2003. **28**(10): p. 825-827.
36. J.M. Christian, E.A. McCoy, G.S. McDonald, J. Sánchez-Curto, and P. Chamorro-Posada *Interaction of Helmholtz bright spatial solitons with power-law optical interfaces*. Journal of Atomic and Molecular Physics, 2012. **2012**, DOI: 137967.
37. J.M. Christian, G.S. McDonald, and P. Chamorro-Posada *Bistable Helmholtz solitons in cubic-quintic materials*. Physical Review A, 2007. **76**, DOI: 033833.
38. J.M. Christian, G.S. McDonald, and P. Chamorro-Posada *Bistable dark solitons of a cubic-quintic Helmholtz equation*. Physical Review A, 2010. **81**, DOI: 053831.
39. J.M. Christian, G.S. McDonald, R.J. Potton, and P. Chamorro-Posada *Helmholtz solitons in power-law optical materials*. Physical Review A, 2007. **76**, DOI: 033834.
40. J. Sánchez-Curto, P. Chamorro-Posada, and G.S. McDonald, *Helmholtz solitons at nonlinear interfaces.* Optics Letters, 2007. **32**(9): p. 1126-1128.
41. J. Sánchez-Curto, P. Chamorro-Posada, and G.S. McDonald *Nonlinear interfaces: intrinsically nonparaxial regimes and effects*. Journal of Optics A: Pure and Applied Optics, 2009. **11**, DOI: 054015.
42. J. Sánchez-Curto, P. Chamorro-Posada, and G.S. McDonald, *Giant Goos-Hänchen shifts and radiation-induced trapping of Helmholtz solitons at nonlinear interfaces.* Optics Letters, 2011. **36**(18): p. 3605-3607.
43. J. Sánchez-Curto, P. Chamorro-Posada, and G.S. McDonald *Black and gray Helmholtz Kerr soliton refraction*. Physical Review A, 2011. **83**, DOI: 013828.
44. B. Bendow, P.D. Gianino, and N. Tzoar, *Theory of continuous-wave beam propagation in nonlinear optical waveguides.* Journal of the Optical Society of America, 1981. **71**(6): p. 656-663.
45. D. Burak and W. Nasalski, *Gaussian beam to spatial soliton formation in Kerr media.* Applied Optics, 1994. **33**(27): p. 6393-6401.
46. Y.S. Kivshar and G.P. Agrawal, *Optical Solitons From Fibers to Photonic Crystals* 2003, California, USA: Academic Press.
47. A.B. Aceves, J.V. Moloney, and A.C. Newell, *Theory of light-beam propagation at nonlinear interfaces. I. Equivalent-particle theory for a single interface.* Physical Review A, 1989. **39**(4): p. 1809-1827.
48. A.B. Aceves, J.V. Moloney, and A.C. Newell, *Theory of light-beam propagation at nonlinear interfaces. II. Multiple-particle and multiple-interface extensions.* Physical Review A, 1989. **39**(4): p. 1828-1840.
49. A.B. Aceves, J.V. Moloney, and A.C. Newell, *Reflection and transmission of self-focused channels at nonlinear dielectric interfaces.* Optics Letters, 1988. **13**(11): p. 1002-1004.
50. A.B. Aceves, J.V. Moloney, and A.C. Newell, *Snell's laws at the interface between nonlinear dielectrics.* Physics Letters A, 1988. **129**(4): p. 231-235.
51. A.W. Snyder and H.T. Tran, *Surface modes of power law nonlinearities.* Optics Communications, 1992. **98**(4-6): p. 309-312.

52. J.-G. Ma and Z. Chen, *Nonlinear surface waves on the interface of two non-Kerr-like nonlinear media.* IEEE Transactions on Microwave theory and Techniques, 1997. **45**(6): p. 924-930.
53. D. Mandelik, H.S. Eisenberg, Y. Silberberg, R. Morandotti, and J.S. Aitchison *Band-Gap Sturucture of Waveguide Arrays and Excitation of Floquet-Bloch Solitons*. Physical Review Letters, 2003. **90**, DOI: 053902.
54. D. Mandelik, R. Morandotti, J.S. Aitchison, and Y. Silberberg *Gap Solitons in Waveguide Arrays*. Physical Review Letters, 2004. **92**, DOI: 093904.
55. A.A. Sukhorukov, D. Neshev, W. Krolikowski, and Y.S. Kivshar *Nonlinear Bloch-Wave Interaction and Bragg Scattering in Optically Induced Lattices*. Physical Review Letters, 2004. **92**, DOI: 093901.
56. A.B. Aceves, P. Varatharajah, A.C. Newell, E.M. Wright, G.I. Stegeman, D.R. Heatley, J.V. Moloney, and H. Adachihara, *Particle aspects of collimated light channel propagation at nonlinear interfaces and in waveguides.* Journal of the Optical Society of America B, 1990. **7**(6): p. 963-974.
57. P. Chamorro-Posada and G.S. McDonald *Time domain analysis of Helmholtz soliton propagation using the TLM method*. Journal of Nonlinear Optical Physics & Materials, 2012. **21**, DOI: 1250031.
58. Y.S. Kivshar and B. Luther-Davis, *Dark optical solitons: physics and applications.* Physics Reports, 1988. **298**(1): p. 81-197.
59. R.A. Sammut, A.V. Buryak, and Y.S. Kivshar, *Modification of solitary waves by third-harmonic generation.* Optics Letters, 1997. **22**(1): p. 1388-1390.

2. Single interfaces I: cubic-quintic systems

2.1 Introduction

This section will focus specifically on the refraction of spatial solitons at the interface between dissimilar cubic-quintic materials (see Figure 3). Examples of such materials include some semiconductors, e.g. AlGaAs [1] and doped filter glasses, e.g. CdS_xSe_{1-x} [2, 3]. This is the first time that Helmholtz soliton theory has been used to investigate refraction with the universal cubic-quintic optical nonlinearity. Previous analyses have considered only Kerr-type [4-6] and more recently, power-law [7] materials (where Helmholtz solitons were shown to well-describe nonparaxial, i.e., arbitrary angle, refraction). The motivation here is to derive a novel Snell's law that may be used to predict the arbitrary-angle refraction of finite-amplitude beams in the most general nonlinear-medium context to date. The problem is first analysed mathematically, and theoretical predictions are subsequently tested computationally.

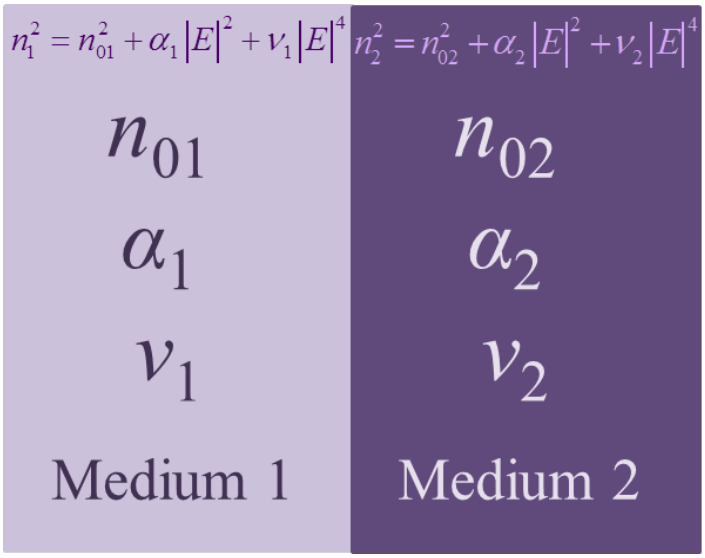

Figure 3. Schematic diagram showing a typical set-up for an interface between dissimilar cubic-quintic materials, and the parameters which can be varied across the interface. The values of these parameters will define whether the interface is linear, nonlinear, or mixed.

2.1.1 Nonlinear Polarisation

The material being investigated in chapters 2 and 3 has the refractive index, seen in Figure 3, which will be discussed more in 2.2.1. Within the assumptions of scalar wave optics, the nonlinear polarisation for such a material can be written as:

$$P = \varepsilon_0 \left[\chi^{(1)} E + \frac{3}{4} \chi^{(3)} |E|^2 E + \frac{5}{8} \chi^{(5)} |E|^4 E \right], \tag{2.1}$$

where E is the (complex) electric field, $\chi^{(1)}$ is the linear susceptibility, while $\chi^{(3)}$ and $\chi^{(5)}$ are the third and fifth order nonlinear susceptibilities, respectively. The first term on the RHS of (2.1) is the linear polarization term and the last two terms are the nonlinear polarisation terms. It is the last two terms in equation (2.1) which give materials with the refractive index (2.4) the name 'cubic-quintic' [8].

2.1.2 Defining Interface Problems

A nonlinear material is one with a contribution to the refractive index n of the form $n_{\mathrm{NL}} = n_{\mathrm{NL}}(E)$, where E is the local electric field amplitude (a more detailed mathematical treatment will be given in section 2.2.1). The incident beam travels from medium $j = 1$ to medium $j = 2$, where the values of n_{0j} (the linear part of the refractive index), α_j and ν_j (nonlinearity coefficients) vary across the interface (strictly, it is the abrupt changes in these parameters that define the interface itself). When $n_{01} = n_{02}$ (no change in linear refractive index), the interface may be classified as *nonlinear*. Similarly, when $\alpha \equiv \alpha_2/\alpha_1 = 1$ and $\nu \equiv \nu_2/\nu_1 = 1$, the interface is classified as *linear*. *Mixed* interfaces have, in general, arbitrary changes in the medium parameters.

2.1.3 Literature Review

The seminal papers dealing with spatial solitons at interfaces were by Aceves and co-workers nearly 30 years ago [9-13]. This extensive body of research explores the behaviour of beams at Kerr-type interfaces within the restriction of paraxial wave optics (see section 1.3). Reference [9] develops an equivalent particle theory, whereby the soliton is modelled as a spatially-averaged particle moving in an equivalent potential (whose shape depends upon, for instance, material mismatches). While this paper has provided general background reading, the paraxial analysis therein is not particularly relevant to the fully angular (i.e., Helmholtz nonparaxial) problem. For instance, a similar description of Helmholtz solitons is of limited practical use: it has no simple 'Newtonian mechanics' interpretation and provides reasonably accurate predictions only at moderate angles of incidence.

The theoretical cornerstone for this chapter is to be found in the papers by Sánchez-Curto, Chamorro-Posada, and McDonald [4, 6]. This work investigates the behaviour of solitons

at Kerr-type interfaces but, crucially, avoids the use of the paraxial approximation. In this way, the first beam-refraction model based on an inhomogeneous nonlinear Helmholtz equation could be developed. Their approach provides an analytical platform that allows for angles (incidence, reflection, and refraction) of *any* size (with respect to the interface) to be investigated. The paper also reports a novel generalisation of Snell's law, which includes a generic multiplicative correction factor. Computer simulations are used to test, and confirm, the appropriateness of the model. Results show excellent agreement between theoretical predictions and full numerical calculations.

The same authors have more recently published a follow-up paper [5]. This article focuses on two particular phenomena under these conditions: nonlinear external refraction and total internal reflection, again, good agreement is shown between the theory and numerics.

The final paper that plays a fundamental role in this chapter is by Christian, McDonald, and Chamorro-Posada [14]. This article reports the first exact analytical bright solitons for a Helmholtz equation with cubic-quintic nonlinearity. Mathematical and computational analyses are used to investigate the stability properties of the new Helmholtz solitons against perturbations to the beam shape.

2.2 Solitons at Interfaces

2.2.1 Model Equation

Underpinning the subsequent analysis is the continuous-wave scalar electric field,

$$\tilde{E}(x,z,t) = E(x,z)\exp(-i\omega t) + E^{*}(x,z)\exp(+i\omega t), \tag{2.2}$$

where x and z are the spatial coordinates in the medium, t is the time coordinate and ω is the optical (angular) frequency. This representation makes sure that $\tilde{E}$ remains real, as should be the case. If the spatial part of the electric field is slowly varying on the scale of the free-space optical wavelength λ, then $E(x,z)$ must satisfy a nonlinear Helmholtz equation on each side of the material boundary:

$$\frac{\partial^2 E}{\partial z^2} + \frac{\partial^2 E}{\partial x^2} + \frac{\omega^2}{c^2} n_j^2(E)E = 0, \tag{2.3}$$

where $j = 1, 2$ denotes the medium and c is the vacuum speed of light. The total refractive index n_j is routinely taken to be the sum of two terms: $n_j = n_{0j} + n_{\mathrm{NL}j}(E)$, where n_{0j} is the linear index of the medium at frequency ω, and $n_{NLj}(E)$ is a (small) field-dependent

contribution. Since equation (2.3) is quadratic in n_j, it follows that $n_j^2 = n_{0j}^2 + 2n_{0j}n_{\mathrm{NL}}(E) + n_{\mathrm{NL}}^2(E)$. However, since $|n_{\mathrm{NL}j}(E)|/n_{0j} << O(1)$, the last term may be safely neglected so that $n_j^2 \approx n_{0j}^2 + 2n_{0j}n_{\mathrm{NL}j}(E)$. For cubic-quintic materials, the nonlinear part of the refractive index may be written as $n_{\mathrm{NL}j}(E) = (2n_{0j})^{-1}(\alpha_j|E|^2 + \nu_j|E|^4)$, and hence

$$n_j^2 \equiv n_{0j}^2 + \alpha_j |E|^2 + \nu_j |E|^4 . \tag{2.4}$$

Here, α_j is the cubic (or Kerr) coefficient, which is taken to be positive, and ν_j is the quintic correction term which can be either positive or negative [14].

To facilitate a straightforward analysis with earlier works [9-13, 15, 16], a carrier-wave component, $\exp(ik_1z)$, can be factored out of $E(x,z)$:

$$E(x,z) = E_0 u(x,z) \exp(ik_1 z). \tag{2.5}$$

Here, E_0 is a real constant, $k_1 = (\omega/c)n_{01}$, and $u(x,z)$ is the dimensionless envelope. The target is now to find an equation for u. It can be shown (see Appendix B) that u satisfies the inhomogeneous nonlinear Helmholtz equation,

$$\kappa \frac{\partial^2 u}{\partial \zeta^2} + i\frac{\partial u}{\partial \zeta} + \frac{1}{2}\frac{\partial^2 u}{\partial \xi^2} + |u|^2 u + \sigma |u|^4 u = \left[\frac{\Delta}{4\kappa} + (1-\alpha)|u|^2 + (1-\nu)\sigma |u|^4 \right] H(\xi) u \tag{2.6}$$

The longitudinal and transverse coordinates are normalised according to $\zeta = z/L_{\mathrm{D1}}$ and $\xi = 2^{1/2}x/w_0$, respectively, where $L_{\mathrm{D1}} = k_1 w_0^2/2$ is the diffraction length of a reference (paraxial) Gaussian beam of full waist w_0. Since the validity of equation (2.6) requires $\varepsilon \equiv \lambda/w_0 << O(1)$ (i.e., that beam waists are much larger than the free-space light wavelength), the inequality $\kappa \equiv (1/k_1 w_0)^2 = \varepsilon^2/4\pi^2 n_{01}^2 << O(1)$ is maintained throughout. By measuring the laboratory electric field in units of $E_0 = (n_0/kn_2L_{\mathrm{D}})^{1/2}$, the small parameter $\sigma \equiv \nu_1 E_0^2/\alpha_1$ describes the ratio of quintic to cubic nonlinear phase shifts. The Heaviside unit function $H(\xi)$ is defined by $H(\xi < 0) = 0$ and $H(\xi > 0) = 1$ (see Figure 2) so that in the domain of medium 1, equation (2.6) is just the conventional cubic-quintic Helmholtz equation [14]. The model is also supplemented by three parameters that describe the mismatch between the linear and nonlinear properties of the two media (note that only relative changes are important):

$$\Delta \equiv 1 - \left(\frac{n_{02}}{n_{01}} \right)^2, \qquad \alpha \equiv \frac{\alpha_2}{\alpha_1}, \qquad \nu \equiv \frac{\nu_2}{\nu_1}. \qquad \text{(2.7) a, b \& c}$$

In the classic paraxial models (based upon the universal nonlinear Schrödinger equation), the Δ parameter is absorbed into system normalisation (the transverse coordinate is scaled by a factor proportional to $\Delta^{1/2}$). One immediate consequence of such a scaling is that only those material configurations with $\Delta > 0$ (i.e., $n_{02} < n_{01}$) may be considered. It will be shown shortly that a refraction regime of fundamental physical importance (namely, *external refraction*) is automatically excluded from the paraxial domain.

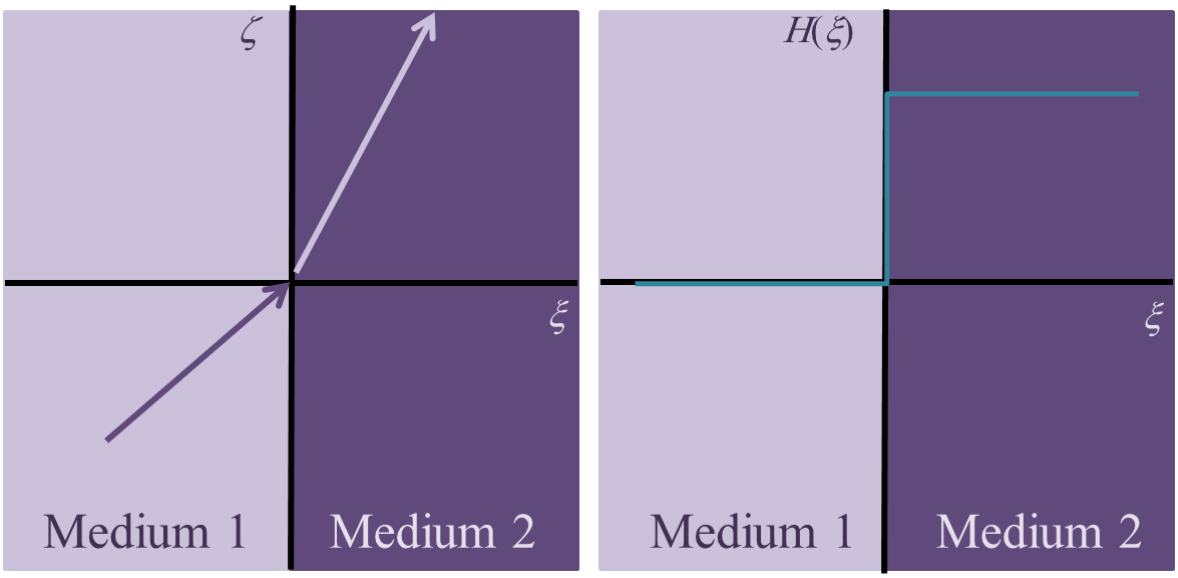

Figure 4. Schematic diagram showing refraction at an interface. In the first medium, ξ is negative and the Heaviside unit function H = 0. In the second medium, ξ is positive and H = 1.

2.2.2 Mathematical Method

The mathematical procedure for deriving Snell's law for soliton beams can be broken down into stages:

i. Derive the exact analytical soliton solutions in the two media,
ii. Apply the continuity conditions at the interface,
iii. Exploit the geometrical relations to find Snell's law in terms of angles.

Strictly, *u* and its normal derivative should be continuous across the interface. However, enforcing these two conditions in the context of scalar modelling can lead to erroneous predictions (mainly, that a finite-amplitude beam can never refract across the interface).

The work of Sánchez-Curto *et al.* [4] showed that Helmholtz solitons at interfaces can be very well described by enforcing only *phase continuity* across the interface.

2.2.3 Exact Bright Solitons

From equation (2.6), the governing equations in each medium can be isolated as:

Medium 1:
$$\kappa\frac{\partial^2 u}{\partial\zeta^2}+i\frac{\partial u}{\partial\zeta}+\frac{1}{2}\frac{\partial^2 u}{\partial\xi^2}+|u|^2 u+\sigma|u|^4 u=0, \tag{2.8}$$

Medium 2:
$$\kappa\frac{\partial^2 u}{\partial\zeta^2}+i\frac{\partial u}{\partial\zeta}+\frac{1}{2}\frac{\partial^2 u}{\partial\xi^2}-\frac{\Delta}{4\kappa}u+\alpha|u|^2 u+\nu\sigma|u|^4 u=0. \tag{2.9}$$

On-axis soliton solutions of equations (2.8) and (2.9) may be sought using an ansatz:

$$u(\xi,\zeta)=A\left[1+B\cosh(C\xi)\right]^{-1/2}\exp\left(ik_\zeta\zeta\right)\exp\left(-i\frac{\zeta}{2\kappa}\right), \tag{2.10}$$

where A, B, C and k_ζ (the propagation constant) are real parameters. Substituting equation (2.10) into equations (2.8) and (2.9) yields

$$k_\zeta=\pm\frac{1}{2\kappa}\sqrt{1+4\kappa\beta}, \tag{2.11}$$

where the ± sign in the phase flags the longitudinal sense of propagation (forward or backwards in z, respectively). The other solution parameters for the solution (2.10) in each medium are given in Table 1:

Medium 1:	Medium 2:
$4\beta=A^2=2\rho_0\left(1+\frac{2}{3}\sigma\rho_0\right)$	$\frac{4}{\alpha}\left(\beta+\frac{\Delta}{4\kappa}\right)=A^2=2\rho_0\left(1+\frac{2}{3}\frac{\nu\sigma\rho_0}{\alpha}\right)$
$B=1+\frac{4}{3}\sigma\rho_0$	$B=1+\frac{4}{3}\frac{\nu\sigma\rho_0}{\alpha}$
$C=2\sqrt{2\beta}=2\left[\rho_0\left(1+\frac{2}{3}\sigma\rho_0\right)\right]^{1/2}$	$C=2\sqrt{2\left(\beta+\frac{\Delta}{4\kappa}\right)}=2\left[\rho_0\left(\alpha+\frac{2}{3}\nu\sigma\rho_0\right)\right]^{1/2}$

Table 1 showing the parameters for the exact soliton solution.

To generate more general off-axis solitons, the following rotational transformation is applied to solution (2.10) (which leaves the parameters A, B, C and β unchanged):

Direct:	Inverse:
$\xi = \frac{\xi' - V\zeta'}{\sqrt{1+2\kappa V^2}}$	$\xi' = \frac{\xi + V\zeta}{\sqrt{1+2\kappa V^2}}$
$\zeta = \frac{2\kappa V\xi' + \zeta'}{\sqrt{1+2\kappa V^2}}$	$\zeta' = \frac{-2\kappa V\xi + \zeta}{\sqrt{1+2\kappa V^2}}$

Table 2 showing the transformations needed to find the off axis solutions.

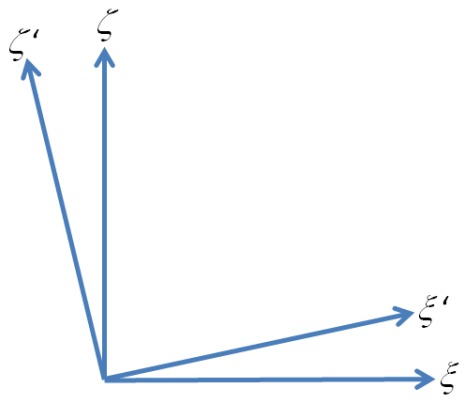

Figure 5 Shows the two coordinate frames of the on, and off axis solutions.

The off axis solution in medium 1 is

$$u(\xi,\zeta) = \left\{\frac{4\beta_{\text{inc}}}{1+B_{\text{inc}}\cosh\left[\Theta_{\text{inc}}(\xi,\zeta)\right]}\right\}^{1/2} \exp\left[\pm i\sqrt{\frac{1+4\kappa\beta_{\text{inc}}}{1+2\kappa V_{\text{inc}}^2}}\left(V_{\text{inc}}\xi + \frac{\zeta}{2\kappa}\right)\right]\exp\left(-i\frac{\zeta}{2\kappa}\right),$$

(2.12)

where $B_{\text{inc}} \equiv 1 + (4/3)\sigma\rho_0$, ρ_0 is the peak intensity of the beam, $\beta_{\text{inc}} \equiv (\rho_0/2)[1 + (2/3)\sigma\rho_0]$ is related to the propagation constant of the corresponding paraxial solution, and $\Theta_{\text{inc}}(\xi,\zeta) = 2(2\beta_{\text{inc}})^{1/2}(\xi - V_{\text{inc}}\zeta)/(1 + 2\kappa V_{\text{inc}}{}^2)^{1/2}$. Similarly, in medium 2,

$$u(\xi,\zeta) = \left\{\frac{4\beta_{\text{ref}}}{1+B_{\text{ref}}\cosh\left[\Theta_{\text{ref}}(\xi,\zeta)\right]}\right\}^{1/2} \times\exp\left[\pm i\sqrt{\frac{1-\Delta+4\kappa\beta_{\text{ref}}}{1+2\kappa V_{\text{ref}}^2}}\left(V_{\text{ref}}\xi + \frac{\zeta}{2\kappa}\right)\right]\exp\left(-i\frac{\zeta}{2\kappa}\right), \quad (2.13)$$

where $B_{\text{ref}} \equiv 1 + (4/3)\nu\sigma\rho_0$, $\beta_{\text{ref}} \equiv (\rho_0/2)[\alpha + (2/3)\nu\sigma\rho_0]$ and $\Theta_{\text{ref}}(\xi,\zeta) = 2(2\beta_{\text{ref}})^{1/2}(\xi - V_{\text{ref}}\zeta)/(1 + 2\kappa V_{\text{ref}}{}^2)^{1/2}$. Thus, the incident and refracted soliton beams [solutions (2.12) and

(2.13), respectively] have very similar mathematical structures. A key distinction is the appearance of the linear mismatch parameter Δ in the phase of the latter.

2.2.4 Universal Snell's Law

For simplicity, the interface in the laboratory frame is aligned along the z axis so that its transverse position is always at $x = 0$. The phase of solutions (2.12) and (2.13) at the interface (i.e., at $\xi = 0$) can be matched only when the incident and refracted beams share a common longitudinal sense. Phase continuity then ensures that:

$$\frac{1+2\kappa\rho_0\left(1+\frac{2}{3}\sigma\rho_0\right)}{1+2\kappa V_{\text{inc}}^2}=\frac{1-\Delta+2\kappa\rho_0\left(\alpha+\frac{2}{3}\nu\sigma\rho_0\right)}{1+2\kappa V_{\text{ref}}^2}, \tag{2.14}$$

which can be rearranged to find $V_{\text{ref}}{}^2$ in terms of $V_{\text{inc}}{}^2$ according to:

$$V_{\text{ref}}^2=V_{\text{inc}}^2-\left(\frac{1}{2\kappa}\right)\frac{1+2\kappa V_{\text{inc}}^2}{1+2\kappa\rho_0\left(1+\frac{2}{3}\sigma\rho_0\right)}\delta, \tag{2.15}$$

$$\delta\equiv\Delta+2\kappa\rho_0\left[\left(1-\alpha\right)+\frac{2}{3}\sigma\rho_0\left(1-\nu\right)\right]. \tag{2.16}$$

While equation (2.15) describes soliton refraction in terms of transverse velocities (in normalised coordinates), it is more instructive to consider propagation angles (in laboratory coordinates). A beam with velocity V in the (ξ, ζ) frame evolves at oblique angle θ relative to the longitudinal axis in the (x, z) frame. The fundamental trigonometric relations [17]:

$$\cos\theta_{\text{inc, ref}}=\frac{1}{\sqrt{1+2\kappa V_{\text{inc, ref}}^2}}, \qquad \sin\theta_{\text{inc, ref}}=\frac{\sqrt{2\kappa}V_{\text{inc, ref}}}{\sqrt{1+2\kappa V_{\text{inc, ref}}^2}}, \tag{2.17}a,b$$

leads to the compact result

$$\tan\theta_{\text{inc, ref}}=\sqrt{2\kappa}V_{\text{inc, ref}}. \tag{2.18}$$

One of the fundamental properties of wave propagation in Helmholtz-type models is that θ_{inc} and θ_{ref} can be of *any* magnitude, even though $\kappa << O(1)$ [18]. By combining equations (2.15) and (2.18), a universal Snell's law can be obtained:

$$\gamma n_{01}\cos\theta_{\text{inc}}=n_{02}\cos\theta_{\text{ref}}, \tag{2.19}$$

$$\gamma \equiv \left[\frac{1+2\kappa\rho_0\left(1+\frac{2}{3}\sigma\rho_0\right)}{1+2\kappa\rho_0\left(\alpha+\frac{2}{3}\nu\sigma\rho_0\right)\left(1-\Delta\right)^{-1}} \right]^{1/2}. \tag{2.20}$$

Equations (2.19) and (2.20) are key results of this research, describing soliton refraction in cubic-quintic systems. It is important to note that equation (2.19) contains a single multiplicative correction factor γ that captures the interplay between material mismatches, a finite beam waist, and system nonlinearity.

2.2.5 Critical Angles

When $\theta_{inc} = \theta_{crit}$, the refracted soliton might be expected to travel along the interface (one also expects surface waves to play a central role in understanding propagation properties in such a regime). More formally, the condition $\theta_{ref} = 0$ at $\theta_{inc} = \theta_{crit}$, when applied to equation (2.19), leads to an algebraic prediction for the critical angle (see Appendix B):

$$\tan\theta_{crit} = \left\{ \frac{\Delta+2\kappa\rho_0\left[\left(1-\alpha\right)+\frac{2}{3}\sigma\rho_0\left(1-\nu\right)\right]}{1-\Delta+2\kappa\rho_0\left(\alpha+\frac{2}{3}\nu\sigma\rho_0\right)} \right\}^{1/2}. \tag{2.21}$$

The existence of a critical angle requires the argument of the square-root in equation (2.21) to be non-negative (e.g., when $\alpha = \nu = 1$ and $\Delta > 0$). In the plane-wave limit, it would seem reasonable for incident waves travelling at $\theta_{inc} = \theta_{crit}$ to be refracted along the interface (as they are according to ray optics in linear systems [19]). In the more complicated case of beams, diffraction (particularly in combination with system nonlinearity) will inevitably lead to more complicated wave phenomena in the vicinity of such critical points.

2.2.6 Interface Transparency

The interface is effectively transparent to the incident beam when $\theta_{ref} = \theta_{inc}$. From equation (2.19), it follows that the condition for interface transparency is $\gamma n_{02} = n_{01}$, which is equivalent to $\delta = 0$ [obtained by setting $V_{ref}^2 = V_{inc}^2$ in equation (2.16)]. Transparency thus occurs when the linear and (peak) nonlinear refractive index mismatches cancel each other *exactly*. It is interesting to note that the transparency condition (where the beam passes through the interface unrefracted) is inherently satisfied by the 'no interface' condition, [i.e., $\Delta = 0$ (since $n_{02} = n_{01}$), $\alpha = 1$ (since $\alpha_2 = \alpha_1$), and $\nu = 1$ (since $\nu_1 = \nu_2$)] even though the two situations are physically different.

2.2.7 Reflection and Refraction

When a beam encounters an interface, generally one of two effects tend to dominate the system behaviour: *reflection* or *refraction*.

Reflection. When medium 2 is less optically dense and $\theta_{inc} < \theta_{crit}$, a refracted beam generally cannot be excited – the incident soliton cannot penetrate across the boundary into the second medium because this would demand $|\cos\theta_{ref}| > 1$. In such cases, the in-going beam will often be totally internally reflected. Since the system at hand is highly nonlinear, *any* beam interaction with the interface may generate radiation (i.e., low-amplitude diffracting waves with sufficient intensity to effectively self-trap). Recent results [7] have also shown that in the presence of strong nonlinearity (e.g., power-law regimes), the incident soliton can simply break up into radiation close to the critical angle.

Refraction. When (i) medium 2 is less optically dense and $\theta_{inc} > \theta_{crit}$, or (ii) medium 2 is more optically dense, the incident beam may be refracted at angle $\theta_{ref} = \cos^{-1}[(n_{01}/\gamma n_{02})\cos\theta_{inc}]$. Refraction characteristics may be sub-classified as *internal* or *external*, depending upon whether the outgoing beam bends toward the interface or away from it, respectively (see Figure 6). This categorisation is most simply described in terms of the sign of δ [see equation (2.16)].

$\delta < 0$ $\quad V_{ref} > V_{inc}$ so that $\theta_{ref} > \theta_{inc}$ … **External refraction**

$\delta = 0$ $\quad V_{ref} = V_{inc}$ so that $\theta_{ref} = \theta_{inc}$ … **Transparency condition**

$\delta > 0$ $\quad V_{ref} < V_{inc}$ so that $\theta_{ref} < \theta_{inc}$ … **Internal refraction**

External refraction is an intrinsically nonparaxial regime, where θ_{ref} can easily violate the paraxial approximation even under the simplest material constraint (e.g., a linear interface with $n_{02} > n_{01}$, and hence $\Delta < 0$).

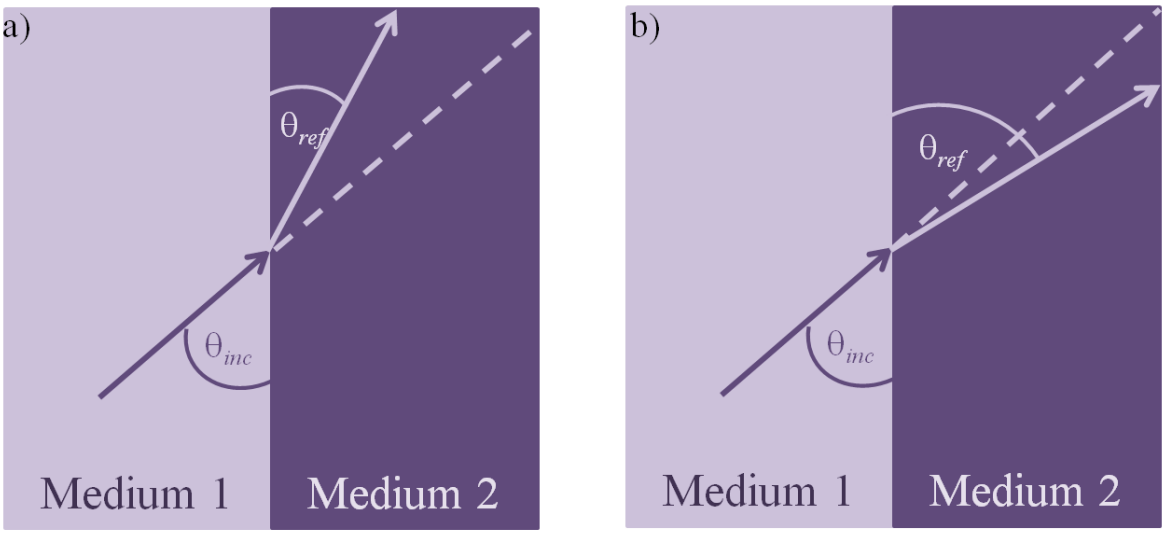

Figure 6. Schematic diagram showing (a) internal refraction where the beam bends towards the interface and (b) external refraction, where the beam bends away from the interface.

2.3 Simulating Solitons at Interfaces

The analysis in the preceding section captures the essence of soliton refraction within the phase-continuity approximation. However, the full complexity of the interface problem can be addressed only through computer simulations. Such simulations will be undertaken here using a suite of Matlab codes that integrate model (2.6) numerically and analyse the dataset using custom curve-fitting routines.

2.3.1 Numerical Methods

Outline of Algorithm

A brief description of the numerical methods used will now be given. This description is relevant to all the simulations carried out for this thesis.

There are three initial steps to simulating the propagation of the beams in the longitudinal direction ζ. Firstly, input conditions must be specified – in this case a cosh-type function such as $u(\xi,0) = A/\{1 + B\cosh[2(2\beta)^{1/2}\xi]\}^{1/2}$. To approximate the solution after the first step (of size $\Delta\zeta$), a split step method is used. This approach (even when symmetrized) can only be deployed for Helmholtz-type models in the short term (in this case, a single longitudinal step) as it proves to be insufficiently accurate [20]. The field at the second step, and every step thereafter, is calculated with a difference-differential algorithm. This method requires information from the two preceding steps before it can be implemented (hence why it cannot be used to find the field after the *first* step). The difference-differential method has been shown to be a highly effective and efficient way to simulate

beam propagation problems of this type [20]. It replaces longitudinal derivatives with their (centred) finite difference approximations, and the transverse diffraction operator is implemented through the use of Fast Fourier Transforms.

Spatial Filtering

The continuum Helmholtz equation (2.6) has an elliptical plane wave dispersion relation given by equation (2.22). Any spatial frequencies k_ξ on the associated computational grid that fall outside this ellipse can result in an unphysical numerical instability; such spectral components must hence be removed from the solution after each propagation step. A full description of the spatial filtering condition traditionally used in homogeneous Helmholtz-type nonparaxial simulations can be found in ref. [20]. Within the linear plane wave approximation, spatial frequencies satisfying $k_\xi^2 > (k_\xi^2)_{\max}$ are eliminated using a top-hat function in Fourier space, where:

$$\left(k_\xi^2\right)_{\max} = \frac{4\kappa}{\Delta\zeta^2}\left[\sqrt{1+\left(\frac{\Delta\zeta}{2\kappa}\right)^2}-1\right]. \tag{2.22}$$

When necessary, equation (2.22) can be easily augmented by a correction term (at $\Delta/2\kappa$) to accommodate interface geometries.

2.3.2 Interface Geometries

In section 2.2, the material boundary was aligned along the *z* axis so that oblique incidence was described in a frame where the ingoing beam was inclined at angle θ_{inc} *relative to the fixed interface.* Such a choice of relative orientation is entirely arbitrary and made purely for mathematical convenience (to facilitate simpler phase matching). In fact, simulating model (2.6) with that particular configuration can lead to numerical difficulties arising from spatial filtering in combination with dense grid discretisation and solution phase sampling requirements [4]. To avoid these complications, all computations have been performed in the frame where the incident soliton is on-axis and the interface is rotated *relative to the fixed input beam* (see Figure 7).

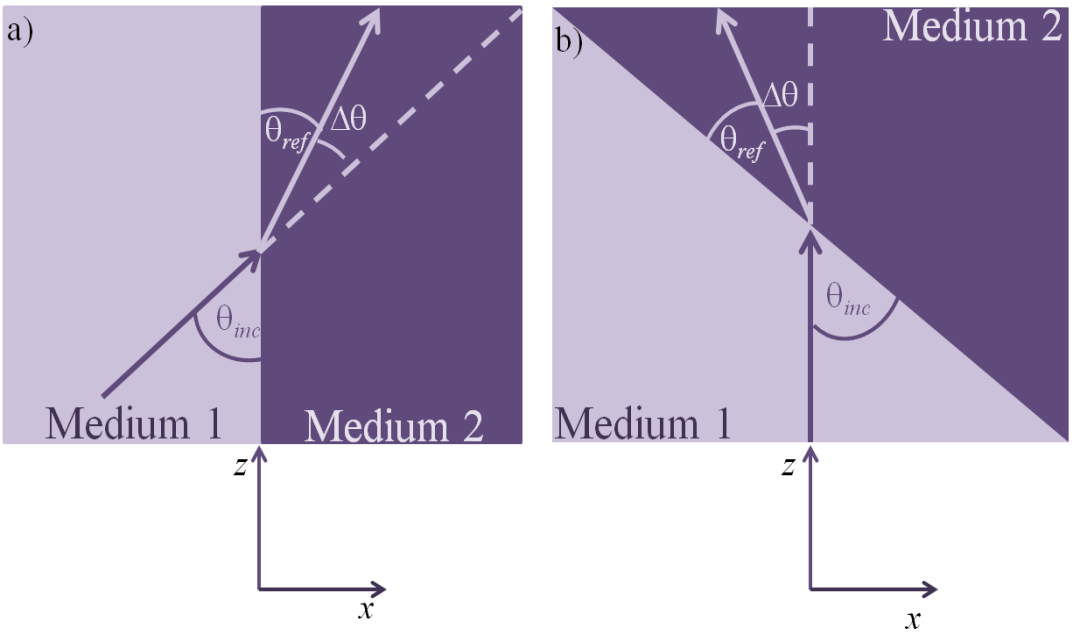

Figure 7a) Schematic diagram showing beam refraction at an interface in the analysis in section 2. b) Shows the interface setup used in the computer simulations, the beam approaches the interface travelling directly down the longitudinal axis, while the analytical problem considers the interface to be aligned along the longitudinal axis.

2.3.3 Calculation of Refraction Angle

Before proceeding with simulations, a way must be found to extract the refraction angle from the numerical dataset. Referring to Figure 7b), the angular deviation φ from the incident (straight-through) line is related to the refraction angle θ_{ref} by:

$$\theta_{\text{ref}} = \theta_{\text{inc}} - \varphi. \tag{2.23}$$

Therefore, it follows that

$$\tan\theta_{\text{ref}} = \tan\left(\theta_{\text{inc}} - \varphi\right) = \frac{\tan\theta_{\text{inc}} - \tan\varphi}{1 + \tan\theta_{\text{inc}}\tan\varphi}, \tag{2.24}$$

where the trigonometric addition formula has been used to obtain the far right-hand side of equation (2.24). In the frame in which the computations are carried out, φ can be identified with a transverse velocity v through

$$\tan\varphi = \sqrt{2\kappa}\ \text{v}. \tag{2.25}$$

By combining equations (2.25) and (2.24), it is straightforward to show that

$$\sqrt{2\kappa}V_{\text{ref}} = \frac{\sqrt{2\kappa}V_{\text{inc}} - \sqrt{2\kappa}\text{v}}{1+\sqrt{2\kappa}V_{\text{inc}}\sqrt{2\kappa}\text{v}}, \tag{2.26}$$

or equivalently,

$$V_{\text{ref}} = \frac{V_{\text{inc}} - \text{v}}{1+2\kappa V_{\text{inc}}\text{v}} \tag{2.27}$$

Since simulations are always performed in the normalised frame of reference, the numerical data can be analysed to yield a value for v. The desired angle θ_{ref} can then be obtained from equations (2.27) and (2.18).

In all simulations, the interface is oriented along the line $\xi + V_{\text{inc}}\zeta = 0$ such that the centre of the beam encounters the interface at $\zeta = \xi = 0$. If the peak of the refracted soliton is supposed to move along the trajectory

$$\xi - \text{v}\zeta = 0, \tag{2.28}$$

then it follows that the local velocity v (far away from the interface in medium 2) may be calculated from the slope

$$\text{v} \equiv \frac{d\xi}{d\zeta}. \tag{2.29}$$

This result is crucial for analysing the numerical data.

2.4 Simulations to test Snell's Law

The results in this section test the predictions of the new Snell's law [equation (2.19)] against fully-nonlinear numerical computations for a variety of interfaces. The line $\theta_{\text{ref}} = \theta_{\text{inc}}$ (marked on all of the following Snell-type plots) represents the transparency condition (where $\delta = 0$ – see section 2.2.6); it differentiates between regimes involving internal (below the line, i.e. $\theta_{\text{ref}} < \theta_{\text{inc}}$) and external (above the line, i.e. $\theta_{\text{ref}} > \theta_{\text{inc}}$) refraction. The full interface problem is associated with a six-dimensional parameter space that must somehow be tamed. For definiteness, the following parameters are chosen for simulations:

$\kappa \propto (\lambda/w_0)^2$ (*inverse beam width*). Two typical values of κ are considered (namely, 2.5×10^{-3} and 1.0×10^{-4}); both respect the inherent inequality for Helmholtz modelling [that $\kappa << O(1)$].

$\alpha \equiv \alpha_2/\alpha_1$ (*ratio of cubic nonlinearity coefficients*). Values of α are chosen to be 0.5, 1.0 or 2.0. The two non-unity cases represent a large change in the strength of the focusing properties of the medium across the interface (a halving and doubling, respectively).

$\nu \equiv \nu_2/\nu_1$ (*ratio of quintic nonlinearity coefficients*). Values of ν are chosen to be 0.5, 1.0 and 2.0 so that the relative change in the quintic coefficients is the same as that for the cubic coefficients.

$\sigma \equiv \nu_1 E_0^2/\alpha_1$ (*ratio of cubic to quintic nonlinear phase shifts*). Typically, the quintic contribution to self-focusing is a small correction to the cubic (Kerr) effect [8]. The competing cubic-quintic nonlinear response can be used as a leading-order approximation to a saturable intensity-dependent refractive index [8]. Here, $\sigma = \pm 0.15$ is used [14].

ρ_0 (*peak intensity*). For $\sigma = -0.15$, the bistability condition means that there are two values of ρ_0 describing solutions with different peak intensities but the same full-width-at-half-maximum: $\rho_0 \approx 1.3$ and $\rho_0 \approx 4.14$ [14]. For $\sigma = +0.15$, the corresponding soliton is monostable and has $\rho_0 \approx 0.87$.

2.4.1 Linear Interfaces

Illustrative results for soliton refraction at a linear interface are shown in Figure 8a) for a relatively narrow beam (where $\kappa = 2.5\times10^{-3}$). Generally, the agreement between theoretical predictions [solid lines – obtained from equations (2.19) and (2.20)] and numerical data (points) is very good. Figure 8b) shows refraction for parameters with a low angle of incidence ($\theta_{inc} = 1.0°$) and $\Delta = -0.01$ (a relatively large step in refractive index). Upon colliding with the interface, the beam splits into a predominant externally-refracted component (well described by the Snell law), accompanied by a lower-amplitude satellite structure (this secondary component does not survive in the long term, having insufficient energy to self-trap and form a solitary wave). The beam/interface interaction also generates radiation modes that are reflected back into medium 1.

The true collision, as predicted by solving equation (2.6) numerically, is much more complicated than the adiabatic assumptions of the analysis is section 2.2 (which allows only for a single stationary refracted beam and no radiation or reflected waves). Such an increase in complexity clearly gives rise to a difference between the Snell's-law prediction

and the true (computed) refraction angle. However, it is interesting to note [from Figure 8a)] that the general trend of the Snell's-law prediction is still well adhered to.

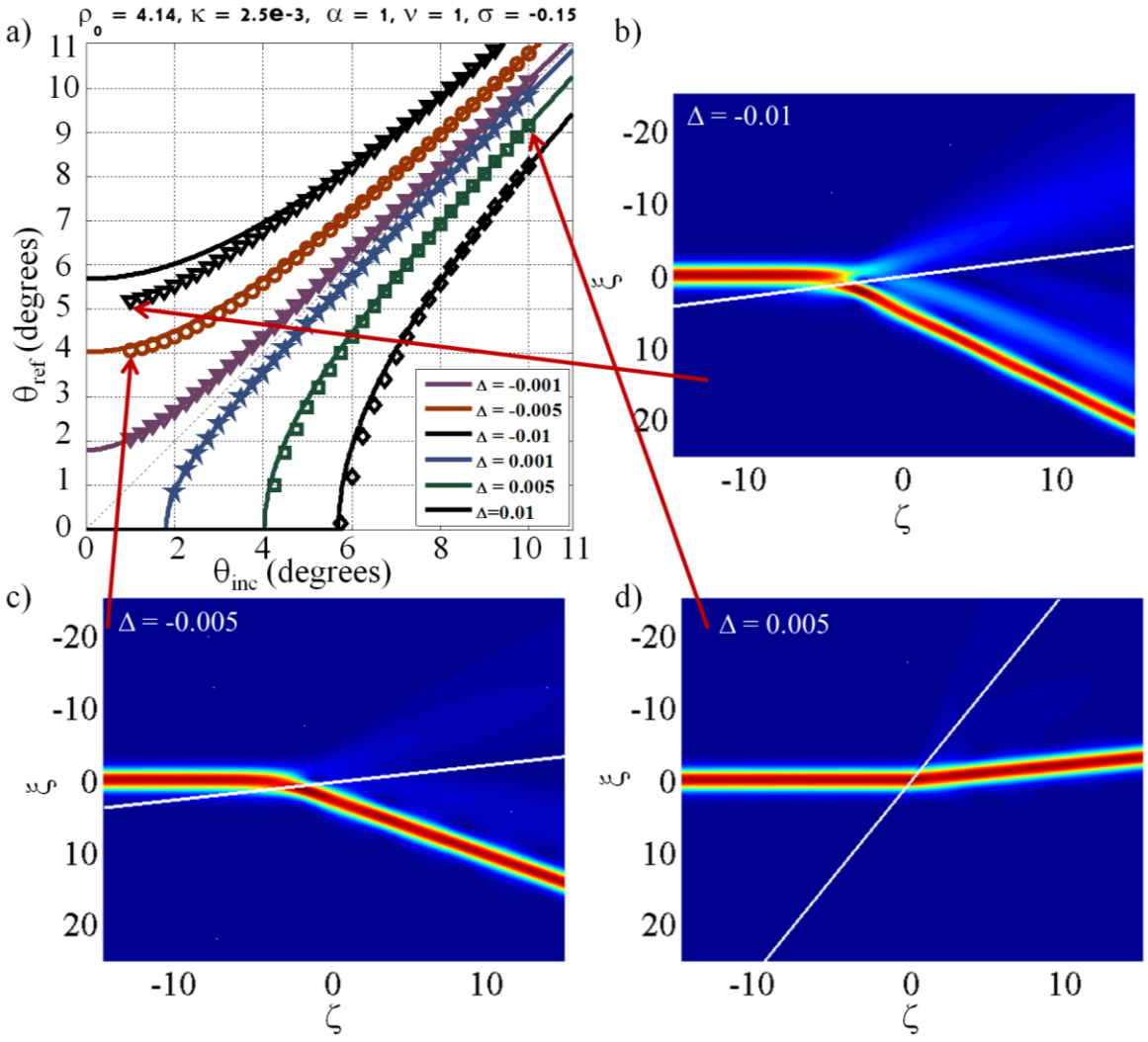

Figure 8a) Shows a Snell's law plot for a linear interface. Figure 8b) Shows the 3d plot for the point: Δ = -0.01 and θ = 1°. Figure 8c) Shows the 3d plot for the point: Δ = -0.005 and θ = 1° and Figure 8d) Shows the 3d plot for the point: Δ = 0.005 and θ = 10°.

Figure 8c) shows a similar example of soliton refraction but with Δ = –0.005 (as opposed to Δ = –0.01). With a smaller index step, the interaction is much 'cleaner': far less radiation is generated, and there is no secondary/satellite structure shadowing the refracted beam. In Figure 8d) the beam is propagating with a larger angle of incidence. Here, the beam can be seen to refract into the second medium without losing much radiation at the interface, and so, the point representing this refraction in Figure 8a) fits well with the theory line.

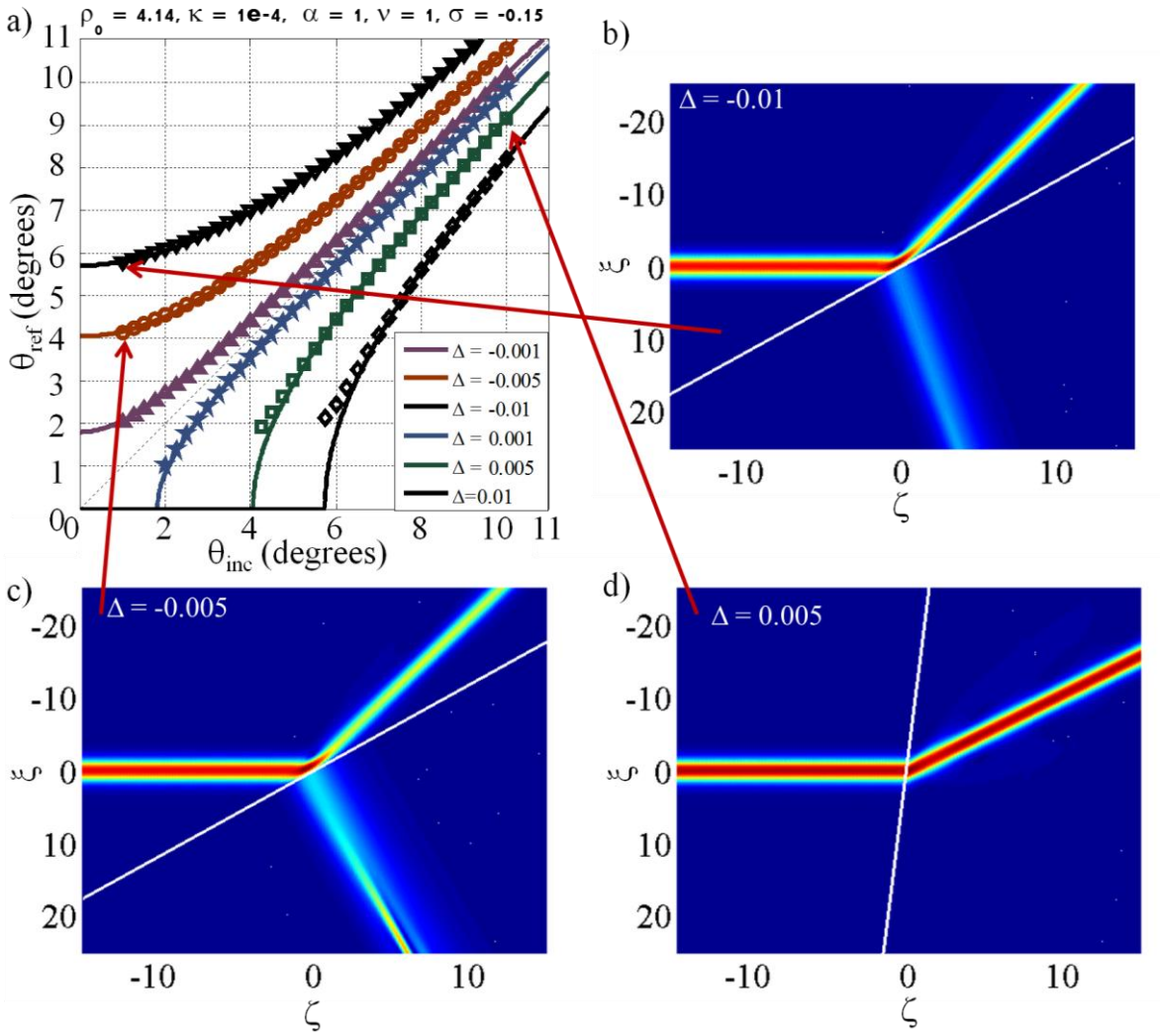

Figure 9a) Shows a Snell's law plot for a linear interface. Figure 9b) Shows the 3d plot for the point: Δ = -0.01 and θ = 1°. Figure 9c) Shows the 3d plot for the point: Δ = -0.005 and θ = 1° and Figure 9d) Shows the 3d plot for the point: Δ = 0.005 and θ = 10°.

Figure 9 repeats the simulations shown in Figure 8, but with incident beams that are broader by a factor of 5 ($\kappa = 1.0\times10^{-4}$). Most notable is that the agreement between the theory and numerics is much improved at lower angles of incidence [compare Figures 8a) and 9a)]. By comparing Figures 8b) and 9b), it is immediately apparent that the splitting phenomenon is much more pronounced for broader beams [for instance, in Figure 9b), the dominant part of the solution (i.e., that component with the highest amplitude) is actually the *reflected*, as opposed to the *refracted*, beam]. However, the interaction (while still being non-adiabatic) is still 'cleaner' (much less radiation is generated) and the refraction angle is more accurately described by the Snell law. Similar trends can also be identified by comparing Figures 8c) and 9c).

A particularly intriguing feature of Figures 9b) and 9c) is the appearance of such a strong reflected component. In the two material configurations, $\Delta < 0$ and there is no critical angle [c.f. equation (2.21)]: refraction is *external*, and one would not traditionally expect to find such prevalent reflected components.

2.4.1.1 Role of Finite Beam Waist

The two Snell's law plots in Figures 10a) and 10b) share a common set of system parameters, and differ only in the nonparaxial parameter κ.

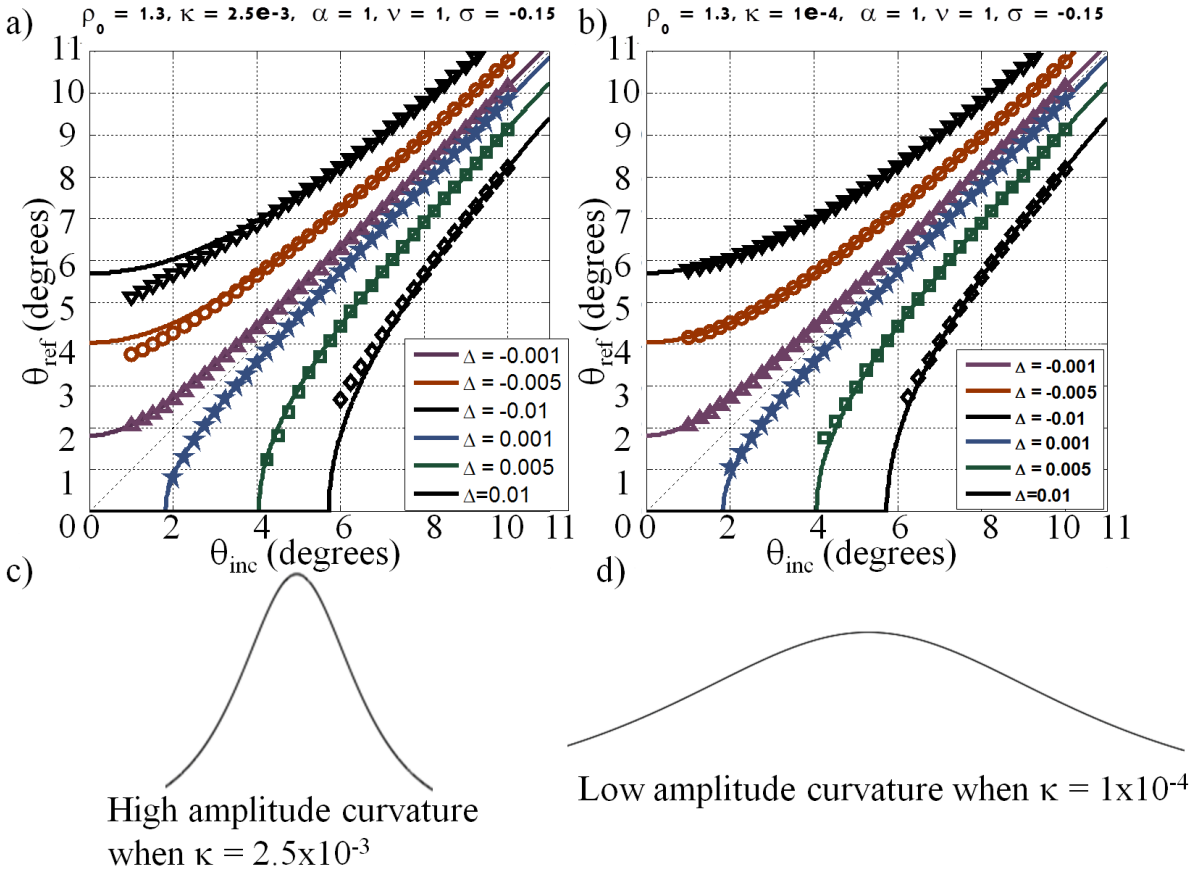

Figure 10a) and b) Showing Snell's law plots with different values of κ. Figure 10c) Shows a schematic of a beam profile with a high amplitude curvature and Figure 10d) Shows a schematic of a beam profile with a low amplitude curvature.

For smaller κ values (broader beams) the theory-numerics agreement is excellent, much better (at lower incidence angles) than for larger values. The results in Figures 8 and 9 appear to suggest that the reason for improved agreement is, surprisingly, *not* due to a cleaner refraction process (e.g., without splitting, or with less radiation); one must thus look elsewhere for a convincing physical explanation. One possibility proposed by Christian *et al.* [7] is that smaller κ values correspond to broader beams which,

accordingly, have lower amplitude curvature [see Figures 10c) and 10d)]. Scenarios involving reduced amplitude curvature map much more closely onto the inherent assumptions of the Snell's-law analysis, which (at least so far as field matching is concerned) treats beams and plane waves (zero amplitude curvature) on an equal footing since only phase continuity is enforced. As κ increases, so too does amplitude curvature and one is more likely to find a divergence between theoretical predictions and simulations.

2.4.1.2 Effect of the Angle of Incidence of the beam

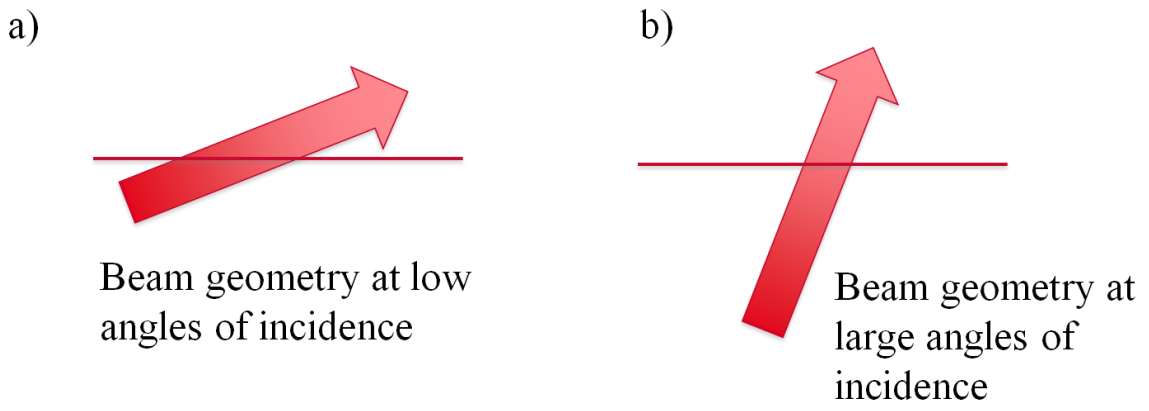

Figure 11a) Showing a beam propagating with the interface at a low angle of incidence, and Figure 11b) Showing a beam propagating at a larger angle of incidence with respect to the interface.

Although the angle of incidence of the beam is a fundamental part of the Snell law derived earlier, the theory cannot account for the changes in the cross-sectional area of the beam interacting with the interface. Figure 11 gives an illustration of how changing the angle of incidence also has an effect on the cross-sectional area of the beam encountering the interface; as the angle of incidence of the beam is decreased, a larger cross-section [in comparison to that at a larger angle of incidence, see Figure 11b)] of the beam comes into contact with the interface. Since beams with low angles of incidence are more affected by the interface's perturbative action (because of the larger cross-sectional area encountering it), and since our theory does not account for this perturbation effect, results for these low angles will be more off-theory than the equivalent beams at higher angles of incidence.

2.4.1.3 Effect of Δ

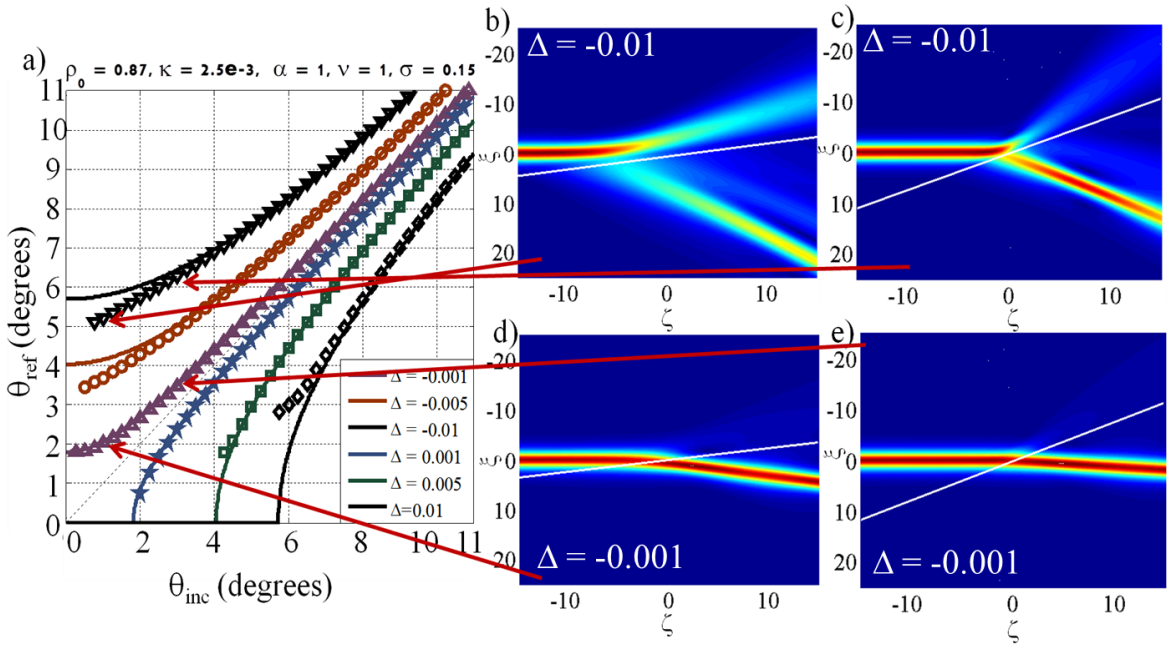

Figure 12 Highlights the effect that changing the value of Δ has on the behaviour of the beam at the interface. Figure 12a) Shows a Snell's law plot for a linear interface. Figure 12b) Shows the 3d plot for the point: Δ = -0.01 and θ = 1°, Figure 12c) has: Δ = -0.01 and θ = 3°, Figure 12d) has: Δ = -0.001 and θ = 1° and Figure 12e) has: Δ = -0.001 and θ = 3°.

As |Δ| is increased, the step in the linear part of the refractive index also increases. This means the beam is propagating into a medium where the linear part of the refractive index is significantly different to the value in the first medium. In many instances, this leads to beam splitting, as is the case in Figures 12b) and c). In Figures 12d) and e) the change in the linear part of the refractive index is much smaller, and the beam can be seen to refract fairly 'cleanly' (that is, it only loses a limited amount of radiation) across the interface. This results in a much better fit between theory and numeric for this set of beams as can be seen in Figure 12.

2.4.2 Mixed Interfaces

The results for mixed interfaces are not as favourable as those for linear interfaces, where the interaction with the nonlinear material boundary can cause strong self-reshaping oscillations in the second medium. Also, if the beam has a high intensity, the likelihood that the beam will split at the interface into multiple reflected and refracted beams is greater.

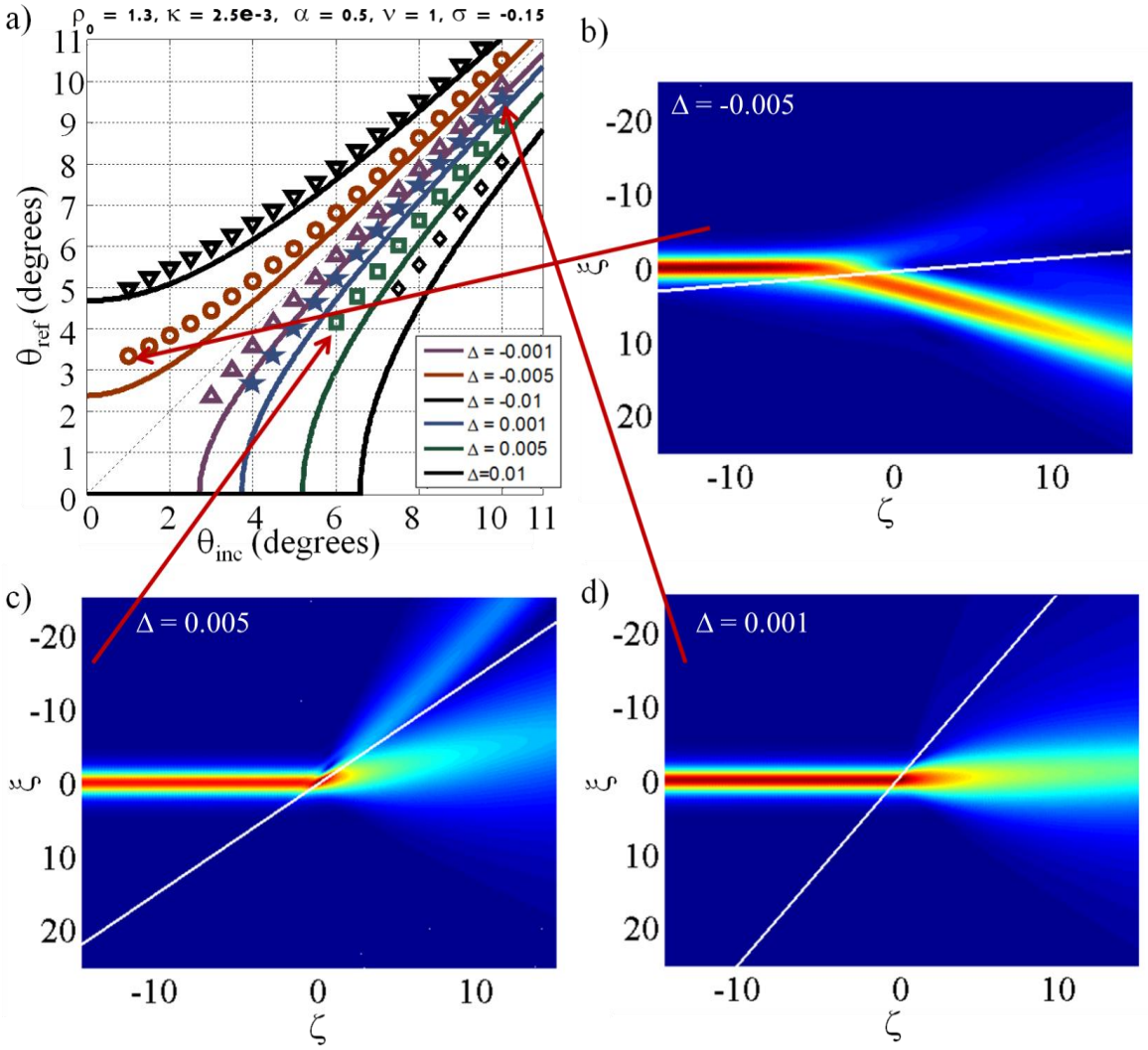

Figure 13 a) Shows a Snell's law plot for a mixed interface (with α = 0.5). Figure 13b) Shows the 3d plot for the point: Δ = -0.005 and θ = 1°. Figure 13c) Shows the 3d plot for the point: Δ = 0.005 and θ = 6° and Figure 13d) Shows the 3d plot for the point: Δ = 0.001 and θ = 10°.

Figure 13b) shows the refraction for a beam propagating at a low angle of incidence (1°). As the beam interacts with the interface, its amplitude changes in the second medium and some radiation is lost during the collision. Figure 13c) shows a beam propagating close to its critical angle, causing the beam to split on interacting with the interface into reflected

and refracted components. Since the scenarios in Figures 13b) and 13c) are not accommodated by our theoretical model, this gives rise to a mismatch between the prediction and the output. Figure 13d), on the other hand, shows a beam refracting into the second medium without loss of radiation (although the beam does reshape in the second medium); this is a situation accommodated adequately by the model and resultantly the point fits well in Figure 13a).

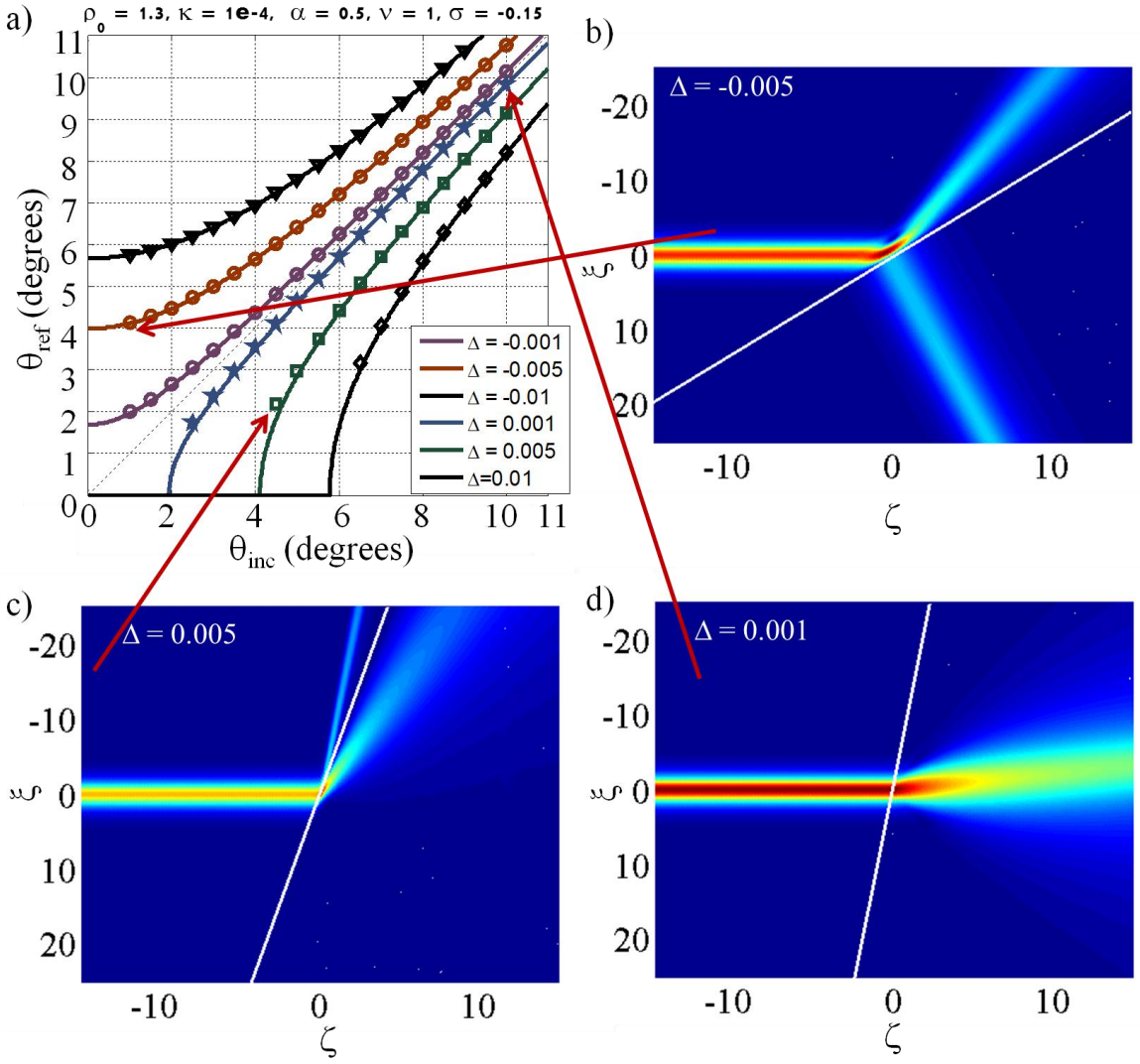

Figure 14 a) Shows a Snell's law plot for a mixed interface (with α = 0.5). Figure 14b) Shows the 3d plot for the point: Δ = -0.005 and θ = 1°. Figure 14c) Shows the 3d plot for the point: Δ = 0.005 and θ = 4.5° and Figure 14d) Shows the 3d plot for the point: Δ = 0.001 and θ = 10°.

Figure 14 shows the refraction of beam for the same parameters as in Figure 13, but with a smaller value of κ. Here, the fit between the theoretical and numerical results is much improved (this is to be expected – see section 2.4.1.1). Figures 14b) and c) provide examples of beams splitting at the interface, though for different reasons [c) splits because

it is close to the critical angle; for b) a critical angle does not exist so the reason for the splitting currently unclear]. These types of result would usually lead to the points in Figure 14a) being off-theory, however it can be seen that the agreement remains surprisingly good. The reason for this appears to relate, again, to the role of the finite beam waist. Figure 14d) shows that the beam passes through the interface losing only a small amount of radiation, and this, therefore, agrees with the results in Figure 14a).

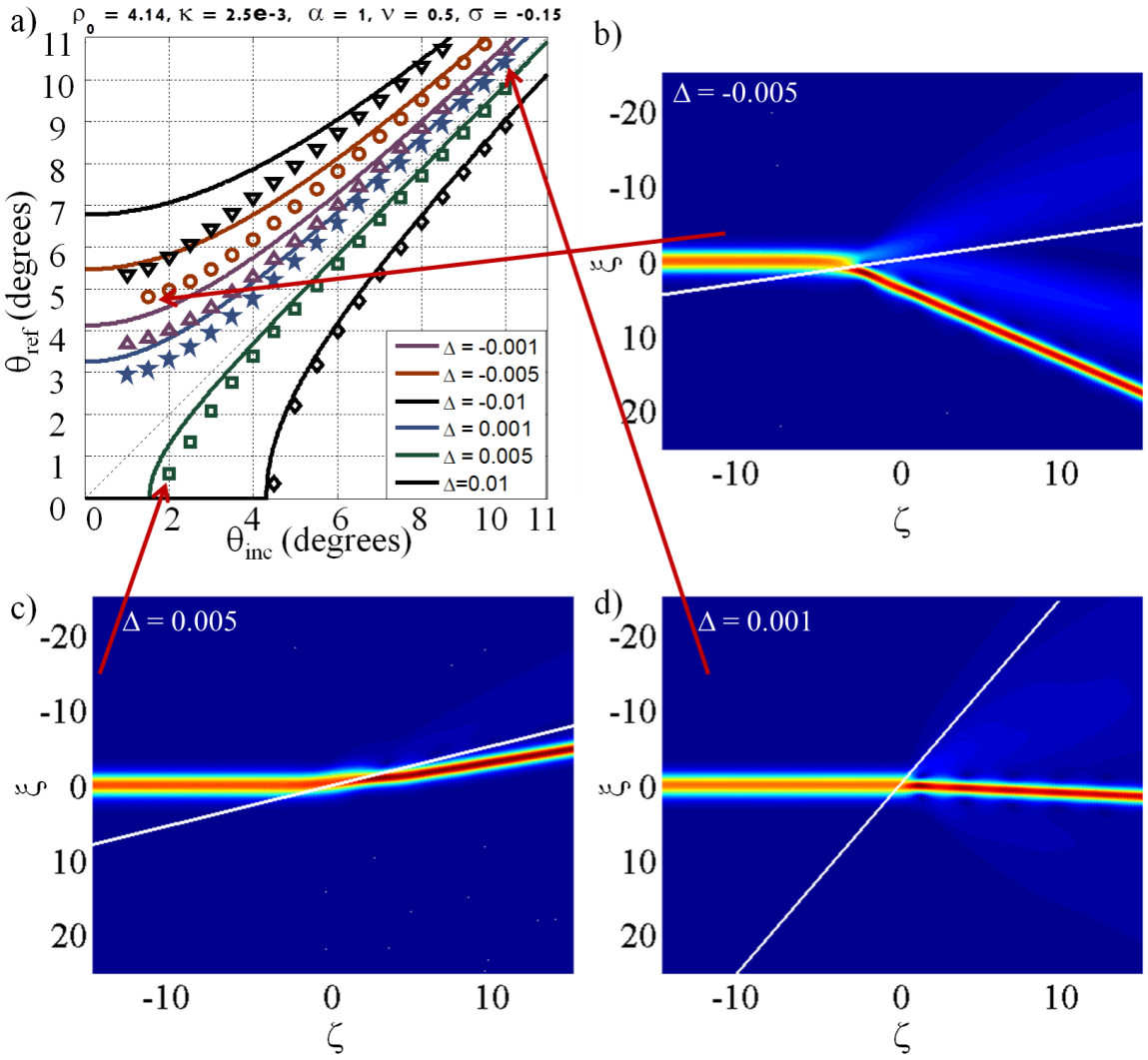

Figure 15 a) Shows a Snell's law plot for a mixed interface (with ν = 0.5). Figure 15b) Shows the 3d plot for the point: Δ = -0.005 and θ = 1°. Figure 15c) Shows the 3d plot for the point: Δ = 0.005 and θ = 2° and Figure 15d) Shows the 3d plot for the point: Δ = 0.001 and θ = 10°.

Figure 15 shows results with the quintic coefficient lower after the interface. Figure 15b) shows a beam interacting with the interface at an angle of incidence of 1°. Significant amounts of radiation are lost on interacting with the interface - some of which is reflected and some refracted. No splitting occurs in Figure 15c), despite the beam propagating close

to its critical angle. All three 3d plots (Figures 15b-d) show beams becoming narrower in the second medium. This effect is predicted by soliton solution (2.13) (c.f., the behaviour of parameter β_{ref} when $0 < \nu < 1$).

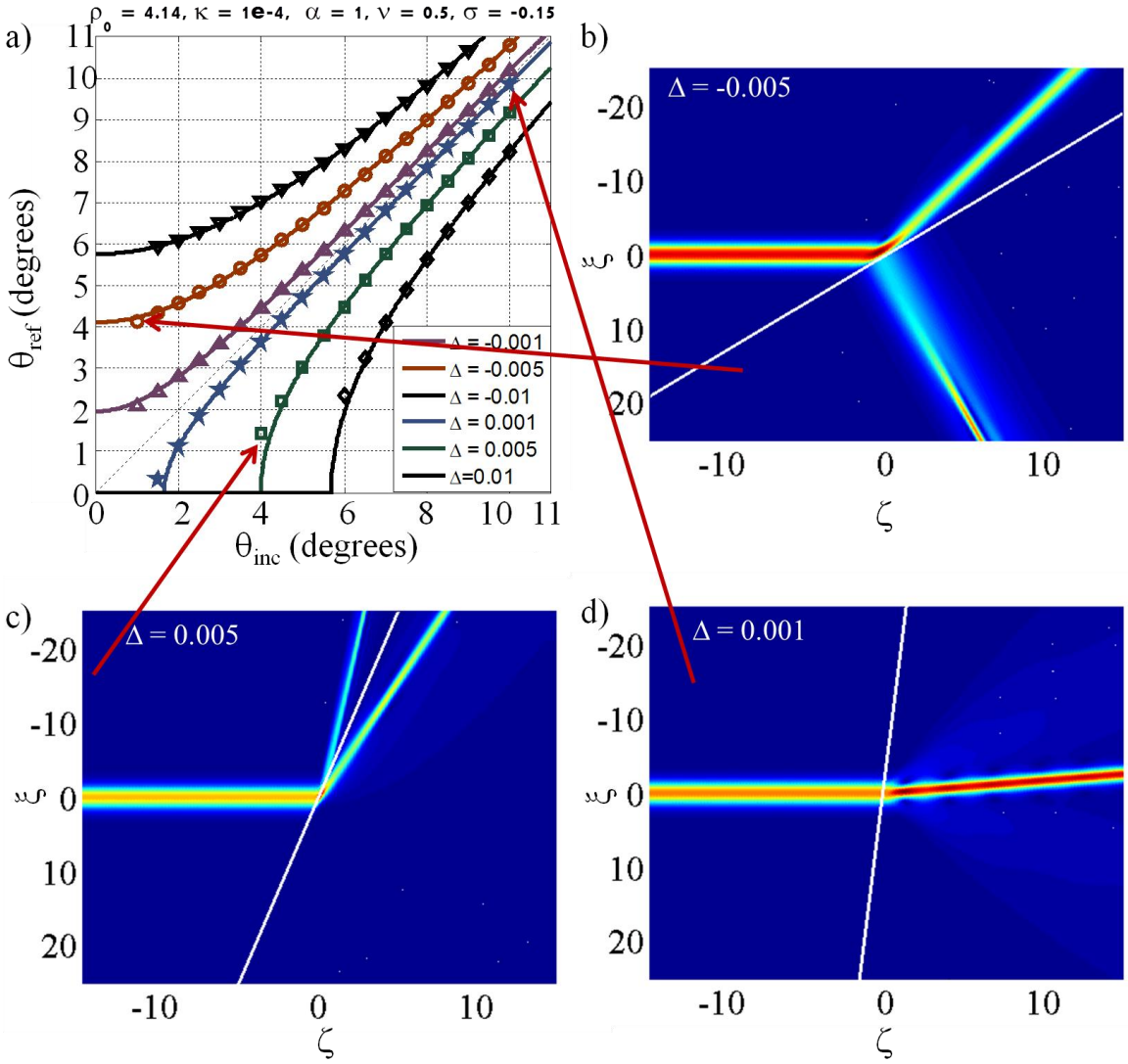

Figure 16 a) Shows a Snell's law plot for a mixed interface (with ν = 0.5). Figure 16b) Shows the 3d plot for the point: Δ = -0.005 and θ = 1°. Figure 16c) Shows the 3d plot for the point: Δ = 0.005 and θ = 4° and Figure 16d) Shows the 3d plot for the point: Δ = 0.001 and θ = 10°.

Figure 16, with a lower value of κ (1 x 10^{-4}), reinforces the previous results. Figure 16b) shows the beam loses a large amount of radiation, yet the fit with the predicted theoretical results remains acceptable; this is also true for Figure 16c). As previously described, the larger beam waist accounts for such agreement. Also noteworthy, in these low κ regimes is the existence of a reflected component of the beam arising on interaction with the interface - despite there being no critical angle in these parameter regimes.

2.4.3 Nonlinear Interfaces

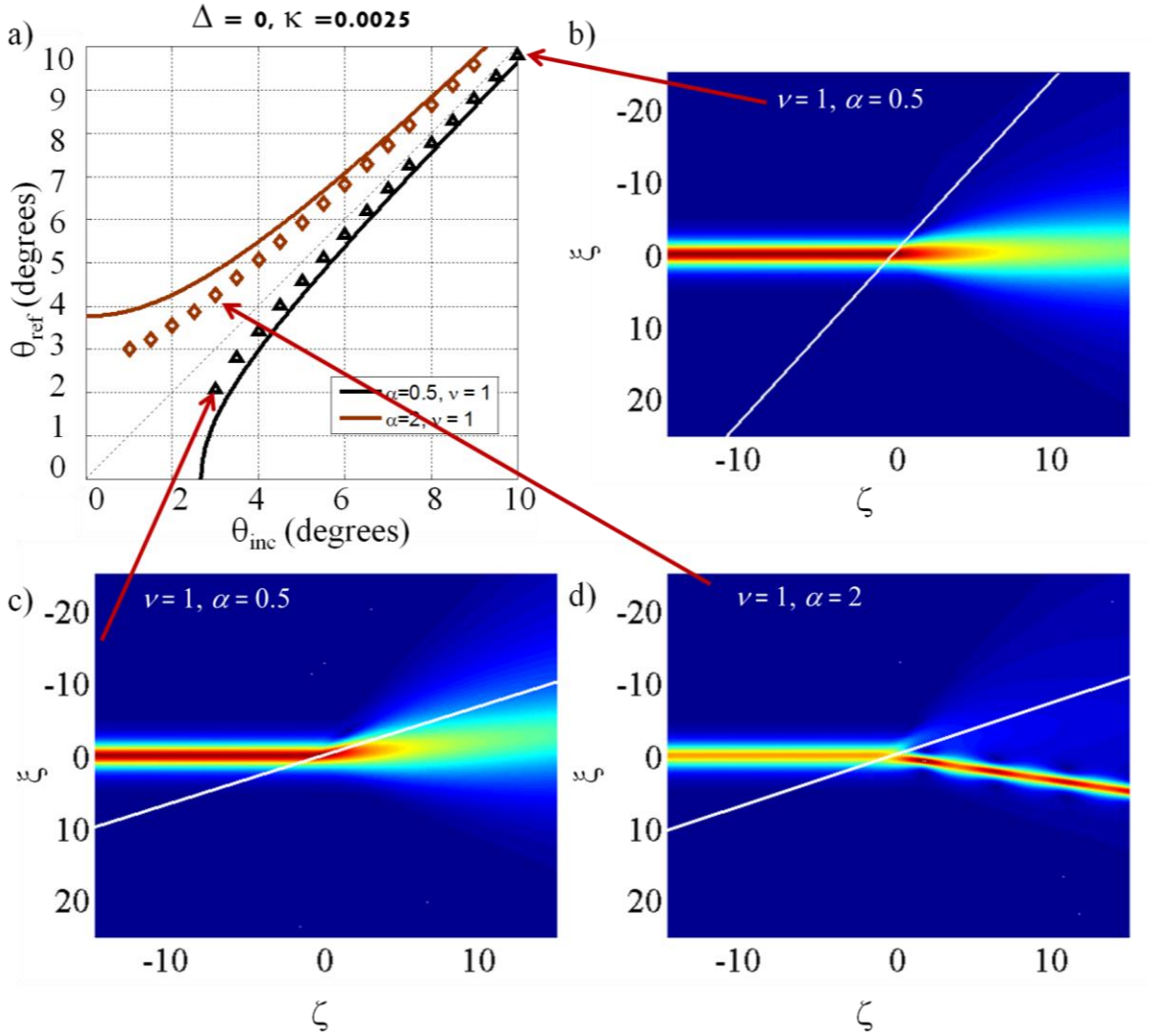

Figure 17a) Shows a Snell's law plot for a nonlinear interface (with $\Delta = 0$ and $\nu = 1$). Figure 17b) Shows the 3d plot for the point: $\rho_0 = 0.87$, $\alpha = 0.5$ and $\theta = 10°$. Figure 17c) Shows the 3d plot for the point: $\rho_0 = 0.87$, $\alpha = 0.5$ and $\theta = 3°$ and Figure 17d) Shows the 3d plot for the point: $\rho_0 = 0.87$, $\alpha = 2$ and $\theta = 3°$.

Figures 17b) and 17c) both represent points which are slightly off theory in Figure 17a). Both beams shed energy into radiation modes at the interface and undergo oscillations in the second medium (which is why results are off-theory). Figure 17d) represents a point which is more off theory. This is because the beam loses radiation at the interface and also reshapes in the second medium.

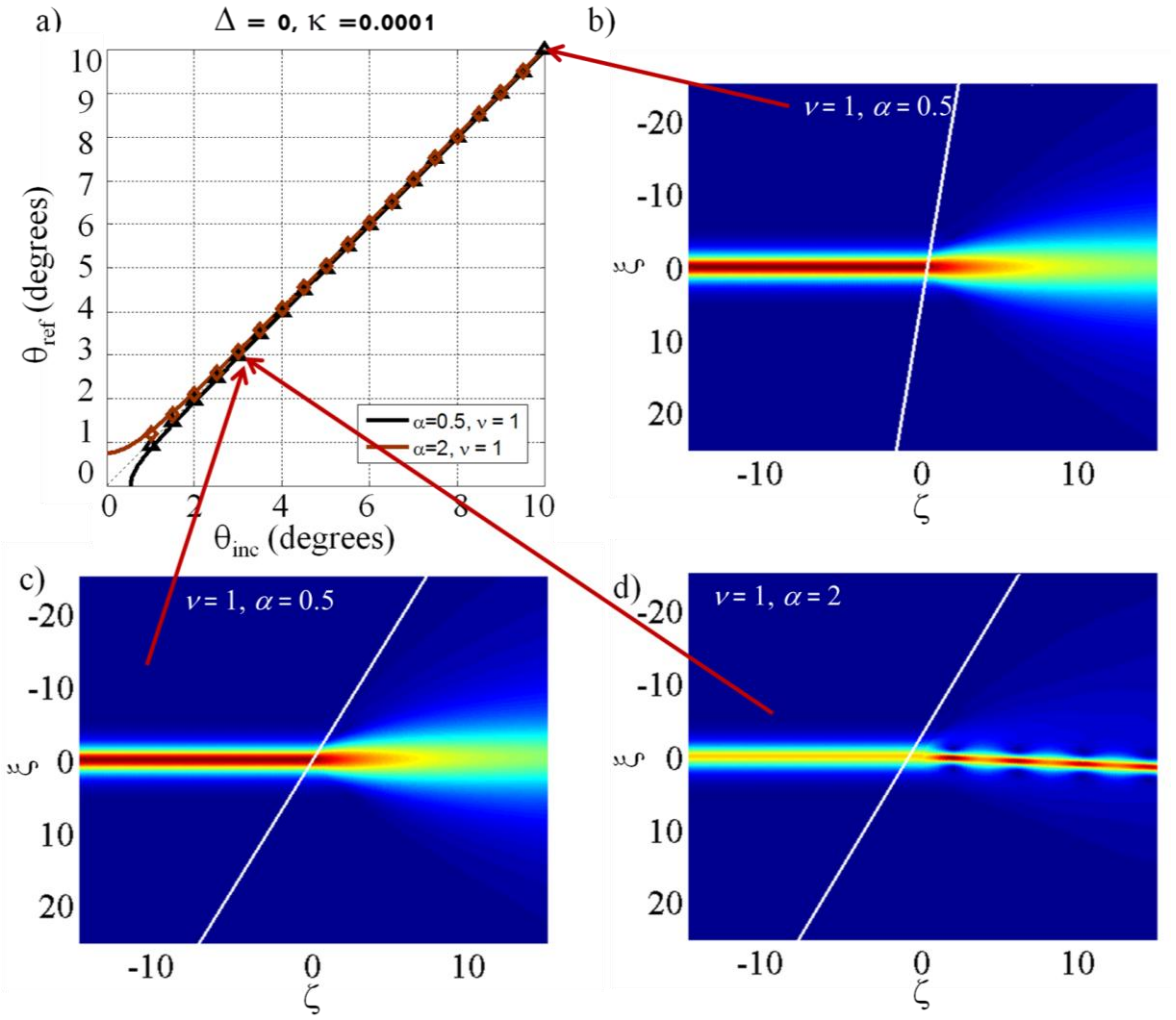

Figure 18a) Shows a Snell's law plot for a nonlinear interface (with $\Delta = 0$ and $\nu = 1$). Figure 18b) Shows the 3d plot for the point: $\rho_0 = 0.87$, $\alpha = 0.5$ and $\theta = 10°$. Figure 18c) Shows the 3d plot for the point: $\rho_0 = 0.87$, $\alpha = 0.5$ and $\theta = 3°$ and Figure 18d) Shows the 3d plot for the point: $\rho_0 = 0.87$, $\alpha = 2$ and $\theta = 3°$.

All the points in Figure 18a) have good agreement between the theoretical and numerical results. The 3d plots show similar beam refraction to those in the previous figure. Figures 18b) and c) show the beam changing in amplitude and losing radiation at the interface. Figure 18d) shows the beam losing radiation and reshaping in the second medium. This is similar to all the small value κ results seen previously in the report.

2.5 Conclusion

For the first time, the behaviour of spatial solitons at the interface between two dissimilar cubic-quintic materials has been investigated. It is important to note at this point the novelty which this work adds to the field of nonlinear photonics: there are, to the best of our knowledge, no published works (paraxial or nonparaxial) concerning soliton refraction contexts with this type of universal system nonlinearity.

The use of an inhomogeneous nonlinear Helmholtz equation, in combination with its exact analytical soliton solutions, has allowed us to derive a generalised Snell's law. This new law gives researchers a tool to predict the refractive properties of nonlinear beams interacting with a generic class of dielectric interface. Extensive computer simulations across a wide range of system parameters have demonstrated generally excellent agreement between numerical calculations and theoretical results. The research presented here thus provides further evidence for the power and applicability of Helmholtz soliton theory in arbitrary-angle optical configurations. Computations have also helped uncover some of the potential limitations of our modelling approach in various physical regimes depending on:

i. The value of κ – lower values of κ mean a lower amplitude curvature. When κ assumes larger values, neglecting amplitude curvature becomes less of a valid approximation and the plane-wave basis of Snell's law starts to break down.

ii. The value of $|\Delta|$ – when $|\Delta|$ is large (corresponding to a large difference in the linear parts of the refractive index in each medium) the beam is much more likely to split, at the interface, into reflected and refracted components. Our adiabatic theory does not accommodate non-adiabatic effects.

iii. Quasi-paraxial incidence angles – when the beam is propagating at a low angle of incidence with respect to the interface, then a much larger cross-sectional area of the beam will interact with the interface. The soliton-interface interaction length is longer in such regimes, so beams can suffer sustained (longitudinally distributed) perturbations.

The results from this work package give a deeper insight into the global properties of Helmholtz solitons that, in future, could be beneficial to the development of novel optical

technologies that exploit single- and multi-layer configurations. This is something which is discussed further throughout this thesis.

2.6 References

1. S. Tanev and D.I. Pushkarov, *Solitary wave propagation and bistability in the normal dispersion region of highly nonlinear optical fibres and waveguides.* Optics Communications, 1997. **141**(5-6): p. 322-328.
2. L.H. Acioli, A.S.L. Gomes, J.M. Hickmann, and C.B.d. Araujo, *Femtosecond dynamics of semiconductor-doped glasses using a new source of incoherent light.* Applied Physics Letters, 1990. **56**(23): p. 2279-2281.
3. P. Roussignol, D. Ricard, J. Lukasik, and C. Flytzanis, *New results on optical phase conjugation in semiconductor-doped glasses.* Journal of the Optical Society of America B, 1987. **4**(1): p. 5-13.
4. J. Sánchez-Curto, P. Chamorro-Posada, and G.S. McDonald, *Helmholtz solitons at nonlinear interfaces.* Optics Letters, 2007. **32**(9): p. 1126-1128.
5. J. Sánchez-Curto, P. Chamorro-Posada, and G.S. McDonald *Nonlinear interfaces: intrinsically nonparaxial regimes and effects.* Journal of Optics A: Pure and Applied Optics, 2009. **11**, DOI: 054015.
6. J. Sánchez-Curto, P. Chamorro-Posada, and G.S. McDonald *Black and gray Helmholtz Kerr soliton refraction.* Physical Review A, 2011. **83**, DOI: 013828.
7. J.M. Christian, E.A. McCoy, G.S. McDonald, J. Sánchez-Curto, and P. Chamorro-Posada *Interaction of Helmholtz bright spatial solitons with power-law optical interfaces.* Journal of Atomic and Molecular Physics, 2012. **2012**, DOI: 137967.
8. K.I. Pushkarov, D.I. Pushkarov, and I.V. Tomov, *Self-action of Light beams in nonlinear media: soliton solutions.* Optical and Quantum Electronics, 1979. **11**(1): p. 471-478.
9. A.B. Aceves, J.V. Moloney, and A.C. Newell, *Theory of light-beam propagation at nonlinear interfaces. I. Equivalent-particle theory for a single interface.* Physical Review A, 1989. **39**(4): p. 1809-1827.
10. A.B. Aceves, J.V. Moloney, and A.C. Newell, *Theory of light-beam propagation at nonlinear interfaces. II. Multiple-particle and multiple-interface extensions.* Physical Review A, 1989. **39**(4): p. 1828-1840.
11. A.B. Aceves, J.V. Moloney, and A.C. Newell, *Reflection and transmission of self-focused channels at nonlinear dielectric interfaces.* Optics Letters, 1988. **13**(11): p. 1002-1004.
12. A.B. Aceves, J.V. Moloney, and A.C. Newell, *Snell's laws at the interface between nonlinear dielectrics.* Physics Letters A, 1988. **129**(4): p. 231-235.
13. A.B. Aceves, P. Varatharajah, A.C. Newell, E.M. Wright, G.I. Stegeman, D.R. Heatley, J.V. Moloney, and H. Adachihara, *Particle aspects of collimated light channel propagation at nonlinear interfaces and in waveguides.* Journal of the Optical Society of America B, 1990. **7**(6): p. 963-974.
14. J.M. Christian, G.S. McDonald, and P. Chamorro-Posada *Bistable Helmholtz solitons in cubic-quintic materials*. Physical Review A, 2007. **76**, DOI: 033833.
15. A.B. Aceves and J.V. Moloney, *Effect of two-photon absorption on bright spatial soliton switches.* Optics Letters, 1992. **17**(21): p. 1488-1490.
16. P. Varatharajah, A.C. Newell, J.V. Moloney, and A.B. Aceves, *Transmission, reflection, and trapping of collimated light beams in diffusive Kerr-like nonlinear media.* Physical Review A, 1990. **42**(3): p. 1767-1774.
17. P. Chamorro-Posada, G.S. McDonald, and G.H.C. New, *Propagation Properties of Nonparaxial Spatial Solitons.* Journal of Modern Optics, 2000. **47**(11): p. 1877-1886.
18. P. Chamorro-Posada, G.S. McDonald, and G.H.C. New, *Non-paraxial solitons.* Journal of Modern Optics, 1998. **45**(6): p. 1111-1121.
19. E. Hecht, *Optics* 2002: Addison Wesley.
20. P. Chamorro-Posada, G.S. McDonald, and G.H.C. New, *Non-paraxial beam propagation methods.* Optics Communications, 2001. **192**(1–2): p. 1-12.

3. Single interfaces II: Goos-Hänchen shifts

3.1 The concept of the Goos-Hänchen shift

This chapter investigates Goos-Hänchen shift (GHS) behaviour at the interface between two dissimilar cubic-quintic materials; this type of interface problem was discussed extensively in Chapter 2. A GHS [1] is a phenomenon that occurs when a collimated light beam interacts with an interface at an angle of incidence that is close to the beam's critical angle. Upon interaction with the interface, rather than being reflected by the interface, the beam becomes trapped by it, propagates along (or close to) it for a distance, and is then reflected back into the first medium (see Figure 19).

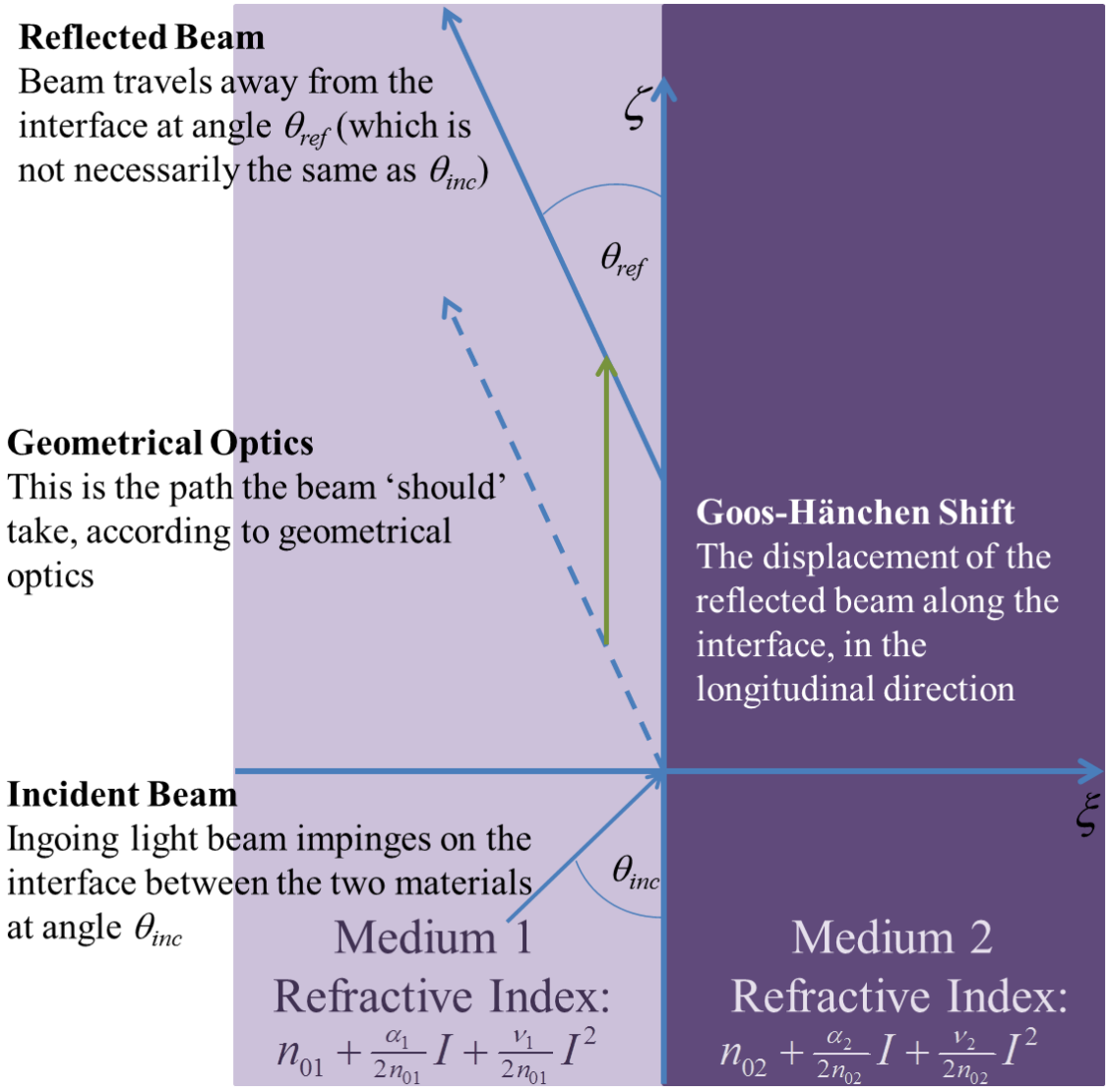

Figure 19 A schematic diagram of a GHS. θ_{ref} is not necessarily the same as θ_{inc}.

Because the beam is trapped along the interface for a distance, it can partially penetrate into the second medium. The beam is not reflected from a single point as a plane wave would be; the reflection process instead, is distributed along the interface, giving rise to the GHS. Here, the shift is defined as the displacement of the beam along the interface, i.e. the difference between the geometrical optical path and the actual path of the reflected beam, in the longitudinal direction, as opposed to being the transverse displacement between the geometrical optical path and the actual path of the beam. Both of these definitions have been used in previous studies: [2] (transverse displacement) and [3] (longitudinal displacement). The two different definitions for quantifying the GHS are highlighted in Figure 20.

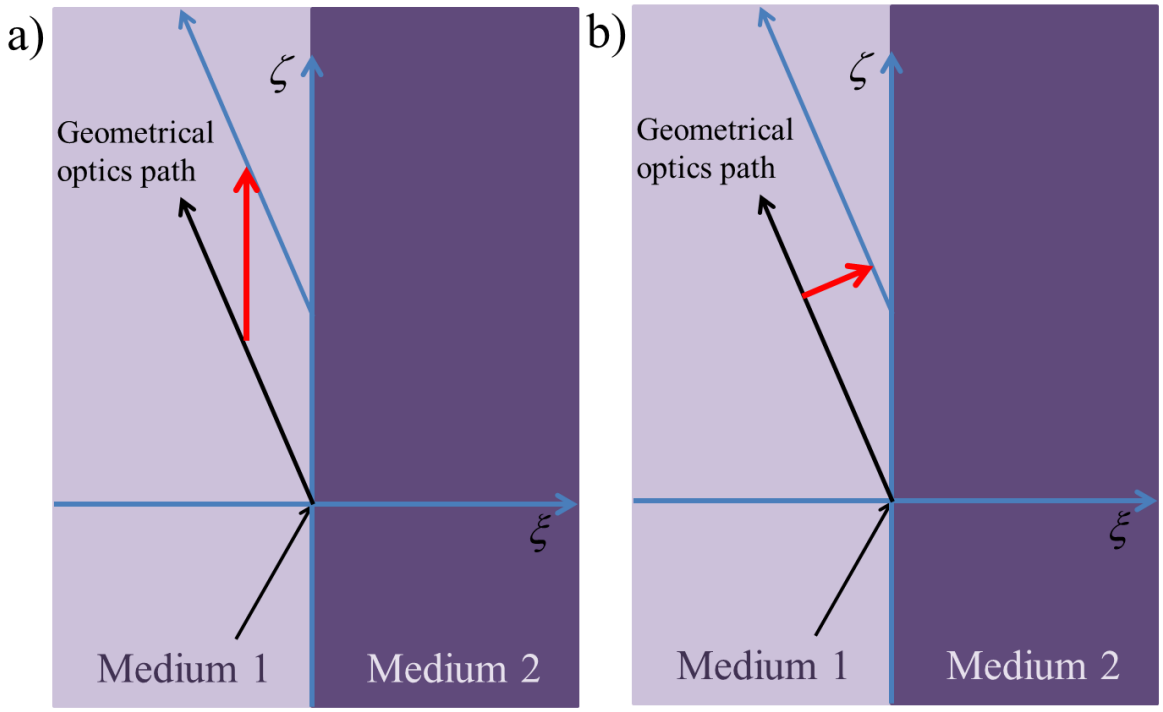

Figure 20 Showing the two definitions of a GHS. The definition shown in a) is used here.

3.1.1 Literature Review

The GHS was first observed and investigated extensively for Gaussian beams at the interface between two linear materials [4-8], where the shifts were found to be of the order of one optical wavelength. It was later found that the nonlinear GHS at the interface between a linear and a nonlinear material [9, 10] or between two nonlinear materials [3, 11, 12] is much larger than the linear GHS. This increase is due to the potential for the beam to become trapped by a nonlinear interface and propagate as a surface wave [13].

Although the Helmholtz wave equation has been used previously in studies investigating GHSs at interfaces between two linear dielectric materials [14], Sánchez-Curto *et al*. in [3] are the first to consider the GHS of Helmholtz solitons. By using this theory, new regimes of shift behaviour have been investigated, which will be discussed in section 3.4.2. One conclusion made in reference [3] is that the broadness of the beam can easily be predicted in the second medium, w.r.t its broadness in medium1, depending upon the parameter regimes being investigated. This is also found to be predictable at cubic-quintic interfaces, however the parameter regimes considered here are more complex than at Kerr interfaces, and thus, making the prediction is not as straight forward. This will be shown in section 3.4.2.2.

In reference [12] the GHSs considered are not within the standard Kerr-type materials, but rather a more general power-law material interface. Again, Helmholtz soliton theory was used to simulate the GHSs, meaning that instances of linear external refraction can be seen. This paper is of importance because it predicted that by changing the nonlinearities of the host materials from Kerr to power-law, new, and qualitatively different phenomena in the behaviour of the GHS can emerge. Amongst other results, it was found that increasing the angle of incidence of the beam does not always mean that the GHS will increase (which is in contrast with reported results for Kerr interfaces, see reference [3]).

Another study of note is reference [11]. In this paper, the authors derive an equation which predicts the length of a GHS as a function of the energy of the beam. Reference [11] shows that there is marginal agreement between this prediction and the numerical results. A similar attempt was made to predict the length of GHSs as part of this work, but it proved ineffectual and is, therefore, not included here. This is an area where further work is needed.

3.2 Critical angles

The critical angle defined in ray optics [15] is rarely seen when investigating spatial solitons at the interface between two nonlinear materials. When the beam is propagating with an angle of incidence which is close to its predicted critical angle, its behaviour on interacting with the interface is very unpredictable. This makes ascertaining a true value for the critical angle problematic. The following schematic shows how the critical angle is defined in geometrical optics, and is adapted directly from reference [15].

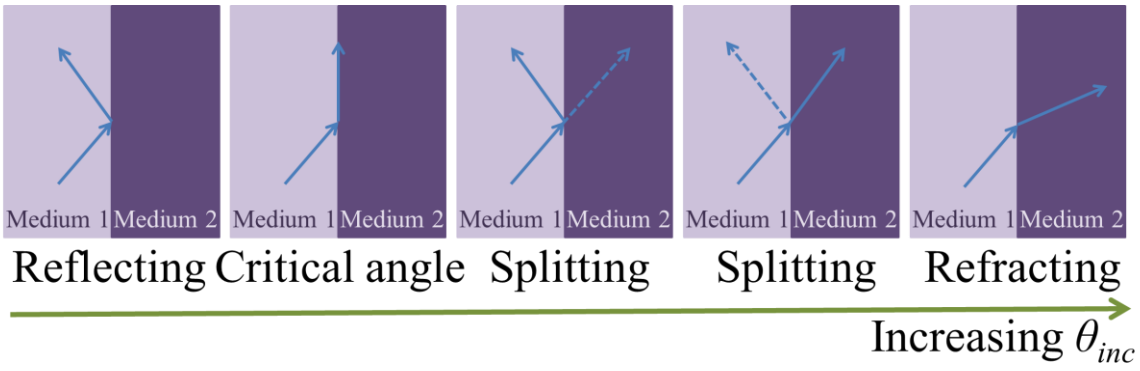

Figure 21 Showing how the behaviour of light at an interface changes, as the angle of incidence is increased.

However, such an idealised manifestation of the behaviour of a beam at its critical angle has never been found in the numerical cubic-quintic results. Changing the angle of incidence by values as low as one millionth of a degree in the range where we would expect to find the critical angle, brings us no closer to finding such an idealised result.

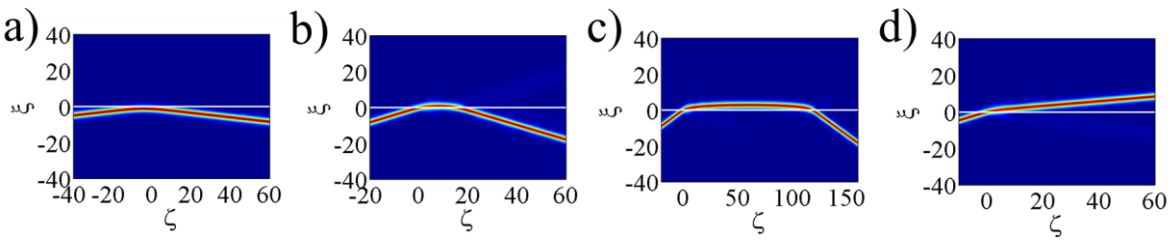

Figure 22 Beam behaviour as the angle of incidence is increased. In this example, giant GHSs are present. The data for these results has: $\rho_0 = 1.3$, $\kappa = 2.5 \times 10^{-3}$, $\alpha = 1$, $\nu = 1$, $\sigma = -0.15$. a) has an angle of incidence of $\theta_{inc} = 0.5°$, b) $\theta_{inc} = 1.674°$, c) $\theta_{inc} = 1.822°$ and d) $\theta_{inc} = 1.9°$. In this example, c) is taken to be the critical angle.

Because the idealised behaviour at the critical angle does not exist for spatial solitons at cubic-quintic interfaces (no assertion is made here about the status of critical angles in other media), a more workable and empirically-useful definition is required. In examples where little or no beam splitting is seen, the actual value for the critical angle is taken to be the angle of incidence which relates to a shift of around $\zeta = 120$, see Figure 22. In these cases, it is almost inevitable that even longer shifts could be found, which would be closer to the 'truer' value of a critical angle since the behaviour of the beam at critical angle is essentially a GHS of infinite length. However, there is a limit to the amount of computing power which can be devoted to finding the value of the critical angle, and so, $\zeta = 120$ is a compromise between rigour and practicality.

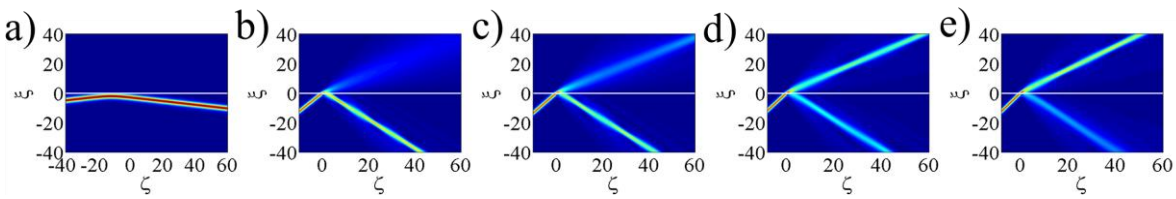

Figure 23 Showing beam behaviour as the angle of incidence is increased. In this example, beam splitting is present in c), d) and e). The data for these results has: ρ_0 = 1.3, κ = 2.5 x 10^{-3}, α = 1, ν = 1, σ = -0.15 and Δ = 0.01. a) has an angle of incidence of θ_{inc} = 0.5°, b) θ_{inc} = 5.045946°, c) θ_{inc} = 5.463964°, d) θ_{inc} = 5.96486° and e) θ_{inc} = 6.3°. In this example, c) is taken to be the critical angle.

In Figure 23, cases where the beam splits as it interacts with the interface can be seen. The actual critical angle is taken to be the lowest angle of incidence where a refracted beam can be seen. This is because this point is realistically the closest point to the critical angle.

Although a theoretical value for the critical angle of the beam at this interface can be calculated using:

$$\tan\theta_{\text{crit}} = \left\{ \frac{\Delta + 2\kappa\rho_0\left[\left(1-\alpha\right) + \frac{2}{3}\sigma\rho_0\left(1-\nu\right)\right]}{1-\Delta+2\kappa\rho_0\left(\alpha+\frac{2}{3}\nu\sigma\rho_0\right)} \right\}^{1/2}, \tag{3.1}$$

it has already been seen in Chapter 2 that this equation has its limitations. In this Chapter, the results will be analysed using the above reasoning and the theoretical value for the critical angle seen in equation (3.1) to pin down the most accurate value for the actual critical angle.

3.3 Computational method for calculating shifts

To calculate the value of the GHS computationally, a way to extract the difference in the longitudinal position of the numerical data and the predicted path of the beam with no shift must be found. The first step in doing this is to locate the centre of the beam from the numerical solution (see line zfit on Figure 24).

3.3.1 Finding zfit

To find the trajectory of the centre of the beam after the interaction with the interface, the data needs to be fitted to a profile resembling the exact cubic-quintic soliton [16]. This is done using the 'fminsearch' function in MATLAB, which tweaks the solution parameters until the profile of the numerical solution best fits an exact analytical solution. A line can then be plotted through the newly tweaked transverse position of the beam, and the

longitudinal position of the beam. This line is zfit, and it is taken to be the actual path of the beam after encountering the interface.

3.3.2 Finding zopt

The initial conditions of the beam are set up so that the centre of the beam interacts with the interface at the origin (see Figure 24). The assumption can then be made that with no shift, the beam would reflect from the interface at this location. To find the trajectory for this predicted path, an assumed value for the gradient must be made. By extracting the gradient for the line zfit (using 'polyfit') and shifting this down to the origin, a line can be plotted to represent the geometrical optical path of the beam (denoted by zopt).

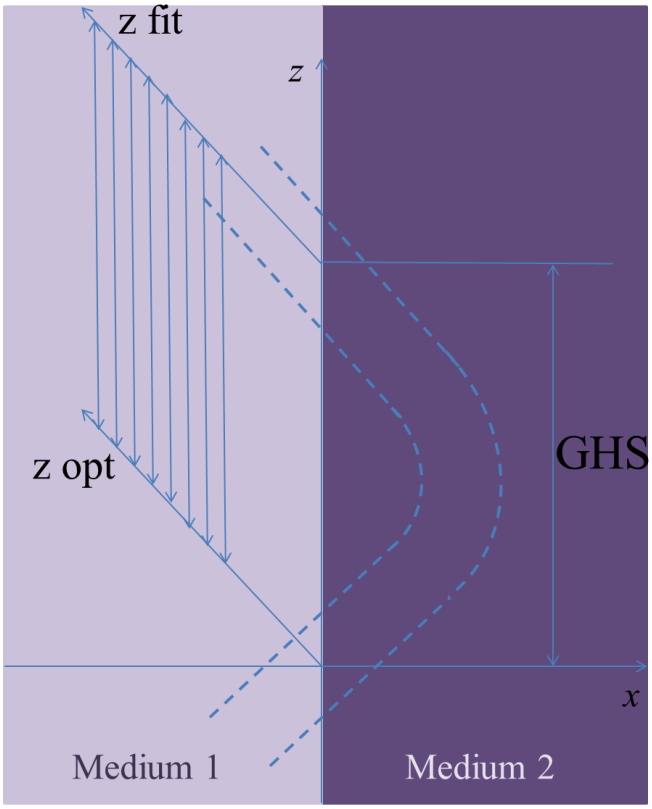

Figure 24 A schematic diagram showing how a value for the GHS is found computationally.

3.3.3 Finding GHSs

Once the steps in sections 3.3.1 and 3.3.2 have been carried out, the GHS can then be calculated easily. An average value for the difference in z location for the last 129 points for the lines zfit and zopt is found, and this is taken to be the value for the GHS.

3.4 Shifts in systems with cubic-quintic nonlinearity

The following equation:

$$\delta = \Delta + 2\kappa\rho_0\left[\left(1-\alpha\right)+\tfrac{2}{3}\sigma\rho_0\left(1-\nu\right)\right], \tag{3.2}$$

is key when analysing the GHS results. The net mismatch parameter δ in equation (3.2) characterises beam refraction at the interface, and was introduced in Chapter 2. It has already been discussed that for a GHS to exist, a critical angle must be real for the parameters chosen. Equation (3.2) can predict, with some accuracy whether or not a real theoretical critical angle exists for the parameters selected (when $\delta > 0$ a critical angle exists, but when $\delta < 0$ the critical angle is imaginary, and thus unphysical).

If Δ (the mismatch in the linear part of the refractive index) is positive, and δ is also positive then the GHSs are *internal*. These shifts have been seen many times in the literature, see references [4-10, 14]. The use of Helmholtz soliton theory means that, physically, Δ can also be negative, and that if other parameters in equation (3.2) are chosen to allow δ to remain positive, *external* shifts can be investigated. These have been seen previously, in ref. [3], however due to the introduction of the quintic term in the refractive index, there is the potential to show qualitatively-new external GHSs. All the results in this section have had parameters selected due to equation (3.2).

In the figures which follow, the graph labelled a) shows how the value of the GHS changes as the angle of incidence is increased between either 0.5° or 0.1° to the value for the theoretical critical angle. The results labelled b), c) and d), are the data from the largest angle of incidence for each value of Δ, and resultantly, the point chosen to be the critical angle.

The parameters used here are the same as those considered in Chapter 0:

$\boldsymbol{\kappa} \propto (\lambda/w_0)^2$ (*inverse beam width*). Two typical values of κ are considered (namely, 2.5×10^{-3} and 1.0×10^{-3}); both respect the inherent inequality for Helmholtz modelling [that $\kappa << O(1)$].

$\boldsymbol{\alpha} \equiv \alpha_2/\alpha_1$ (*ratio of cubic nonlinearity coefficients*). Values of α are chosen to be 0.1, 0.5, 1.0 or 2.0. The two non-unity cases represent a change in the strength of the focusing properties of the medium across the interface.

$\nu \equiv \nu_2/\nu_1$ (*ratio of quintic nonlinearity coefficients*). Values of ν are chosen to be 0.1, 0.5, 1.0, 2.0 or 2.5.

$\sigma \equiv \nu_1 E_0^2/\alpha_1$ (*ratio of cubic to quintic nonlinear phase shifts*). Typically, the quintic contribution to self-focusing is a small correction to the cubic (Kerr) effect [17]. The competing cubic-quintic nonlinear response can be used as a leading-order approximation to a saturable intensity-dependent refractive index [17]. Here, $\sigma = \pm 0.15$ is used [16].

ρ_0 (*peak intensity*). For $\sigma = -0.15$, the bistability condition means that there are two values of ρ_0 describing solutions with different peak intensities but the same full-width-at-half-maximum: $\rho_0 \approx 1.3$ and $\rho_0 \approx 4.14$ [16]. For $\sigma = +0.15$, the corresponding soliton is monostable and has $\rho_0 \approx 0.87$.

3.4.1 Linear Interfaces

For a GHS to exist, the parameter regimes being considered must be those where a critical angle exists (GHSs are found when the angle of incidence of a beam is close to its critical angle). For a critical angle to exist here, then $\delta > 0$. At linear interfaces (defined as having $\alpha = 1$ and $\nu = 1$), from equation (3.2) one has $\delta = \Delta$. This means for the purposes of this section on linear interfaces, only results with $\Delta > 0$ were explored further, since instances of $\Delta < 0$ would not give rise to GHSs at this interface type.

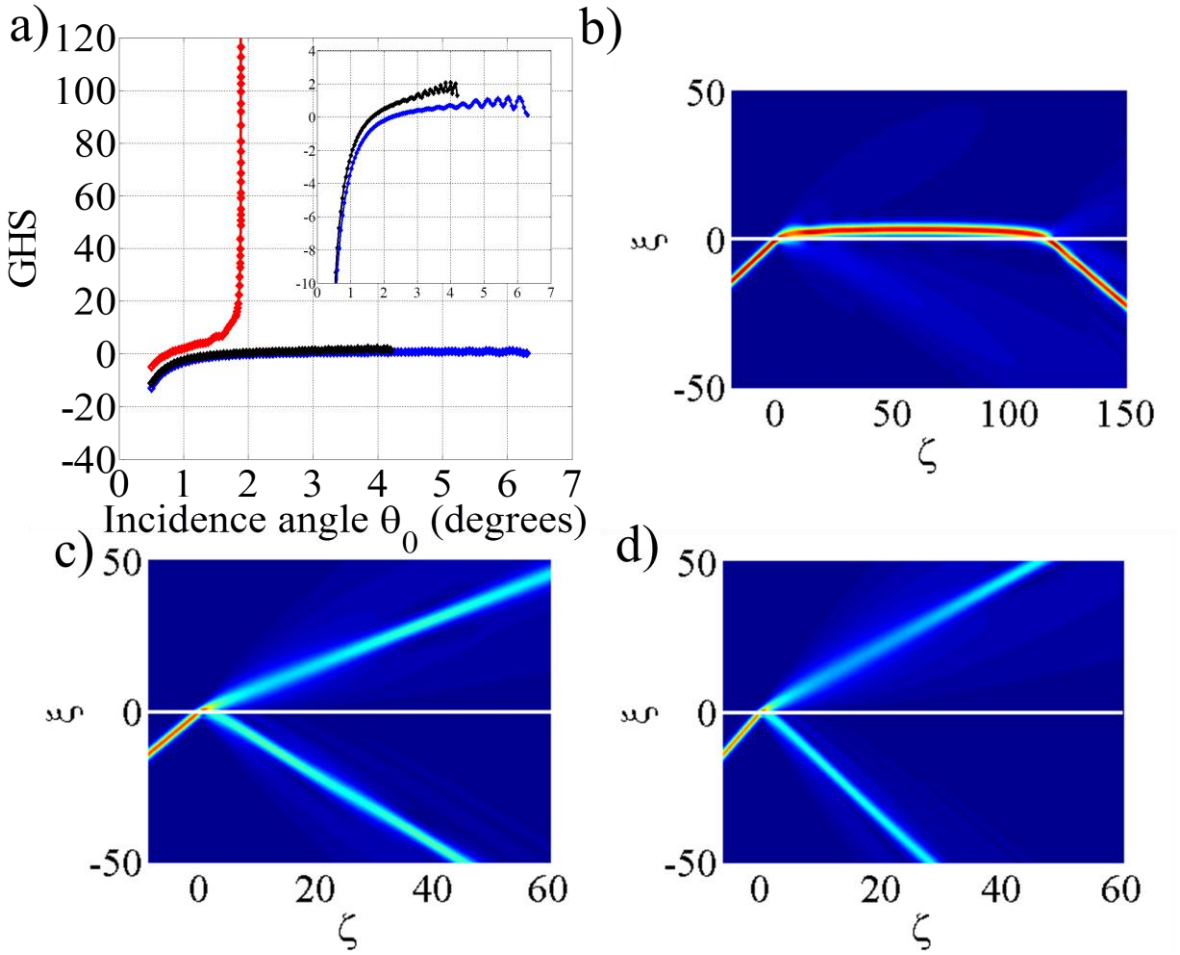

Figure 25 Shown here are GHSs for the parameters: $\rho_0 = 1.3$, $\kappa = 2.5 \times 10^{-3}$, $\alpha = 1$, $\nu = 1$ and $\sigma = -0.15$. The figure labelled a) shows the relationship between the angle of incidence of the beam, and its GHS value. b), c) and d) show the full results for the highest value of the angle of incidence shown in a) (and hence the critical angle) for values of $\Delta = 0.001$ ($\theta_{crit(act)} = 1.822°$), 0.005 ($\theta_{crit(act)} = 3.582883°$) and 0.01($\theta_{crit(act)} = 5.463964°$), respectively.

The results shown in Figures 25-27 are all examples of internal shifts (where $\Delta > 0$). The plots in pane a) show the changes in the length of the shift as the angle of incidence is increased. In the majority of these results, when $\Delta = 0.001$ (which is the smallest value of Δ investigated here), increasing the angle of incidence of the beam increases the length of the shift. The closer the angle of incidence of the beam gets to its actual critical angle, the larger the increases in the shift become.

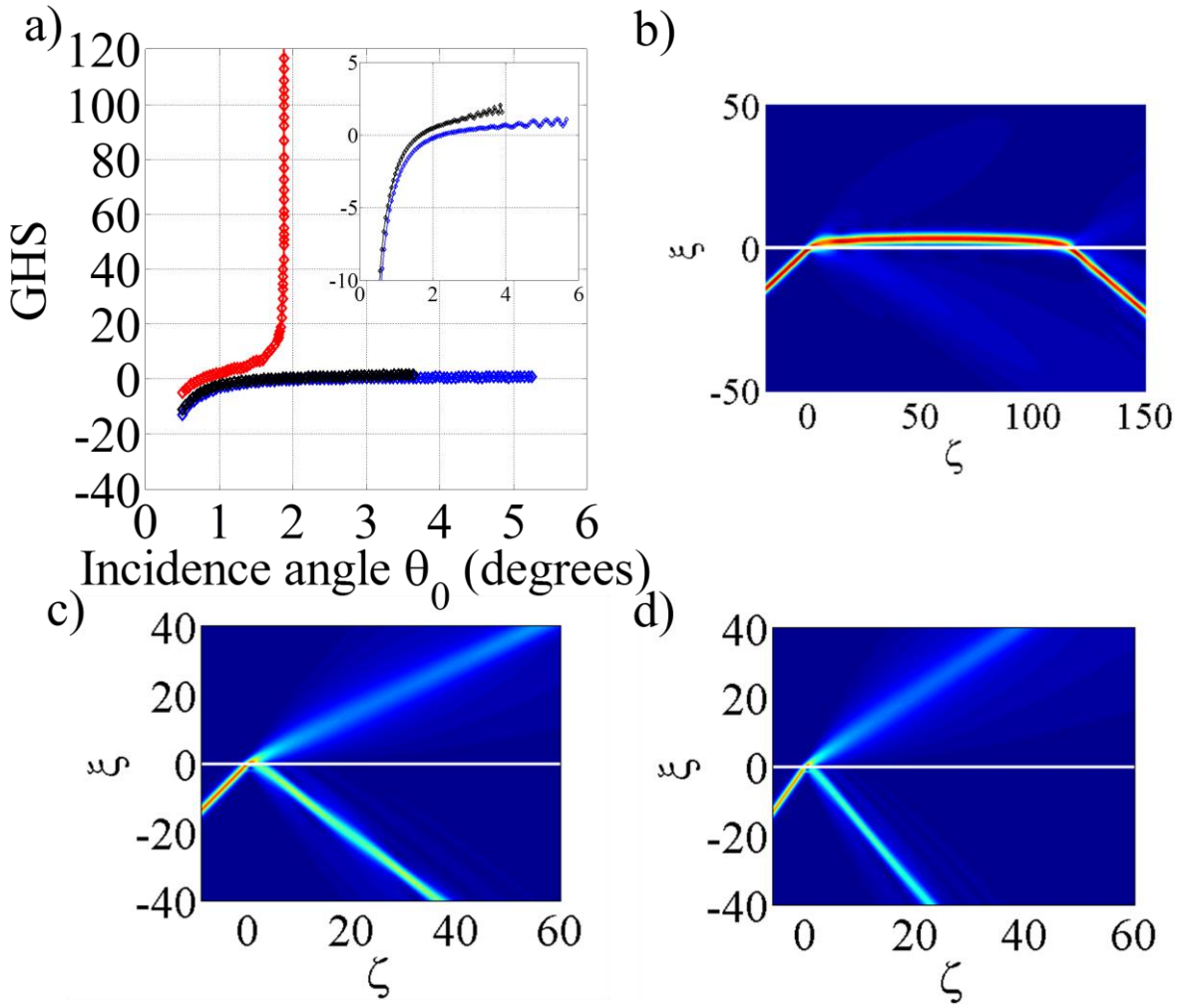

Figure 26 Shown here are GHSs for the parameters: ρ_0 = 1.3, κ = 1 x 10^{-3}, α = 1, ν = 1 and σ = -0.15. The figure labelled a) shows the relationship between the angle of incidence of the beam, and its GHS value. b), c) and d) show the full results for the highest value of the angle of incidence shown in a) (and hence the critical angle) for values of Δ = 0.001 ($\theta_{crit(act)}$ = 1.886°), 0.005 ($\theta_{crit(act)}$ = 3.892405°) and 0.01 ($\theta_{crit(act)}$ = 5.672973°) respectively.

As Δ is increased, it becomes more likely that the values for the shifts will be significantly smaller. Although the shifts increase when the angle of incidence is between 0.5° and 2°, for angles of incidence above this, the value of the shift tails off, and an oscillatory relationship emerges. Also common for larger Δ is that close to the critical angle, the beam splits into reflected and refracted components on encountering the interface. This makes it much more difficult to ascertain an actual value for the critical angle, and this is seen in Figures 25-26 b) and c), and 27d).

For all these results the actual critical angle is found to be less than the theoretical critical angle.

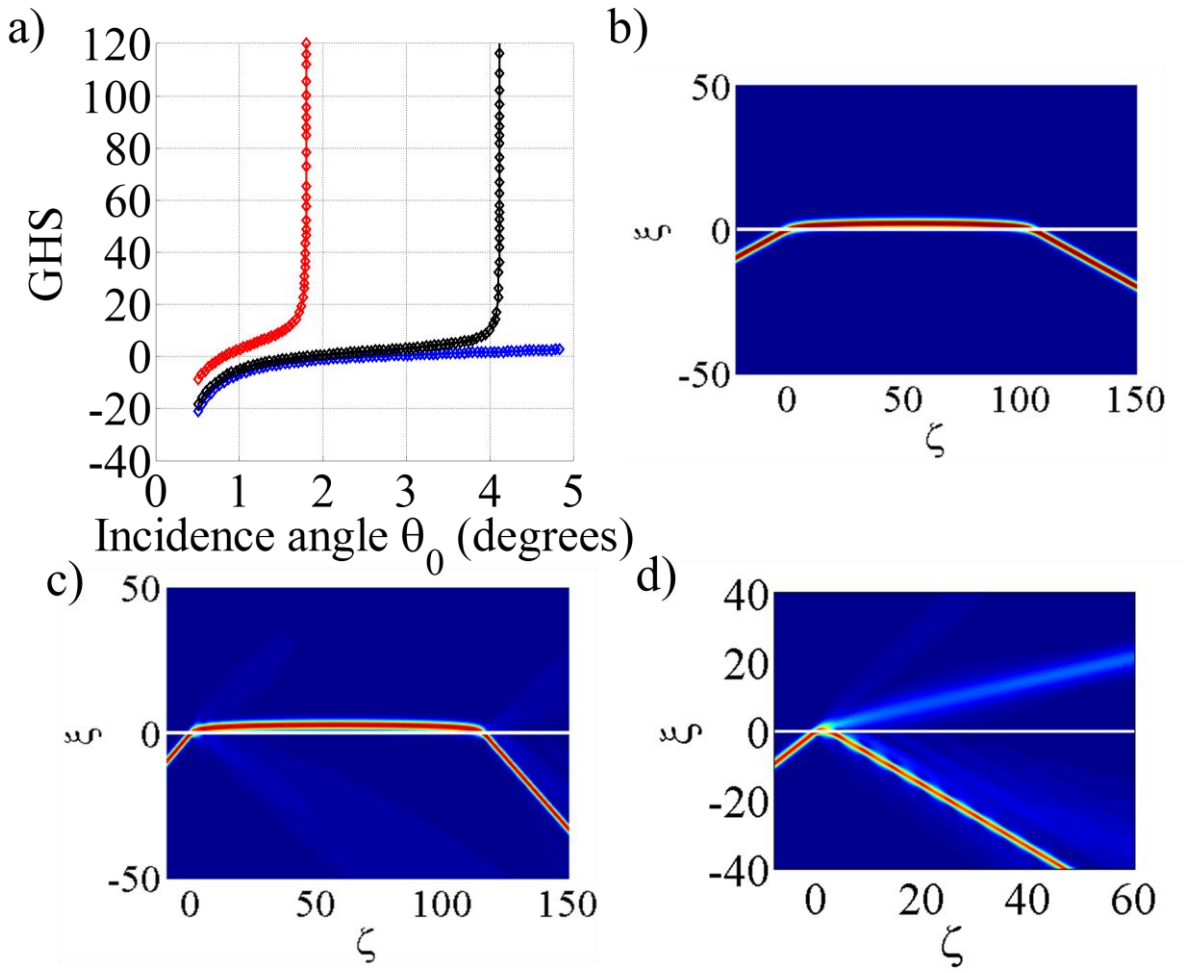

Figure 27 Shown here are GHSs for the parameters: ρ_0 = 4.14, κ = 2.5 x 10^{-3}, α = 1, ν = 1 and σ = -0.15. a) shows the relationship between the angle of incidence of the beam, and its GHS value. b), c) and d) show the full results for the highest value of the angle of incidence shown in a) (and hence the critical angle) for values of Δ = 0.001 ($\theta_{crit(act)}$ = 1.8024°), 0.005 ($\theta_{crit(act)}$ = 4.1137°) and 0.01 ($\theta_{crit(act)}$ = 4.836937°) respectively.

Figure 27 shows an unusual result, in that for Δ = 0.005 (Figure 27c), the relationship between θ and GHS is similar to that expected when Δ = 0.001; contrary to expectation (i.e., with respect to Figure 25), we find less beam splitting at Δ = 0.005 and more giant GHSs. Beam splitting at larger values of Δ is due to the mismatch between the linear part of the refractive index in each medium being too great to allow for the beam to penetrate into the second medium, causing beam splitting at the point of interaction with the interface [18]. Figure 27c) shows that giant GHS can exist when Δ = 0.005. More work is needed to explain fully this unusual result, but it is probably related to the relative narrowness of the beam [3].

3.4.1.1 Giant Goos-Hänchen Shifts

Although the preceding plots show values of shift up to $\zeta_0 = 120$, it has been shown that shifts of much larger values may exist; see ref. [3] and Figure 28 below. Figures 28 and 29 above that Giant GHS can be found with both low and high amplitude beams.

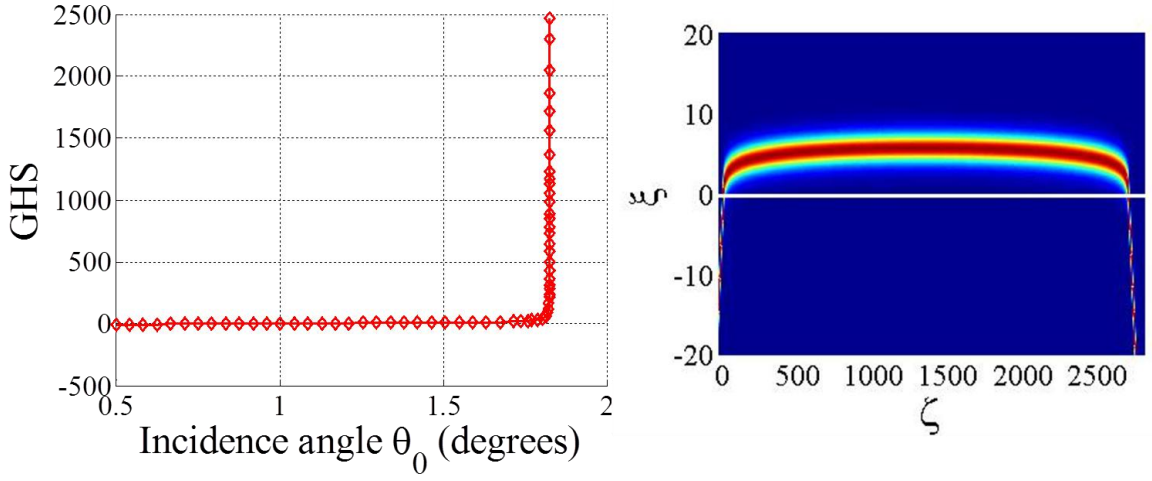

Figure 28 Showing a GHS for the parameters $\rho_0 = 1.3$, $\kappa = 2.5 \times 10^{-3}$ and $\Delta = 0.001$. The value of the shift here is $\zeta_0 = 2470.7$, and corresponds to an angle of incidence of 1.82491°.

In ref. [3] giant GHSs are shown at dissimilar Kerr-type interfaces. In that paper, shifts are seen with values up to $\zeta_0 = 200$. Figure 28 shows a giant GHS at a cubic-quintic interface, where the shift is $\zeta_0 = 2470.7$. This is, to the best of my knowledge, the largest GHS found at a nonlinear interface.

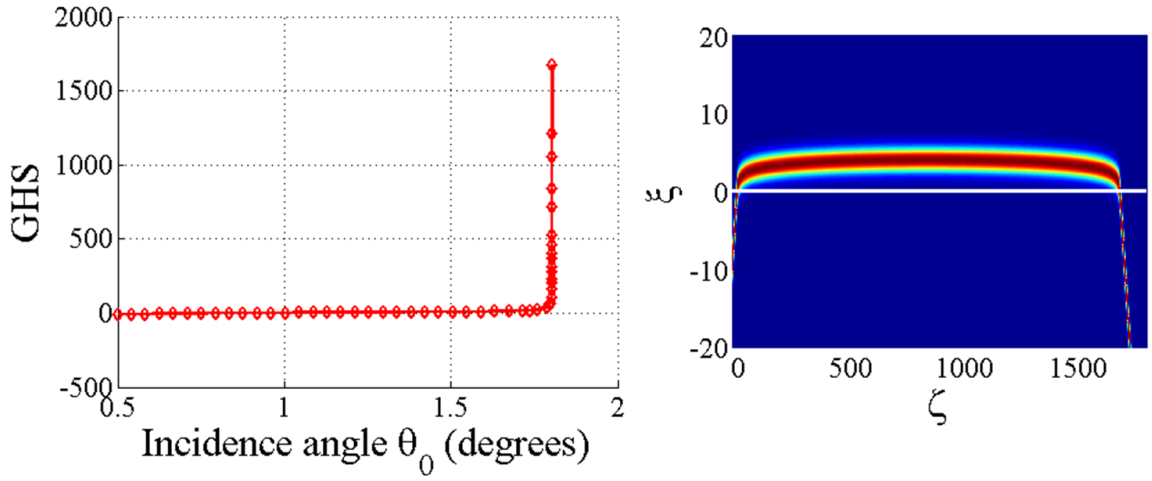

Figure 29 Showing a GHS for the parameters $\rho_0 = 4.14$, $\kappa = 2.5 \times 10^{-3}$ and $\Delta = 0.001$. The value of the shift here is $\zeta_0 = 1678.1$, and corresponds to an angle of incidence of 1.80374°.

It is thought that the shift size for results with smaller values of Δ will increase indefinitely because the GHSs appear to diverge asymptotically; that is to say ever smaller increments in θ_{inc} result in vastly larger shifts. Both the results in Figures 28 and 29 show the beams penetrating a significant distance into the second medium, before being reflected back into the first.

3.4.1.2 Negative GHS

When the angle of incidence of the beam is 0.5°, $\zeta_0 < 0$. A negative value for a GHS occurs when the beam 'feels the effect' of the interface before encountering it, and is repelled by the interface. This results in a reflected beam that has interacted only very weakly with the interface.

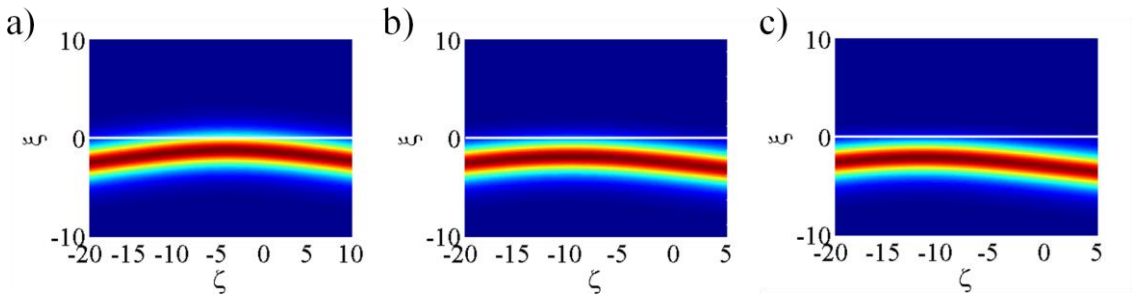

Figure 30 Shows examples of negative GHS. It can be seen in all three examples that the beam reflects without the centre of the beam encountering the interface. Parameters of the beams are: $\rho_0 = 1.3$, $\kappa = 2.5\text{x}10^{-3}$, $\alpha = 1$, $\nu = 1$, $\sigma = -0.15$, $\theta_{inc} = 0.5°$ with $\Delta = 0.001$, 0.005 and 0.01 in a), b) and c) respectively.

Because the value of the GHS is calculated according to:

$$\text{GHS} = \text{actual reflected path} - \text{predicted optical path}, \tag{3.3}$$

the shift being a longitudinal *displacement* means that the value will be negative when reflecting before interacting with the interface. The geometrical optical path of the beam will then have larger ζ values than the beam's actual reflected path.

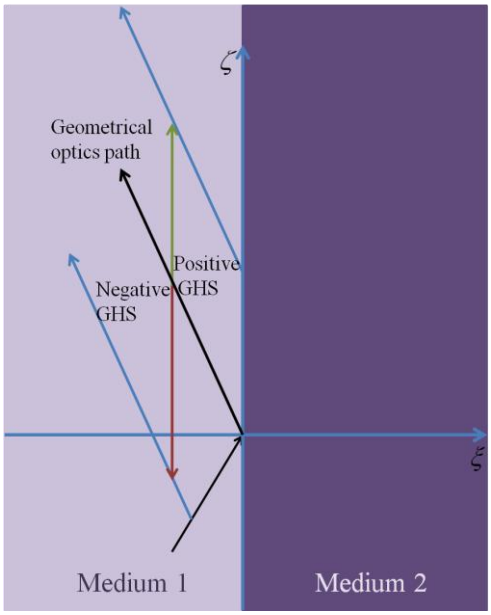

Figure 31 Schematic diagram showing the negative GHS arises as a result of reversing the direction of a displacement.

3.4.2 Shifts at mixed interfaces

Results at mixed interfaces can be categorised as either internal or external GHSs. Internal GHSs will be considered first in this section. They are a more 'standard' type of shift, having been seen previously in this chapter (all GHSs at linear interfaces are instances of internal GHSs) and are prominent in the literature [1, 4-11].

3.4.2.1 Internal shifts at mixed interfaces

Internal shifts arise when the parameters are chosen such that $\delta > 0$ (which is always required for GHSs to occur) and $\Delta > 0$ (as was necessary when looking at linear interfaces).

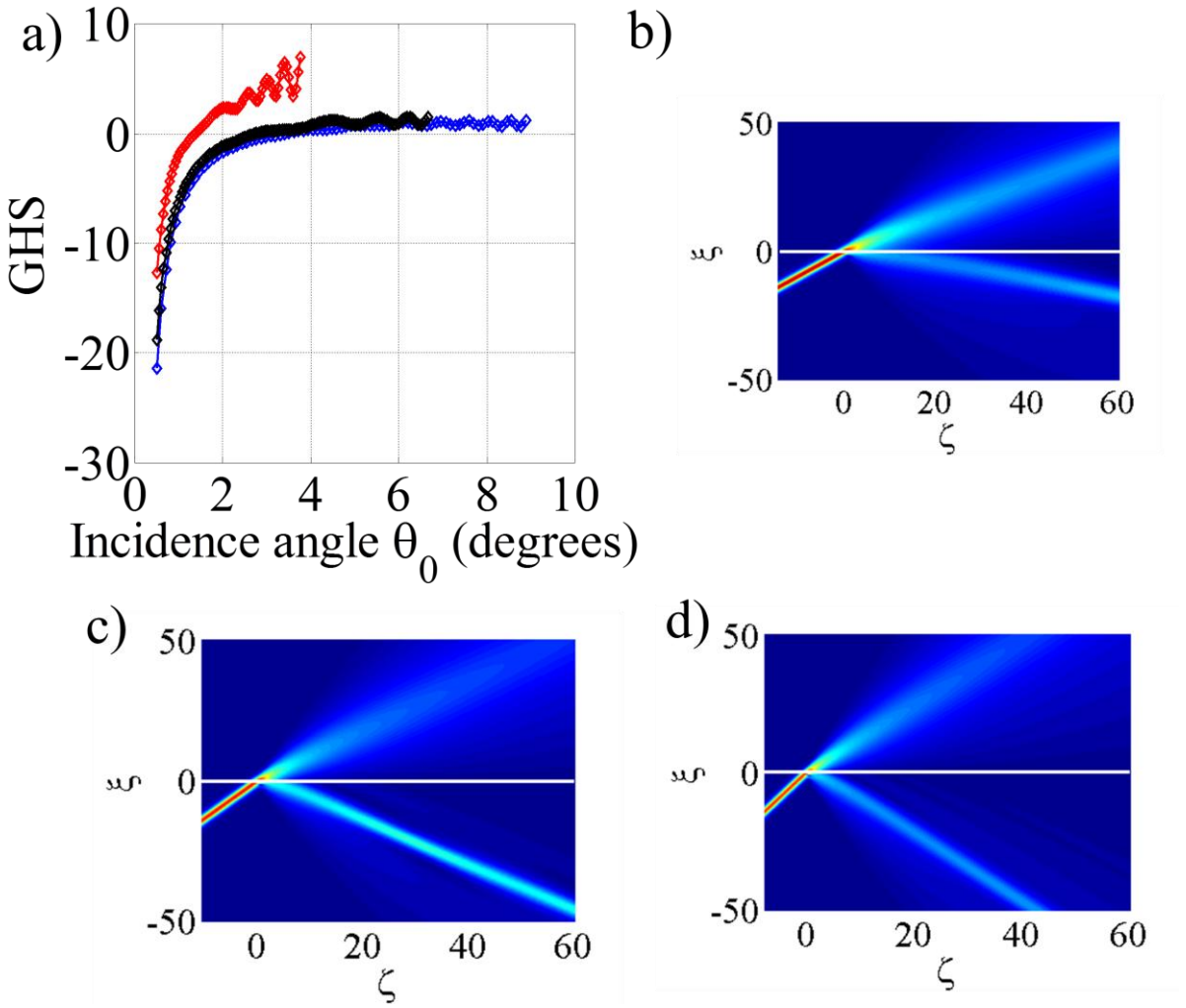

Figure 32 Shown here are GHSs for the parameters: ρ_0 = 1.3, κ = 2.5 x 10^{-3}, α = 0.5, ν = 1 and σ = -0.15. a) Shows the relationship between the angle of incidence of the beam, and its GHS value. b), c) and d) show the full results for the highest value of the angle of incidence shown in a) (and hence the critical angle) for values of Δ = 0.001 ($\theta_{crit(act)}$ = 3.774°), 0.005 ($\theta_{crit(act)}$ = 6.672°) and 0.01($\theta_{crit(act)}$ = 8.892°) respectively.

One obvious difference between the internal shifts at mixed interfaces, and the results in any other section of this chapter, is that the beam will invariably split on interacting with the interface when the angle of incidence is close to its critical angle. The splitting manifests as the GHS goes from negative to positive. One question that may arise from this is 'how meaningful is the shift value when a beam splits?' Due to the way in which the shift is calculated, the shift value is still accurate when a significant amount of beam splitting is seen, however, as has already been mentioned, the difficulty lies in finding a true value for the critical angle. Figures 32-34, b), c) and d) show the beam propagating with an angle of incidence which is as close to the critical angle of the beam as possible.

Figure 32a) shows the relationship between the GHS and the angle of incidence of the beam. Beam splitting causes reductions in the magnitude of the GHS.

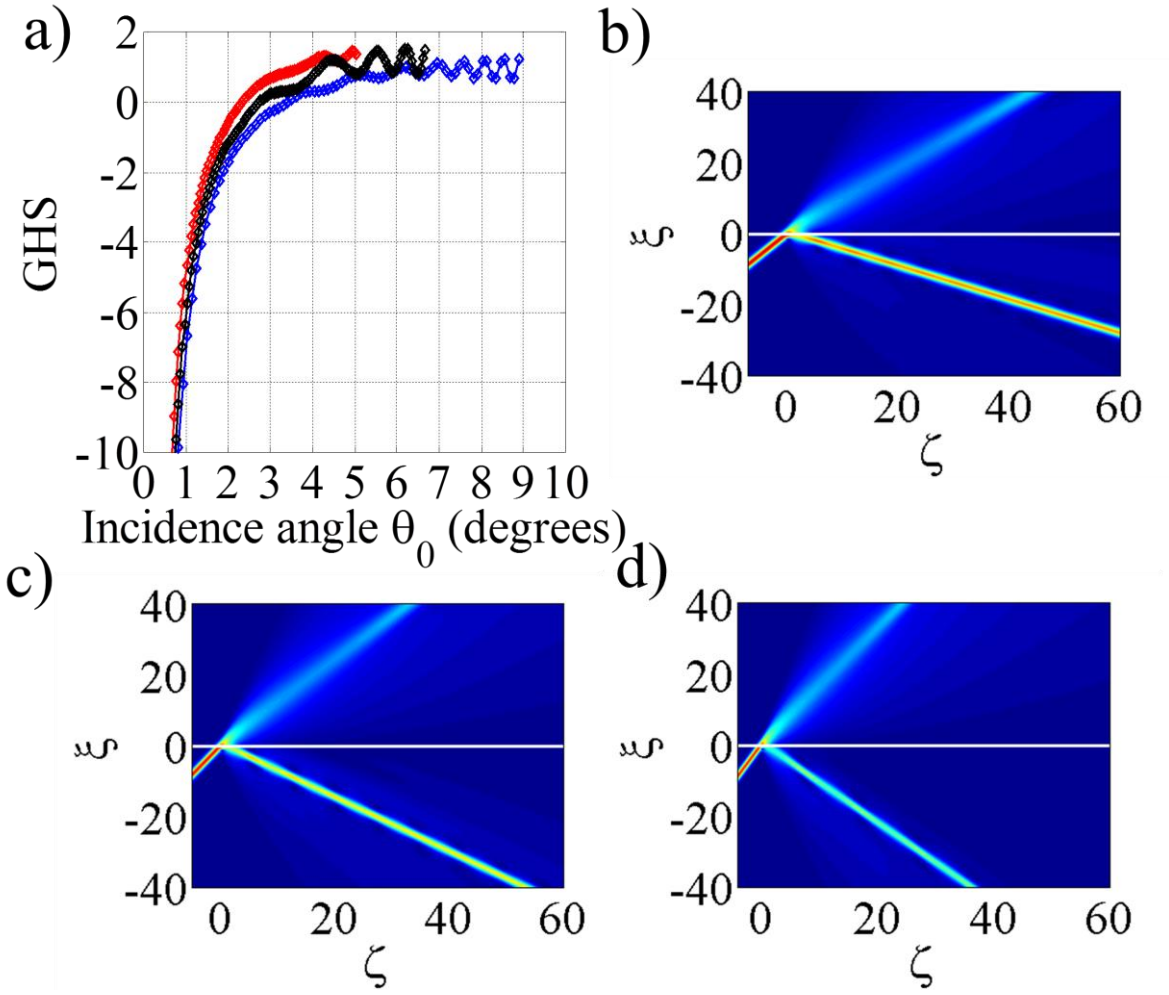

Figure 33 Shown here are GHSs for the parameters: ρ_0 = 4.14, κ = 2.5 x 10^{-3}, α = 0.5, ν = 1 and σ = -0.15. a) Shows the relationship between the angle of incidence of the beam, and its GHS value. b), c) and d) show the full results for the highest value of the angle of incidence shown in a) (and hence the critical angle) for values of Δ = 0.001 ($\theta_{crit(act)}$ = 5.045946°), 0.005 ($\theta_{crit(act)}$ = 6.672441°) and 0.01($\theta_{crit(act)}$ = 8.892405°) respectively.

Figure 33 shows similar results to Figure 32, however the magnitudes of the shift are much reduced, with increasing the intensity of the beam. The reflected beams are much stronger as the refracted beam forms than in Figure 32.

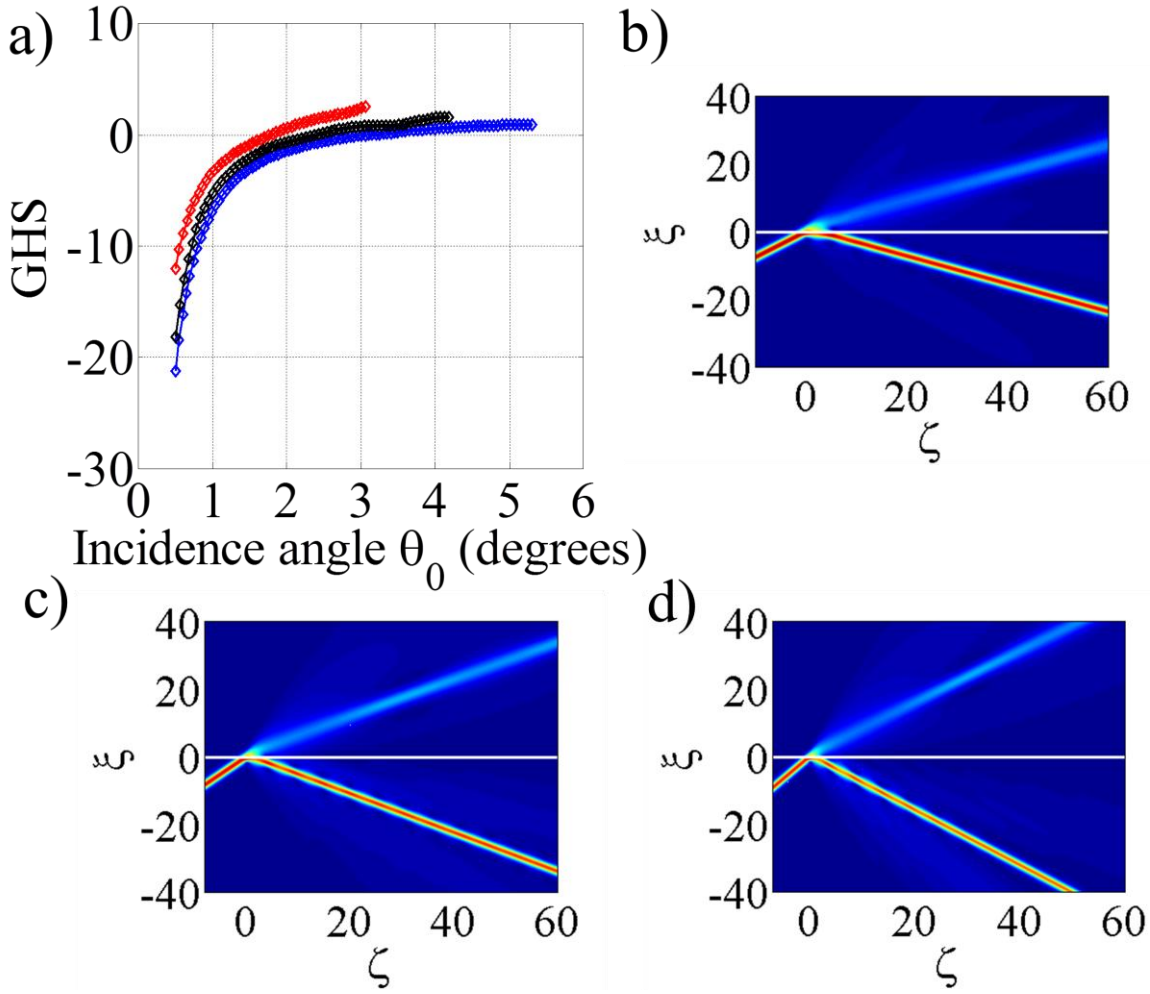

Figure 34 Shown here are Goos-Hänchen shifts for the parameters: ρ_0 = 4.14, κ = 2.5 x 10^{-3}, α = 1, ν = 2 and σ = -0.15. a) Shows the relationship between the angle of incidence of the beam, and its GHS value. b), c) and d) show the full results for the highest value of the angle of incidence shown in a) (and hence the critical angle) for values of Δ = 0.001 ($\theta_{crit(act)}$ = 3.06036°), 0.005 ($\theta_{crit(act)}$ = 4.185039°) and 0.01($\theta_{crit(act)}$ = 5.308861°) respectively.

Here, in Figure 34, the shifts are very small. It is interesting to note that it seems, on close inspection of the figures presented, that the results in a) appear more accurate than in Figures 32-33. Accuracy here is judged manually, by finding what the length of the shift is 'supposed to be' from the graph in a) and comparing this to the 'actual' shift lengths in figures b) through d). In doing this we find that the values in the graph in Figure 34a) are closer to the lengths of the shifts found in the 3-d plots in Figure 34b)-d) than is the case for the respective results in highlighted in Figures 32 and 33. In Figures 32-34 it can be seen that the values are more accurate when the reflected beam is stronger (i.e. has a higher amplitude and looks more 'beam like') when the refracted beam forms. In Figure 34 it can be seen that the beam is, indeed, stronger when the refracted beam forms than is the

case in Figures 32-33 and so it may be postulated that this is the reason for the more accurate results in this case.

3.4.2.2 External shifts at mixed interfaces

As can be seen from equation (3.2) there are three cases investigated here to find external GHSs at mixed interfaces:

- Case 1: $\alpha < 1$
- Case 2: $\nu < 1$ and $\sigma > 0$ ($\alpha = 1$)
- Case 3: $\nu > 1$ and $\sigma < 0$ ($\alpha = 1$)

Although external GHSs also exist when case 2 is combined with case 1, only the three separate cases mentioned were investigated (due to time constraints).

Case 1: $\alpha < 1$

External results when $\alpha < 1$ have been investigated before at Kerr interfaces, see reference [3]. The results discussed below are novel: this is the first time external GHSs have been simulated at cubic-quintic interfaces.

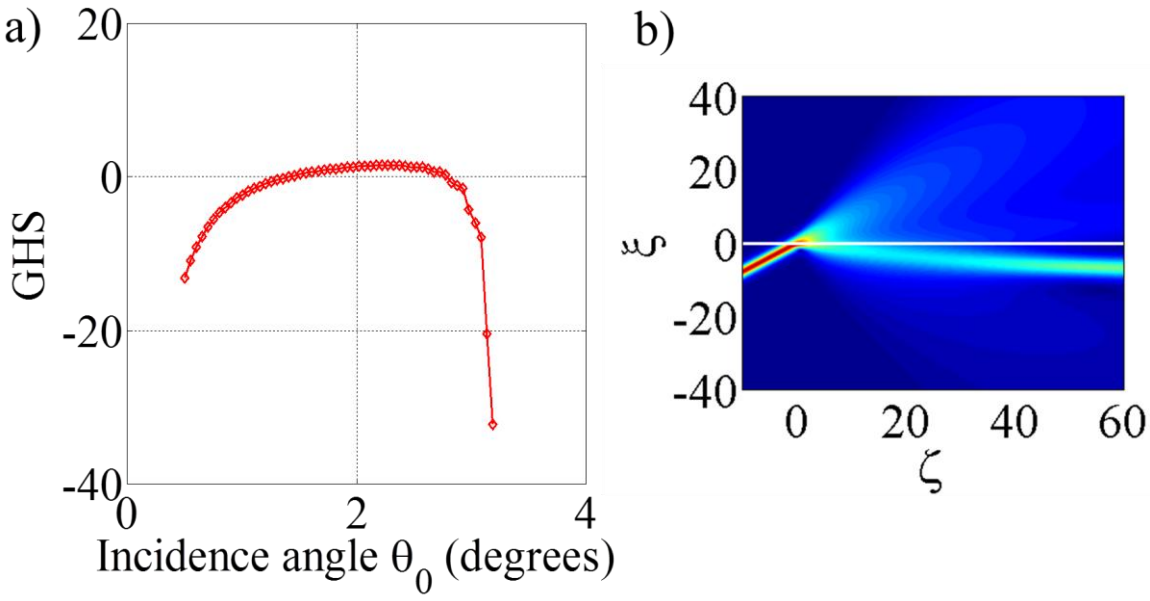

Figure 35 Shown here are GHSs for the parameters: $\rho_0 = 1.3$, $\kappa = 2.5 \times 10^{-3}$, $\alpha = 0.1$, $\nu = 1$ and $\sigma = -0.15$. a) Shows the relationship between the angle of incidence of the beam, and its GHS value. b) Shows the full result for the highest value of the angle of incidence shown in a) (and hence the critical angle) for $\Delta = -0.001$ ($\theta_{crit(act)} = 3.2342°$). Other values of Δ investigated are $\Delta = -0.005$ and $\Delta = -0.01$, however these value proved to have no critical angle.

Although the predicted theoretical critical angles for case 1 are quite large, sometimes as large as 4°, the results for the simulations show the critical angle for many of the chosen

parameters cannot be found. Figure 35 shows the results for the smallest |Δ|. It can be seen that the value of the shift only just gets above 0. At the point chosen as the critical angle, a lot of radiation can be seen crossing the interface, and the reflected beam is beginning to break down, as well as the path of the beam bending after the interaction with the interface. The negative shifts that occur at around 3° are potentially caused by the beam splitting.

Case 2: $\nu < 1$, $\sigma > 0$

The following two cases of external shifting rely on the values of ν, so these cases show new results.

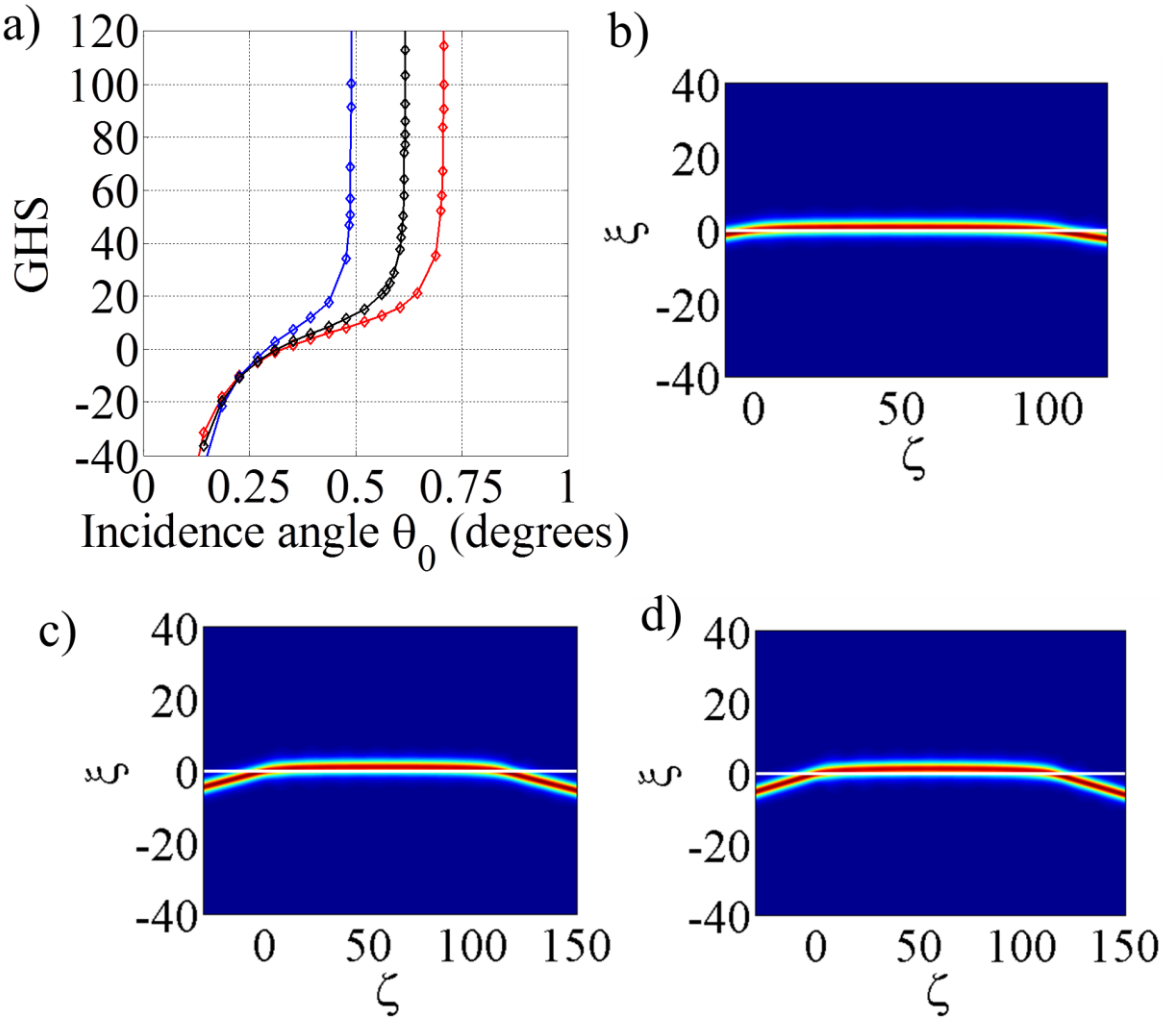

Figure 36 Shown here are GHSs for the parameters: $\rho_0 = 0.87$, $\kappa = 2.5 \times 10^{-3}$, $\alpha = 1$, $\nu = 0.1$ and $\sigma = 0.15$. a) Shows the relationship between the angle of incidence of the beam, and its GHS value. b), c) and d) show the full results for the highest value of the angle of incidence shown in a) (and hence the critical angle) for values of Δ = -0.0001 ($\theta_{crit(act)} = 0.14194°$), -0.00005 ($\theta_{crit(act)} = 0.6161°$) and -0.00001($\theta_{crit(act)} = 0.7075°$) respectively.

All results for case 2 present clear examples of giant GHSs. The predicted critical angles are very small (around 1°), and the mismatch parameters had to be chosen carefully to allow for the (potential) existence of a critical angle, and therefore the values of Δ used in Figure 36 are an order of magnitude smaller than those used in the linear interfaces section. Although the theoretical critical angles are small it was still possible in the simulations to find examples of beam reflection. Moreover, shifts of a significant length were found. The actual critical angles for the case 2 results are always slightly smaller than the theoretical predicted angles.

Case 3 - $\nu > 1$, $\sigma < 0$

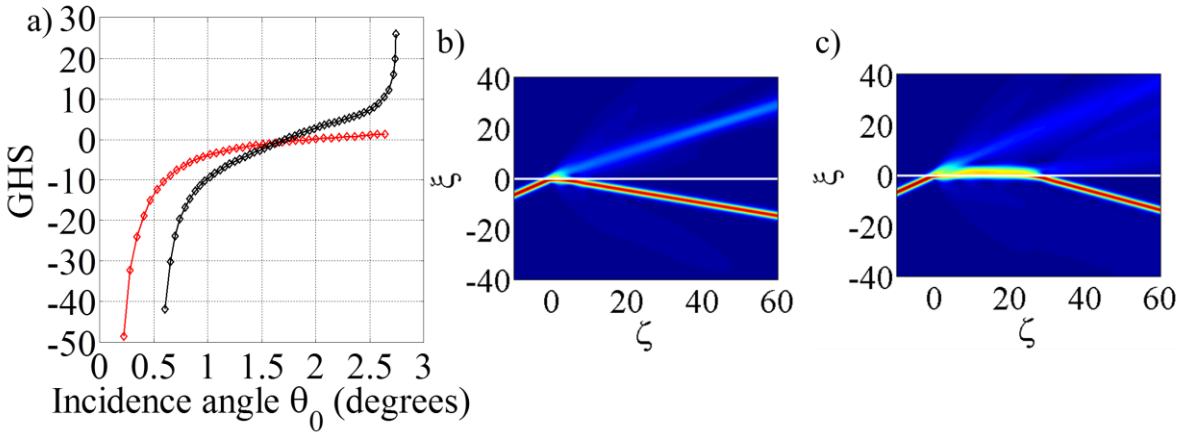

Figure 37 Shown here are GHSs for the parameters: $\rho_0 = 4.14$, $\kappa = 2.5 \times 10^{-3}$, $\alpha = 1$, $\nu = 2.5$ and $\sigma = -0.15$. a) Shows the relationship between the angle of incidence of the beam, and its GHS value. b) and c) show the full results for the highest value of the angle of incidence shown in a) (and hence the critical angle) for values of Δ = -0.001 ($\theta_{crit(act)}$ = 2.74°) and -0.0025 ($\theta_{crit(act)}$ = 2.643°). Δ = -0.005 was also investigated, however no critical angle was found.

For Case 3, the results are mixed. From the simulations, it would seem that the results are more like the results at linear interfaces, with significant shifts when |Δ| is smaller, and then as this is increased, beam splitting becomes the predominant behaviour. As was true in case 1, there are differences in the theoretical and actual critical angles (the figure shows results for two values of Δ, the third value investigated, Δ = -0.005, did not reflect, even at small incidence angles). Again, the actual critical angle is lower than the theoretical one, although the difference between the two is much greater than it was for case 2, results tables showing this can be found in Appendix C.

3.4.2.3 Nonlinear Interfaces

By looking at purely nonlinear interfaces (with $\Delta = 0$), the effect of varying the mismatch in the cubic and quintic contributions can be seen. This is the first time Helmholtz cubic-quintic GHSs have been investigated, so the parameter regimes where any effect could be solely linked to the quintic term is where novelty will lie (since it is the addition of the quintic term which distinguishes cubic-quintic material from Kerr materials).

As with every section in this chapter, the parameters have been chosen to ensure that a critical angle exists [see equation(3.2)]. When $\Delta = 0$, to ensure $\delta > 0$, there are two regimes considered:

- $\nu = 1$, $\alpha = 0.5$ (shows the effect of varying the cubic contribution across the interface)
- $\nu = 2$, $\alpha = 1$ (shows the effect of varying the quintic contribution across the interface. Results for this have not been seen in literature before. The effects are a direct result of the $\chi^{(5)}$ parameter)

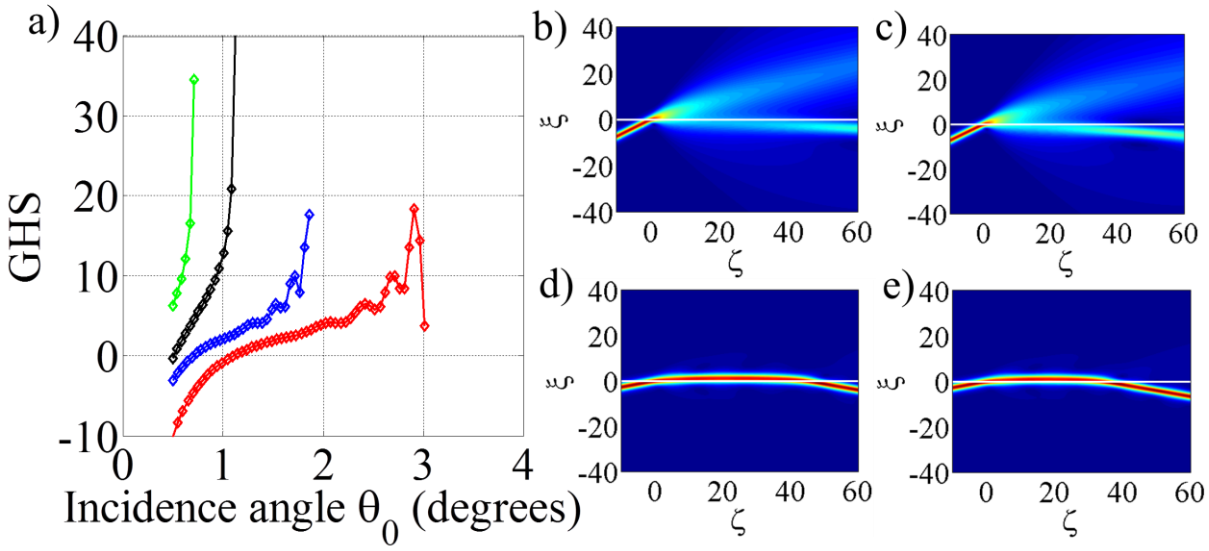

Figure 38 Shown here are GHSs for the parameters: $\rho_0 = 1.3$, $\Delta = 0$ and $\sigma = -0.15$. a) Shows the relationship between the angle of incidence of the beam, and its GHS value. b) ($\kappa = 2.5 \times 10^{-3}$) and c) ($\kappa = 1 \times 10^{-3}$) show the full results for the highest value of the angle of incidence shown in a) (and hence the critical angle) for values of $\nu = 1$ and $\alpha = 0.5$. d) ($\kappa = 2.5 \times 10^{-3}$) and e) ($\kappa = 1 \times 10^{-3}$) show the critical angle results for $\alpha = 1$ and $\nu = 2$.

Figures 38 and 39 show results at a purely nonlinear interface. The results here are striking. A strong trend is seen between the behaviour of the beam close to the critical angle and the value of α and ν.

When α = 0.5, the beam splits as it encounters the interface. In previous sections (at mixed interfaces), when the beams split, the reflected beam decreased (in strength) gradually as the refracted beam increased (in strength), as the angle of incidence was increased. A reflected beam was always present until the point where the refracted beam was fully formed. However, here, it is the case that the reflected beam starts to 'disintegrate' before a refracted beam is fully formed. The highest value for the angle of incidence before the beam 'disintegrates' is taken to be the critical angle. At this point the refracted beam is beginning to be formed, and just above this point, the refracted beam is 'fully formed'.

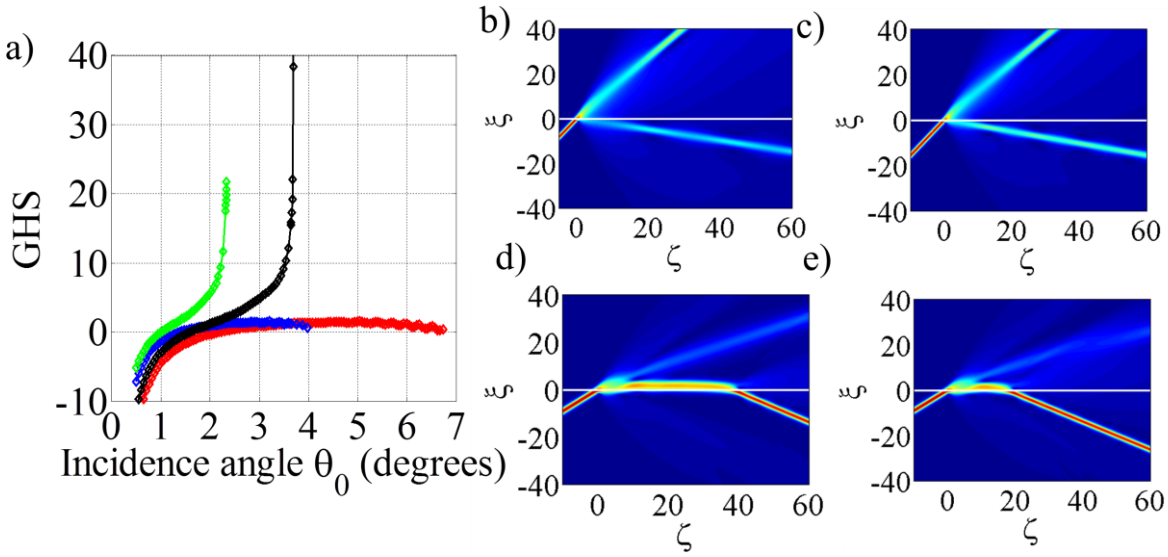

Figure 39 Shown here are Goos-Hänchen shifts for the parameters: ρ_0 = 4.14, Δ = 0 and σ = -0.15. a) Shows the relationship between the angle of incidence of the beam, and its GHS value. b) (κ = 2.5 x 10^{-3}) and c) (κ = 1 x 10^{-3}) show the full results for the highest value of the angle of incidence shown in a) (and hence the critical angle) for values of ν = 1 and α = 0.5. d) (κ = 2.5 x 10^{-3}) and e) (κ = 1 x 10^{-3}) show the critical angle results for α = 1 and ν = 2.

When ν = 2, and the quintic contribution to the refractive index is varied across the interface, the beam becomes trapped by the interface at the point of interaction. This means that as the angle of incidence increases, the GHS increases, and the GHS is sensitive to very small changes in the angle of incidence. This leads to the giant GHS being present in regimes where ν = 2. These results are novel, as results in these parameter regimes have not be presented in any literature before.

3.4.3 Comparison with Shifts at Dissimilar Kerr Interfaces

This section will compare interesting features of the GHS results at cubic-quintic interfaces to similar parameter regimes at an interface between Kerr type materials. Extensive results of the latter can be found in ref. [3]. In making these comparisons, it will become evident as to the effect that the quintic term in the refractive index has on beam propagation in near-critical-angle regimes.

The dissimilar Kerr-type interface problem has a refractive index of $n = n_{0i} + (\alpha_i/2n_{0i})I$, where n_{0i} is the linear refractive index, $\alpha_i > 0$ (for bright solitons) is the cubic coefficient and I is the optical intensity. The subscript i is 1 in medium 1, and 2 in medium 2. By comparing this refractive index with that seen in Figure 19, it becomes clear that changes in the behaviour of the shifts for similar parameter regimes are a result of the quintic term present only in the cubic-quintic refractive index.

There is one cause for concern for the results in this section: changing the materials that the beam is propagating in also modifies the critical angle. The behaviour depends strongly on the critical angle, and for this reason the results in this section will consider beams propagating at their *theoretical* critical angle.

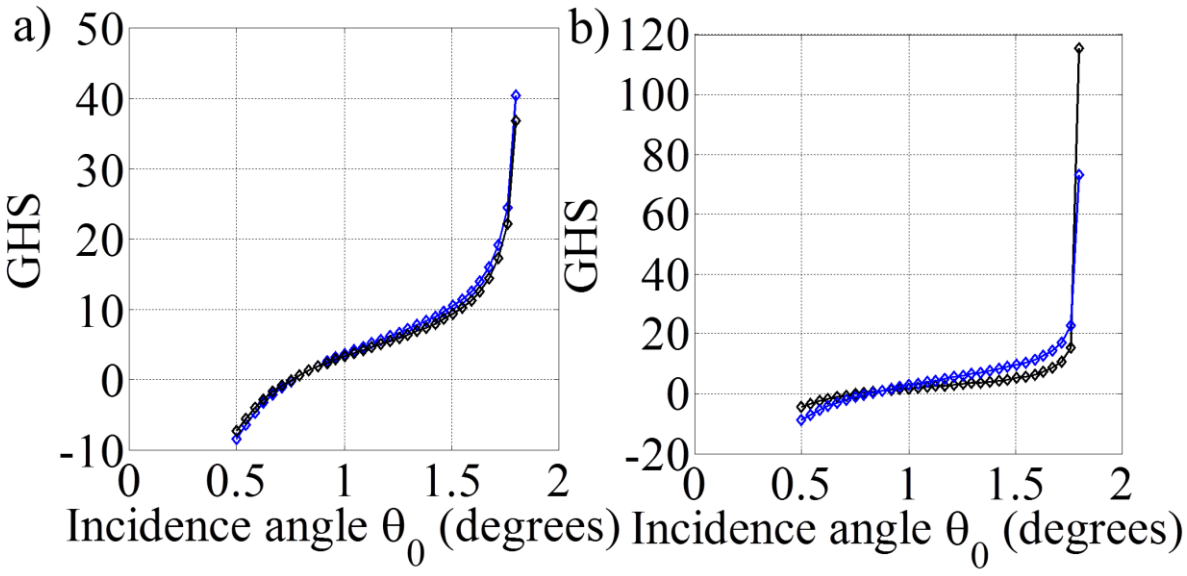

Figure 40 Shows the relationship between the angle of incidence and the length of the GHS in both Kerr (blue line) and cubic-quintic (black line) materials, when $\kappa = 2.5 \times 10^{-3}$. a) Has $\rho_0 = 1.3$ and b) has $\rho_0 = 4.14$.

The results shown in Figure 40 are in linear interface parameter regimes. Simulations were run between 0.5° and 1.8° in both Kerr (blue line) and cubic-quintic (black line)

materials. At linear interfaces, Kerr and cubic-quintic materials have the same predicted critical angle, so the results are directly comparable. Because the theoretical critical angles are the same, it is unsurprising that the results for the two materials are similar. The results differ more when the peak intensity of the beam is larger.

For the following results, a) shows a beam propagating at its theoretical critical angle for particular parameters in a cubic-quintic material, while b) shows a beam propagating with the same parameters (though $\sigma = 0$, making the material Kerr-type) at the theoretical critical angle predicted for a Kerr material. When the interfaces are linear ($\alpha = 1$ and $\nu = 1$) the predicted critical angles become the same.

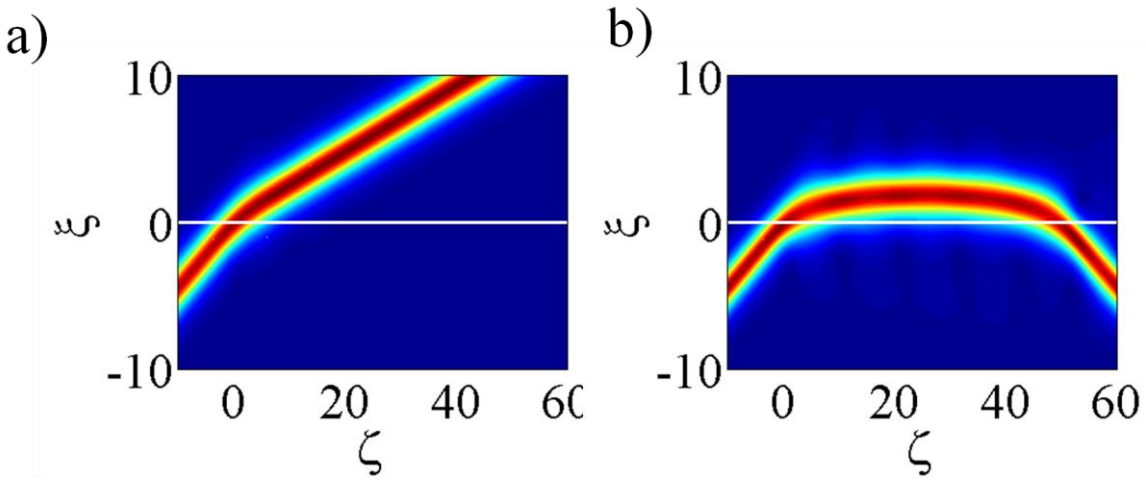

Figure 41 Shows beam behaviour at its theoretical critical angle for a) cubic-quintic ($\theta_{crit(theoretical)}$ = 1.81121°) and b) Kerr ($\theta_{crit(theoretical)}$ = 1.81121°). ρ_0 = 1.3, Δ = 0.001, α = 1, ν = 1, κ = 2.5 x 10^{-3}.

The results here are for a linear interface. This means that the predicted critical angle is the same in both the Kerr and cubic-quintic media. The results here are significantly different from one another (with one reflecting and one refracting), which shows that qualitatively new results are found when the quintic term is introduced into the refractive index.

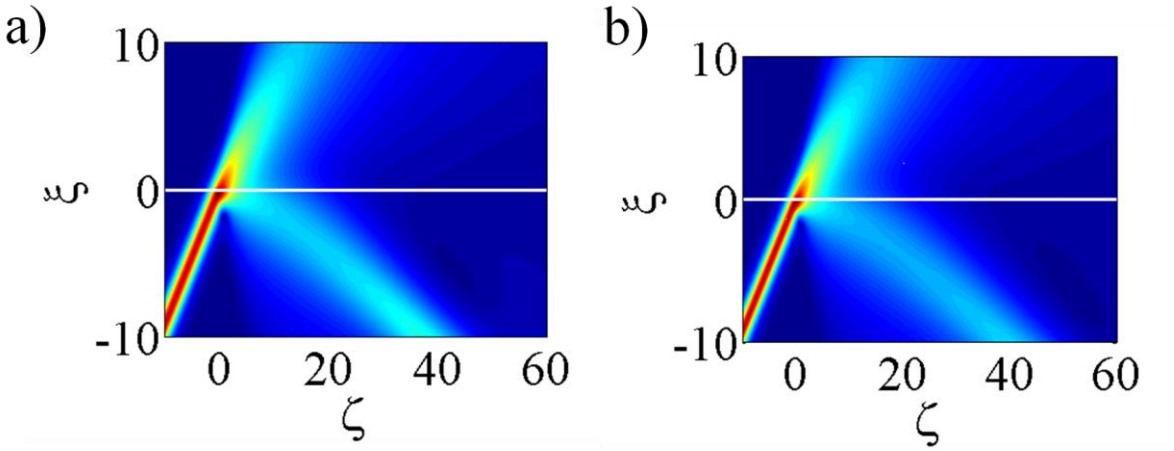

Figure 42 Shows beam behaviour at its theoretical critical angle for a) cubic-quintic ($\theta_{crit(theoretical)}$ = 3.7280°) and b) Kerr ($\theta_{crit(theoretical)}$ = 3.7268°). ρ_0 = 1.3, Δ = 0.001, α = 0.5, ν = 1, κ = 2.5 x 10^{-3}.

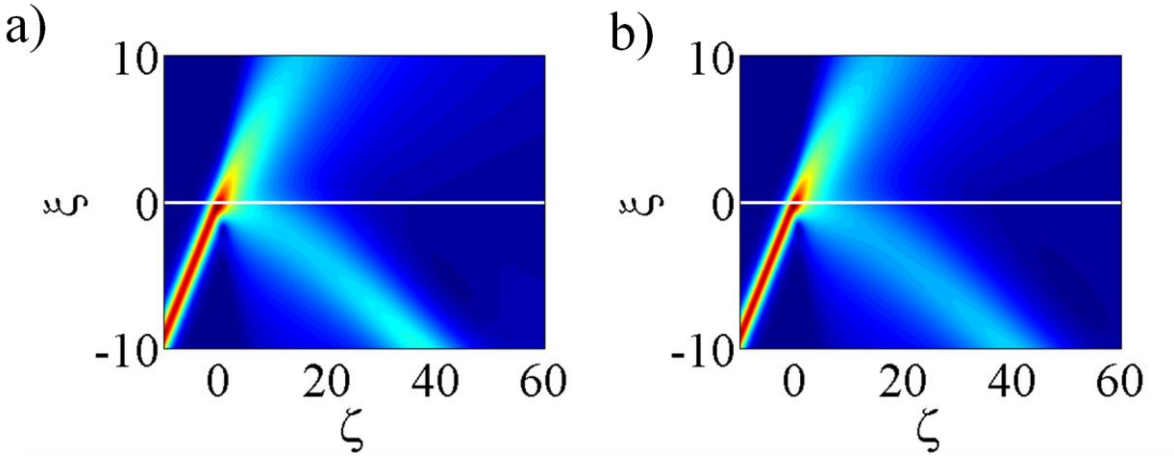

Figure 43 Shows beam behaviour at its theoretical critical angle for a) cubic-quintic ($\theta_{crit(theoretical)}$ = 1.3792°) and b) Kerr ($\theta_{crit(theoretical)}$ = 1.8112°). ρ_0 = 1.3, Δ = 0.001, α = 1, ν = 0.5, κ = 2.5 x 10^{-3}.

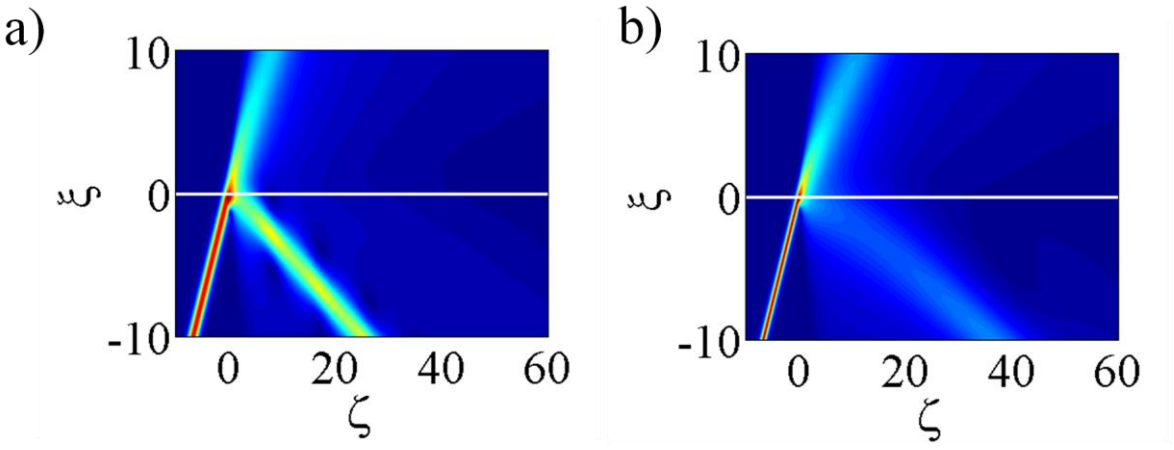

Figure 44 Shows beam behaviour at its theoretical critical angle for a) cubic-quintic ($\theta_{crit(theoretical)}$ = 6.0790°) and b) Kerr ($\theta_{crit(theoretical)}$ = 6.0556°). ρ_0 = 4.14, Δ = 0.001, α = 0.5, ν = 1, κ = 2.5 x 10^{-3}.

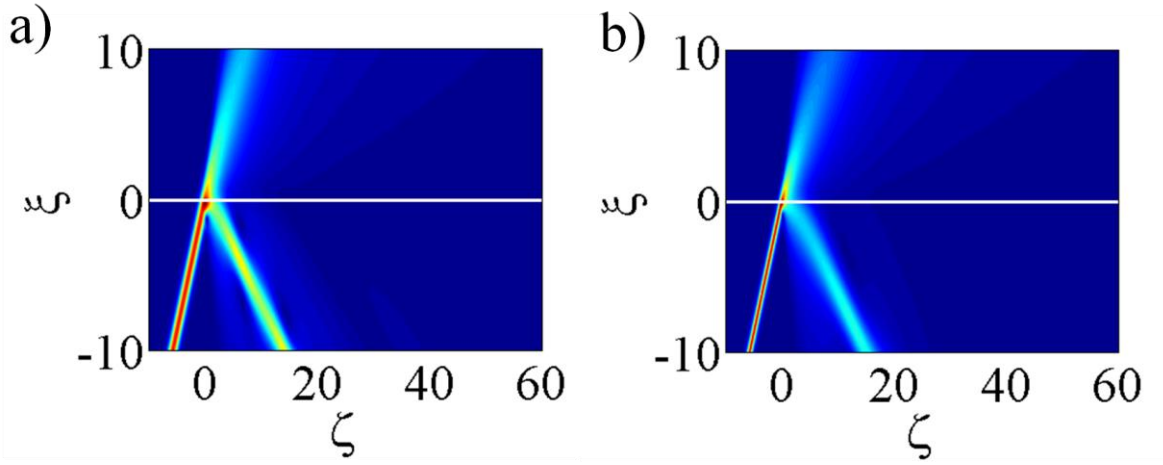

Figure 45 Shows beam behaviour at its theoretical critical angle for a) cubic-quintic ($\theta_{crit(theoretical)}$ = 7.0703°) and b) Kerr ($\theta_{crit(theoretical)}$ = 7.0501°). ρ_0 = 4.14, Δ = 0.005, α = 0.5, ν = 1, κ = 2.5 x 10^{-3}.

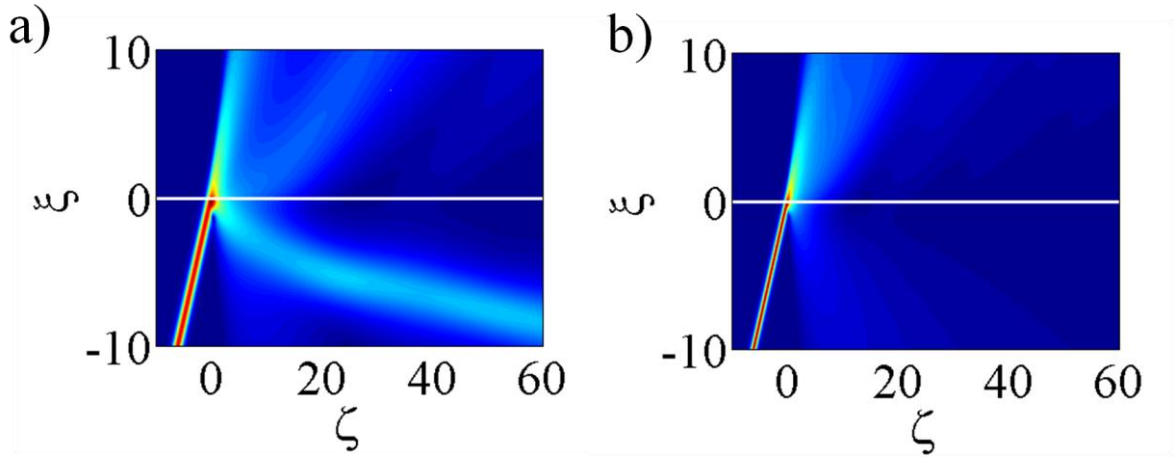

Figure 46 Shows beam behaviour at its theoretical critical angle for a) cubic-quintic ($\theta_{crit(theoretical)}$ = 6.6658°) and b) Kerr ($\theta_{crit(theoretical)}$ = 6.6273°). ρ_0 = 4.14, Δ = -0.005, α = 0.1, ν = 1, κ = 2.5 x 10^{-3}.

Figures 39-43 all show similar results. At the predicted value for the theoretical critical angle the beams split on interacting with the interface. For all five figures, the reflected beam is less well defined in the Kerr material than it is in the cubic-quintic material. For Figures 39 and 40 both the reflected and refracted beams are less well defined than those found in Figures 41-43. Figure 43 (where the parameter regimes are external) shows the most striking difference in the beam behaviour in the different materials. For the cubic-quintic material the path of the reflected beam is distorted by the interface, whereas in the Kerr material only radiation is reflected by the interface.

3.5 Conclusions

This chapter has presented in-depth results into phenomena which arise when a beam is propagating at an angle of incidence that is close to its critical angle. Although the simulations carried out for this chapter are exhaustive, there is much scope for further work based on the results found here.

Results at linear interfaces show that when Δ is small, giant GHSs can be found in near-critical-angle regimes. As the value of Δ is increased, the GHS is drastically reduced, as beam splitting becomes a major feature. At mixed interfaces, two classes of result were considered; firstly, internal GHS at mixed interfaces ($\Delta > 0$), where giant shifts were not found. The beams here always split on interacting with the interface. It has been shown that the way the beam splits has an effect on the magnitude of the GHS (if the reflected beam is strong (high amplitude) as the refracted beam begins to form, then this results in smaller GHSs).

The story becomes slightly less clear when external GHSs at a mixed interface are considered. There are three parameter cases to investigate when $\Delta < 0$. Case 1 has $\alpha < 1$ and here the predicted critical angles are the most inaccurate, moreover, many theoretical critical angles do not appear in the simulated results (even when these small angles are increased incrementally by millionths of a degree). For case 2, giant GHSs were common in the results. The theoretical critical angles are of the order of 1°, and as a result Δ (the mismatch in the linear part of the refractive index) was kept small (by an order of magnitude compared to the values used in linear-interface calculations). Case 3 shows similar results to those at linear interfaces, where giant GHSs are present at small $|\Delta|$, and then as the mismatch increases, beam splitting starts to dominate and the value of the GHS dramatically decreases.

For purely nonlinear interfaces ($\Delta = 0$) the results are noteworthy because the effect of a mismatch in the quintic contribution can be isolated. For valid results, parameters investigated were $\alpha = 0.5$ and $\nu = 1$ (where the beam splits at the interface) and $\alpha = 1$ and $\nu = 2$ (where giant GHS are often seen). These are a result of the mismatch in the quintic term, and are therefore qualitatively new. The trend is found to be the same when looking at high and low intensity beams.

The investigation and comparisons found in this chapter have shown that the GHSs at cubic-quintic materials may be qualitatively different from those found at Kerr interfaces.

3.6 References

1. F. Goos and H. Hänchen, *Ein neuer und fundamentaler Versuch zur Totalreflexion.* Annalen der Physik, 1947. **436**(7-8): p. 333-346.
2. J.B. Gotte, S. Shinohara, and M. Hentschel *Are Fresnel filtering and the angular Goos-Hanchen shift the same?* Journal of Optics, 2013. **15**, DOI: 014009.
3. J. Sánchez-Curto, P. Chamorro-Posada, and G.S. McDonald, *Giant Goos-Hänchen shifts and radiation-induced trapping of Helmholtz solitons at nonlinear interfaces.* Optics Letters, 2011. **36**(18): p. 3605-3607.
4. B.R. Horowitz and T. Tamir, *Lateral Displacement of a Light Beam at a Dielectirc Interface.* Journal of the Optical Society of America 1971. **61**(5): p. 586-594.
5. T. Tamir and H.L. Bertoni, *Lateral Displacement of Optical Beams at Multilayered Periodic Structures.* Journal of the Optical Society of America, 1971. **61**(10): p. 1397-1413.
6. H.M. Lai, C.W. Kwok, Y.W. Loo, and B.Y. Xu, *Energy-flux pattern in the Goos-Hänchen effect.* Physical Review E, 2000. **62**(5): p. 7330-7339.
7. F. Bretenaker, A. Le Floch, and L. Dutriaux, *Direct measurement of the optical Goos -Hänchen effect in lasers.* Physical Review Letters, 1992. **68**(7): p. 931-933.
8. E. Pfleghaar, A. Marseille, and A. Weis, *Quantitative investigation of the effect of resonant absorbers on the Goos-Hänchen shift.* Physical Review Letters, 1993. **70**(15): p. 2281-2284.
9. D. Marcuse, *Reflection of a Gaussian beam from a nonlinear interface.* Applied Optics, 1980. **19**(18): p. 3130-3139.
10. W.J. Tomlinson, J.P. Gordon, P.W. Smith, and A.E. Kaplan, *Reflection of a Gaussian beam at a nonlinear interface.* Applied Optics, 1982. **21**(11): p. 2041-2051.
11. A.B. Aceves, J.V. Moloney, and A.C. Newell, *Theory of light-beam propagation at nonlinear interfaces. I. Equivalent-particle theory for a single interface.* Physical Review A, 1989. **39**(4): p. 1809-1827.
12. J.M. Christian, E.A. McCoy, G.S. McDonald, J. Sánchez-Curto, and P. Chamorro-Posada *Interaction of Helmholtz bright spatial solitons with power-law optical interfaces.* Journal of Atomic and Molecular Physics, 2012. **2012**, DOI: 137967.
13. N.N. Akhmediev, V.I. Korneev, and Y.V. Kuz'menko, *Excitation of nonlinear surface waves by Gaussian light beams.* Zhurnal Eksperimental'noi i Teoreticheskoi Fiziki, 1985. **88**: p. 107.
14. M.A. Jezzini and J.C. Gutierrez-Vega, *The Goos-Hänchen shift in Helmholtz-Gauss beams.* SPIE Proceedings, 2006. **6290**.
15. E. Hecht, *Optics* 2002: Addison Wesley.
16. J.M. Christian, G.S. McDonald, and P. Chamorro-Posada *Bistable Helmholtz solitons in cubic-quintic materials*. Physical Review A, 2007. **76**, DOI: 033833.
17. K.I. Pushkarov, D.I. Pushkarov, and I.V. Tomov, *Self-action of Light beams in nonlinear media: soliton solutions.* Optical and Quantum Electronics, 1979. **11**(1): p. 471-478.
18. J. Sánchez-Curto, P. Chamorro-Posada, and G.S. McDonald *Black and gray Helmholtz Kerr soliton refraction.* Physical Review A, 2011. **83**, DOI: 013828.

4. Single interfaces III: nonlinear surface waves[1]

4.1 Introduction

In an optical context, surface waves are localised stationary states of light that propagate along the interface between two dissimilar materials. Since the light straddles both media simultaneously, it follows that there is usually an inherent asymmetry in its transverse profile (the strength of this asymmetry depends upon the interplay between mismatch parameters and the wave's nonlinear phase shift). The stability properties of surface waves are of fundamental interest in nonlinear science. Classic methods routinely deployed for predicting the robustness of solitons in homogeneous systems [2] cannot necessarily be applied to surface waves in inhomogeneous systems [3]. In the absence of any rigorously-derived integral criterion, surface wave stability must be addressed numerically.

Surface waves are familiar phenomena in photonics. In the nonlinear domain, they have been extensively investigated in both Kerr-type and power-law media over the past two decades. Analyses have tended to fall into one of two categories: *analytical* (finding solutions to governing equations, but with no complementary numerical investigations) or *computational* (simulating surface waves within the paraxial limit only). Until very recently [1], there was no complete analysis (i.e., theory with supporting simulations to provide evidence of solution stability) of surface waves in the Helmholtz nonparaxial regime. It is precisely this regime that is of interest for the remainder of this chapter.

4.1.1 Power-Law Interfaces

For maximum generality, attention will be paid to the planar interface defined by two dissimilar power-law type materials (see Figure 47). The refractive-index distributions are described by

$$n_j^2 \equiv n_{0j}^2 + \alpha_j |E|^q , \tag{4.1}$$

where the nonlinearity exponent $q > 0$. In this simple generalisation, the coefficients α_j are taken to be positive and the universal Kerr-type response corresponds to the special case of $q = 2$. Examples of optical materials that can exhibit power-law characteristics include some semiconductors (e.g., InSb [4], GaAs and GaAlAs [5]), doped filter glasses (e.g.,

[1] The work presented in this chapter has been published in a peer-reviewed journal [1]

CdS_xSe_{1-x} [6]), and liquid crystals (e.g., methoxybenzilidene butylanaline (MBBA) [7]). Both paraxial- [8] and Helmholtz-type [9] governing equations with nonlinearity (4.1) admit a continuum of exact analytical *sech*-type solitons. These solutions are generally stable against perturbations within the range $0 < q < 4$.

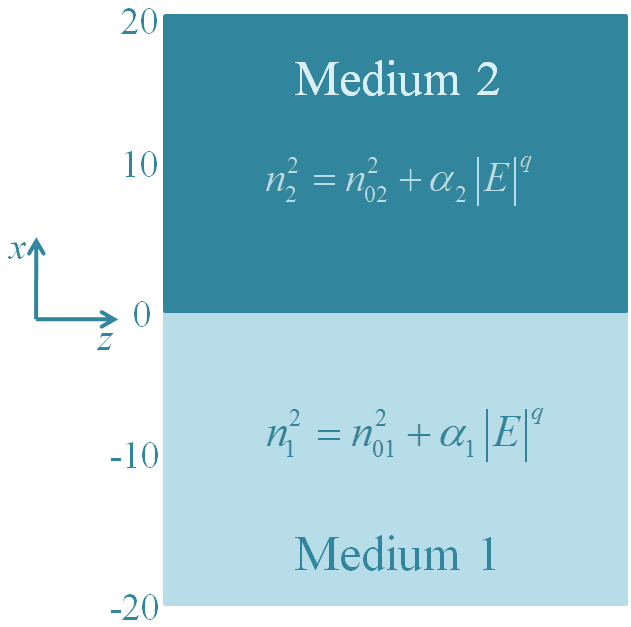

Figure 47 Schematic diagram showing a typical set-up for an interface between dissimilar power-law materials, and the parameters which can be varied across the interface. The values of these parameters will define whether the interface is linear, nonlinear, or mixed.

4.1.2 Literature Review

In previous literature concerning nonlinear surface waves [2, 3, 10, 11] the focus of the research has been to try and link the stability of the surface wave to the VK criterion. The VK criterion can accurately predict the stability of solitons, but does not necessarily extend to predicting that of surface waves. The criterion is related to the value of $dP/d\beta$, where P is the beam power, and β is related to the propagation constant of the beam.

Aceves, Moloney and Newell provided the first investigations into nonlinear surface waves at the interface of two nonlinear materials [3]. The interface is one between two dissimilar Kerr materials. The stability of the surface waves are considered, although not through the use of numerical analysis, and they conclude that the stability criterion proposed in earlier work analysing surface waves at a linear-nonlinear interface ($dP/d\beta > 0$ will have stable surface waves, while $dP/d\beta < 0$ means that the surface waves will be

unstable) is not necessarily applicable for interfaces between two nonlinear materials. This is also found to be the case here; sections 4.4 and 4.3 show the VK criterion is a *necessary but not sufficient condition* for stability. Aceves *et al.*'s finding that stable solutions only occur when the peak of the beam is in the material with the higher nonlinear refractive index, is also supported by the results in this study.

The paper by Snyder and Tran [11] is the first to look at surface waves at the interface of power-law materials. This paper considers two different interface scenarios: the right hand medium (or medium 1) is always self-focusing, however in the first scenario the left hand medium (or medium 2) is considered to be self-focusing, and in the second scenario medium 2 is thought of as self-defocusing. The surface mode solutions are found by inverting the solution to a linear waveguide. It was only after the solution had been inverted that the authors could identify that the nonlinear mode is one of a power-law nonlinearity.

This paper makes inferences about the stability of these surface waves, stating that those on the lower branch are always unstable, where as those on the upper branch ($\mathrm{d}P/\mathrm{d}\beta > 0$) are possibly stable, but that the stability of the upper branch is dependent on the value of the nonlinear index. These predictions are not explored further by Snyder and Tran, but are tested extensively in this chapter (see 4.4 and 4.3).

Ma and Chen's [10] is the first paper to find exact analytical solutions for nonlinear surface waves at the interface of two non-Kerr like media. Once again in this work, both of the materials have a power-law nonlinearity. Four different interface scenarios are investigated here, all four permutations of medium 1 and medium 2 being either self-focusing or self-defocusing. One area which is investigated in Ref. [10] but neglected here are dissimilar values for the nonlinear index of the materials, both analytically and numerically. Their findings focus only on a few special cases, and make no mention of surface wave stability or any stability criterion. For this reason, the results are not discussed further here.

The work which follows gives analytical results for Helmholtz surface waves at a power-law interface. It then goes on to give a full numerical investigation of the stability of such surface waves, with reference to the VK criterion.

4.2 Nonlinear Surface Waves

4.2.1 Model Equation

By using the same approach as in section 2.2.1 and deploying instead the refractive index model of equation(4.1), the dimensionless envelope *u* must satisfy

$$\kappa\frac{\partial^2 u}{\partial\zeta^2}+i\frac{\partial u}{\partial\zeta}+\frac{1}{2}\frac{\partial^2 u}{\partial\xi^2}+|u|^q u=\left[\frac{\Delta}{4\kappa}+(1-\alpha)|u|^q\right]H(\xi)u. \tag{4.2}$$

The material mismatch parameters, Δ and α, retain their earlier definitions [see equations (2.7)], and the normalisation is the same as before except that the laboratory electric field is now measured in units of $E_0 = (n_{01}/k\alpha_1 L_D)^{1/q}$.

4.2.2 Exact Analytical Solutions

To proceed, equation (4.2) is separated into its forms for medium 1 and medium 2:

$$\kappa\frac{\partial^2 u}{\partial\zeta^2}+i\frac{\partial u}{\partial\zeta}+\frac{1}{2}\frac{\partial^2 u}{\partial\xi^2}+|u|^q u=0, \tag{4.3}$$

$$\kappa\frac{\partial^2 u}{\partial\zeta^2}+i\frac{\partial u}{\partial\zeta}+\frac{1}{2}\frac{\partial^2 u}{\partial\xi^2}-\frac{\Delta}{4\kappa}u+\alpha|u|^q u=0, \tag{4.4}$$

and exact surface wave solutions are sought using the following ansatz:

$$u(\xi,\zeta)=F(\xi-\xi_j)\exp(ik_\zeta\zeta)\exp\left(-i\frac{\zeta}{2\kappa}\right), \tag{4.5}$$

where $F(\xi-\xi_j)$ is the transverse profile centred on ξ_j. By substituting into equations (4.3) and (4.4), it can be shown that the solutions in medium 1 and medium 2 are:

$$u(\xi,\zeta)=\left(\frac{2+q}{2}\beta\right)^{1/q}\operatorname{sech}^{2/q}\left[q\left(\frac{\beta}{2}\right)^{1/2}(\xi-\xi_1)\right]\exp\left(\pm i\sqrt{1+4\kappa\beta}\,\frac{\zeta}{2\kappa}\right)\exp\left(-i\frac{\zeta}{2\kappa}\right), \tag{4.6}$$

and

$$\begin{aligned}u(\xi,\zeta)=&\left[\frac{2+q}{2}\left(\frac{1}{\alpha}\right)\left(\beta+\frac{\Delta}{4\kappa}\right)\right]^{1/q}\operatorname{sech}^{2/q}\left[\frac{q}{\sqrt{2}}\left(\beta+\frac{\Delta}{4\kappa}\right)^{1/2}(\xi-\xi_2)\right]\\&\times\exp\left(\pm i\sqrt{1+4\kappa\beta}\,\frac{\zeta}{2\kappa}\right)\exp\left(-i\frac{\zeta}{2\kappa}\right),\end{aligned} \tag{4.7}$$

respectively. The solution contains a parameter β whose value determines the profile of the surface wave. To find the displacements ξ_1 and ξ_2, the field u and its normal derivative (in this case, $\partial u/\partial \xi$) must be continuous across the interface. These conditions yield a pair of auxiliary equations

$$\beta^{1/q}\operatorname{sech}^{2/q}\left[q\left(\frac{\beta}{2}\right)^{1/2}\xi_1\right]=\left[\frac{1}{\alpha}\left(\beta+\frac{\Delta}{4\kappa}\right)\right]^{1/q}\operatorname{sech}^{2/q}\left[\frac{q}{\sqrt{2}}\left(\beta+\frac{\Delta}{4\kappa}\right)^{1/2}\xi_2\right], \tag{4.8}$$

$$\beta^{1/q}\tanh^{2/q}\left[q\left(\frac{\beta}{2}\right)^{1/2}\xi_1\right]=\left(\beta+\frac{\Delta}{4\kappa}\right)^{1/2}\tanh^{2/q}\left[\frac{q}{\sqrt{2}}\left(\beta+\frac{\Delta}{4\kappa}\right)^{1/2}\xi_2\right], \tag{4.9}$$

which may be solved to give:

$$\xi_1=\frac{1}{q}\left(\frac{2}{\beta}\right)^{1/2}\ln\left(\frac{1\pm\sqrt{1-\delta^2}}{\delta}\right), \tag{4.10}$$

$$\xi_2=\frac{2}{q}\left(\beta+\frac{\Delta}{4\kappa}\right)^{-1/2}\ln\left(\frac{1\pm\sqrt{1-\mu^2}}{\mu}\right), \tag{4.11}$$

$$\delta\equiv\sqrt{\frac{\Delta}{4\kappa}\frac{1}{\beta(\alpha-1)}}, \tag{4.12}$$

$$\mu\equiv\sqrt{\frac{\Delta}{4\kappa}\left(\beta+\frac{\Delta}{4\kappa}\right)^{-1}\left(1-\frac{1}{\alpha}\right)^{-1}}. \tag{4.13}$$

Equations (4.6), (4.7) and (4.10)-(4.13) are exact analytical surface waves of model (4.2). The full derivations can be found in Appendix D.

4.2.3 Existence Criterion

The realness of displacements ξ_1 and ξ_2 demands that $\delta^2 < 1$ and $\mu^2 < 1$, and these two simultaneous conditions lead to a constraint on the product $4\kappa\beta$:

$$4\kappa\beta > 4\kappa\beta_{\min}\equiv\frac{\Delta}{\alpha-1}. \tag{4.14}$$

When considering any given interface (described by Δ and α), it now becomes obvious that surface waves may only exist when the product $4\kappa\beta$ exceeds a minimum (positive)

numerical value denoted by $4\kappa\beta_{\min}$. As a consequence, surface wave solutions may exist only for those interfaces that fall into one of two categories: regime 1 ($\Delta > 0$ and $\alpha > 1$) or regime 2 ($\Delta < 0$ and $0 < \alpha < 1$).

4.3 Stability of Lower-Branch Solutions

Extensive computations have investigated the validity of the VK criterion [2] (which states that's solutions will be stable when $dP/d\beta > 0$ is satisfied) in the context of predicting the stability of Helmholtz surface waves lying on the lower branch (see Appendix D). Simulations demonstrate repeatedly (over a wide parameter choice) that such solutions tend to be stable if the condition $dP/d\beta > 0$ is met: the initial profile is preserved (exhibiting no change in shape) as the wave propagates along the interface. Solutions with $dP/d\beta < 0$ have been found to exhibit a variety of qualitatively different instabilities that will be explored in detail.

4.3.1 Regime 1

Illustrative examples of instabilities when $dP/d\beta < 0$ are shown in Figure 48 for nonlinearity exponents $q = 1$, 2 and 3 (when $\kappa = 2.5\times10^{-3}$, $\beta_{\min} = 1.00$ and β has been set to 1.01). As each surface wave travels along the interface, their profiles 'wobble' in the transverse direction. For $q = 1$ and $q = 2$, the oscillation is approximately periodic in the longitudinal direction (a property that is perhaps related to weak asymmetry in the input beam – the peak of the profile is always located in medium 2); also, a smaller q value leads to an oscillation on a longer scalelength in ζ. For $q = 3$, the evolution of the unstable surface wave is initially much more erratic than in the previous two cases, and clearly nonperiodic. Another immediately apparent feature is that systems with higher q exponents (e.g., $q = 3$) generate much more radiation than systems with lower q (e.g., $q = 1$). Radiation tends to be shed into medium 1 (the domain $\xi < 0$), where the linear refractive index is higher (this phenomenon could be related to the total internal reflection of low-amplitude waves, which do not greatly experience system nonlinearity). A third interesting observation is that all three surface waves, despite being unstable, nevertheless remain localised within the vicinity of the interface in both the short and long term.

If parameter β is increased slightly from 1.01 to 1.08, then $dP/d\beta > 0$ for $q = 1$ while $dP/d\beta < 0$ for $q = 2$ and $q = 3$. Accordingly, the surface wave for $q = 1$ is stable and propagates with invariant shape. The waves for $q = 2$ and $q = 3$ are both found to be unstable. While

the qualitative aspects of these two instabilities remain unchanged, two notable differences can be clearly identified in their quantitative properties (compare Figures 48 and 49). Firstly, the longitudinal scalelength of the oscillations is increased; secondly, much less radiation is generated in the q = 3 systems [compare Figures 48d) and 49d)]. These differences (longer scale-lengths and less generated radiation) are augmented further if β is increased (e.g., to 1.3 – see Figure 50).

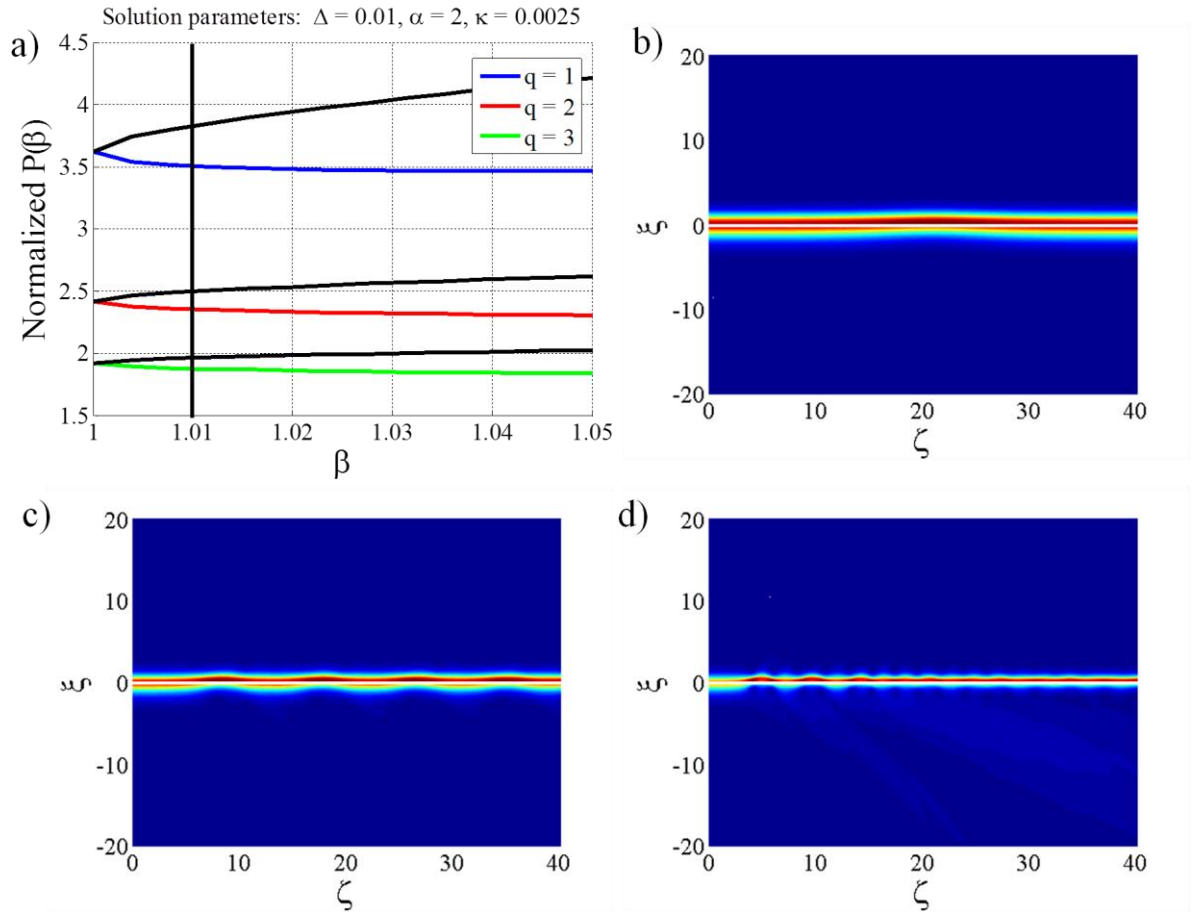

Figure 48 Shows the effect of changing β for lower branch surface waves. Figures b), c) and d) show q = 1, 2 and 3 surface waves respectively. Here, β = 1.01 and is chosen such that all three lower branch curves have a negative gradient.

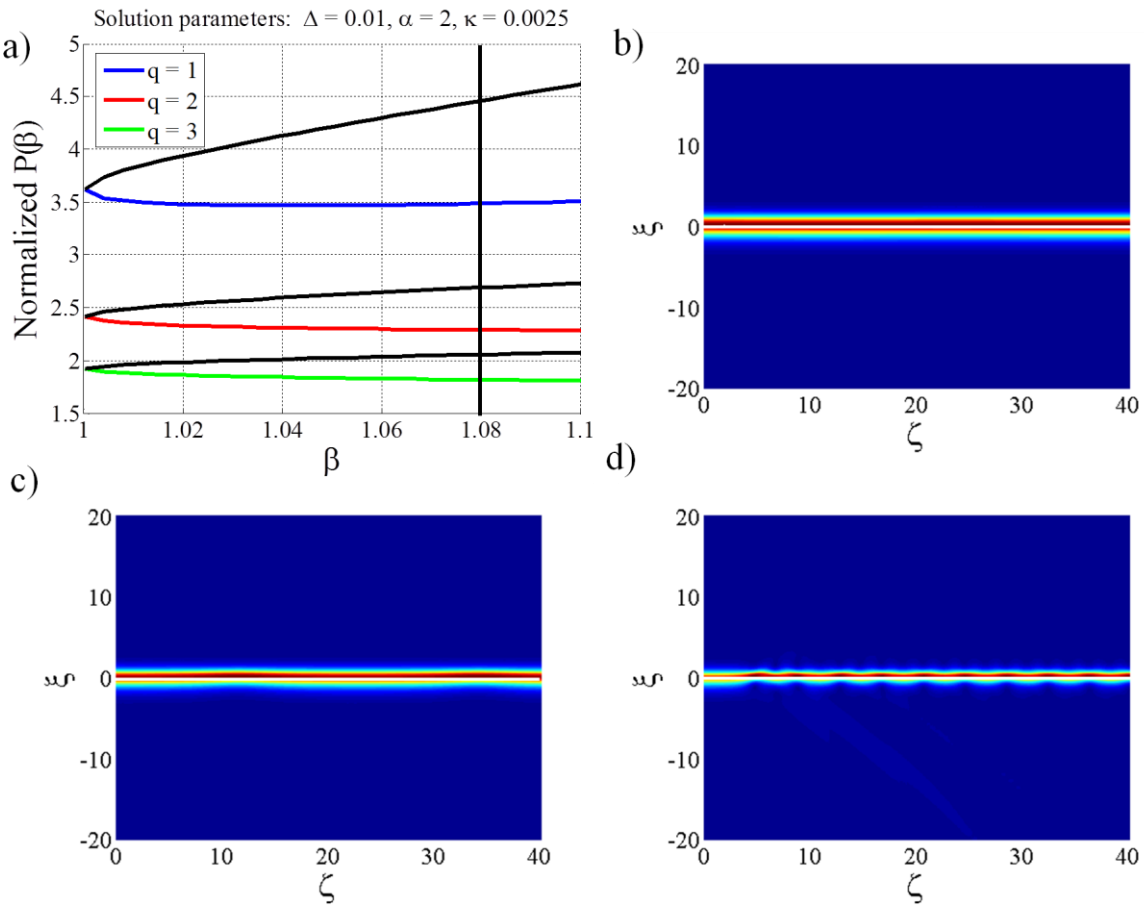

Figure 49 Shows the effect of changing β for lower branch surface waves. Figures b), c) and d) show q = 1, 2 and 3 surface waves respectively. Here, β = 1.08 and is chosen so that for q = 1 the lower branch curve has a positive gradient, but q = 2 and q = 3 have negative gradients.

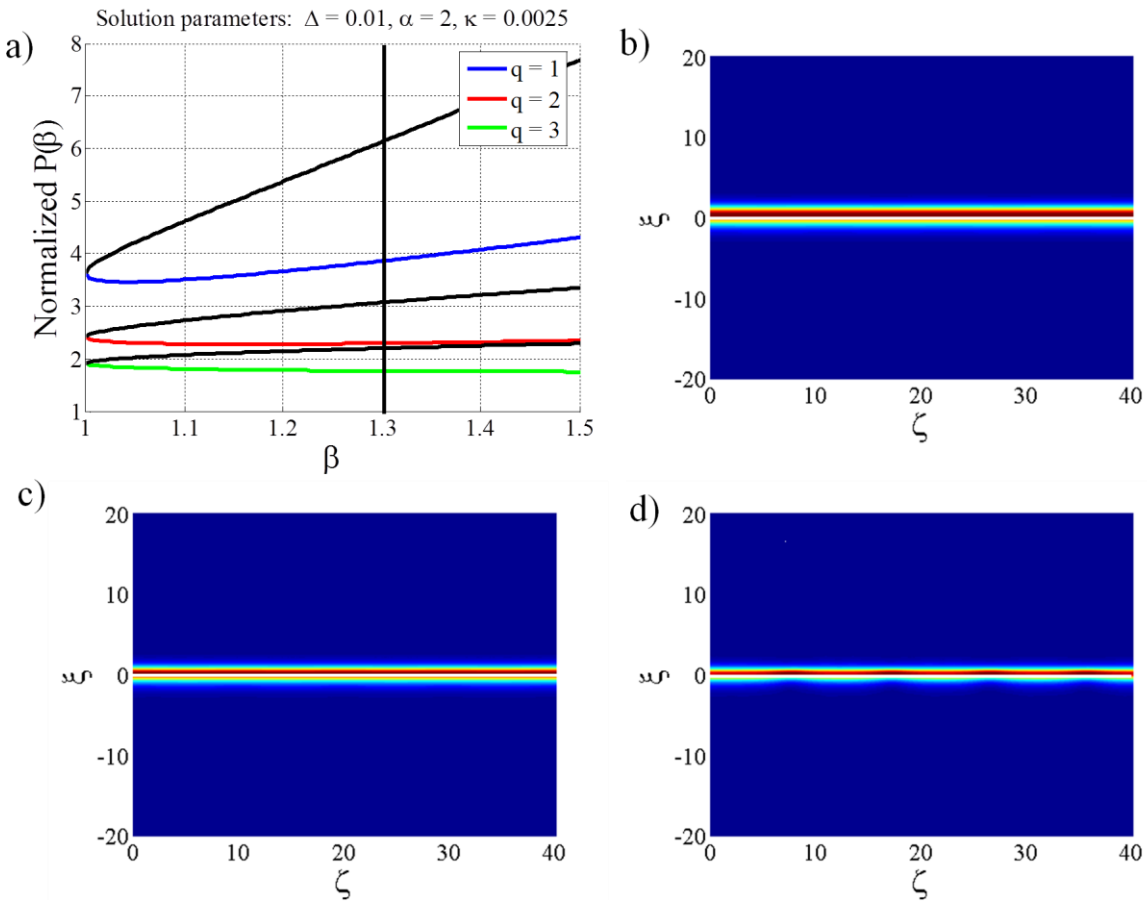

Figure 50 Shows the effect of changing β for lower branch surface waves. Figures b), c) and d) show q = 1, 2 and 3 surface waves respectively. Here, β = 1.3 and is chosen so that for q = 1 and q = 2 the lower branch curves have a positive gradient, but q = 3 has a negative gradient.

4.3.2 Regime 2

As in regime 1, solutions with $dP/d\beta > 0$ have been found to be stable (propagating with invariant profiles over arbitrarily long distances). However, simulations have uncovered a qualitatively new characteristic of lower-branch instabilities when $dP/d\beta < 0$. After a sufficiently long propagation distance, an unstable *surface wave* (i.e., a stationary wave travelling along the interface) transforms spontaneously into an obliquely-propagating *soliton* (i.e., a stationary beam travelling at a finite angle with respect to the interface). This process is much 'cleaner' than the corresponding instability in regime 1, where surface waves remain quasi-bound to the interface and (for q = 3) generates more radiation.

Inspection of Figure 51 shows that the instability growth rate depends upon the exponent q when other parameters remain fixed. That is, systems with stronger nonlinearity (i.e., those described by larger q values) have a higher instability growth rate. In regime 2, the peak of the surface wave resides in medium 2 and it is always this medium into which the soliton has been seen to escape.

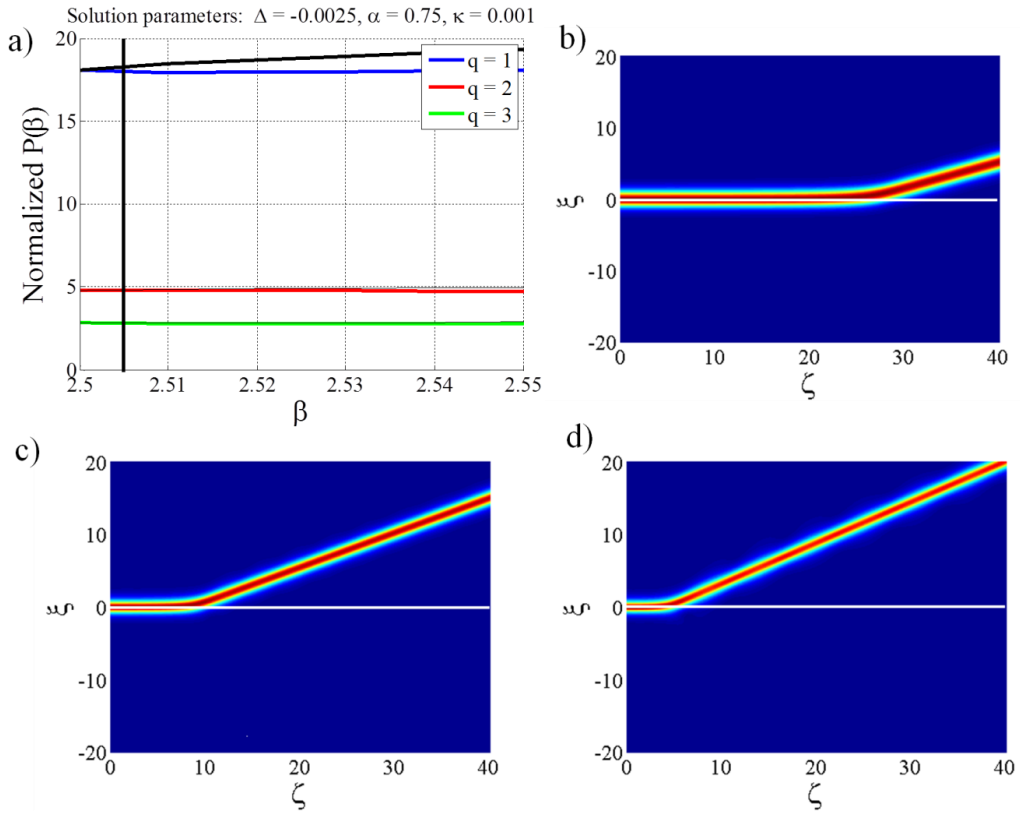

Figure 51 Shows the effect of changing β for lower branch surface waves. Figures b), c) and d) show q = 1, 2 and 3 surface waves respectively. Here, β = 2.505 and is chosen such that all three lower branch curves have a negative gradient.

Further simulations (in Figures 52 and 53) have shown that the instability growth rate also depends upon β.

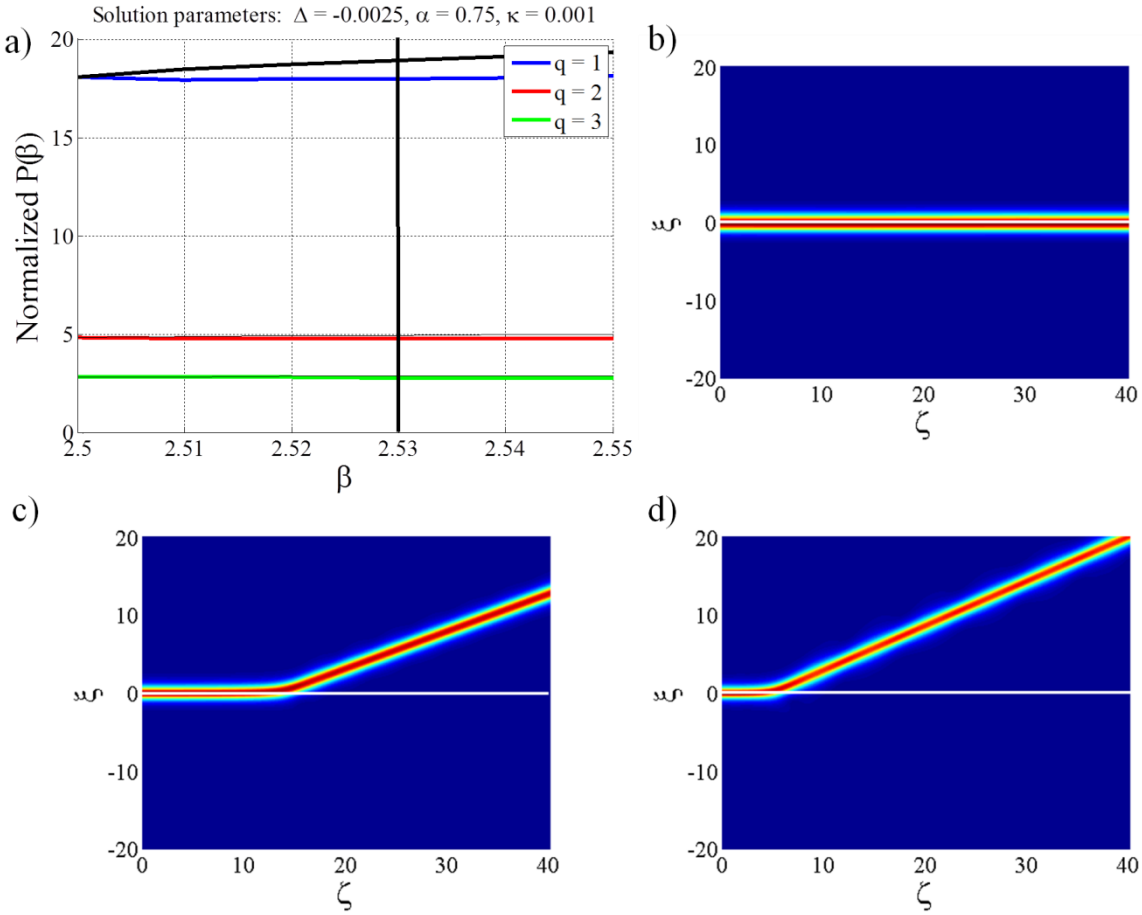

Figure 52 Shows the effect of changing β for lower branch surface waves. Figures b), c) and d) show q = 1, 2 and 3 surface waves respectively. Here, β = 1.08 and is chosen such that for q = 1 the lower branch curve has a positive gradient, but q = 2 and q = 3 both have negative gradients.

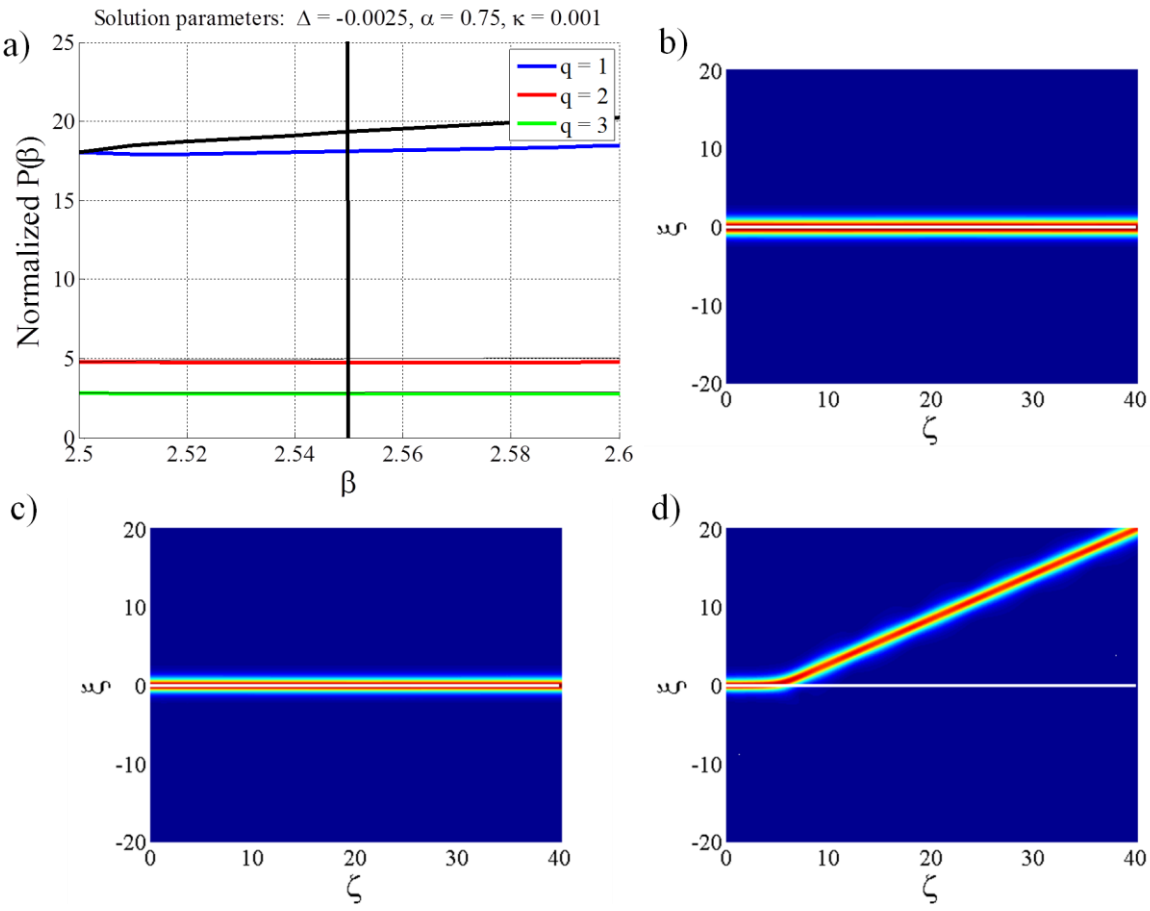

Figure 53 Shows the effect of changing β for lower branch surface waves. Figures b), c) and d) show q = 1, 2 and 3 surface waves respectively. Here, β = 2.55 and is chosen such that for q = 1 and q = 2 the lower branch curves have a positive gradient, but q = 3 has a negative gradient.

4.3.3 Interim Conclusion

Simulations have been deployed to investigate the stability problem for Helmholtz surface wave states on the lower branch. Strong numerical evidence has been gathered which supports the assertion that the VK criterion provides a reliable indicator of solution robustness. However, that criterion provides no information about the qualitative features of instabilities when $dP/d\beta < 0$.

Detailed computations have established that lower-branch surface-wave solutions satisfying $dP/d\beta > 0$ tend to be strongly stable entities, evolving over long distances without changing their shape. A full numerical perturbative analysis (e.g., considering local disturbances to the beam shape [9, 12]) could provide further information on this. However, very small perturbations still exist within the system (e.g., in the form of finite machine precision and algorithm accuracy); these same perturbations are still sufficiently large to seed instabilities (in regimes with $dP/d\beta < 0$) whose characteristics depend heavily upon the parameters defining the interface. In regime 1 ($\Delta > 0$, $\alpha > 1$), the surface wave can acquire oscillatory characteristics but, crucially, the wave remains essentially intact and bound to the interface. In other words, the surface wave is unstable (in the sense that propagation is no longer stationary) but it still remains bound to the interface. Such solutions may be classified as *weakly unstable* as their defining physical property (localised excitations travelling along a material boundary) is preserved. In regime 2 ($\Delta < 0$, $0 < \alpha < 1$), a different class of instability has been uncovered. The unstable surface wave decays very cleanly (e.g., with almost no radiation) into a soliton that propagates at an oblique angle to the interface (and always in medium 2). Such solutions may be classified as *strongly unstable*: the surface wave ceases to exist and transforms completely into a soliton.

4.4 Stability of Upper-Branch Solutions

4.4.1 Upper Branch regime 1

Upper branch surface waves are found to be inherently unstable. This section of the report will look in detail at the surface waves in regime 1, that is where $\Delta > 0$, and $\alpha > 1$. Figure 54a) shows the upper branch solutions in blue, red and green lines, for q = 1, 2 and 3 respectively.

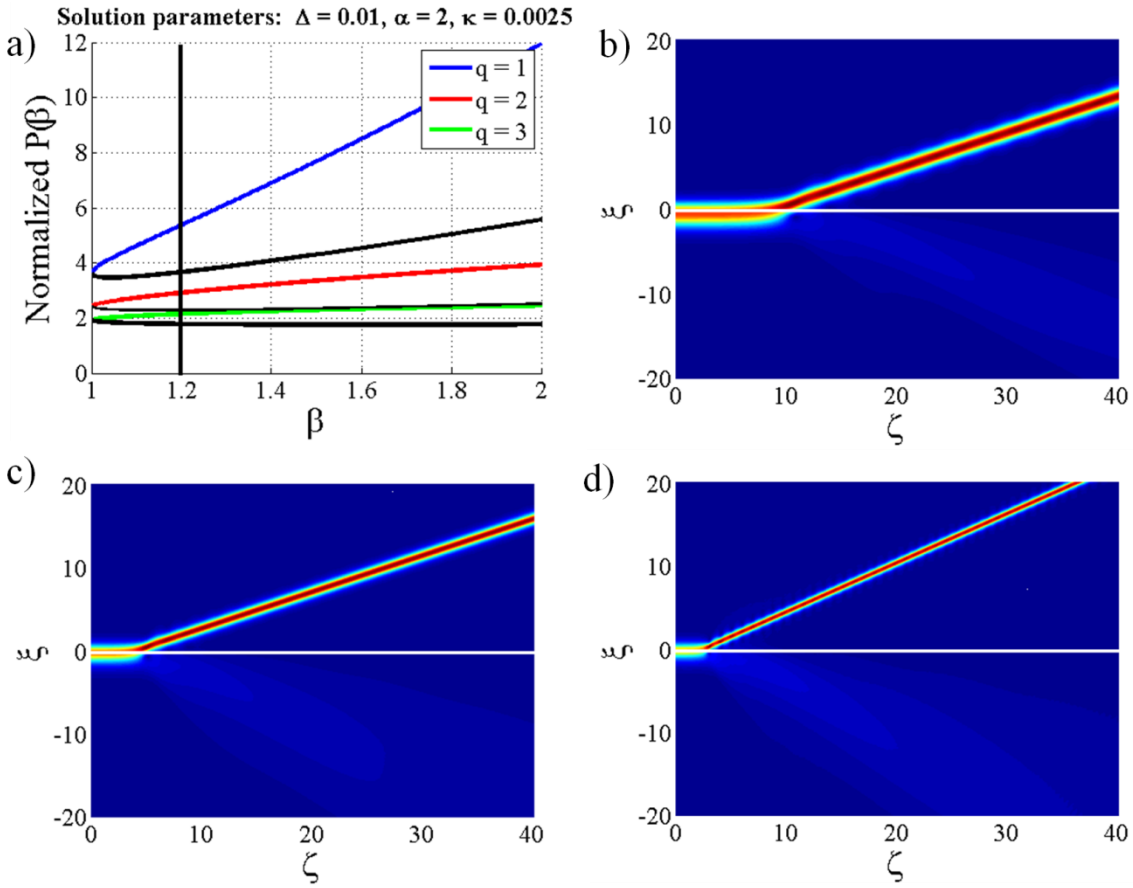

Figure 54 Showing a) P(β) vs. β curves with the upper branches of the curves in colours representing q = 1, 2 or 3 and the lower branches shown in black (it is just the upper branches that are being considered at this point). b), c) and d) show the surface wave solutions for q = 1, 2 and 3 respectively. The interface is represented by a white line, and β = 1.2 in all three cases.

Figures 54-57 show that, no matter the change in the parameter regime, all surface waves are unstable, i.e. the surface wave deflects from the interface. The peak of the beam is also shown to be in medium 1 before it is deflected into the second medium, i.e. the peak of the beam is on different sides of the interface before and after the instability. As q increases, the distance that the surface wave propagates along the interface before becoming unstable

is decreased and, in addition, the width of the solution appears to decrease with increasing q.

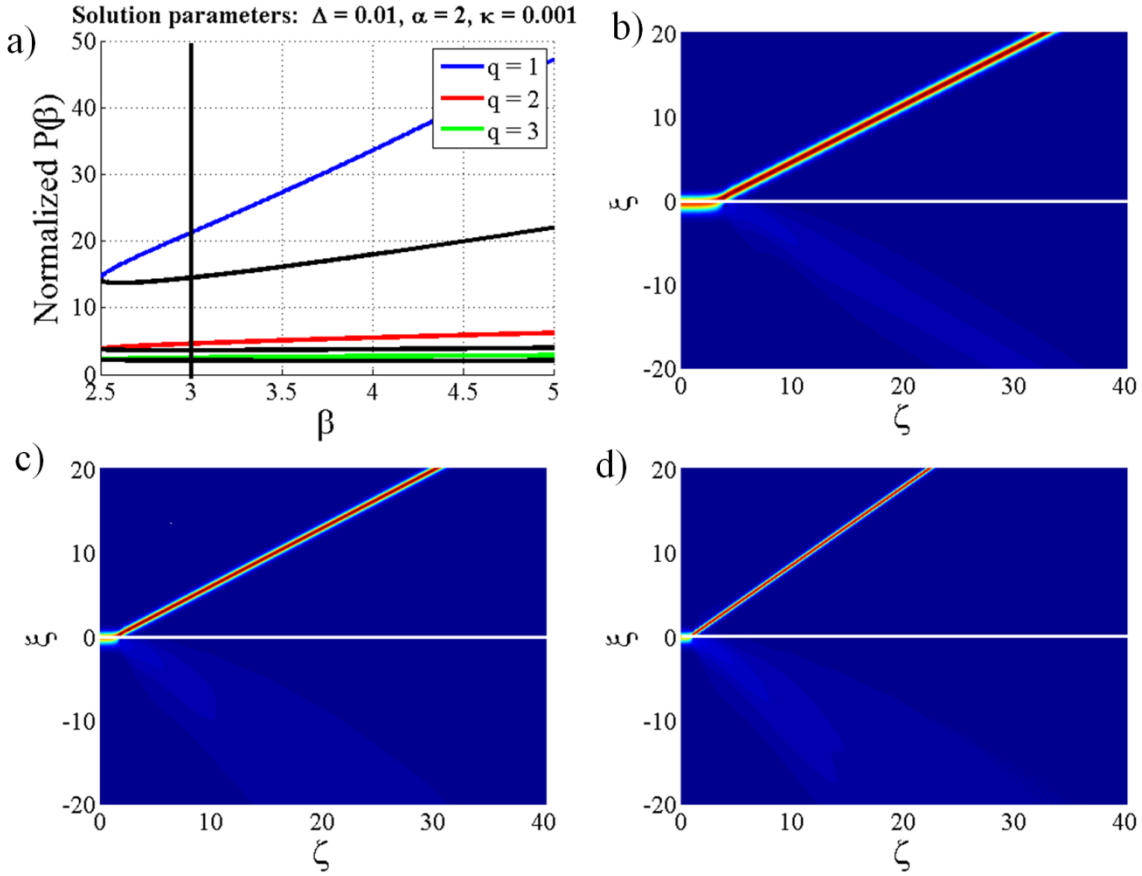

Figure 55 Showing a) P(β) vs. β curves with the upper branches of the curves in colours representing q = 1, 2 or 3 and the lower branches shown in black (it is just the upper branches that are being considered at this point). b), c) and d) show the surface wave solutions for q = 1, 2 and 3 respectively. The interface is represented by a white line and β = 3 in all three cases.

By decreasing κ, all of the beams appear to be narrower than the case where $\kappa = 2.5 \times 10^{-3}$, and also in all three examples the instability occurs after a shorter ζ length than in Figure 54.

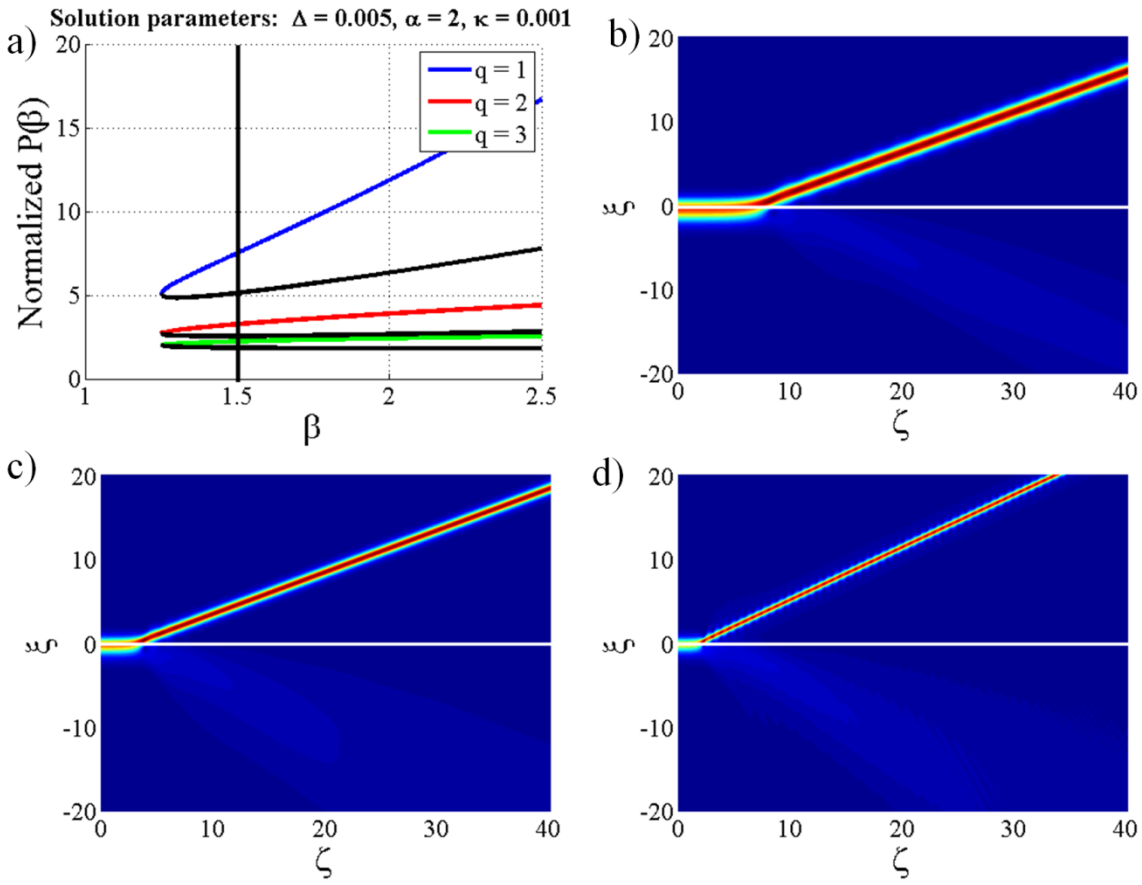

Figure 56 Showing a) P(β) vs. β curves with the upper branches of the curves in colours representing q = 1, 2 or 3 and the lower branches shown in black (it is just the upper branches that are being considered at this point). b), c) and d) show the surface wave solutions for q = 1, 2 and 3 respectively. The interface is represented by a white line and β = 1.5 in all three cases.

Δ in Figure 56 has been decreased by a factor of 2 compared to Figure 55. By halving the value of Δ, all three solutions appear broader, but the propagation length before the beam becomes unstable is increased in comparison to that of Figure 55.

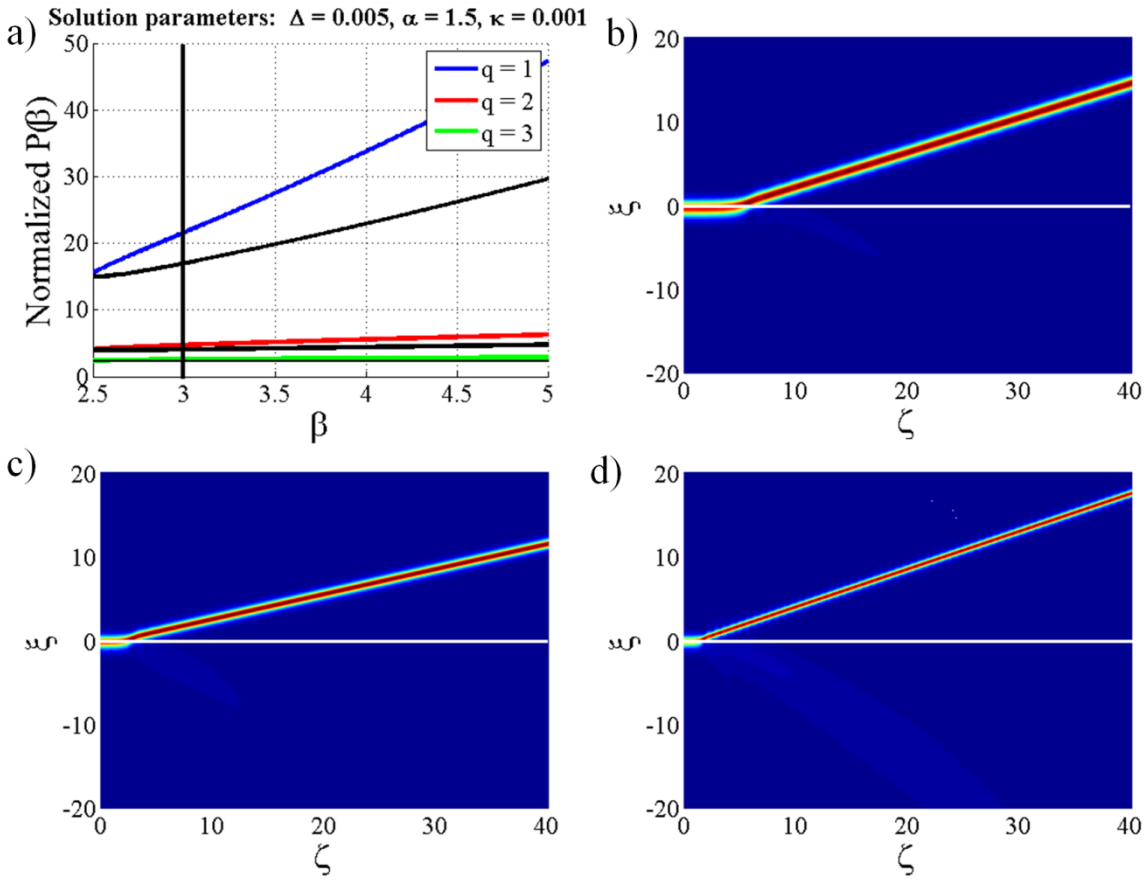

Figure 57 Showing a) P(β) vs. β curves with the upper branches of the curves in colours representing q = 1, 2 or 3 and the lower branches shown in black (it is just the upper branches that are being considered at this point). b), c) and d) show the surface wave solutions for q = 1, 2 and 3 respectively. The interface is represented by a white line and $\beta = 3$ in all three cases.

A reduction in α has occurred between Figures 56-57. By decreasing α, the instability occurs over a shorter distance in the ζ direction and there is no obvious difference in the width of the beam.

4.4.2 Upper Branch Regime 1 Changing β

The results here look specifically at surface waves with different values of β for three different values of q.

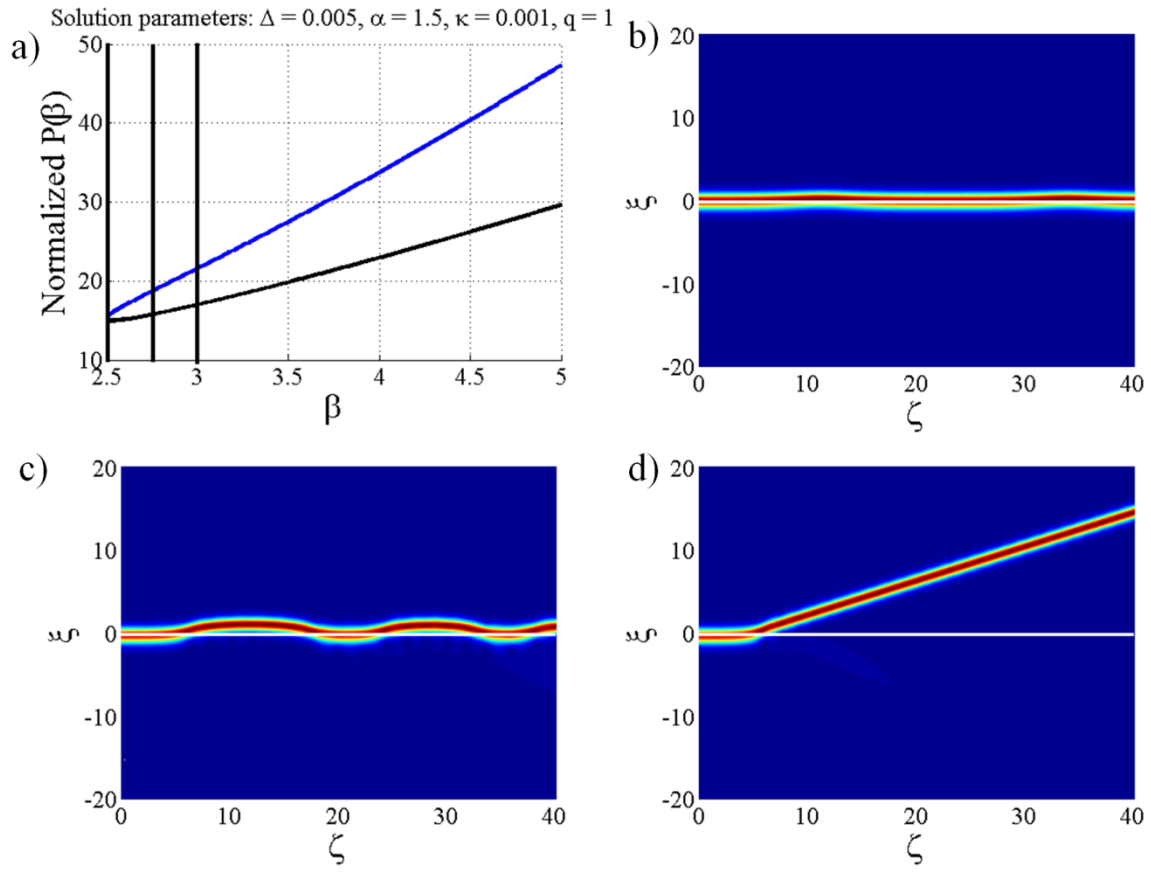

Figure 58 Shows the effect of varying the parameter β, when q = 1. a) Shows the beam powers for all the values of β tested. b) has β = 2.5 (or $\beta = \beta_{min}$), c) has β = 2.75 (or β = 1.1 x β_{min}) and d) has β = 3 (or β = 1.2 x β_{min}).

Figure 58 shows how increasing the value of β affects the stability of the surface wave solutions. Figure 58b) shows the surface wave solution when $\beta = \beta_{min}$. The solution 'skims' the interface and can, therefore, be described as being unstable. Figure 58c), where the value of β has been increased to $\beta = 1.1\beta_{min}$, the oscillations are more rapid in ζ, and they are larger in ξ. Figure 58d) show results similar to those in the previous section where the beam is deflected into the second medium. As the value of β increases, the beam oscillations increase in ζ until β reaches a point where the beam is so unstable that it completely leaves the interface to propagate in the second medium. Put simply, as the value of β increases, the beam becomes more unstable.

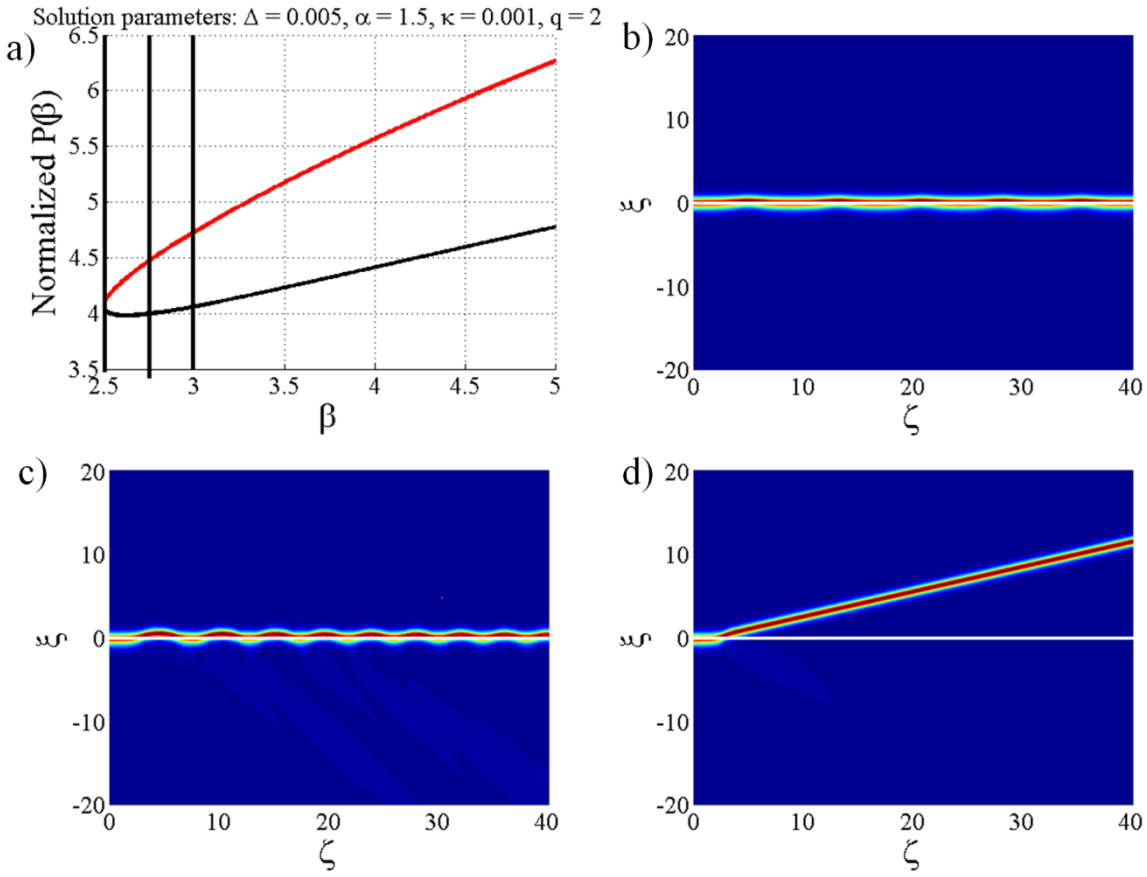

Figure 59 Shows the effect of varying the parameter β, when q = 2. a) Shows the beam powers for all the values of β tested. b) has β = 2.5 (or $\beta = \beta_{min}$), c) has β = 2.75 (or β = 1.1 x β_{min}) and d) has β = 3 (or β = 1.2 x β_{min}).

Figure 59b), which has $\beta = \beta_{min}$, shows a skimming mode along the interface, but the beam does not leave the interface. By increasing β to 2.75, the longitudinal oscillations of the skimming mode become more rapid, c.f. Figures 59b) and c). Figure 59d) shows the beam propagating along the interface until a certain point where the beam is deflected and propagates into medium 2. Again, as the value of β has increased, the surface wave solutions become more unstable.

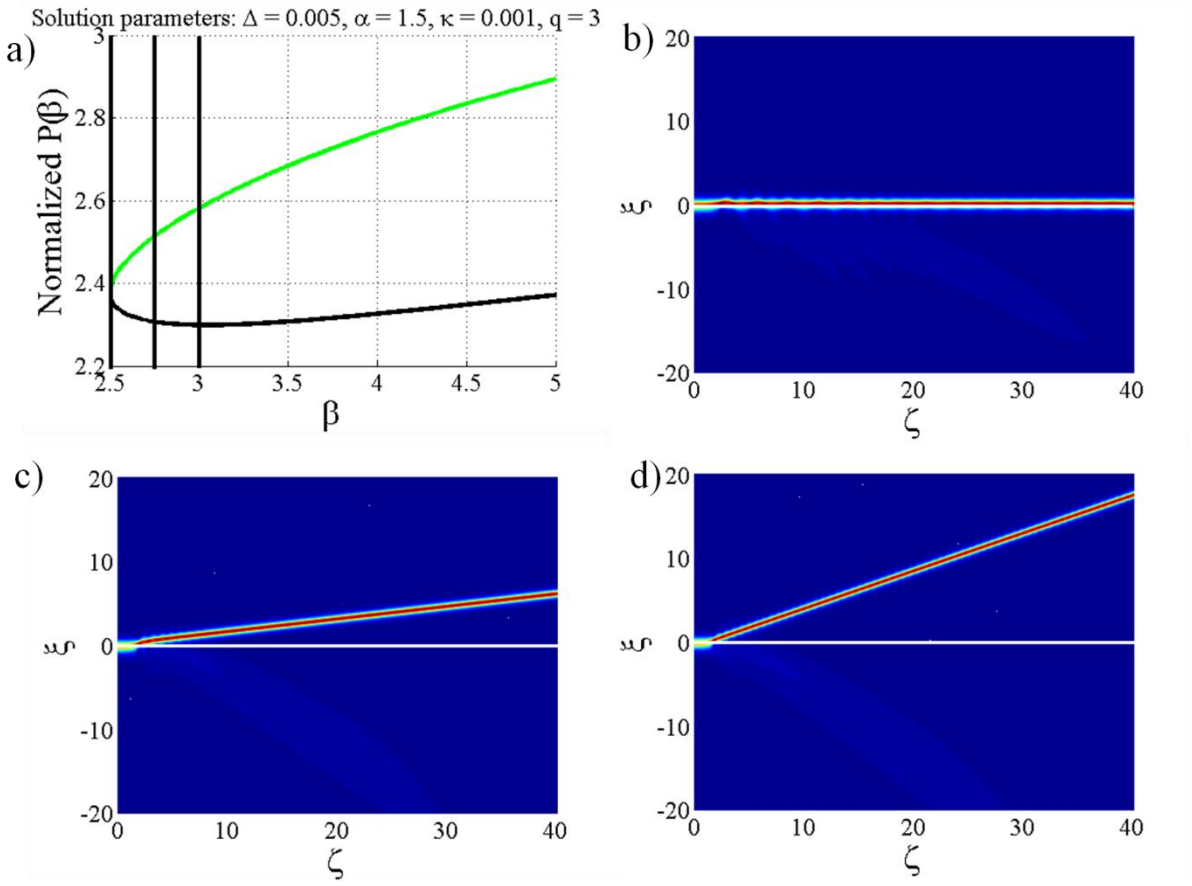

Figure 60 Shows the effect of varying the parameter β, when q = 3. a) Shows the beam powers for all the values of β tested. b) has $\beta = 2.5$ (or $\beta = \beta_{min}$), c) has $\beta = 2.75$ (or $\beta = 1.1 \times \beta_{min}$) and d) has $\beta = 3$ (or $\beta = 1.2 \times \beta_{min}$).

In Figure 60 the value of q has been increased to 3. Figure 60b) shows the surface wave solution when $\beta = \beta_{min}$. The surface wave appears to propagate along the interface until it begins to oscillate. These oscillations become much smaller in ξ with increasing ζ, until the beam appears to be propagating along the interface without any oscillations in ξ. Figures 60c) and d) show the beams being deflected into the second medium, though the beam in Figure 60d) propagates at a larger angle with respect to the interface.

Summary

When q = 1 and q = 2, the results show that as β increases the surface waves develop more instability. For $\beta = \beta_{min}$ there are small oscillations, for $\beta = 1.1\beta_{min}$ the oscillations are larger in ξ and more rapid in ζ, and for $\beta = 1.2\beta_{min}$, the beam leaves the interface altogether.

When q = 3, the results are slightly different. For $\beta = \beta_{min}$ the beam does start oscillating, but these oscillations appear to die out at ζ increases. For $\beta = 1.1\beta_{min}$ and $\beta = 1.2\beta_{min}$ the

beam leaves the interface, in the case of $\beta = 1.2\beta_{min}$, after less ζ distance when compared with $\beta = 1.1\beta_{min}$. For $q = 3$ as the value of β increases the beam does become more unstable (as it does when $q = 1$ and $q = 2$), however the instabilities of the beam are not manifest in the same way when $q = 2$ and $q = 3$.

4.4.3 Upper Branch regime 2

This section of the report will look in detail at the upper branch surface waves in regime 2, where $\Delta < 0$, and $0 < \alpha < 1$. Upper branch surface waves are unstable in this regime just as they are in regime 1. Figure 61a) shows the upper branch solutions in blue, red and green lines, for q = 1, 2 and 3 respectively.

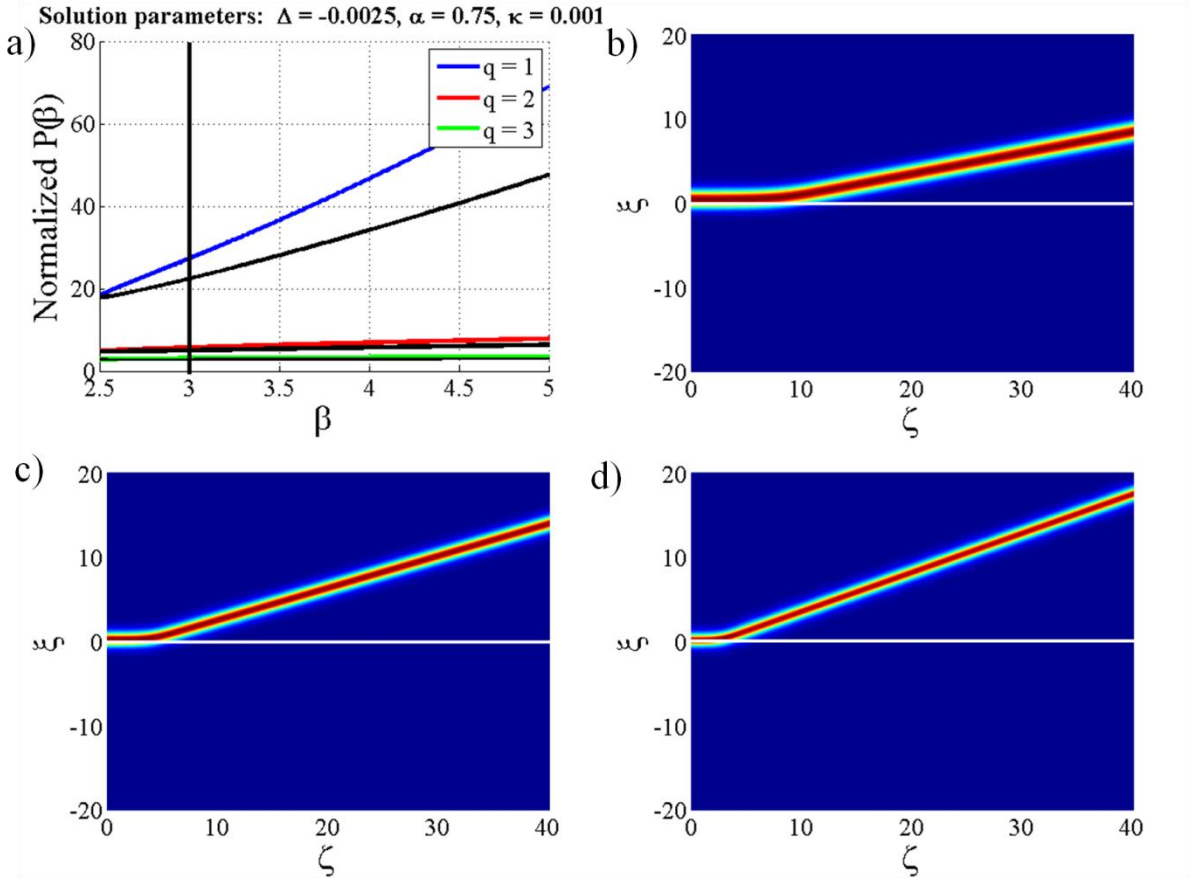

Figure 61 Showing a) P(β) vs. β curves with the upper branches of the curves in colours representing q = 1, 2 or 3 and the lower branches shown in black (it is just the upper branches that are being considered at this point). b), c) and d) show the surface wave solutions for q = 1, 2 and 3 respectively. The interface is represented by a white line and $\beta = 3$ in all three cases.

Figure 61 shows the stability of a regime 2 upper branch surface wave. No exact comparison can be carried out between regime 1 and 2, since more than one parameter has been changed between the two systems. Despite this, one noticeable feature of regime 2 is that the peak of the beam before and after the point of deflection is on the same side of the interface, unlike in regime 1 where the peak of the beam crosses the interface, c.f. Figures 62-64. As with the regime 1 results, increasing q decreases the distance the surface wave will propagate before becoming unstable.

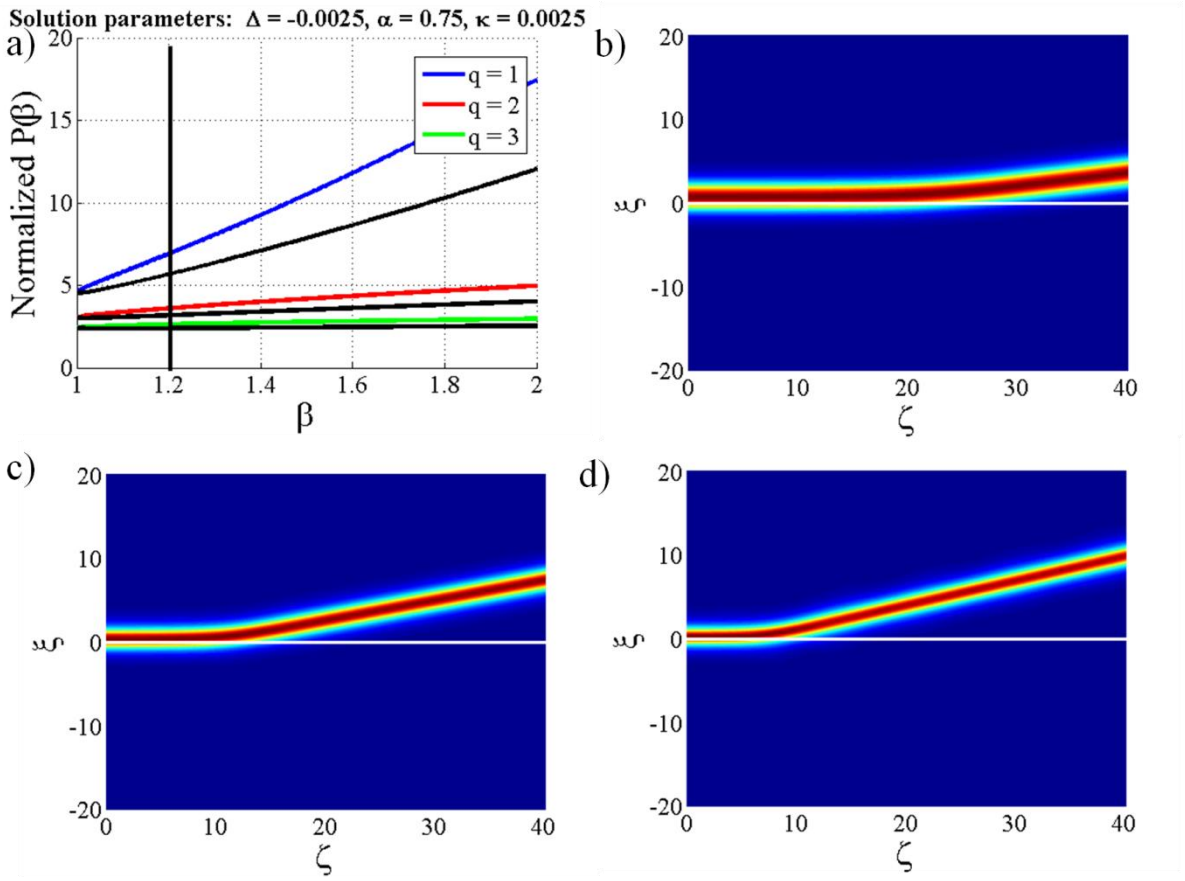

Figure 62 Showing a) P(β) vs. β curves with the upper branches of the curves in colours representing q = 1, 2 or 3 and the lower branches shown in black (it is just the upper branches that are being considered at this point). b), c) and d) show the surface wave solutions for q = 1, 2 and 3 respectively. The interface is represented by a white line and β = 1.2 in all three cases.

As κ is increased, the distance the surface wave propagates along the interface before being deflected is also increased, compare Figures 61 and 62. Also the beams all appear broader in Figure 62 than in Figure 61.

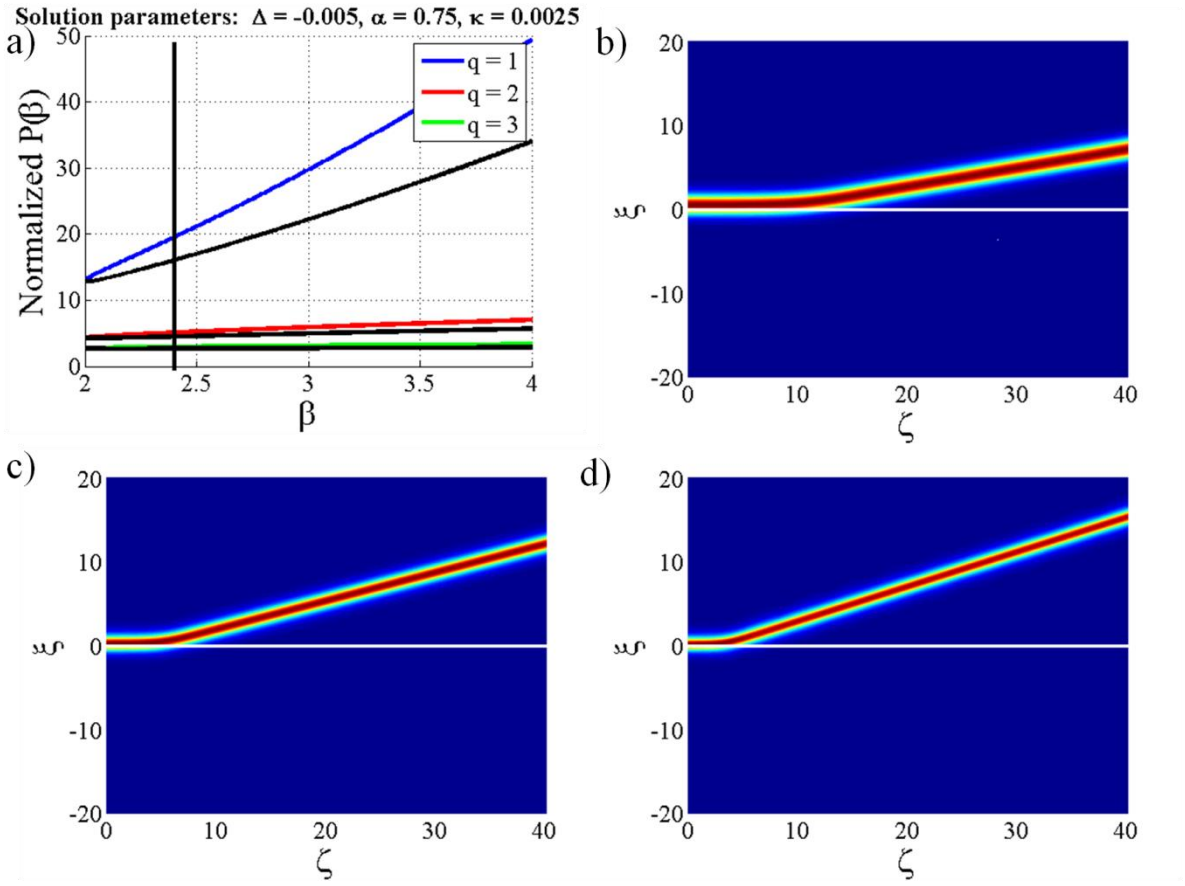

Figure 63 Showing a) P(β) vs. β curves with the upper branches of the curves in colours representing q = 1, 2 or 3 and the lower branches shown in black (it is just the upper branches that are being considered at this point). b), c) and d) show the surface wave solutions for q = 1, 2 and 3 respectively. The interface is represented by a white line and $\beta = 2.4$ in all three cases.

Increasing |Δ| leads to the instability becoming apparent at a decreased distance along the ζ axis, compare Figures 62 and 63. Again, the peak of the beam initially and the peak of the beam after the instability are at the same side of the interface (in medium 2), and as q increases, the distance the beam travels along the interface before becoming unstable decreases.

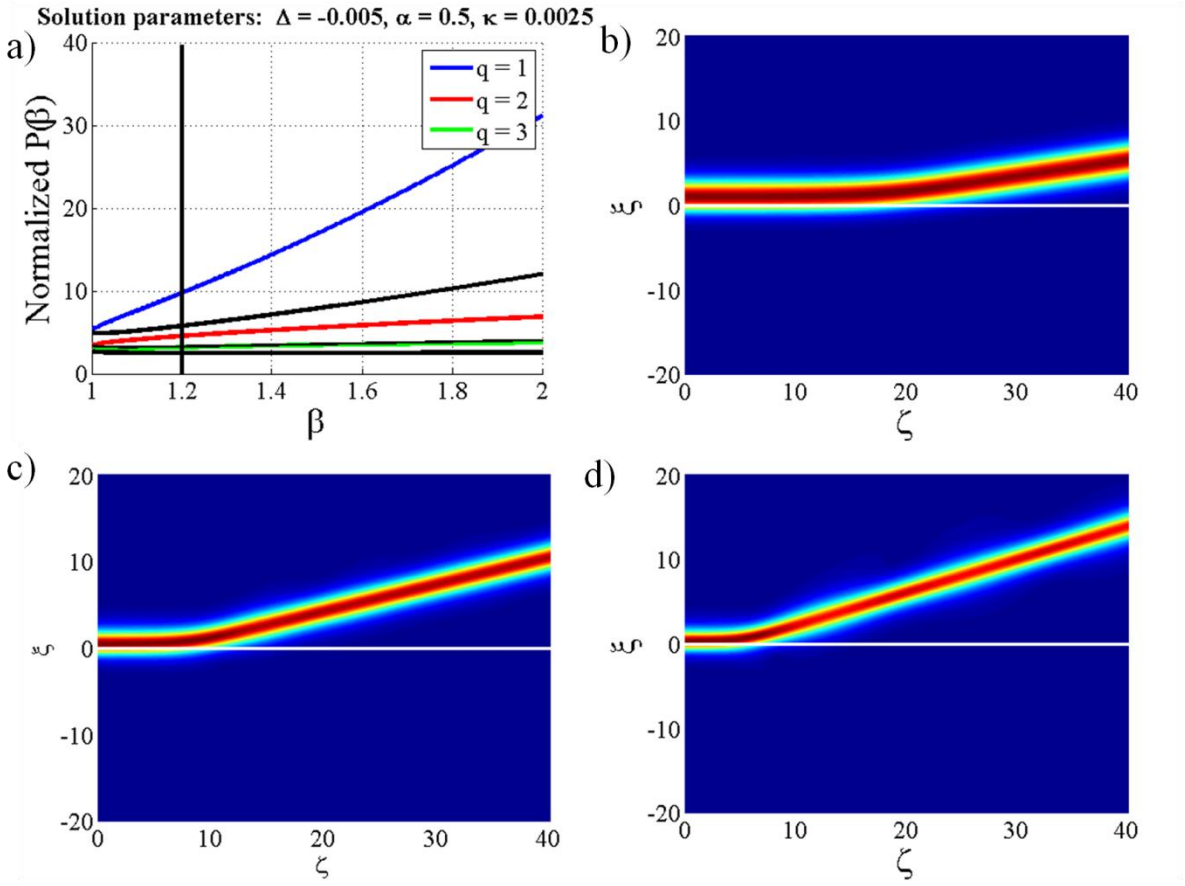

Figure 64 Showing a) P(β) vs. β curves with the upper branches of the curves in colours representing q = 1, 2 or 3 and the lower branches shown in black (it is just the upper branches that are being considered at this point). b), c) and d) show the surface wave solutions for q = 1, 2 and 3 respectively. The interface is represented by a white line and $\beta = 1.2$ in all three cases.

When comparing Figures 63 and 64, the value of α has been decreased by 2/3. By decreasing α, the distance the surface wave propagates along the interface before it becomes unstable is slightly increased for all three q values. It shows that as q increases, the distance the beam propagates along the interface before deflecting decreases.

4.4.4 Upper Branch Regime 2 Changing β

As in section 4.4.2, our interest here is on the effect of changing β on the behaviour of surface waves, in this instance in regime 2 conditions.

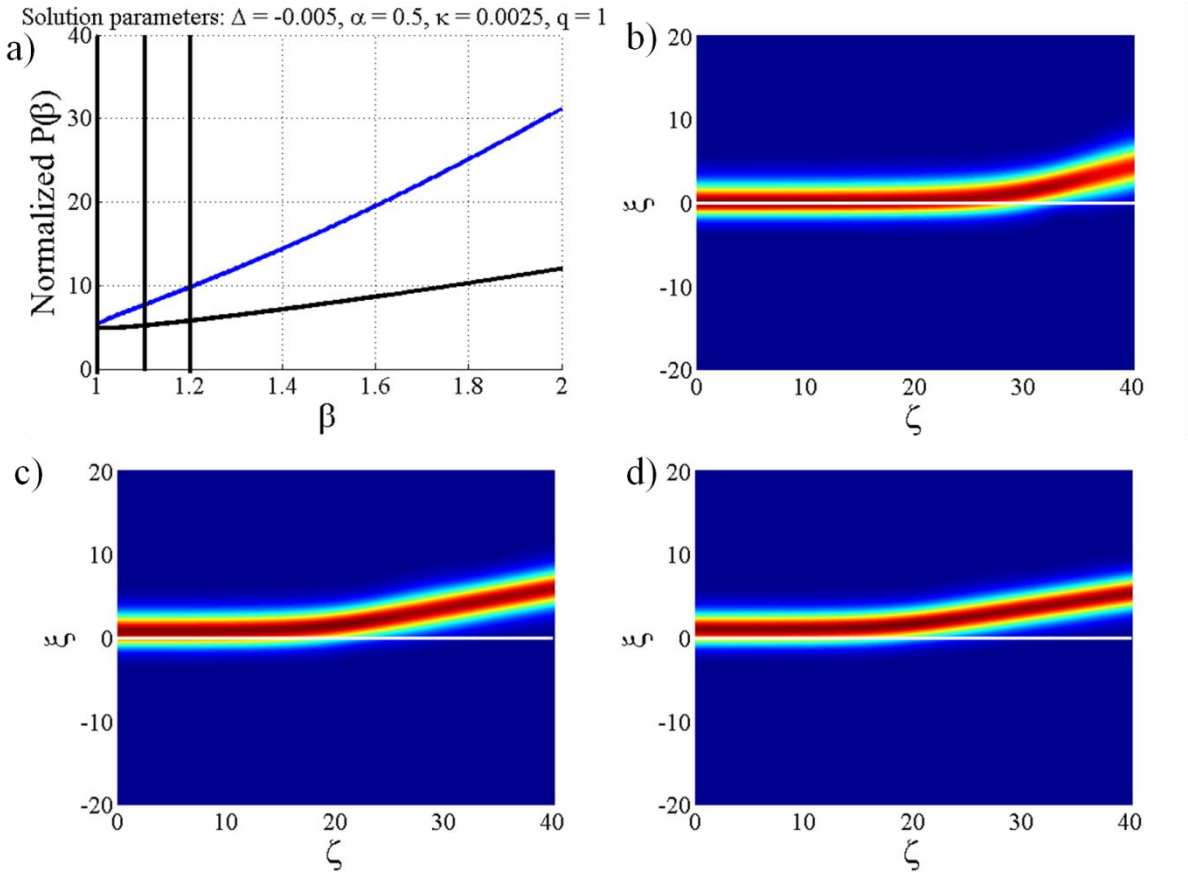

Figure 65 Shows the effect of varying the parameter β, when q = 1. Figure a) shows the beam powers for all the values of β tested. Figure b) has β = 1 (or $\beta = \beta_{min}$), Figure c) has β = 1.1 (or β = 1.1 x β_{min}) and Figure d) has β = 1.2 (or β = 1.2 x β_{min}).

Unlike the results for regime 1 (where the instability looked different as the value of β changed), the instabilities within regime 2 parameters are always of the same type (i.e. the surface wave deflects). This is highlighted in Figures 65-67 – they all show that as β is increased from β_{min} the surface wave propagates along the interface for a decreasing distance before the beam becomes unstable.

It is interesting to note that for all the results thus far, increasing β makes the beam more unstable. In regime 1, this meant qualitatively different results as β increased (from beams oscillating, to beams completely leaving the interface). Here, in regime 2, all the beams leave the interface, increasing β just decreases the propagation distance before this happens.

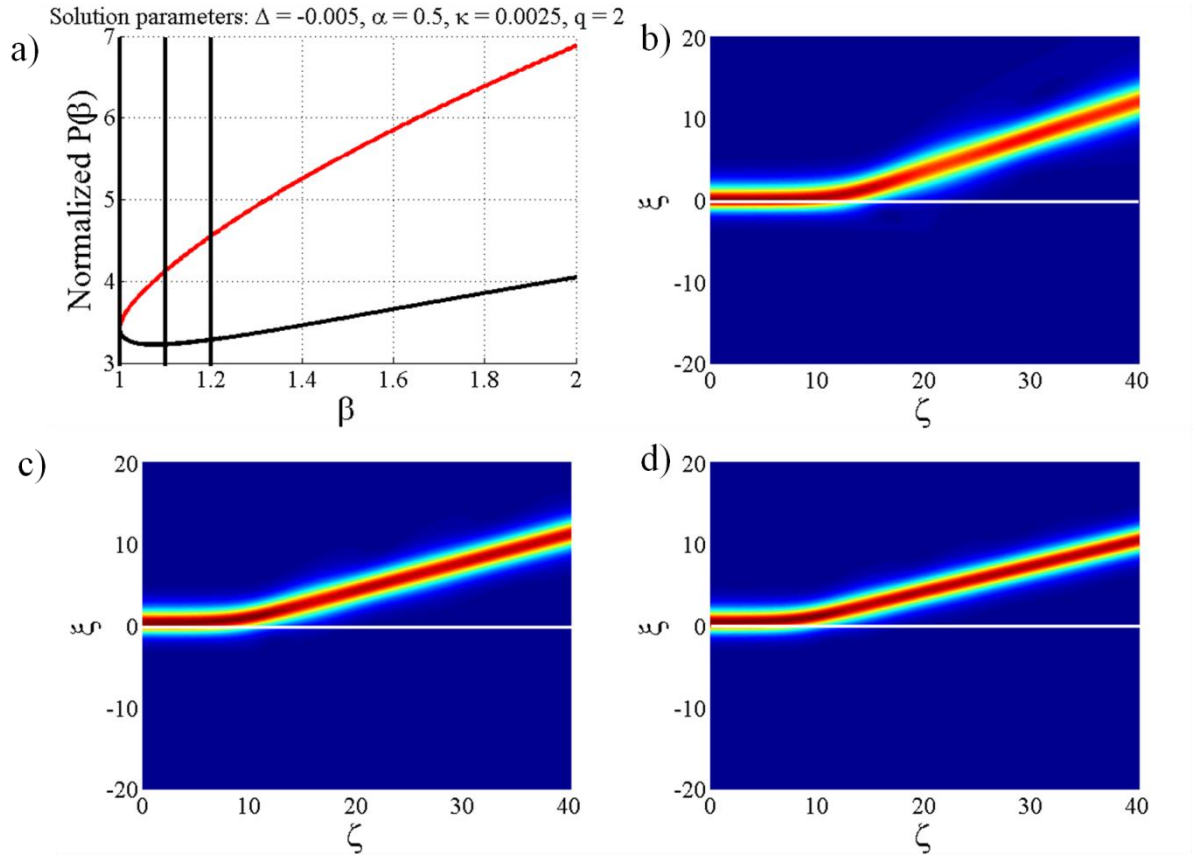

Figure 66 Shows the effect of varying the parameter β, when q = 2. Figure a) shows the beam powers for all the values of β tested. Figure b) has β = 1 (or $\beta = \beta_{min}$), Figure c) has β = 1.1 (or β = 1.1 x β_{min}) and Figure d) has β = 1.2 (or β = 1.2 x β_{min}).

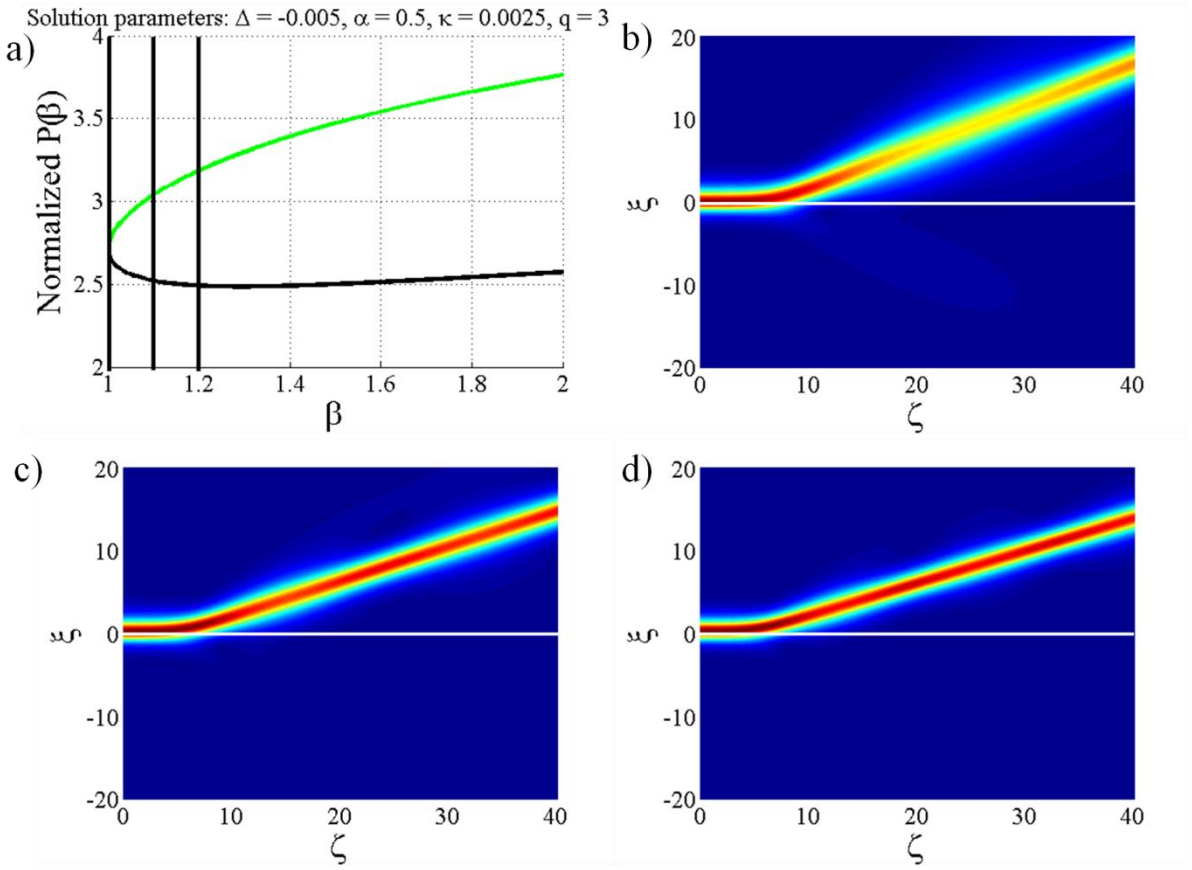

Figure 67 Shows the effect of varying the parameter β, when $q = 3$. Figure a) shows the beam powers for at all the values of β tested. Figure b) has $\beta = 1$ (or $\beta = \beta_{min}$), figure c) has $\beta = 1.1$ (or $\beta = 1.1 \times \beta_{min}$) and figure d) has $\beta = 1.2$ (or $\beta = 1.2 \times \beta_{min}$).

4.4.5 Interaction Between Surface Waves and Solitons

In section 4.3, the stability of lower-branch surface waves was investigated numerically by using initial conditions for equation (4.2) that corresponded to exact solutions. The only perturbation in the system was due to finite machine precision and algorithm accuracy. There are, of course, other methods to test solution stability against stronger disturbances. Two standard approaches involve adding a pre-determined level of (suitably filtered) complex noise to the initial condition, or by introducing a smooth modulation to the input profile.

Here, the stability of lower-branch stable surface waves (i.e., those satisfying $dP/d\beta > 0$) is tested by considering their interactions with an obliquely-incident soliton. When considering the refraction of an incident soliton, changes in material mismatches have no influence at all on the input beam. However, even small variations in Δ and/or α can lead to dramatic changes in surface-wave profiles precisely because the surface wave itself is characterised in terms of such mismatches. The parameter κ plays a more subtle role by also affecting the numerical value of $\beta_{\min}$ (see equation (4.14)) and, subsequently, changing the $P(\beta)$ curves (here, $\beta = 1.8\beta_{\min}$ is fixed throughout). An investigation of this type is thus awkward to formulate in terms of a systematic variation of a single parameter.

In the following simulations, the parameters have been chosen so that, in the absence of any collision, the surface wave would propagate indefinitely without any change in shape. These results will start to provide deeper insight into the stability problem since collisions, in general, cannot be considered a small perturbation. The soliton will be injected from well inside medium 1 (ensuring there is effectively zero interference between the soliton and surface wave at the start of the simulation), in which case equation (4.2) has the exact analytical solution [9]

$$u_{\mathrm{sol}}(\xi,\zeta) = \rho_0^{1/2}\,\mathrm{sech}^{2/q}\Theta \exp\left[\pm i\sqrt{\frac{1+4\kappa\beta_{\mathrm{sol}}}{1+2\kappa V_{\mathrm{sol}}^2}}\left(V_{\mathrm{sol}}\xi + \frac{\zeta}{2\kappa}\right)\right]\exp\left(-i\frac{\zeta}{2\kappa}\right), \qquad (4.15)$$

where

$$\Theta = \left(a_{\mathrm{sol}}\frac{\xi - V_{\mathrm{sol}}\zeta}{\sqrt{1+2\kappa V_{\mathrm{sol}}^2}}\right) \qquad (4.16)$$

also $a_{\mathrm{sol}} \equiv q[\eta_0^2/(2+q)]^{1/2}$ and the propagation angle in the laboratory frame is

$\theta_{sol} = \tan^{-1}[(2\kappa)^{1/2}V_{sol}]$. Surface waves in regimes 1 and 2 will be considered and, for definiteness, the incoming soliton will be travelling at either a quasi-paraxial ($\theta_{sol} = 2°$) or fully nonparaxial ($\theta_{sol} = 10°$) angle. At quasi-paraxial angles, one can expect to find a wide variety of inelastic behaviours – such as annihilation, fission (splitting) and fusion (coalescence) [13] – that are universal features of nonlinear wave interactions. These phenomena typically exhibit a strong sensitivity on the relative phase difference between the interacting entities (here, the surface wave and the soliton are always launched in-phase); they are highly non-adiabatic processes that are often accompanied by the generation of much radiation.

In contrast, such behaviour might be expected to largely disappear at nonparaxial angles and the general complexity of the behaviour should be greatly reduced. For all interfaces considered in regime 1, the incidence angle of $\theta_{inc} = 10°$ is well above the critical angle so that the soliton always passes through the surface wave.

4.4.5.1 Interactions in Regime 1

The top row of simulations in Figures 68-71 all show solitons propagating at an angle of incidence of 2° without any surface wave present, in order to highlight the soliton's behaviour in the absence of more complicated interactions. The figures all show that, in spite of the changes in a variety of parameters, the soliton behaviour remains broadly the same – with beams reflected by the interface, which is to be expected since the angle of incidence is significantly lower than the critical angle.

For a quasi-paraxial interaction between relatively narrow beams, there is one key trend that is immediately apparent (see Figure 68): the soliton reflects from the interface and the energy initially localised in the surface wave is scattered into medium 2. The collision itself thus deflects the surface wave, transforming it into an obliquely-propagating soliton-like beam (this wave can no longer be classed as a *surface* excitation since it is no longer bound to the interface). Both spatial structures retain their distinctive identities (i.e., there is no splitting or coalescence) and the interaction generates radiation. The surface wave also remains unstable against nonparaxial collisions. As the nonlinearity exponent is increased from $q = 1$ to $q = 2$, the propagation angle of the deflected surface wave (relative to the interface) approaches that of the refracted soliton. For $q = 3$, these two entities coalesce into a single high-intensity narrow filament.

At this point, the role played by κ in the surface wave solutions becomes more apparent. While decreasing κ (to capture broader beams) leaves the normalised soliton profile essentially unchanged, there is a large effect on the surface wave (whose peak intensity can increase dramatically). One can reasonably anticipate that such a change may have a profound impact on the system evolution (see Figure 69). For q = 1 and a quasiparaxial incidence angle, the surface wave clearly dominates the system: the soliton refracts from the interface and the collision induces only small modulations in the surviving surface wave [see Figure 69d)]. This type of surface-wave modulation has previously been referred to as 'skimming' [1]. For q = 2, coalescence has been uncovered wherein the energy of the surface wave becomes coupled into the trajectory of the reflected soliton [see Figure 69e)]. For q = 3 [see Figure 69f)], one finds a similar type of coalescence but the radiation pattern (particularly in medium 1) is becoming more visible in the solution.

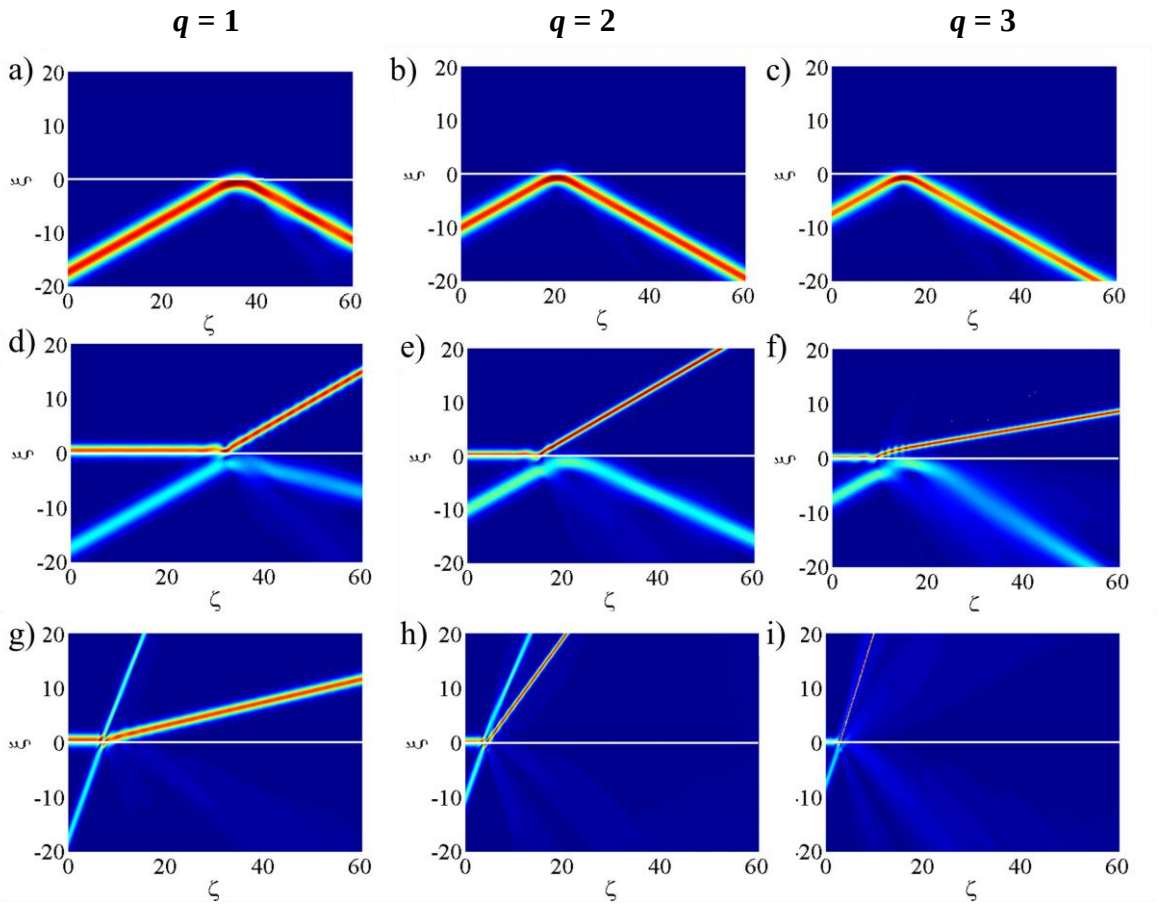

Figure 68. Top row: Soliton interaction with an interface (Δ = 0.01 and α = 2.0) at the quasi-paraxial incidence angle θ_{inc} = 2° and with $\kappa = 2.5\times10^{-3}$. Middle row: same configuration as the top row, but with a regime 1 surface wave (with $\beta = 1.8\beta_{min}$) travelling along the interface. Bottom row: similar configuration to the middle row, except with a nonparaxial incidence angle of θ_{inc} = 10°.

This pattern has distinct fringes that may be connected to the interference between radiation shed by the dominant post-collision filament and radiation that has been totally internally-reflected by the interface. Another interesting and rather subtle aspect of Figure 69f) is the degree of spatial asymmetry in the solution (introduced by the material interface itself). For a nonparaxial incidence angle, the skimming mode appears in the $q = 1$ system (as opposed to inducing surface-wave deflection). For $q = 2$ and $q = 3$, phenomena that are qualitatively similar to those in Figure 68 are uncovered.

By maintaining the broader-beams regime ($\kappa = 1.0\times10^{-3}$) but lowering the linear refractive index step (from $\Delta = 0.01$ to $\Delta = 0.005$), the peak amplitude of the surface wave is decreased.

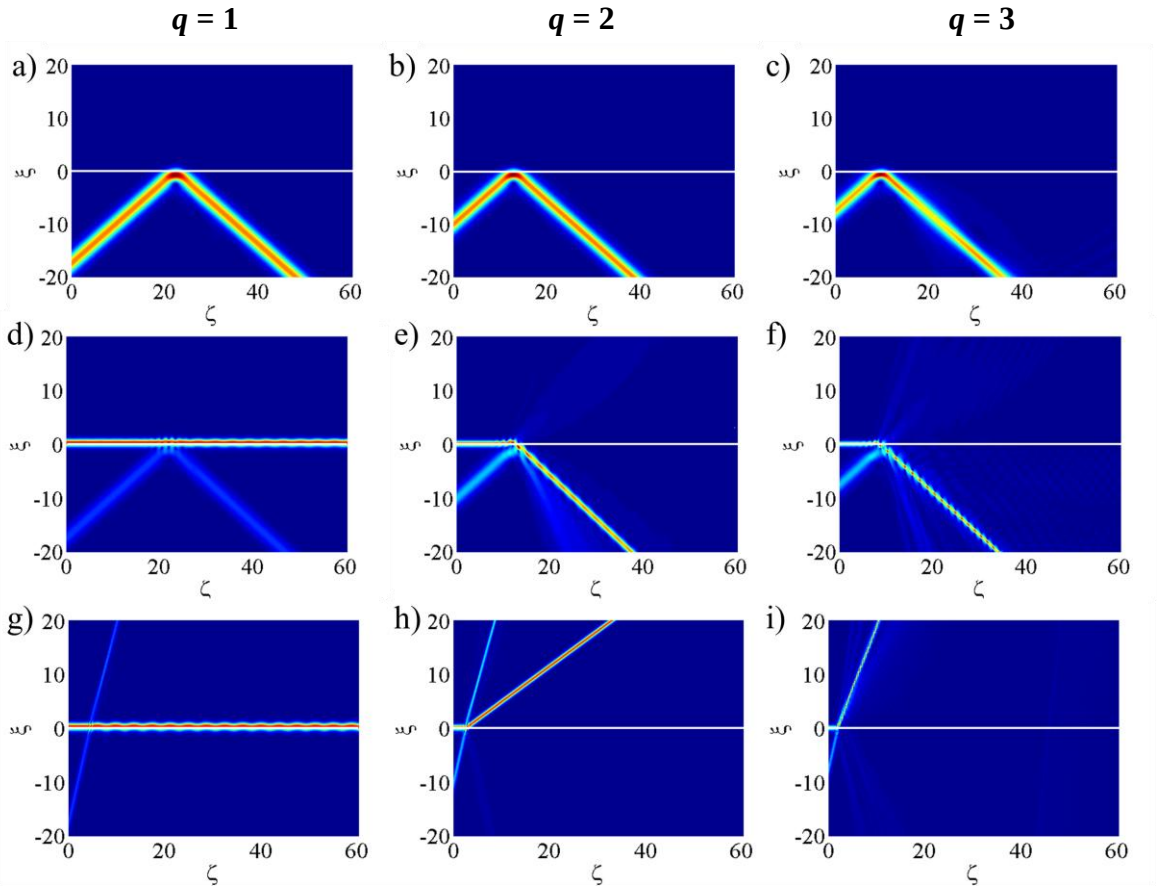

Figure 69. Top row: Soliton interaction with an interface (Δ = 0.01 and α = 2.0) at the quasi-paraxial incidence angle θ_{inc} = 2° and with $\kappa = 1.0\times10^{-3}$. Middle row: same configuration as the top row, but with a regime 1 surface wave (with $\beta = 1.8\beta_{min}$) travelling along the interface. Bottom row: similar configuration to the middle row, except with a nonparaxial incidence angle of θ_{inc} = 10°.

One then finds similar qualitative behaviour to that encountered for narrower beams with a larger linear-index step (compare Figures 70 and 68). Here, it is interesting that for q = 3, the reflecting soliton is annihilated by the collision and the surface wave is transformed to an off-axis soliton-like beam in medium 2.

By weakening the self-focusing properties of medium 2 (e.g., reducing α = 2.0 to α = 1.5), the quasi-paraxial collision can start to excite skimming modes. Inspection of Figure 71 reveals that the longitudinal oscillations of the skimming are more rapid for q = 2 than for q = 1. Nonparaxial collisions for q = 1 and q = 2 trigger skimming and surface-wave deflection, respectively. However, in the case of q = 3, simulations reveal splitting rather than coalescence (i.e., after the collision, there are three distinct beams propagating in medium 2).

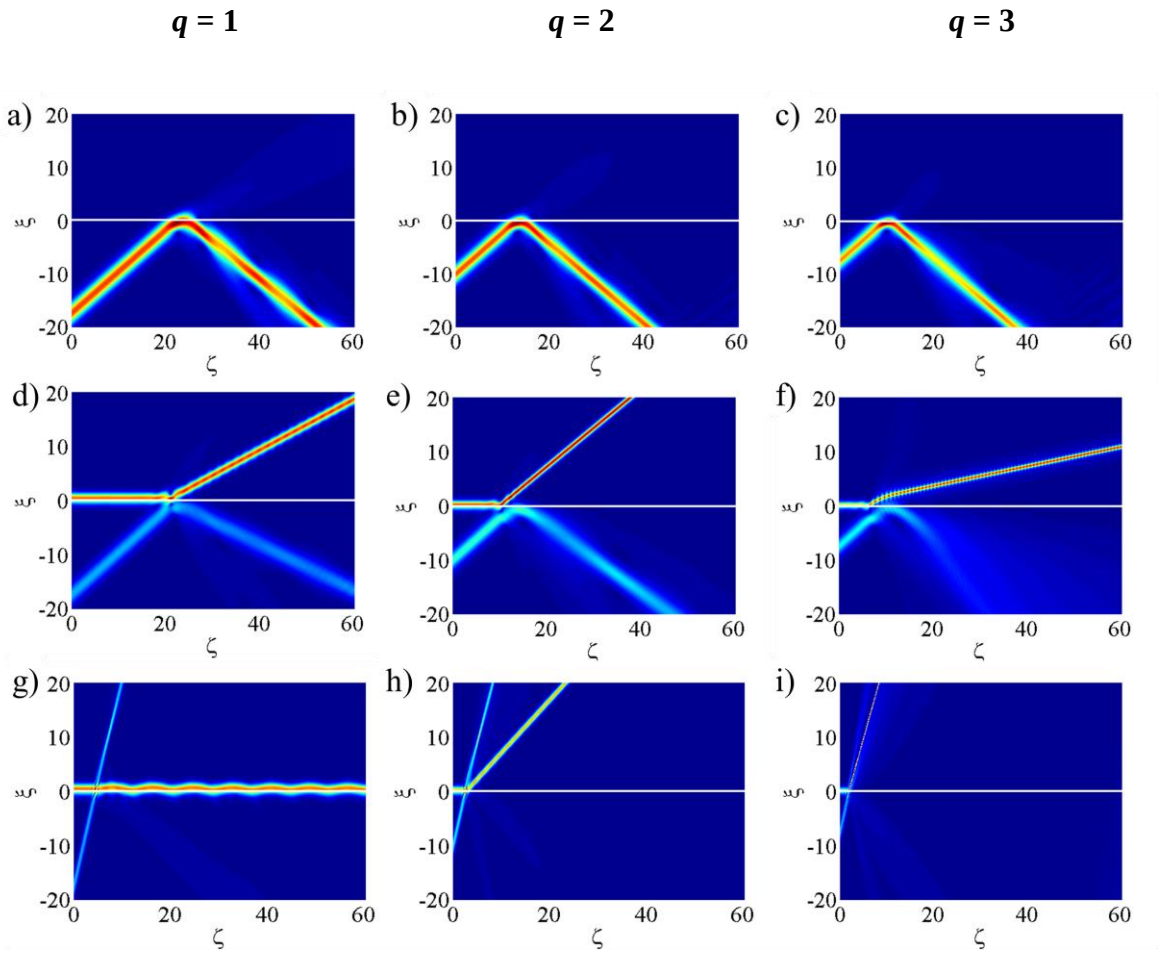

Figure 70. Top row: Soliton interaction with an interface ($\Delta = 0.005$ and $\alpha = 2.0$) at the quasi-paraxial incidence angle $\theta_{inc} = 2°$ and with $\kappa = 1.0\times10^{-3}$. Middle row: same configuration as the top row, but with a regime 1 surface wave (with $\beta = 1.8\beta_{min}$) travelling along the interface. Bottom row: similar configuration to the middle row, except with a nonparaxial incidence angle of $\theta_{inc} = 10°$.

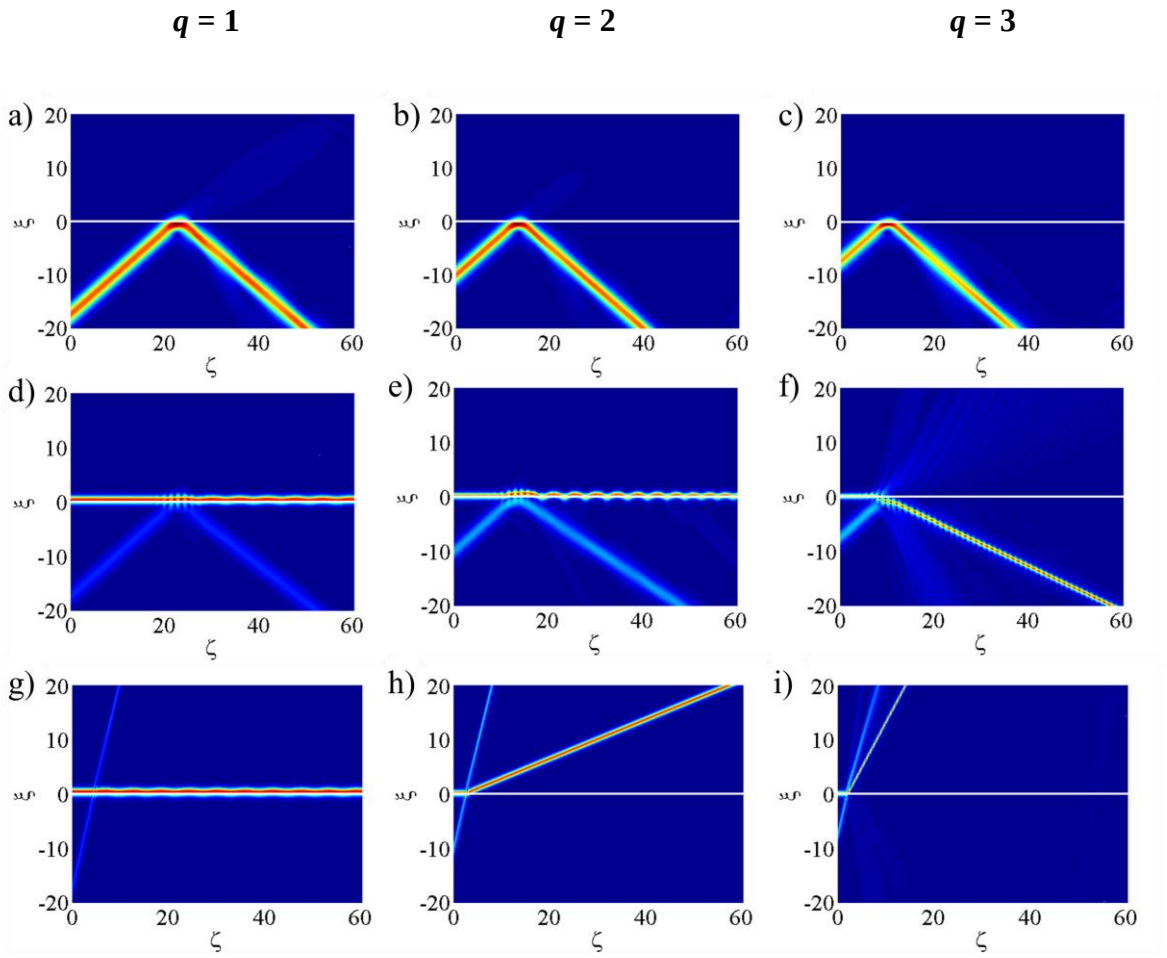

Figure 71. Top row: Soliton interaction with an interface (Δ = 0.005 and α = 1.5) at the quasi-paraxial incidence angle θ_{inc} = 2° and with κ = 1.0×10^{-3}. Middle row: same configuration as the top row, but with a regime 1 surface wave (with β = 1.8β_{min}) travelling along the interface. Bottom row: similar configuration to the middle row, except with a nonparaxial incidence angle of θ_{inc} = 10°.

4.4.5.2 Surface Waves in Regime 2

As in section 4.4.5.1, reference simulations have been carried out in order to demonstrate soliton behaviour in the absence of a surface wave. The top row of 3d plots in Figures 72-75 show a soliton interacting with the interface at an angle of 2°; unlike the same results for regime 1, the soliton is always refracted into the second medium (rather than being reflected). This is explained by the fact that, in regime 2, Δ is always negative, meaning (on the whole) no critical angle exists, giving rise to beam refraction.

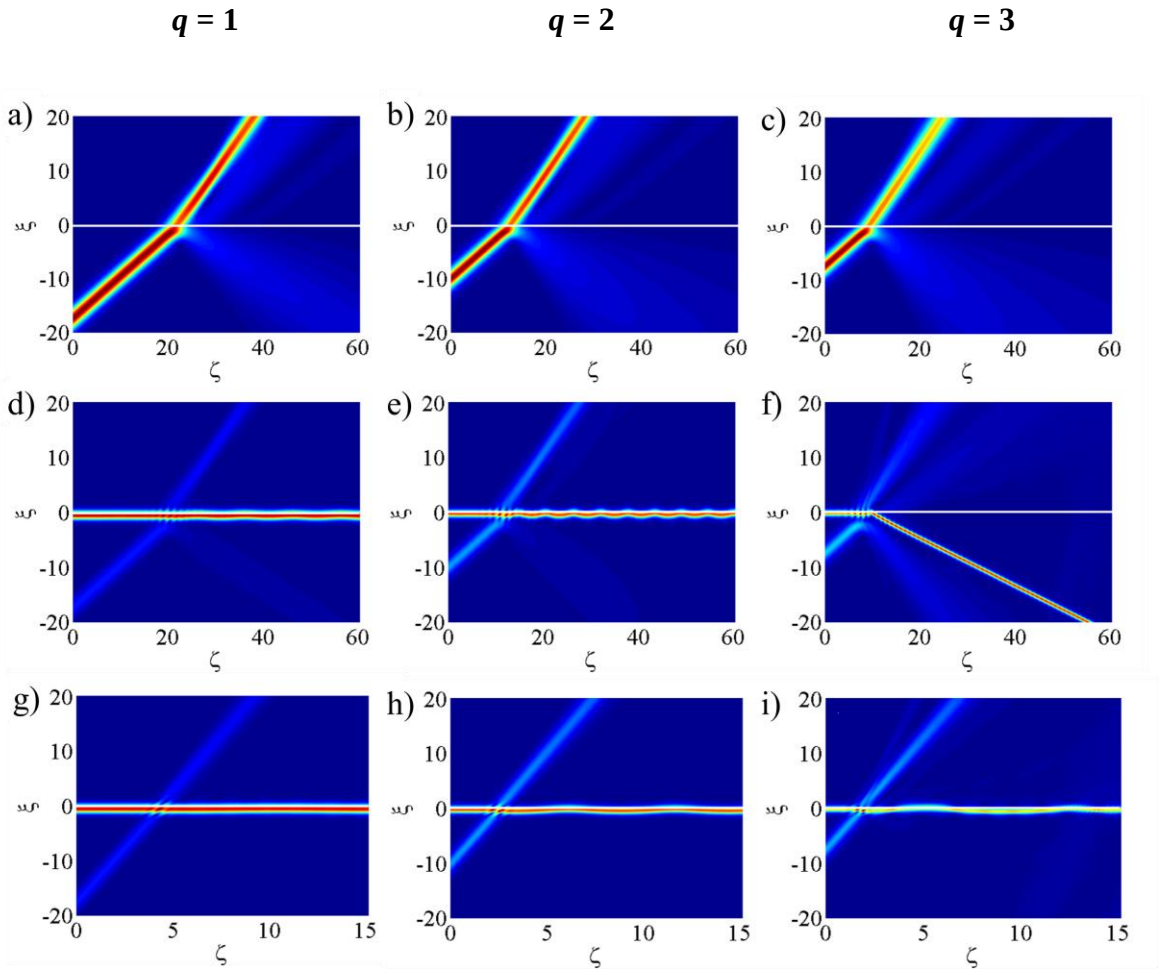

Figure 72 Top row: Soliton interaction with an interface (Δ = -0.0025 and α = 0.75) at the quasi-paraxial incidence angle θ_{inc} = 2° and with $\kappa = 1.0\times10^{-3}$. Middle row: same configuration as the top row, but with a regime 2 surface wave (with $\beta = 1.8\beta_{min}$) travelling along the interface. Bottom row: similar configuration to the middle row, except with a nonparaxial incidence angle of θ_{inc} = 10°.

The behaviour of the soliton following its interaction with the surface wave is much more consistent in regime 2 than it is in regime 1. When θ_{inc} = 2° (shown in the middle rows of Figures 72-75), and q = 1, there is a skimming mode after the interaction with the interface. As q is increased to 2, the longitudinal skimming oscillations, after the

interaction, become more rapid. When q = 3, the surface-wave is deflected into the first medium. This is a general pattern is borne out for solitons propagating at an angle of incidence of 2°, c.f. Figures 72, 73 and 74 d)-f).

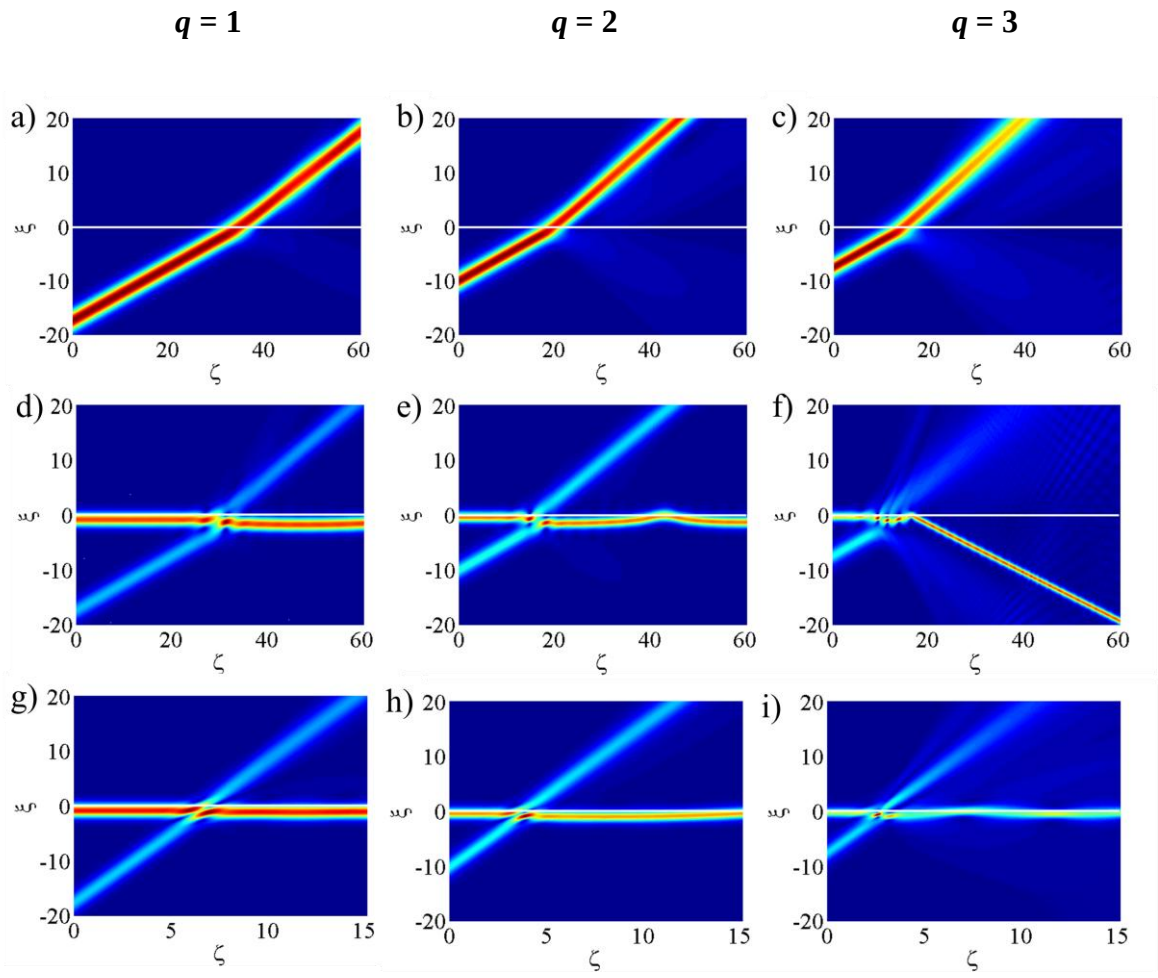

Figure 73. Top row: Soliton interaction with an interface (Δ = -0.0025 and α = 0.75) at the quasi-paraxial incidence angle θ_{inc} = 2° and with $\kappa = 2.5\times10^{-3}$. Middle row: same configuration as the top row, but with a regime 2 surface wave (with $\beta = 1.8\beta_{min}$) travelling along the interface. Bottom row: similar configuration to the middle row, except with a nonparaxial incidence angle of θ_{inc} = 10°.

When inspecting the interactions with solitons propagating at a nonparaxial angle (i.e. the bottom row of Figures 72-75) a skimming mode is present along the interface, after the interaction with the soliton. As q is increased, the longitudinal skimming oscillations become more rapid, which has been seen in a number of the results above. This applies to results in Figures 72-74 g)-i).

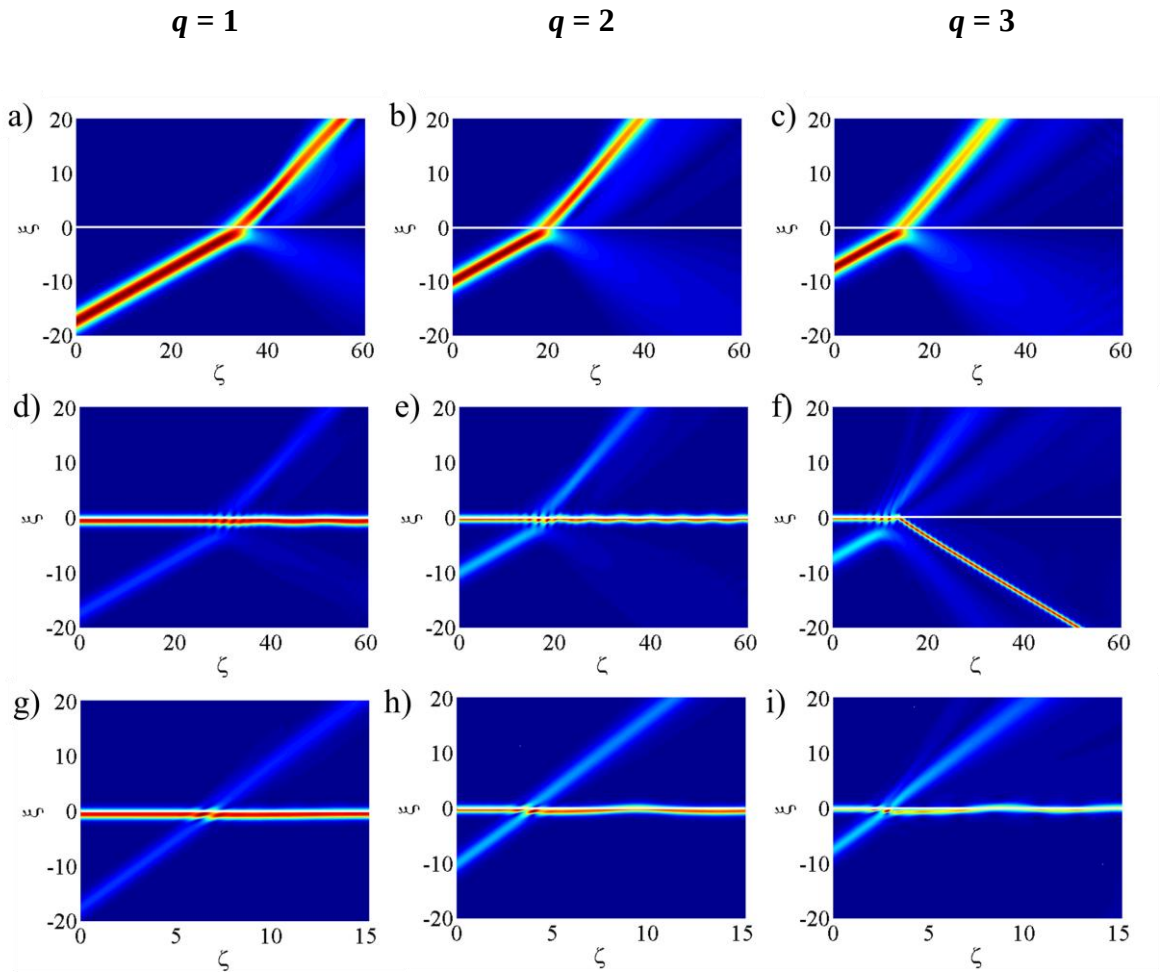

Figure 74. Top row: Soliton interaction with an interface (Δ = -0.005 and α = 0.75) at the quasi-paraxial incidence angle θ_{inc} = 2° and with $\kappa = 2.5\times10^{-3}$. Middle row: same configuration as the top row, but with a regime 2 surface wave (with $\beta = 1.8\beta_{min}$) travelling along the interface. Bottom row: similar configuration to the middle row, except with a nonparaxial incidence angle of θ_{inc} = 10°.

It is noteworthy that the results in Figures 72-74 show no qualitative differences, despite changes to the inverse beam width and to the size of the linear refractive index step. It has been mentioned previously that small changes to any one parameter means significant differences in the input properties of the surface wave. Further work needs to be carried out to in order to find a convincing explanation for this seemingly aberrant behaviour.

q = 1 **q = 2** **q = 3**

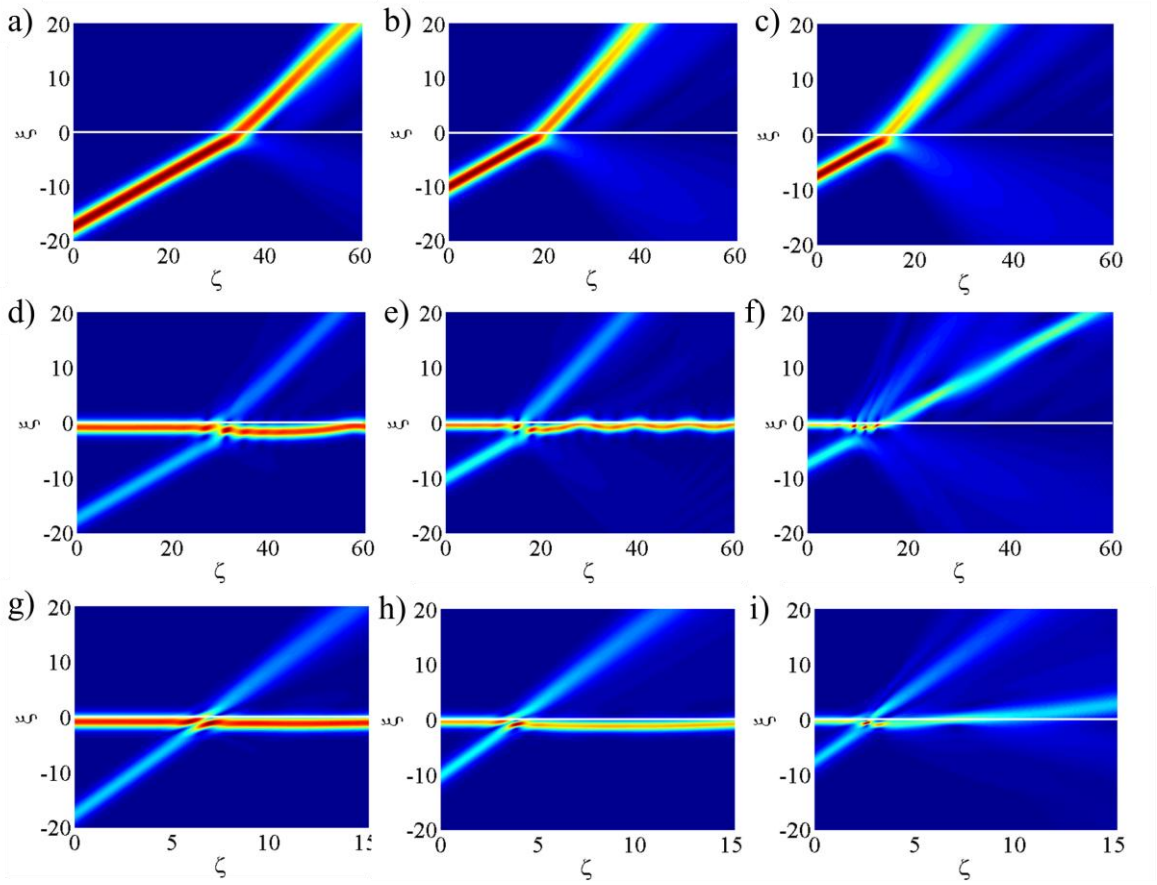

Figure 75. Top row: Soliton interaction with an interface (Δ = -0.005 and α = 0.5) at the quasi-paraxial incidence angle θ_{inc} = 2° and with κ = 2.5×10^{-3}. Middle row: same configuration as the top row, but with a regime 2 surface wave (with β = 1.8β_{min}) travelling along the interface. Bottom row: similar configuration to the middle row, except with a nonparaxial incidence angle of θ_{inc} = 10°.

The results in Figure 75 differ from those shown in the previous three sets of results, but only when q = 3. When the soliton is propagating at a low angles of incidence, the surface wave is deflected into medium 2 rather than medium 1 (compare Figures 74 and 75). At nonparaxial angles, with q = 3, the beam is also deflected into medium 2, where previously a skimming mode could be seen at the interface see Figures 72-74.

4.5 Conclusion

Exact Helmholtz surface wave solutions have, for the first time, been found for interfaces between dissimilar power-law materials. The stability of these surface waves has been tested, and several trends have been identified.

For upper branch surface waves with regime 1 parameters, an instability is always present irrespective of the sign of $dP/d\beta$. The peak of the initial condition in all solutions of this type resides in medium 1, until the solution reaches a state of instability at which point the beam propagates into the second medium. As q increases, the propagation length before the instability decreases, and the broadness of the beams seems to decrease with increasing q. This is much the same for upper branch surface waves in regime 2, except that the peak of the beam remains at the same side of the interface, in medium 2, regardless of the instability. Also, although changing κ has a similar effect for both regimes 1 and 2, the same cannot be said for the effect when changing Δ and α. In regime 1, decreasing Δ increases the distance the beam propagates before becoming unstable, whereas in regime 2 decreasing Δ decreases the distance before the surface wave becomes unstable. Decreasing α in regime 1 decreases the distance the surface wave propagates along the interface before becoming unstable, but decreasing α in regime 2 increases the distance of stable propagation before becoming unstable (the value of β is changed through all these results so it is difficult to say whether the change in propagation length before the instability is directly related to α and Δ).

For lower branch solutions, the surface waves tend to be stable when $dP/d\beta > 0$ and unstable when $dP/d\beta < 0$ (which occurs when β is close to β_{min}). The instability in regime 1 usually appears as oscillations along the interface. The signature of instability in regime 2 is usually the spontaneous deflection of the surface excitation away from the interface (i.e., transformation into an obliquely-propagating soliton-like beam).

Also tested was the stability of lower-branch surface waves against collisions with solitons. For regime 1 and when the angle of incidence is small (2°), the surface waves are always unstable after the interaction. Typically, the surface wave deviates away from the interface entirely, although there are some cases (e.g., for $q = 1$ and $q = 2$) when it oscillates along the interface after the interaction. When the angle of incidence is increased to 10°, the surface-wave solution often oscillates along the interface where $q = 1$. When $q = 2$ all of the examples given in the previous section show that the surface wave is deflected into medium 2 (transforming into a soliton-like beam). When $q = 3$, the surface wave and soliton may merge into a single high-intensity filament propagating obliquely into medium 2. In regime 2 for a soliton propagating with an angle of incidence of 2°, when $q = 1$ and $q = 2$ the surface wave oscillates along the interface after the interaction.

When q = 3 the surface wave always deviates away from the interface after the interaction with the soliton. For larger angles of incidence (10°), as the value of q increases, the surface wave becomes more unstable after the collision.

4.6 References

1. J.M. Christian, E.A. McCoy, G.S. McDonald, J. Sánchez-Curto, and P. Chamorro-Posada *Interaction of Helmholtz bright spatial solitons with power-law optical interfaces.* Journal of Atomic and Molecular Physics, 2012. **2012**, DOI: 137967.
2. N.G. Vakhitov and A.A. Kolokolov, *Stationary solutions of the wave equation in a medium with nonlinearity saturation.* Radiophysics and Quantum Electronics, 1973. **16**(7): p. 783-789.
3. A.B. Aceves, J.V. Moloney, and A.C. Newell, *Theory of light-beam propagation at nonlinear interfaces. I. Equivalent-particle theory for a single interface.* Physical Review A, 1989. **39**(4): p. 1809-1827.
4. J. Mathew, A. Kar, N. Heckenburg, and I. Galbraith, *Time resolved self-defocusing in InSb at room temperature.* IEEE Journal of Quantum Electronics, 1985. **21**(1): p. 94-99.
5. D.S. Chemla, D.A.B. Miller, and P.W. Smith, *Nonlinear optical properties of GaAs/GaAlAs multiple quantum well material: phenomena and applications.* Optical Engineering, 1985. **24**(4): p. 556-564.
6. S.S. Yao, C. Karaguleff, A. Gabel, C. Fortenberry, C.T. Seaton, and G.I. Stegeman, *Ultrafast carrier and grating lifetimes in semiconductor-doped glasses.* Applied Physics Letters, 1985. **46**(9): p. 801-803.
7. D. Mihalache, M. Bertolotti, and C. Sibilia, *Nonlinear wave propagation in planar structures.* Progress in Optics, 1989. **27**(1): p. 229-313.
8. A.W. Snyder and D.J. Mitchell, *Spatial solitons of the power-law nonlinearity.* Opt. Lett., 1993. **18**(2): p. 101-103.
9. J.M. Christian, G.S. McDonald, R.J. Potton, and P. Chamorro-Posada *Helmholtz solitons in power-law optical materials*. Physical Review A, 2007. **76**, DOI: 033834.
10. J.-G. Ma and Z. Chen, *Nonlinear surface waves on the interface of two non-Kerr-like nonlinear media.* IEEE Transactions on Microwave theory and Techniques, 1997. **45**(6): p. 924-930.
11. A.W. Snyder and H.T. Tran, *Surface modes of power law nonlinearities.* Optics Communications, 1992. **98**(4-6): p. 309-312.
12. P. Chamorro-Posada, G.S. McDonald, and G.H.C. New, *Propagation Properties of Nonparaxial Spatial Solitons.* Journal of Modern Optics, 2000. **47**(11): p. 1877-1886.
13. S. Gatz and J. Herrmann, *Soliton propagation in materials with saturable nonlinearity.* Journal of the Optical Society of America B, 1991. **8**(11): p. 2296-2302.

5. Coupled Waveguide Arrays: linear patterning

This chapter is concerned with the refraction and propagation properties of Helmholtz spatial solitons in a coupled waveguide array (CWA). A CWA is a material which has a periodically patterned refractive index. Under investigation in this chapter is the behaviour of solitons moving from a standard Kerr-type material (medium 1) into a CWA (medium 2). The reason for starting with a uniform Kerr material is that there is a need for the soliton shape to be controllable as it reaches the interface. The interface setup can be seen in Figure 76:

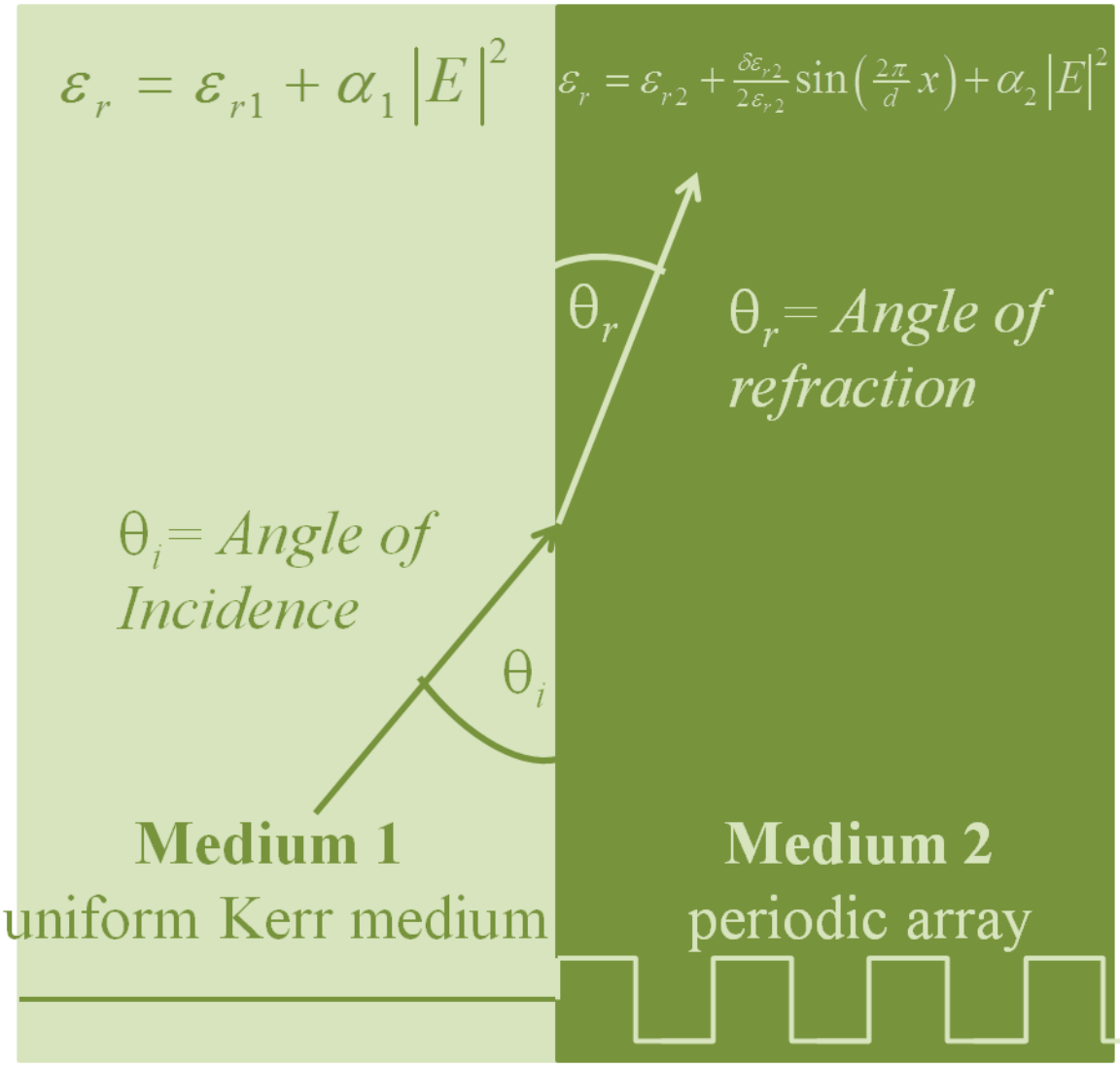

Figure 76 Showing the interface setup considered in this chapter

The use of Helmholtz soliton theory sets this research apart from other related studies involving CWAs [1-3]. One exception is the very recent work by Shi, Guo and Li [4],

who consider a Helmholtz-type model for optical propagation in systems with diffusive nonlinearity. Helmholtz soliton theory's main advantage of allowing beams to propagate at arbitrary angles of incidence with respect to any reference direction, is highly beneficial for modelling geometries of this type. The possibility of accommodating arbitrary angles allows us, in this chapter, to identify a key physical relationship between two fundamental periodic systems seen commonly in the literature (see Figure 77).

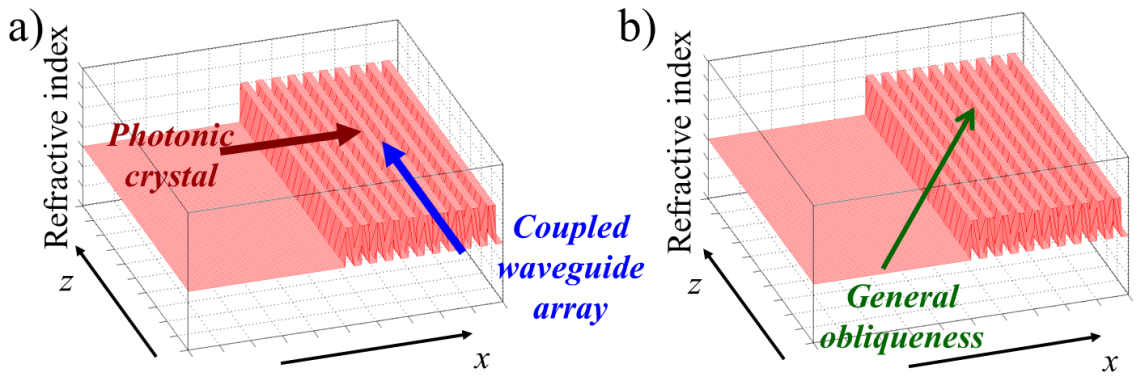

Figure 77 a) Showing the difference in relative orientation between a photonic crystal and a waveguide array. Figure b) Shows how these two separate problems can become one through the use of Helmholtz modelling

Figure 77 shows two distinct interface setups. Due to the inherent angular restrictions of paraxial analyses, these two configurations (photonic crystals and waveguide arrays) have tended to be considered independently of one another. The relaxation of angular restrictions makes for a more general (and powerful) study, wherein a single governing equation can, in principle, capture the full range of angles. Such a prospect clearly opens-up controllability of one of the most important experimental parameters (the angle of incidence).

This chapter is also novel in its approach to investigating the CWA problem. Many previous research papers addressing beam propagation in periodic structures have resorted to discrete analyses [5-10]. The only research using continuous models – which is found in this study – looks at gap solitons and Floquet-Bloch modes [2, 3, 11], rather than the soliton propagation which is of principle interest here.

Following a survey of the limited literature in this area, a derivation of the model equation will be presented. Next, descriptions of the benefits of considering continuous models over there simpler discrete counterparts will be given, as well as discussing the nature of

the beam interaction with the interface (head-on vs. side-coupling geometries). Extensive results from simulations are presented, before conclusions are drawn.

5.1 Literature Review

Three key papers which use continuous methods in analysing beams in CWAs are of most interest [2, 3, 12]. Their approach is similar to that deployed here, although they differ in that Floquet-Bloch modes are their primary focus. Mandelik *et al*. explore the band gap structure of periodic waveguide arrays in linear and nonlinear regimes [12]. This paper gives a clear account of coupled-mode theory, and highlights the difficulties with that method (namely that its results do not necessarily describe excitations in higher bands than band 2). The same authors return to localised waves in CWAs but investigate the behaviour of bright and dark spatial gap solitons [2]. Gap solitons are nonlinear waves propagating in patterned systems whose linear refractive index has a periodic modulation (see [11] for more detailed information on gap solitons), Also discussed in [2] is how the transverse velocity of a beam differs in waveguide arrays from its more traditional continuum analogue. This effect has been taken into consideration in section 5.6. The results presented in [2] compare the propagation of a beam encountering a waveguide array with the same beam in the absence of any interface, thereby highlighting the effect of periodicity and paraxial-type side coupling on transverse velocity. The paper also provides an in-depth discussion of the two different geometries that need to be considered when investigating beam behaviour at CWAs: head-on and side-coupling (this will be expanded upon in the next section).

A paper which is directly related to the research in this chapter is [4]. That work, conducted independently from this thesis, is couched in terms of Helmholtz soliton theory, and involved a governing equation which is similar to model (5.5). Shi *et al*. [4] highlight that the depth of the modulation of the lattice can affect the beam behaviour; the role of modulation depth has been extensively explored this thesis, with results presented in section 5.6. The findings of this thesis confirm what is suggested by Shi *et al*., that by changing the depth of the modulation, qualitative differences can be seen in predicted beam behaviour. A significant difference between the work in [4] and that found in this thesis is Shi et al.'s use of diffusive nonlinearity (i.e. a nonlinearity with a nonlocal response). This study focuses on non-diffusive nonlinearity, and this is along with arbitrary angle considerations is where the novelty of this study can be found.

Lastly, reference [9] has also been a study of interest. This paper discusses some of the fundamental aspects of discrete spatial solitons, and has been used because a detailed description of a CWA has been given, along with more information on coupled mode theory.

5.2 Discrete versus continuous models

There are two main methods for modelling scalar beam propagation in CWAs: *discrete* (where the beams considered are discrete solitons) and *continuous* (where beams may be described by Floquet-Bloch modes).

5.2.1 Discrete

Discrete solitons can be investigated using coupled mode theory. The basis of this approach is the discrete nonlinear Schrödinger equation (or DNLS):

$$i\frac{d\phi_n}{d\zeta} + c\left(\phi_{n+1} - 2\phi_n + \phi_{n-1}\right) + \lambda\left|\phi_n\right|^2\phi_n = 0, \tag{5.1}$$

where c is a coupling constant, $\phi_{n+1} - 2\phi_n + \phi_{n-1}$ is effectively a discrete transverse 1d Laplacian and λ parameterises the strength of the Kerr-type self-interaction. Coupled mode theory describes the longitudinal propagation of the complex amplitude ϕ_n in waveguide channel n. The field in any particular channel is typically subject to evanescent nearest-neighbour liner coupling, since the governing equation for ϕ_n depends on both ϕ_{n+1} and ϕ_{n-1}, see [12-14] and Figure 78:

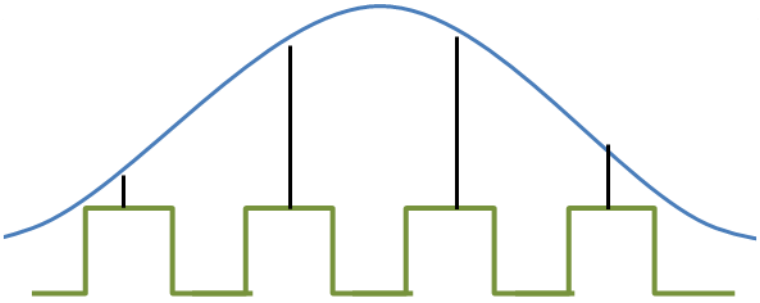

Figure 78 Showing where the amplitudes are calculated from with discrete methods

Collectively, these individual waveguides are considered as a 'supermode'. The information about the field between the gaps comes from the coupling constant *c* (the

contribution from the averaging process) in equation(5.1). A large *c* value means strong overlap and a low *c* value will imply a weak overlap [1].

5.2.2 Continuous

The work presented in this chapter uses a continuous model. Such a method is advantageous because there are no assumptions made as to the character of the field in between the waveguide channels. There are two different analyses that can be made using continuous methods: i) Floquet-Bloch analysis; investigation into band gaps, Floquet-Bloch modes (a solution for an optical wave propagating in a periodic structure), gap solitons and Bragg scattering, see [2, 12] and ii) Helmholtz soliton theory, which leads to an 'averaged Snell's law approach,' the theory for which will be developed in this chapter, see section 5.4 (and see also [4], for a less fulsome account).

5.3 Side-coupling and head-on geometries

Unlike previous chapters, where both materials had uniform refractive index, there are two different geometries in which beams can be excited in the waveguide array. This arises as a result of the 2d nature of the waveguide.

5.3.1 Head-on geometry

The first way to excite beam propagation in the waveguide array, but not considered further here, is to use head-on geometry (see section 5.5 for further discussion as to why this geometry is not investigated). This method can be used to excite a Floquet-Bloch mode at the edge of a band [2], if the beam is spatially shaped to match the beam shape of the desired mode before it enters the waveguide array, see Figure 79, adapted from [2].

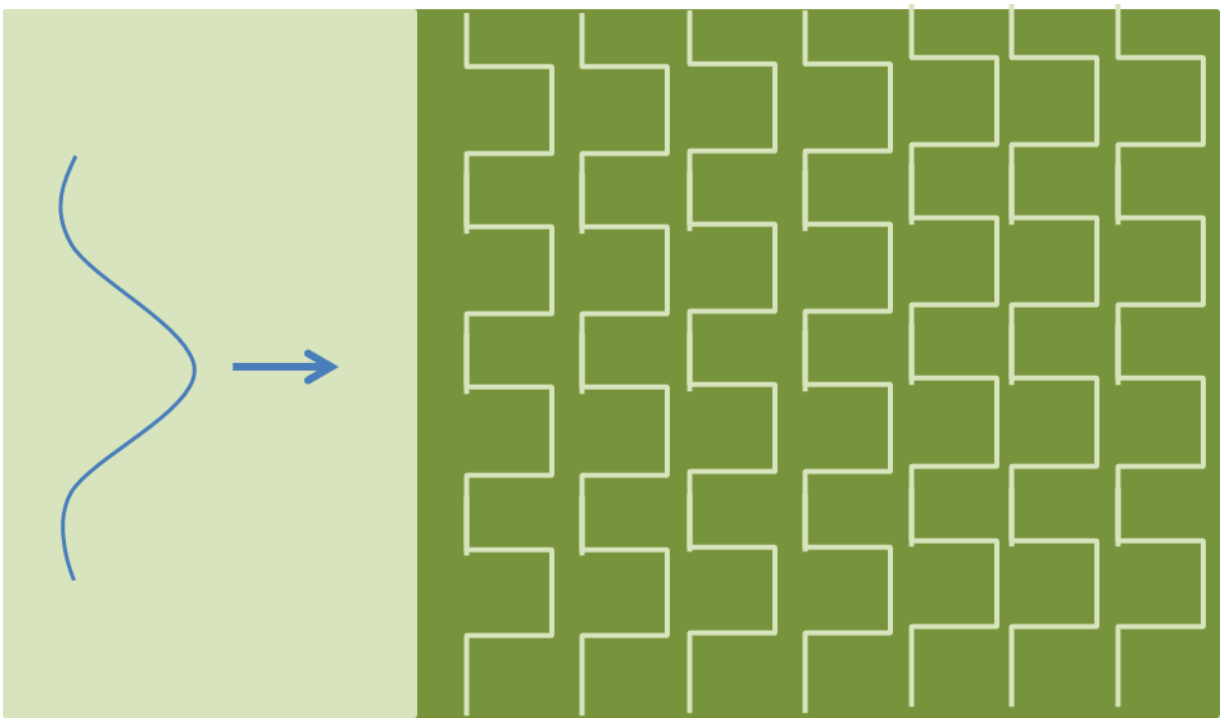

Figure 79 Showing a beam propagating in head-on geometry. This geometry is explored in [2].

It will be shown in 5.5 why this approach is not explored further in this thesis.

5.3.2 Side-Coupling geometry

Side-coupling geometry is used in this study to inject a soliton beam into the array (results of which will be shown in section 5.6). The beam is initiated in medium 1, taken to be a uniform Kerr medium. When the beam interacts with the interface, any light transmitted into the second medium is propagating in the waveguide array. Figure 80 shows the orientation of the array with respect to the continuum, so it can be seen that with this geometry, it is impossible for the beam to interact 'head-on' with the waveguide array, regardless of the beam's angle of incidence (if the beam is propagating at 90° to the waveguide, the channels are the 'wrong way round').

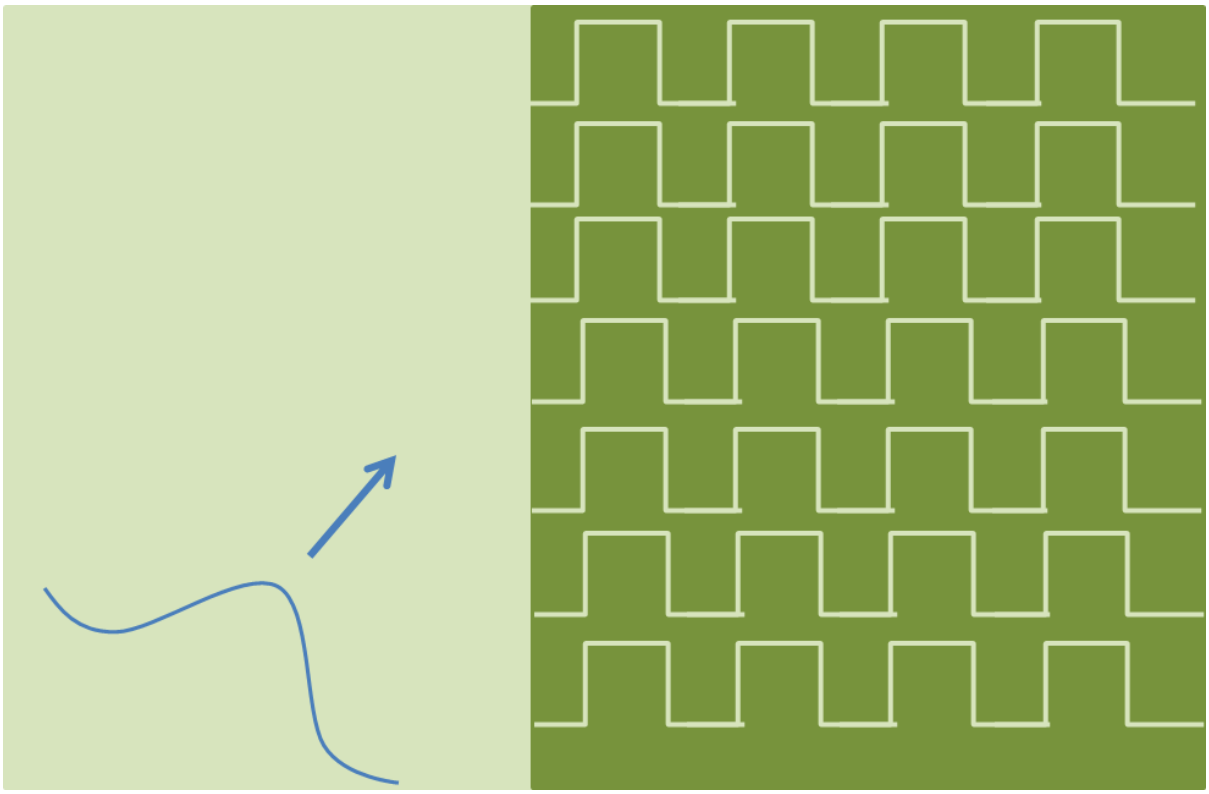

Figure 80 Showing a beam propagating in side-coupling geometry. This geometry is the focus of the investigation in this chapter.

The use of the geometry is further discussed 5.5, with a particular emphasis on how this relates to the results in 5.6.

5.4 Derivation of Helmholtz model equation

The first step when exploring this material geometry (as it has been in all the previous chapters) is to derive the model equation for the interface at hand, shown in Figure 81:

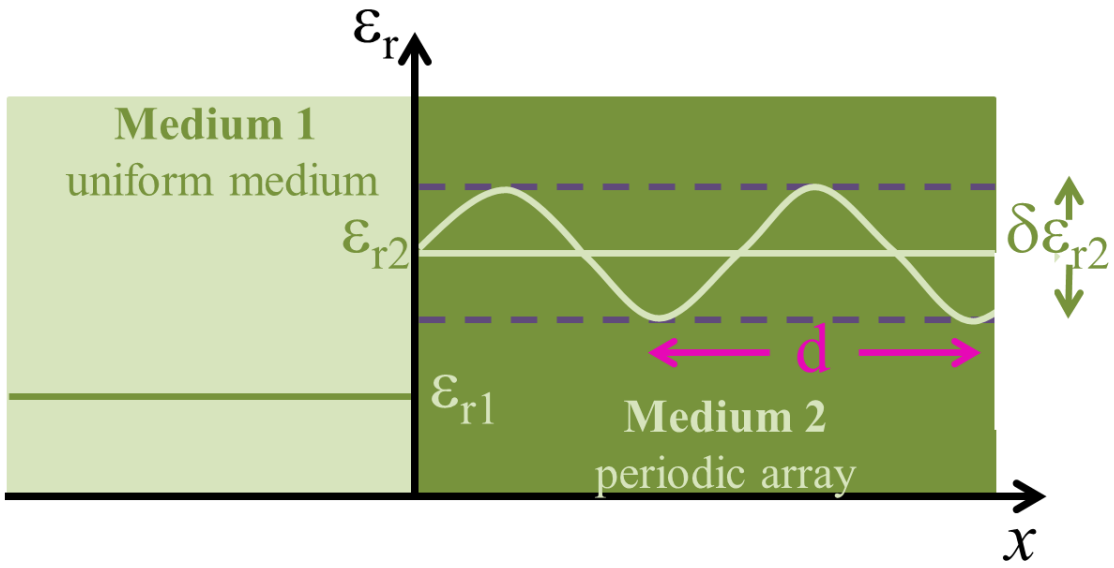

Figure 81 Showing the interface setup that the model equation needs to relate to.

The refractive index n is in terms of the relative permittivity ε_r of the materials, where $\varepsilon_r = n^2$. The permittivity in medium 1 is taken to be:

$$\varepsilon_{r(medium1)} = \varepsilon_{r1} + \alpha_1 |E|^2, \tag{5.2}$$

i.e., that of a standard Kerr material, and in medium 2:

$$\varepsilon_{r(medium2)} = \varepsilon_{r2} + \frac{\delta\varepsilon_{r2}}{2\varepsilon_{r2}} \sin\left(\frac{2\pi}{d}x\right) + \alpha_2 |E|^2, \tag{5.3}$$

where ε_{rj} is the average linear permittivity in the array and α_j the coefficient of the nonlinear contribution to the refractive index (j = 1,2), d is the periodicity of the array (along the x direction) and E is the electric field. As mentioned in section 1.4, the electric field E must satisfy the nonlinear Helmholtz equation on either side of the material boundary:

$$\frac{\partial^2 E}{\partial z^2} + \frac{\partial^2 E}{\partial x^2} + \frac{\omega^2}{c^2}\varepsilon_{rj}(E)E = 0, \tag{5.4}$$

The same method is followed that is seen in Chapter 2, and the full model equation is found to be:

$$\kappa\frac{\partial^2 u}{\partial\zeta^2}+i\frac{\partial u}{\partial\zeta}+\frac{1}{2}\frac{\partial^2 u}{\partial\xi^2}+|u|^2 u=\left[\frac{\Delta}{4\kappa}-\frac{1-\Delta}{8\kappa}\sigma\sin\left(\frac{2\pi}{\Lambda}\xi\right)+(1-\alpha)|u|^2\right]H\xi(u), \qquad (5.5)$$

where Δ = 1-($\varepsilon_{r2}/\varepsilon_{r1}$) is the mismatch in the linear permittivity, $\alpha = \alpha_2/\alpha_1$ is the mismatch in the nonlinear permittivity, $\sigma = \delta\varepsilon_{r2}/\varepsilon_{r2}$ is the relative modulation depth of the linear permittivity in the array and $\Lambda = \sqrt{2}\,d/w_0$ is the period of the array.

For the purposes of computational modelling, equation (5.5) is modified so that the waveguides are square rather than sinusoidal:

$$\kappa\frac{\partial^2 u}{\partial\zeta^2}+i\frac{\partial u}{\partial\zeta}+\frac{1}{2}\frac{\partial^2 u}{\partial\xi^2}+|u|^2 u=\left\{\frac{\Delta}{4\kappa}-\frac{1-\Delta}{8\kappa}\sigma\,\mathrm{sgn}\left[\sin\left(\frac{2\pi}{\Lambda}\xi\right)\right]+(1-\alpha)|u|^2\right\}H\xi(u). \qquad (5.6)$$

Where the sgn term reduces to + or -1 depending on whether $\sin[(2\pi/\Lambda)\xi]$ is positive or negative.

5.5 Computational Considerations

As far as simulating these beams is concerned, only minor alterations are needed to the code (discussed in section 2.3) in order to ensure it captures the physical properties of CWA. The alteration is made to the boundary conditions that governs the refractive index in the second medium, which is done through the use of equation (5.5). This particular refractive index set-up can cause problems if initiated incorrectly, as outlined below.

5.5.1 Geometrical Considerations

In section 2.3, it was noted that the computer simulations must be set up so that the interface is rotated to change the angle of incidence of the beam (this prevents certain computational issues, such as needing dense grid discretisation for accurate solutions). Having the interface at an angle adds extra complications to initiating the CWA in the second medium, this is due to the 2d nature of the waveguide array. Figure 82 shows the interface set-up if the interface was vertical.

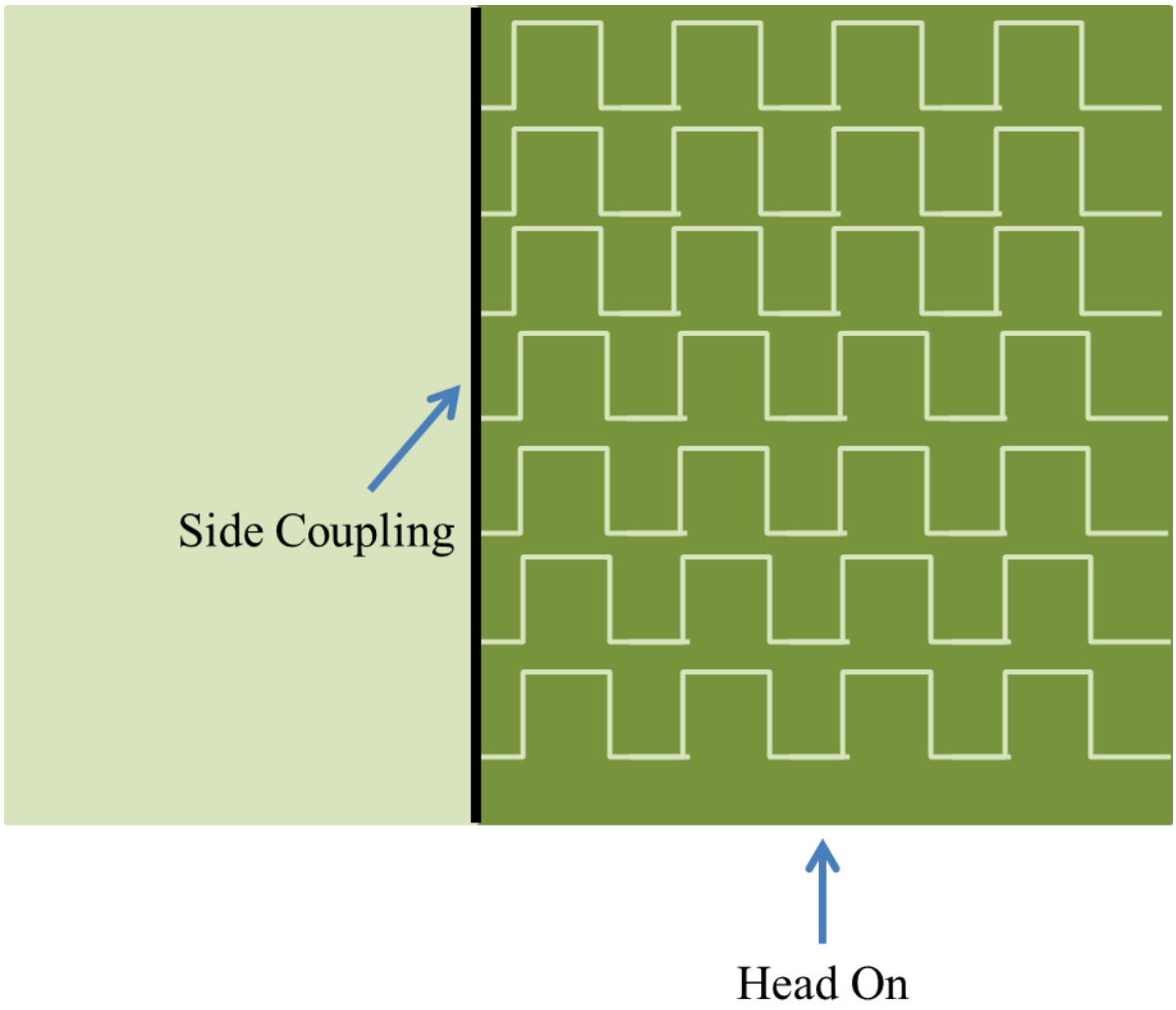

Figure 82 Showing how the computational analysis would be performed if the interface were vertical.

Each step of the refractive index is initiated at the same point, and all the steps 'line up'. However, because the interface is angled, careful consideration has to be made to ensure that the CWA is initiated at the right point at every step in the z direction. The figure below highlights the importance of this:

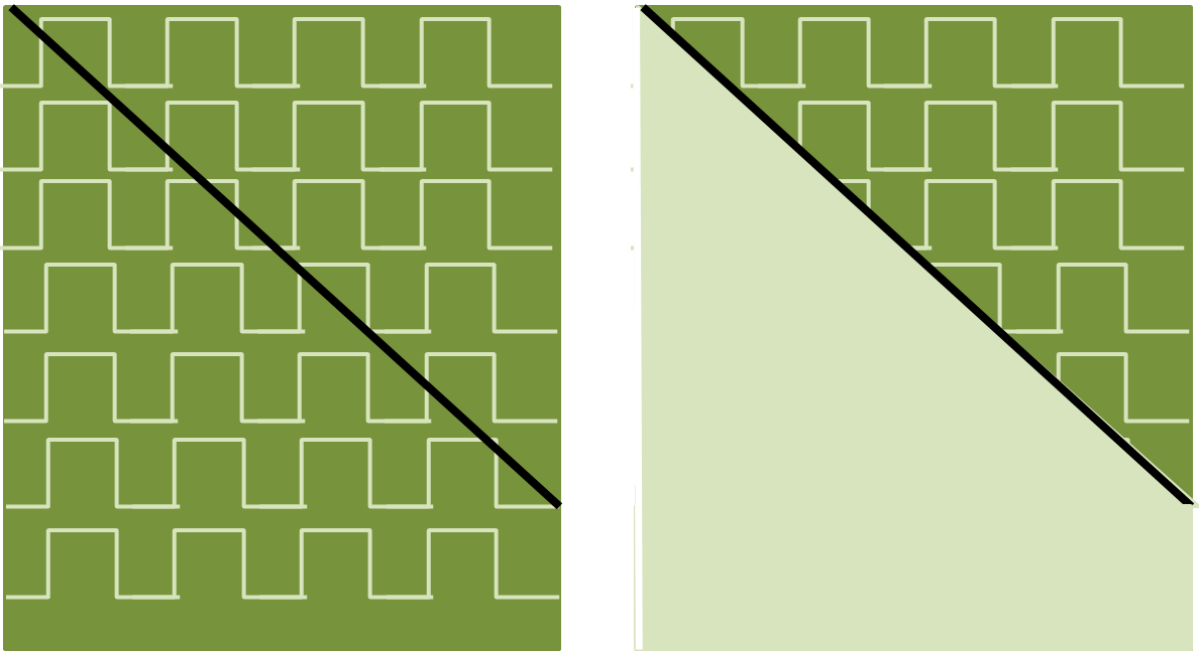

Figure 83 Showing an inappropriate method of simulating the CWA's refractive index.

The CWA must be set up in such a way that the refractive index for each step begins at the same point relative to the interface to prevent the CWA being initiated as in Figure 83. This is important because if the CWA has always been considered with a boundary as in Figure 82, then the CWA should start in the same way when the interface is tilted.

From Figures 82 and 83, we can see that using this particular method of computational analysis, Head-on Geometry cannot be investigated here, because even if the beam heads straight towards the CWA, the interface the beam interacts with is 'tilted' so the whole of the beam won't interact with the CWA in the same way.

5.6 Solitons in linearly-patterned structures

This section presents the results from extensive simulations run on the basis of the theoretical work presented in the previous sections. The difference in behaviour between beams propagating in a nonlinear medium with a periodically patterned refractive index, and those at a single interface Kerr material, will be illustrated. This single interface is created by setting the depth of the modulation to 0 - since a modulation size of 0 is implicit for uniform materials. For clarity, the following parameters are chosen for simulations:

$\kappa \propto (\lambda/w_0)^2$ (*inverse beam width*). Values of κ explored previously are considered again here (namely, 2.5×10^{-3}, 1×10^{-3} and 1.0×10^{-4}); these values respect the inherent inequality for Helmholtz modelling [i.e. that $\kappa << O(1)$].

$\Delta = 1-(\varepsilon_{r2}/\varepsilon_{r1})$ (*mismatch in linear permittivity*). Values of Δ are set as 0.0025 and 0.005. These values are consistent with the Δ values chosen in other chapters of this thesis, and so allow for ease of comparability across the thesis.

$\alpha \equiv \alpha_2/\alpha_1$ (*ratio of cubic nonlinearity coefficients*). Values of α are chosen to be 0.5, 1.0 or 2.0. The two non-unity cases represent a large change in the strength of the focusing properties of the medium across the interface (a halving and doubling).

$\sigma \equiv \delta\varepsilon_{r2}/\varepsilon_{r2}$ (*relative modulation depth*). Values of σ are chosen to be 0, 0.0175, 0.035 or 0.07. 0.07 is chosen to be the highest value because the results become increasingly unstable above this point. When $\sigma = 0$, the interface becomes a dissimilar Kerr interface, and results for this configuration are shown here as a comparison.

η (*peak amplitude of the beam*). η is always 1.

$\Lambda = \sqrt{2}\, d/w_0$ (*period of array*). The value of Λ is 0.6465 for all results shown here.

There are two figures shown for each set of parameters; the first being a 3d plot showing the beam propagation from above. On these figures, the beam can be seen approaching the interface, interacting with the interface, and its behaviour thereafter. The second figure is a plot of the profile of the beam at the last step of the simulation. At this stage the beam has encountered the interface and has propagated some distance into the array. The green lines on these plots are a representation of the linear refractive index (included to highlight the effect the patterning has on the shape of the beam profile).

5.6.1 Linear Interfaces

Firstly, results from a linear interface (α = 1) are considered. For the purposes of this chapter, when the theoretical critical angle, $\theta_{crit(theoretical)}$ is mentioned, it refers to the critical angle predicted by the Snell law between two dissimilar uniform Kerr materials (see ref. [15], i.e with $\sigma = 0$). This is because (as yet) no soliton solutions have been found for the model used is this chapter. The limitations of basing the value of the critical angle on that for dissimilar Kerr interfaces will be discussed in section 5.6.2.

It can be seen from Figures 84-86 that when the angle of incidence of the beam is below $\theta_{crit(theoretical)}$, the beam is reflected by the interface. As the $\theta_{(incidence)}$ is increased beyond $\theta_{crit(theoretical)}$, the beams pass into the waveguide array.

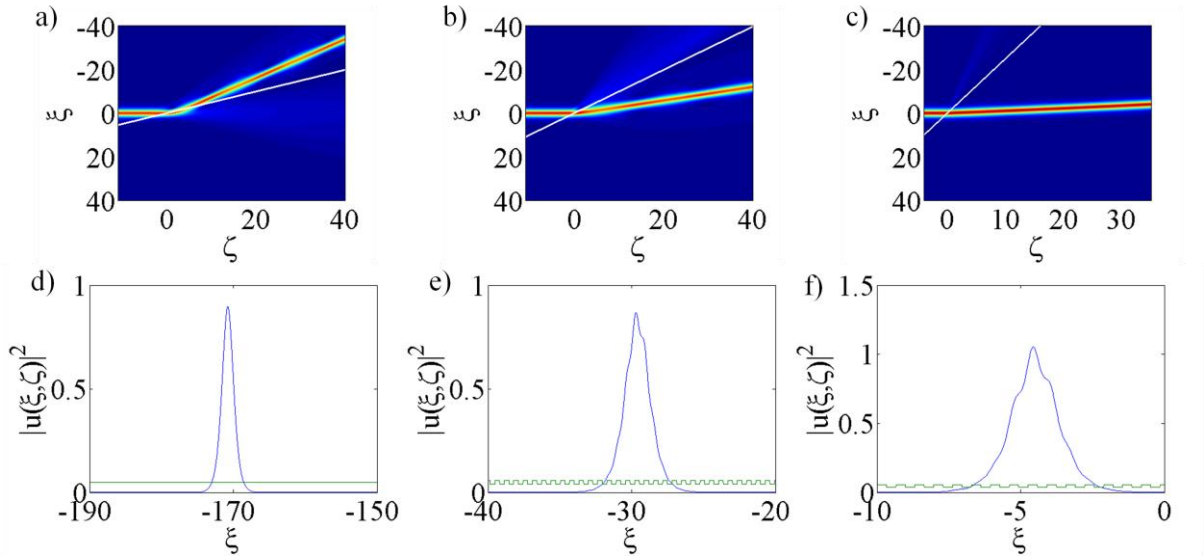

Figure 84 Showing the results for beam propagation in coupled waveguide arrays, where $\kappa = 2.5\text{x}10^{-3}$, $\Delta = 0.0025$, $\sigma = 0.0175$ and a) and d) have $\theta = 2°$, b) and e) $\theta = 4°$ and c) and f) $\theta = 10°$. The theoretical value for $\theta_{crit} = 2.8553°$. The green lines on these plots are a representation of the linear refractive index.

The plots d), e) and f) show the profile of the beam after the interaction with the interface. When the beam is below the critical angle, and therefore reflected by the interface, the profile of the beam remains smooth. When the beam is refracted into the array, the effect of the periodically patterned refractive index can be seen i.e. that the beam intensity drops slightly between each waveguide, causing the beam profile to have a modulated shape, which is a manifestation of the array periodicity.

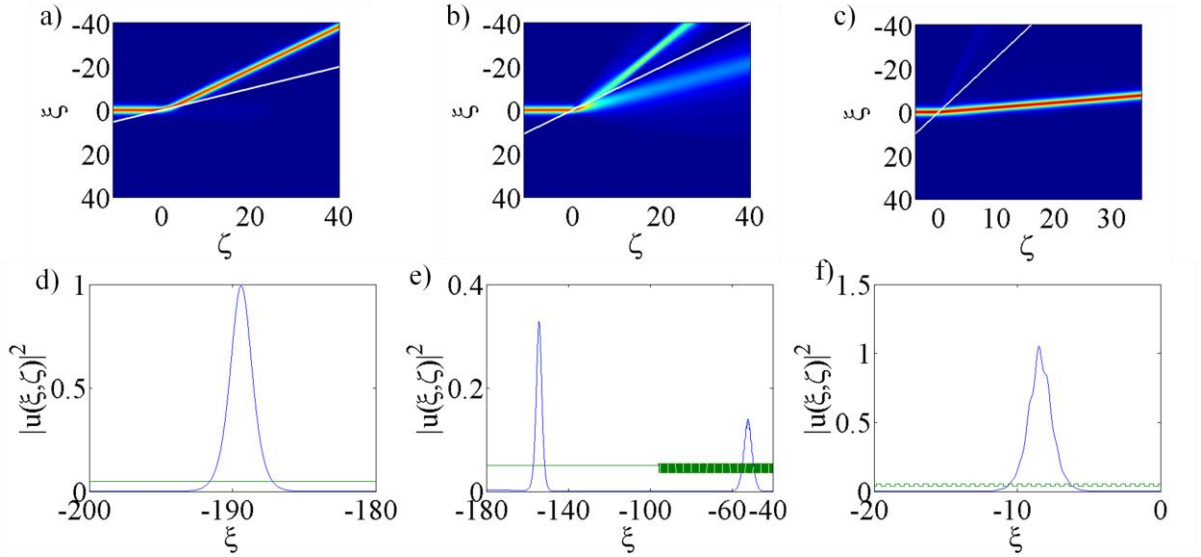

Figure 85 Showing the results for beam propagation in coupled waveguide arrays, where $\kappa = 2.5\text{x}10^{-3}$, $\Delta = 0.005$, $\sigma = 0.0175$ and a) and d) have $\theta = 2°$, b) and e) $\theta = 4°$ and c) and f) $\theta = 10°$. The theoretical value for $\theta_{crit} = 4.0447°$. The green lines on these plots are a representation of the linear refractive index.

When the beam is propagating close to $\theta_{crit(theoretical)}$, see [Figure 85b) and e)], it splits at the interface into reflected and refracted components. The reflected beam retains a smooth profile and the refracted beam acquires a modulation profile which relates to the refractive index periodicity of the CWA.

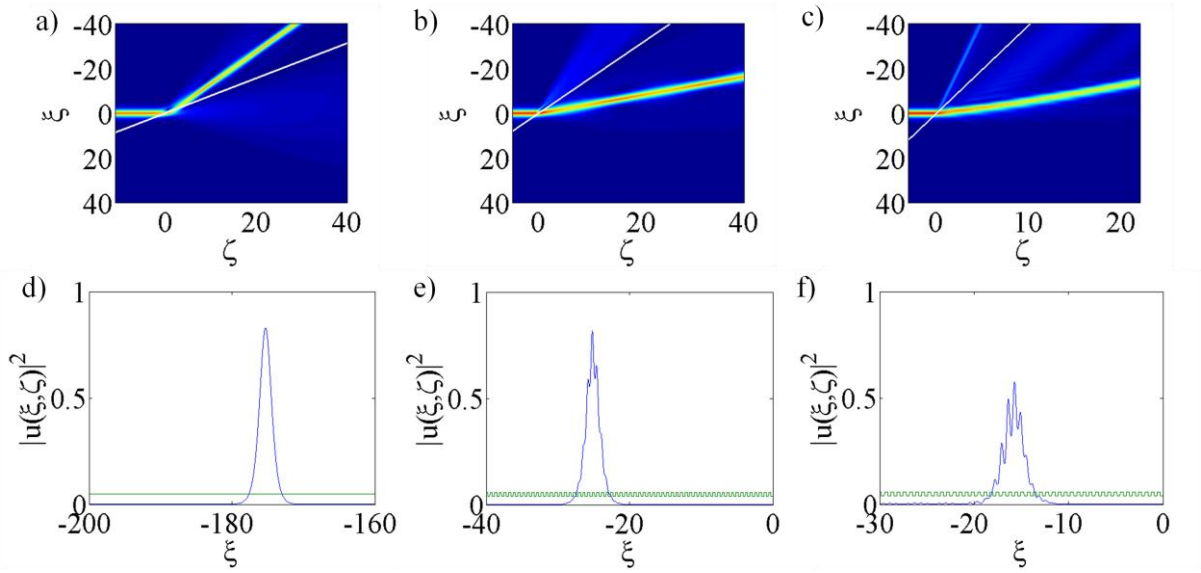

Figure 86 Showing the results for beam propagation in coupled waveguide arrays, where $\kappa = 1\text{x}10^{-3}$, $\Delta = 0.0025$, $\sigma = 0.0175$ and a) and d) have $\theta = 2°$, b) and e) $\theta = 4°$ and c) and f) $\theta = 10°$. The theoretical value for $\theta_{crit} = 2.8638°$. The green lines on these plots are a representation of the linear refractive index.

When κ is decreased to 1 x 10^{-4}, the results become slightly less reliable (as was encountered earlier in Chapter 2, and was described in some detail in section 2.4.1.1). In Figures 87b) and e) the beam is propagating at $\theta_{crit(theoretical)}$ of 4°, which is well above its theoretical critical value of 2.8690°. It would be expected that the beam should penetrate into the second medium, however, this is not the case. It is possible that the nature of the amplitude curvature of solutions in combination with CWA periodicity, is having a strong effect on refraction effects as compared to the single interface problem.

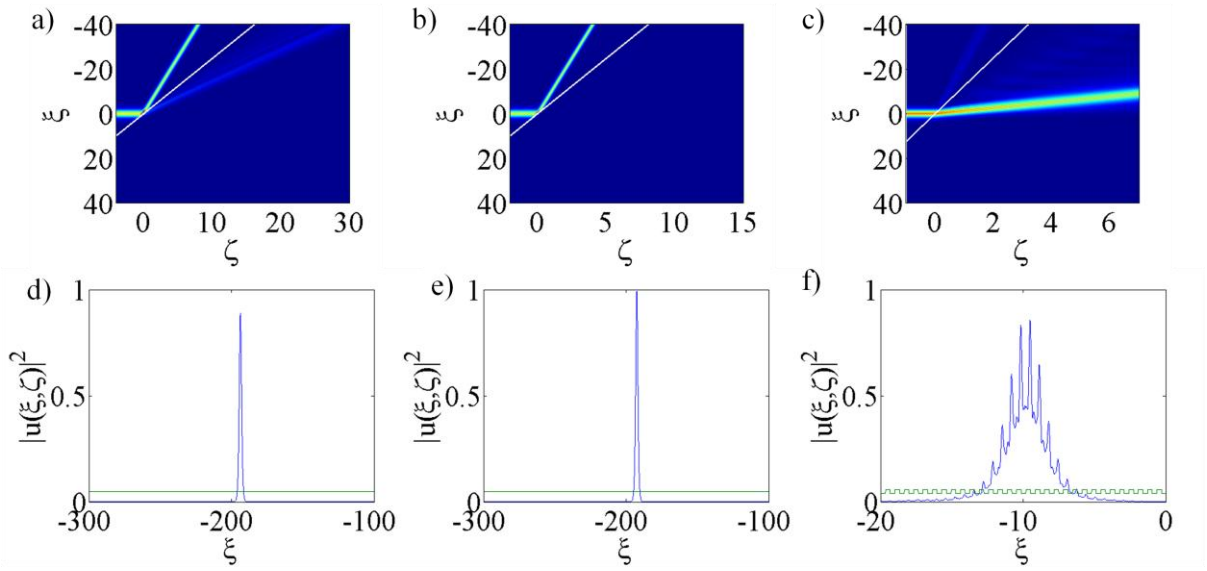

Figure 87 Showing the results for beam propagation in coupled waveguide arrays, where $\kappa = 1x10^{-4}$, $\Delta = 0.0025$, $\sigma = 0.0175$ and a) and d) have $\theta = 2°$, b) and e) $\theta = 4°$ and c) and f) $\theta = 10°$. The theoretical value for $\theta_{crit} = 2.8638°$. The green lines on these plots are a representation of the linear refractive index.

5.6.2 Effect of changing the depth of the modulation

One of the key points of interest in this chapter is how the depth of the modulation (σ) affects the beam propagation. The results shown in this subsection and the next, compare beam propagation for different values of σ, starting with $\sigma = 0$ (which is a standard Kerr material), and then with $\sigma = 0.0175$, 0.035 and 0.07.

The results in Figure 88 all have $\theta_{(incidence)}$ of 10° which is well above $\theta_{crit(theoretical)}$ of 2.8553°, and as a result, there is very little in the way of reflected light. It can also be seen that as σ increases, the shape of the profile of the beam can be strongly affected, when $\sigma = 0$, the beam profile is a smooth 'bell-shape' because the refractive index is uniform. As σ is increased, the modulation depth in the profile becomes increasingly sharp.

In Figure 89, the beams are propagating with $\theta_{(incidence)}$ of 4°, which is close to $\theta_{crit(theoretical)}$. In these results, all the beams split on encountering the interface. As before, when the beam splits, the reflected beam has a smooth profile, whereas the refracted beam acquires a modulation. As σ is increased, more incident light is coupled into the array and the refracted beam has a high degree of self-collimation. This is an interesting result because it leads to the suggestion that changing the depth of the modulation changes the critical angle, which is an idea that has been neglected up to this point (previous analyses have sometimes assumed that the critical angle for the CWA is the same as that at its single interface counterpart, also neglected are the nonparaxial aspects of the coupling). These are matters that will be returned to later in the chapter.

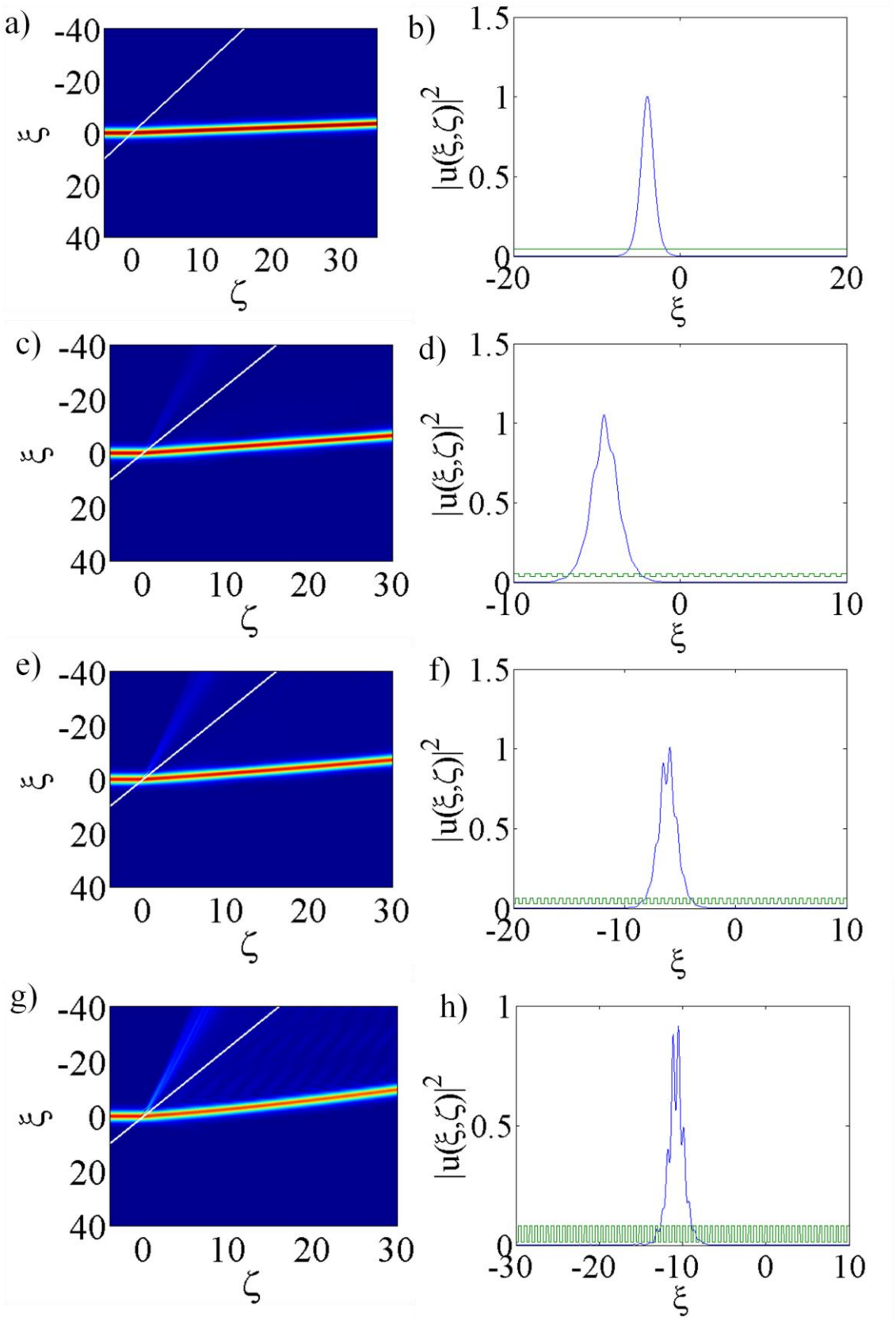

Figure 88 Showing the results for beam propagation in coupled waveguide arrays, where $\kappa = 2.5\text{x}10^{-3}$, $\Delta = 0.0025$, $\theta = 10°$ and a) and b) have $\sigma = 0$, c) and d) $\sigma = 0.0175$, e) and f) $\sigma = 0.035$ and g) and h) $\sigma = 0.07$. The green lines on these plots are a representation of the linear refractive index.

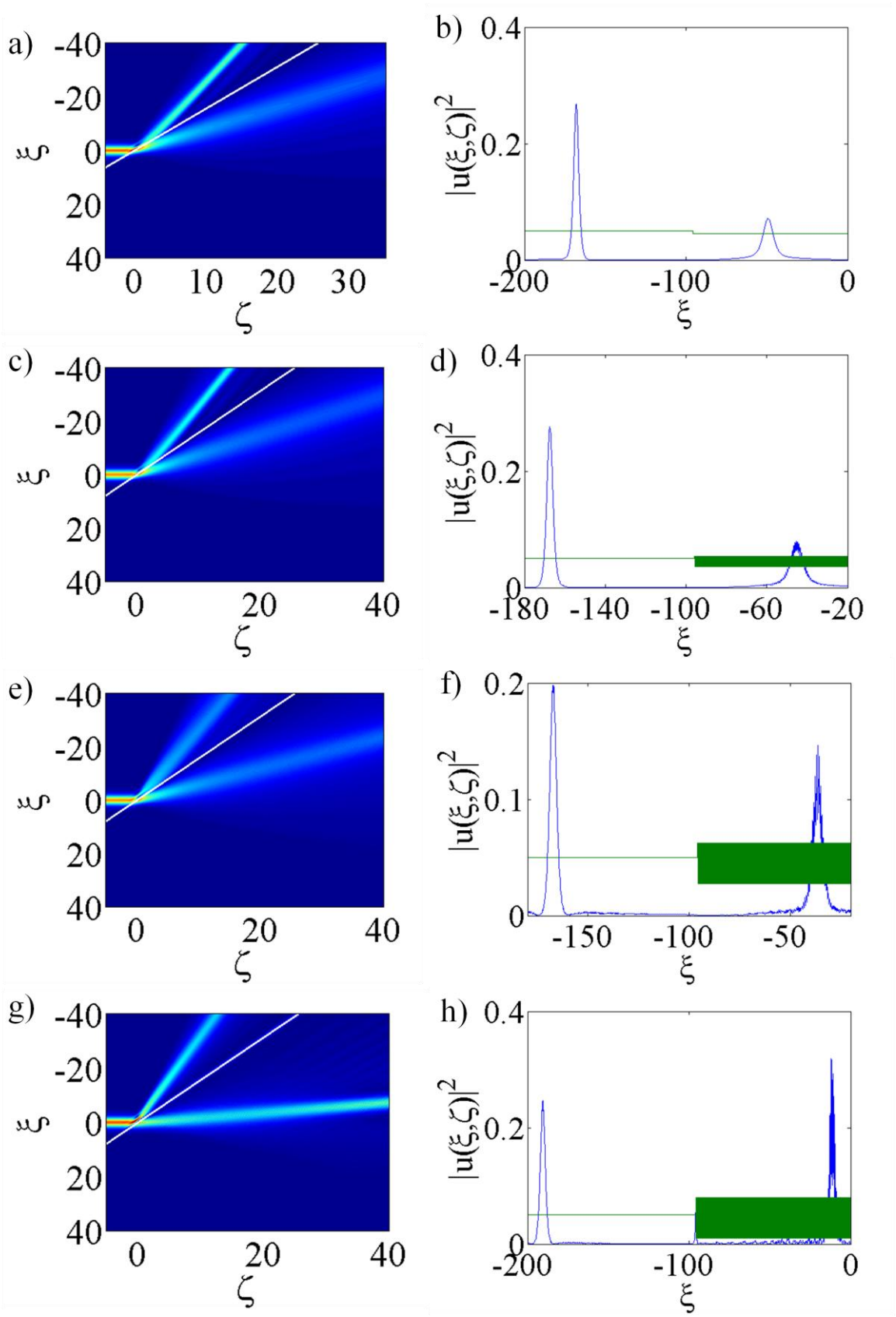

Figure 89 Showing the results for beam propagation in coupled waveguide arrays, where $\kappa = 1x10^{-3}$, $\Delta = 0.005$, $\theta = 4°$ and a) and b) have $\sigma = 0$, c) and d) $\sigma = 0.0175$, e) and f) $\sigma = 0.035$ and g) and h) $\sigma = 0.07$. The green lines on these plots are a representation of the linear refractive index.

5.6.3 Near Critical-Angle Regimes

The investigation now considers beams propagating in near critical-angle regimes, with a view to providing further evidence for the hypothesis that the depth of the modulation does affect the critical angle of the beam. The beams have $\theta_{(incidence)} = \theta_{crit(theoretical)}$, and the only parameter which is varied is σ i.e. the variable governing the depth of the modulations in the CWA. Figure 90 shows the results for a beam with $\theta_{crit(theoretical)}$ of 2.8553°. Figures a)-e) show that as σ is increased, the beam gets increasingly close to its actual critical angle, as the main component of the beam (the reflected component) gets closer toward travelling along the interface (c.f. chapter 3). Figures g) and h) show the beam splitting into three components: one that propagates along the interface (at least up until $\zeta = 35$), reflected radiation and refracted radiation. This is again closer to the actual critical angle than those with lower σ values, so the results in Figure 90 suggest that by increasing σ the beams propagate closer to their actual critical angle, and therefore changing σ changes the actual critical angle associated with the parameters.

In Figure 91, the actual critical angle seems to be slightly below $\theta_{crit(theoretical)} = \theta_{(incidence)}$, since the majority of the beam is transmitted into the array. As σ is increased, it appears that despite the refracted beam getting weaker, the refraction angle increases and so the angle of incidence is further away from the actual critical angle when $\sigma = 0.07$ [Figure 91 g) and h)] than $\sigma = 0$ [Figure 91 a)and b)].

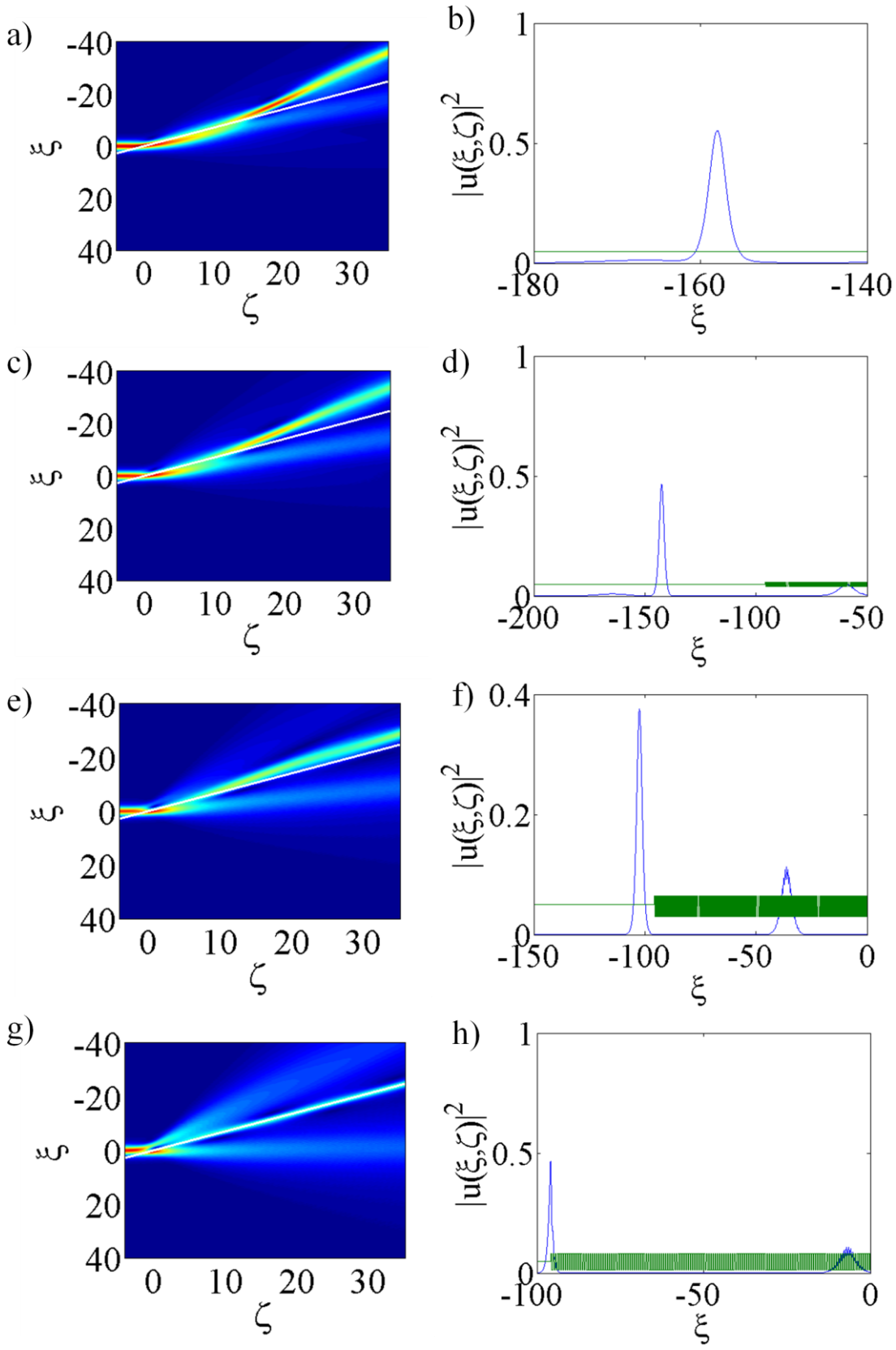

Figure 90 Showing the results for beam propagation in coupled waveguide arrays, where $\kappa = 2.5\text{x}10^{-3}$, $\Delta = 0.0025$, $\theta = 2.8553°$ and a) and b) have $\sigma = 0$, c) and d) $\sigma = 0.0175$, e) and f) $\sigma = 0.035$ and g) and h) $\sigma = 0.07$. The green lines on these plots are a representation of the linear refractive index.

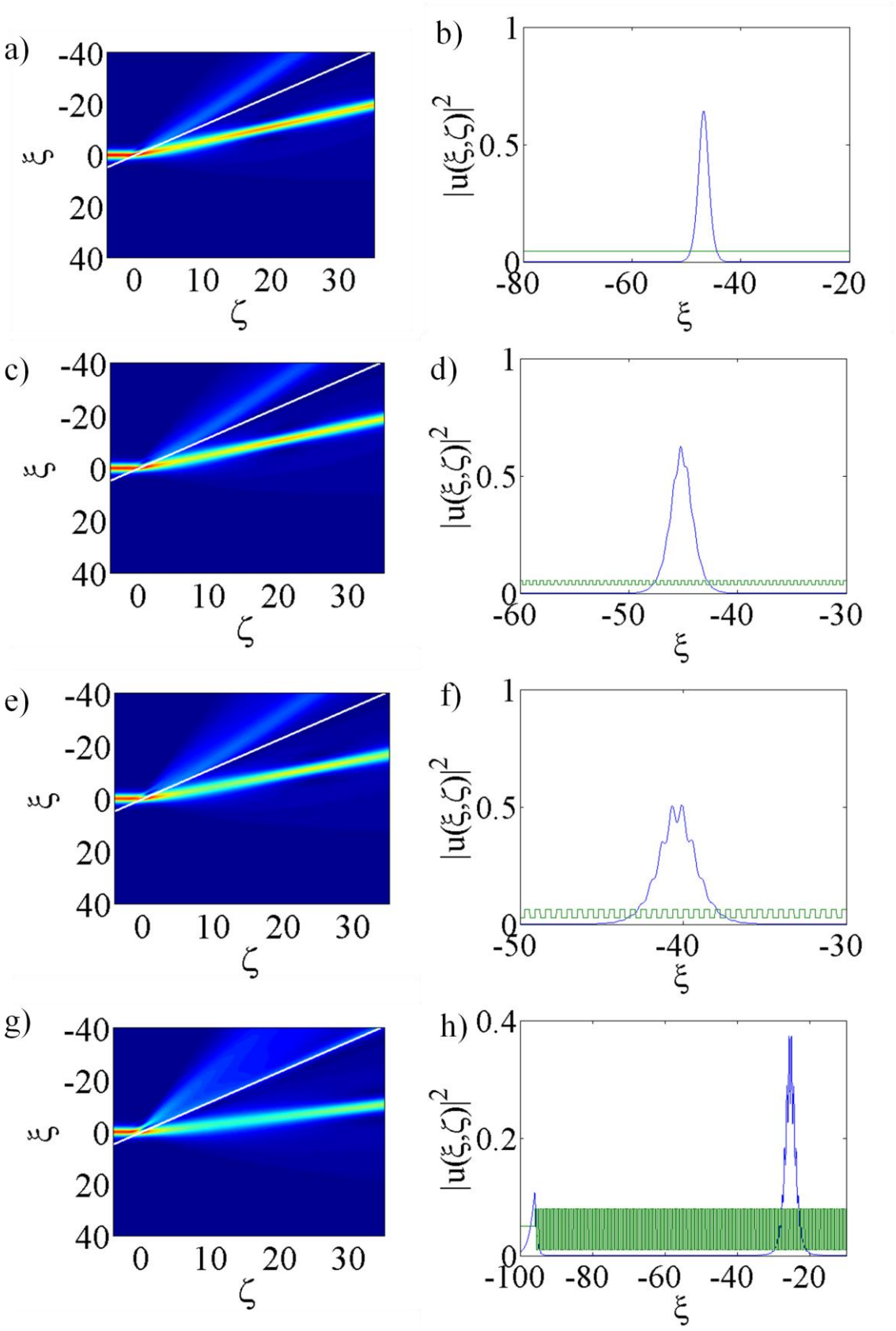

Figure 91 Showing the results for beam propagation in coupled waveguide arrays, where $\kappa = 2.5\text{x}10^{-3}$, $\Delta = 0.005$, $\theta = 4.70447°$ and a) and b) have $\sigma = 0$, c) and d) $\sigma = 0.0175$, e) and f) $\sigma = 0.035$ and g) and h) $\sigma = 0.07$. The green lines on these plots are a representation of the linear refractive index.

5.6.4 Mixed Interfaces

The results for mixed interfaces ($\alpha \neq 1$ and $\Delta \neq 0$) will be presented here, and in particular, two values of α will be considered ($\alpha = 0.5$ and $\alpha = 2$). These values have been chosen in order to allow for comparability with previous chapters.

First to be considered are cases where $\alpha = 0.5$. In Figure 92 the angle of incidence is 10°, which is again well above $\theta_{crit(theoretical)}$. As a result, all the figures show beams propagating into the CWA. As has been mentioned previously, by increasing the depth of the modulation of the array, the depth of the modulation of the beam profile also increases. When σ is at its largest ($\sigma = 0.07$), the beam in the CWA is much narrower and has a much higher intensity than for the other values of σ.

Figure 93 shows the same parameters as Figure 92, but the angle of incidence is chosen to be $\theta_{crit(theoretical)} = \theta_{(incidence)} = 4.0447°$. For all four of the results, the beam splits on encountering the interface. These results show that as σ is increased to 0.07, the beam gets closer to its actual value for the critical angle (as σ is increased, the reflected beam has a smaller angle of reflection, and when $\sigma = 0.07$, the dominant part of the beam propagates along the interface).

Figure 94 has $\alpha = 2$ and an angle of incidence of 2°. The refraction in these figures is external (i.e. the refracted beam deviates away from the interface). From the beam profile figures, it can be seen that the modulations in the beam profile which are associated with propagation in a CWA, are much smaller than those seen when $\alpha = 0.5$, or at linear interfaces. From the figure, it seems as if the CWA hardly has an effect on the beam profile at all. When $\sigma = 0.07$, part of the beam 'snakes' along the interface, which is unexpected as no critical angle exists for these parameters.

Figure 95 has the same parameters as Figure 94, apart from Δ which has doubled from 0.0025 to 0.005. This figure gives the greatest evidence yet that by varying the depth of the modulations of the CWA, the actual value for the critical angle changes. In Figures 95a) and c), the beam refracts into the CWA (and as with Figure 94, the modulations in the beam profile are much less predominant than when $\alpha = 0.5$, and at linear interfaces). As the depth of the modulations is increased to $\sigma = 0.035$ in Figures 95e) and f), the dominant

component of the solution propagates along the interface (at least up to $\zeta = 30$), and when σ is increased again to 0.07, the beam is reflected by the interface in Figures 95g) and h).

Figure 96 show results for a smaller κ (κ = 1 x 10^{-3}) compared with results shown in Figures 92-95 (where κ was consistently set at 2.5 x 10^{-3}). Here it can be seen that all the beams transmit into the CWA. The angle of incidence of the beam is 4°, which is higher than $\theta_{crit(theoretical)}$ = 1.2790°. Again, the refraction is internal. Inside the CWA [i.e. Figures 96c), e) and g)], the beam propagates in a curved path. This is something that has often been seen in the results at mixed interfaces, but only when $\alpha = 2$.

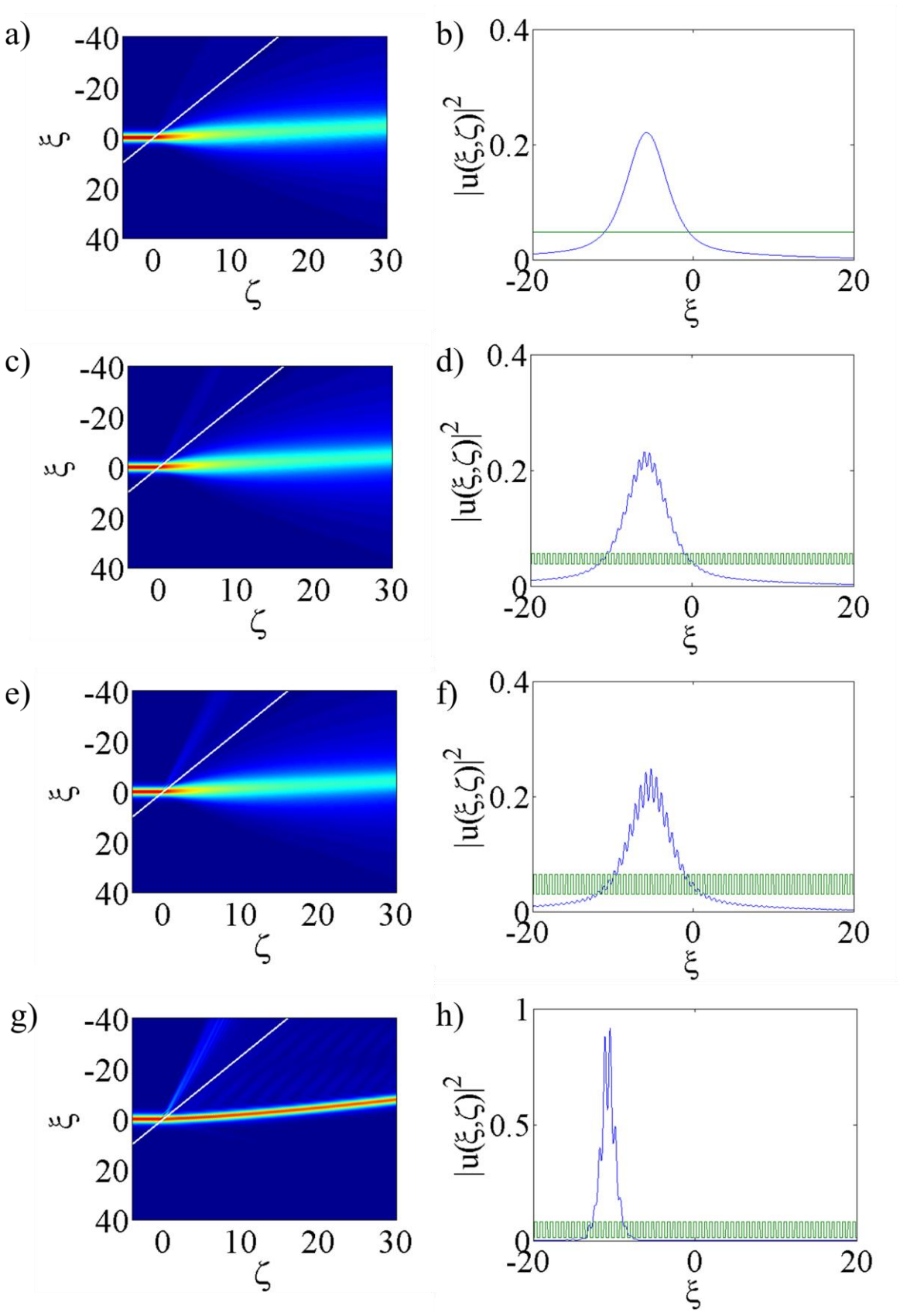

Figure 92 Showing the results for beam propagation in coupled waveguide arrays, where $\kappa = 2.5\times10^{-3}$, $\Delta = 0.0025$, $\alpha = 0.5$, $\theta = 10°$ and a) and b) have $\sigma = 0$, c) and d) $\sigma = 0.0175$, e) and f) $\sigma = 0.035$ and g) and h) $\sigma = 0.07$. The green lines on these plots are a representation of the linear refractive index.

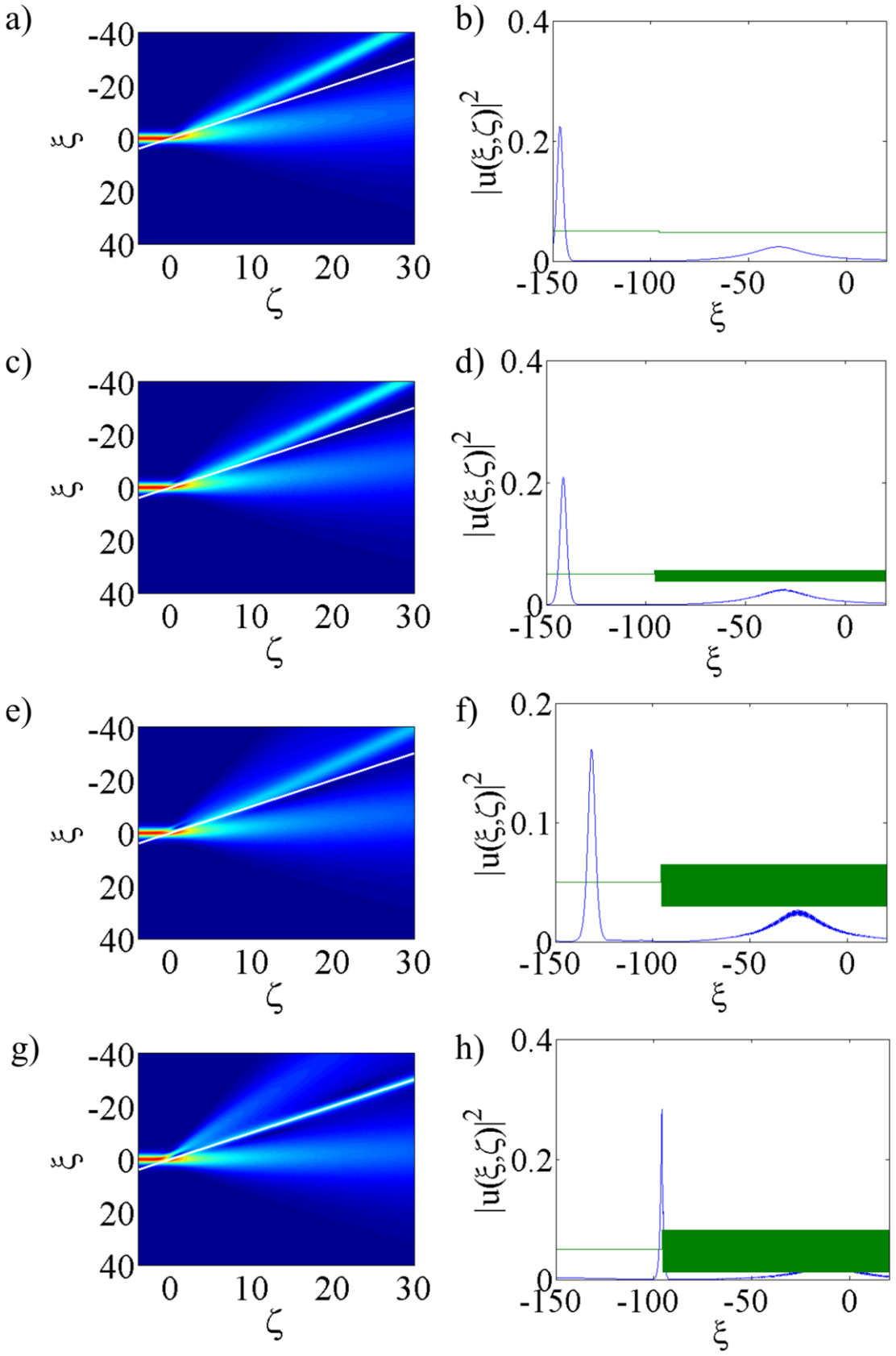

Figure 93 Showing the results for beam propagation in coupled waveguide arrays, where $\kappa = 2.5\text{x}10^{-3}$, $\Delta = 0.0025$, $\alpha = 0.5$, $\theta = 4.04469°$ and a) and b) have $\sigma = 0$, c) and d) $\sigma = 0.0175$, e) and f) $\sigma = 0.035$ and g) and h) $\sigma = 0.07$. The green lines on these plots are a representation of the linear refractive index.

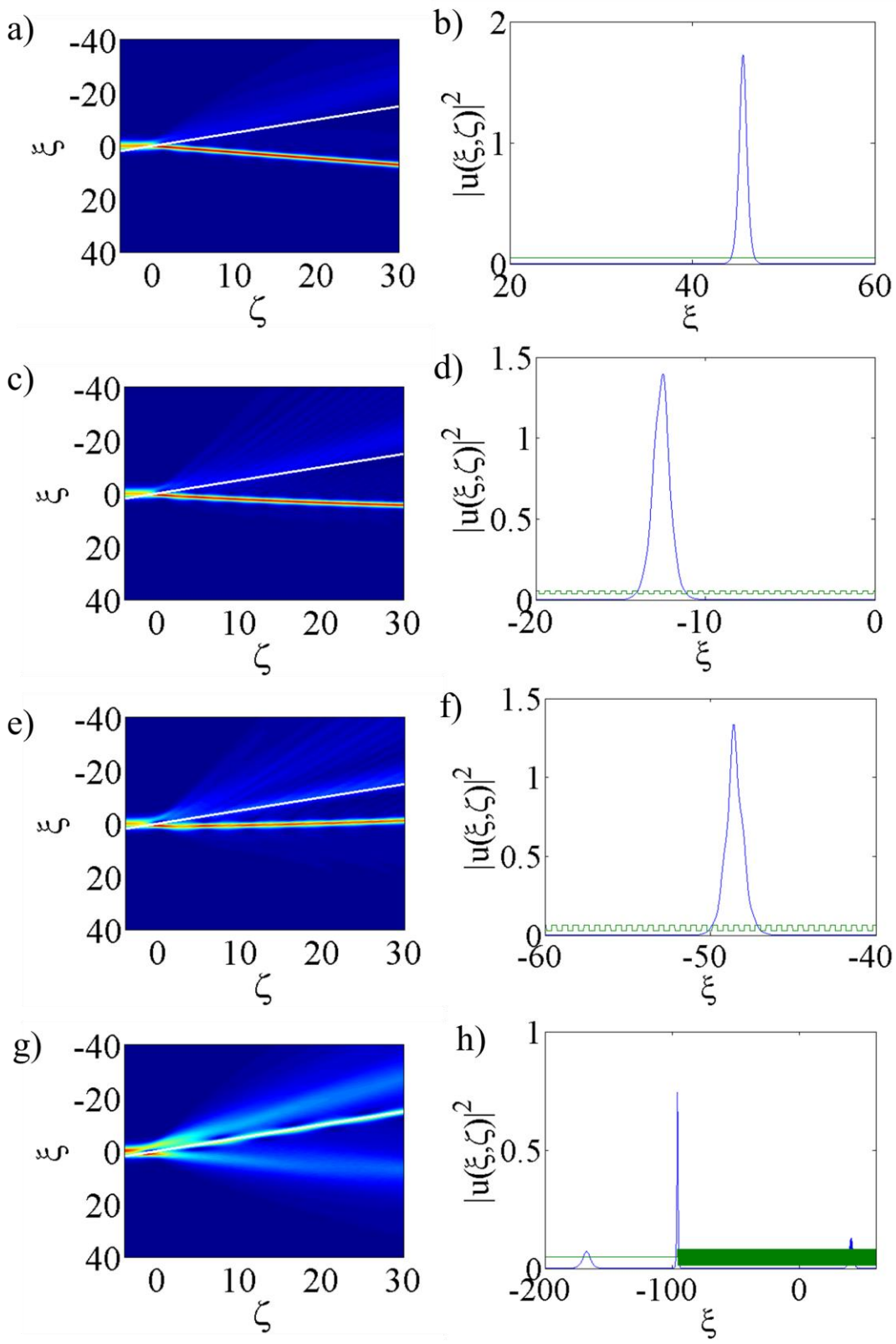

Figure 94 Showing the results for beam propagation in coupled waveguide arrays, where $\kappa = 2.5\text{x}10^{-3}$, $\Delta = 0.0025$, $\alpha = 2.0$, $\theta = 2°$ and a) and b) have $\sigma = 0$, c) and d) $\sigma = 0.0175$, e) and f) $\sigma = 0.035$ and g) and h) $\sigma = 0.07$. The green lines on these plots are a representation of the linear refractive index.

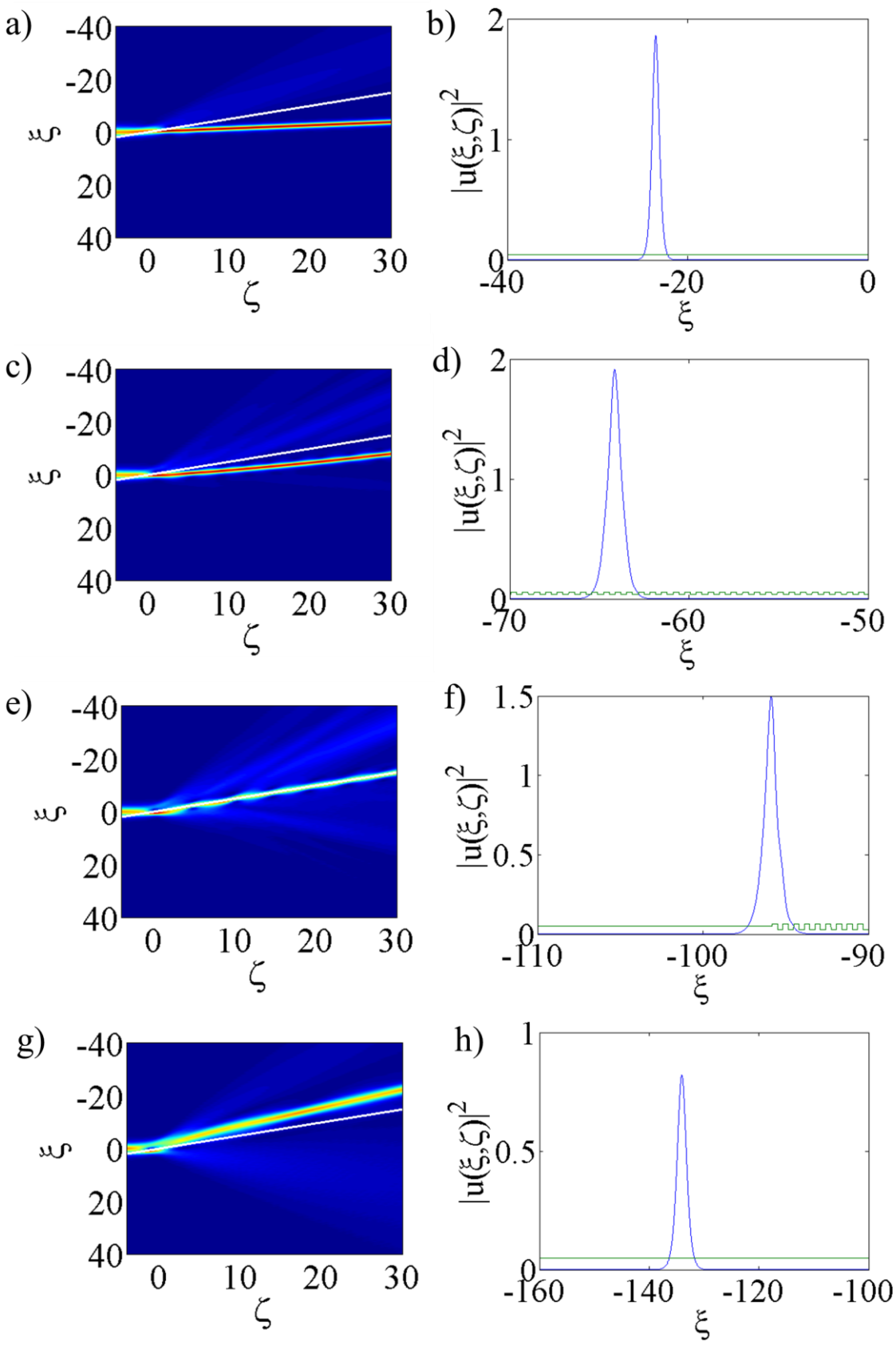

Figure 95 Showing the results for beam propagation in coupled waveguide arrays, where $\kappa = 2.5\text{x}10^{-3}$, $\Delta = 0.005$, $\alpha = 2.0$, $\theta = 2°$ and a) and b) have $\sigma = 0$, c) and d) $\sigma = 0.0175$, e) and f) $\sigma = 0.035$ and g) and h) $\sigma = 0.07$. The green lines on these plots are a representation of the linear refractive index.

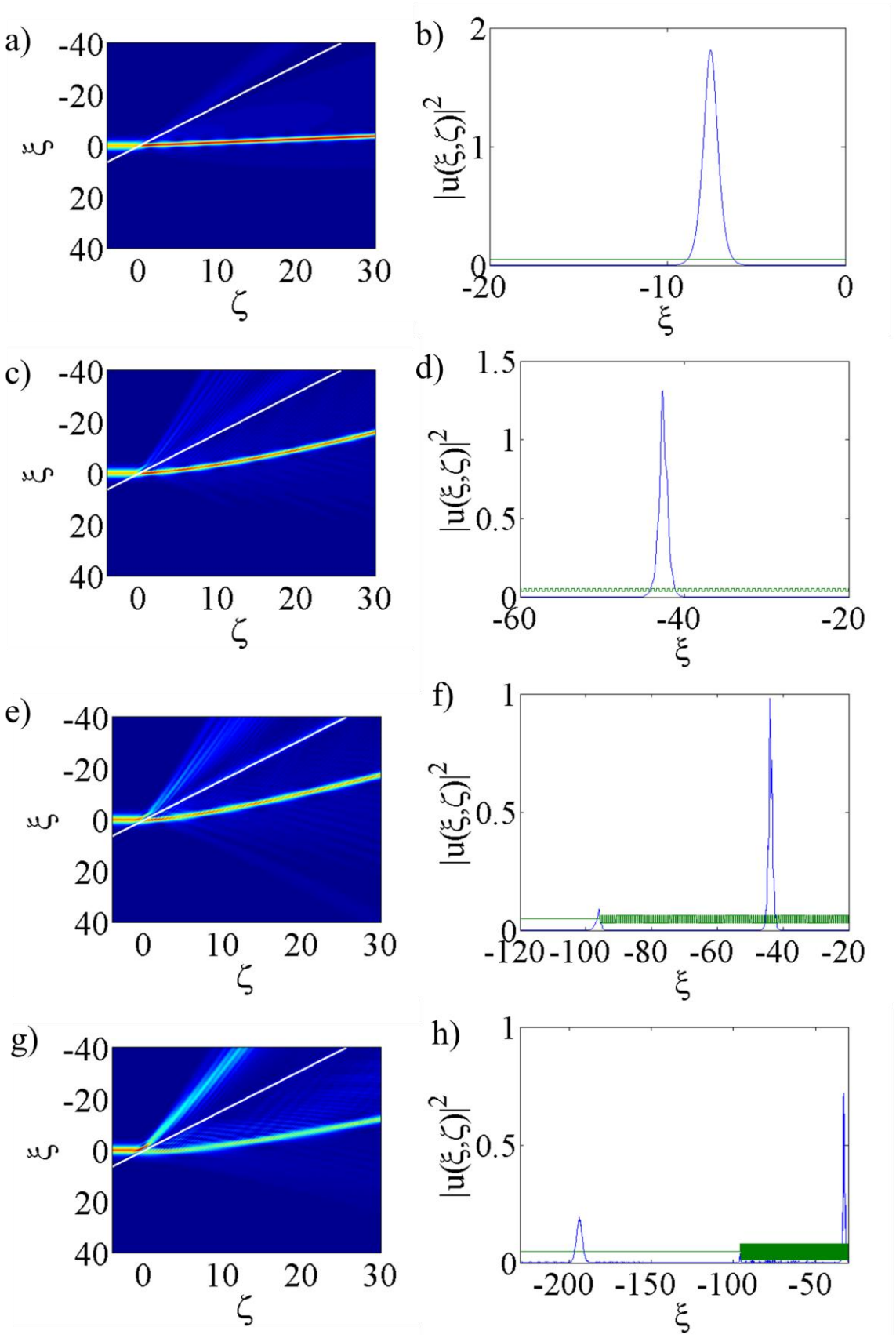

Figure 96 Showing the results for beam propagation in coupled waveguide arrays, where $\kappa = 1x10^{-3}$, $\Delta = 0.0025$, $\alpha = 2.0$, $\theta = 4°$ and a) and b) have $\sigma = 0$, c) and d) $\sigma = 0.0175$, e) and f) $\sigma = 0.035$ and g) and h) $\sigma = 0.07$. The green lines on these plots are a representation of the linear refractive index.

5.6.5 Nonlinear Interfaces

This section will explore results at nonlinear interfaces (i.e. where $\Delta = 0$ and $\alpha \neq 1$). When $\Delta = 0$, the linear permittivities are the same on either side of the interface, though the periodicity still remains.

Figure 97 shows results when $\alpha = 0.5$ and $\theta_{inc} = 2°$. $\theta_{crit(theoretical)} = 2.8553°$, and one can immediately see that θ_{inc} is close to $\theta_{crit(actual)}$ from the simulations presented. Figure a) has $\sigma = 0$ and the beam is reflected by the interface, after shifting along it. As σ is increased to 0.0175, the beam becomes trapped by the interface and propagates along it for a distance (at least greater than the simulation length). Further increases of σ to 0.035 and 0.07 show the beam beginning to form reflected and refracted components, and these increase in amplitude.

Both Figures 98 and 99 show results for $\alpha = 2$, neither of which have critical angles. Figure 98 shows external refraction. Figure 98g) ($\sigma = 0.07$) shows that the beam appears to be approaching θ_{crit} (although it has just been mentioned that according to the Snell's law, no critical angle exists). The beam splits into three components; one of which becomes trapped by the interface, which is behaviour associated with beams propagating close to θ_{crit}. This unusual behaviour occurs solely as a result of the CWA.

For Figure 99a), when $\sigma = 0$ (a uniform material) the refraction appears to be external. As σ is increased to 0.0175 (so that medium 2 is a CWA) the path of beam propagation becomes curved, and it becomes difficult to assess whether the refraction is internal or external. As σ increases, the path of the beam becomes increasingly curved, and deviates towards the interface more. The modulations in the beam profile also increase as σ is increased. As well as this, radiation is reflected by the interface. This behaviour should not be seen in external regimes, and is related solely to the CWA.

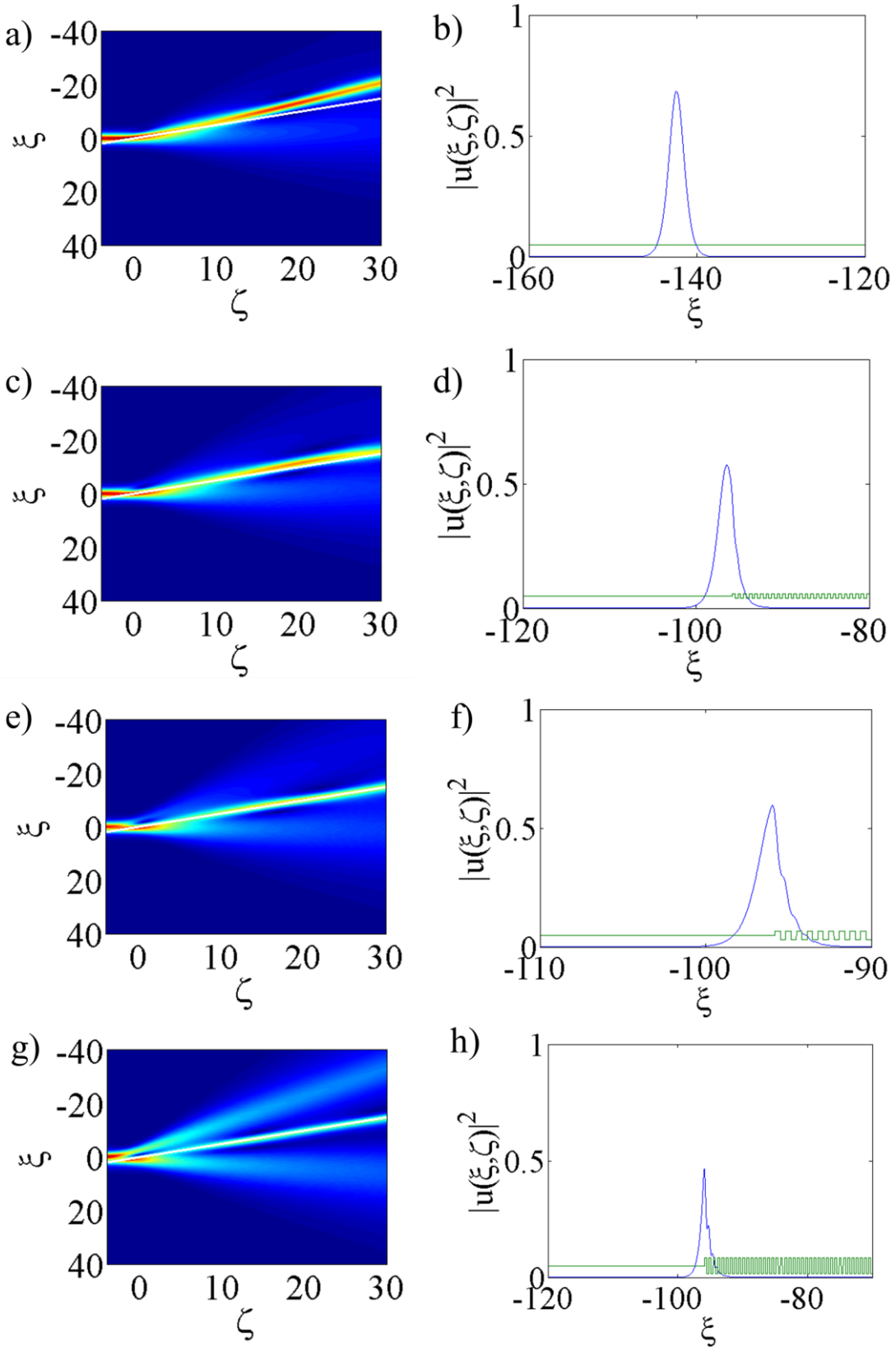

Figure 97 Showing the results for beam propagation in coupled waveguide arrays, where $\kappa = 2.5\text{x}10^{-3}$, $\Delta = 0$, $\alpha = 0.5$, $\theta = 2°$ and a) and b) have $\sigma = 0$, c) and d) $\sigma = 0.0175$, e) and f) $\sigma = 0.035$ and g) and h) $\sigma = 0.07$. The green lines on these plots are a representation of the linear refractive index.

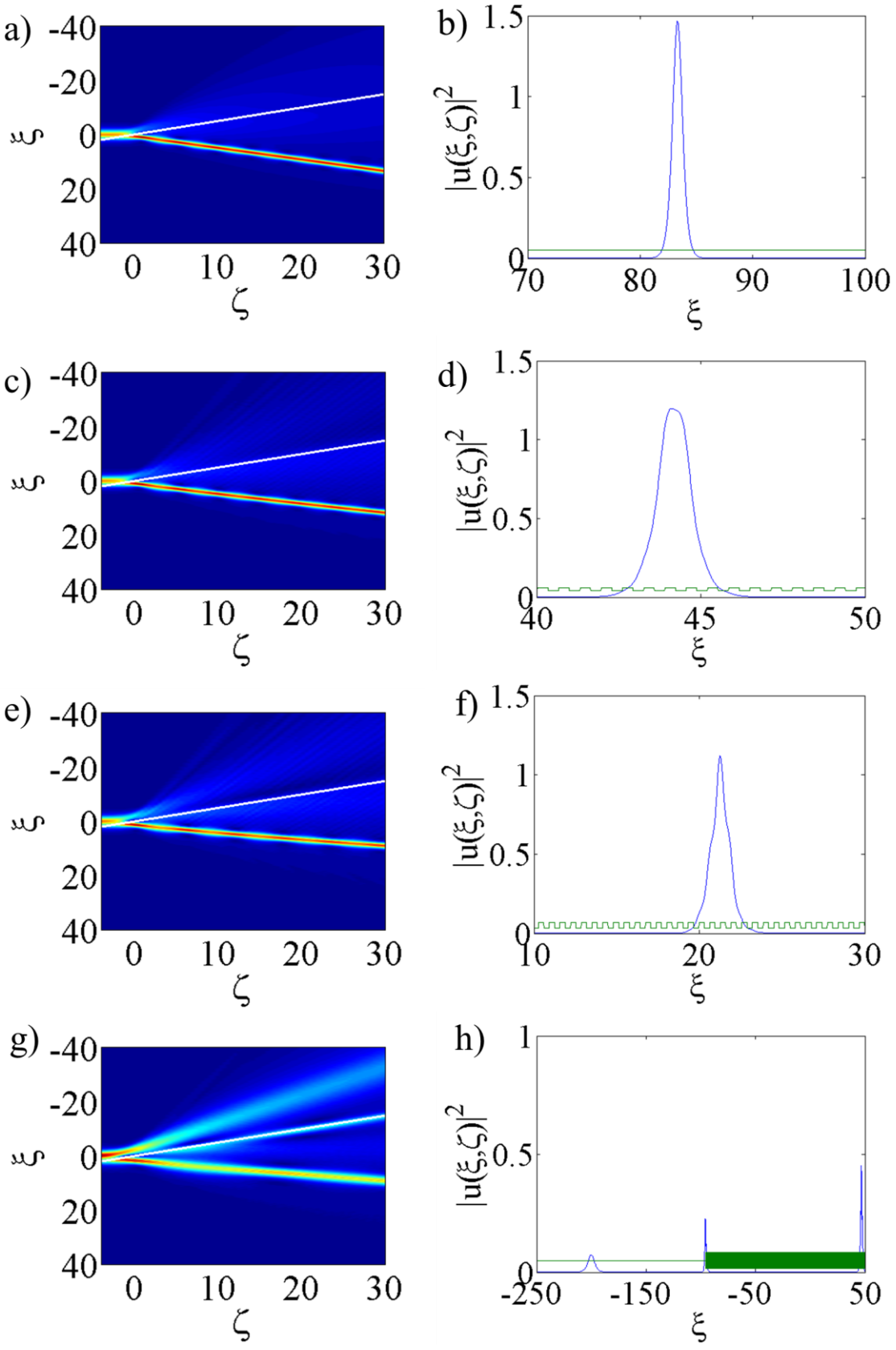

Figure 98 Showing the results for beam propagation in coupled waveguide arrays, where $\kappa = 2.5\text{x}10^{-3}$, $\Delta = 0$, $\alpha = 2.0$, $\theta = 2°$ and a) and b) have $\sigma = 0$, c) and d) $\sigma = 0.0175$, e) and f) $\sigma = 0.035$ and g) and h) $\sigma = 0.07$. The green lines on these plots are a representation of the linear refractive index.

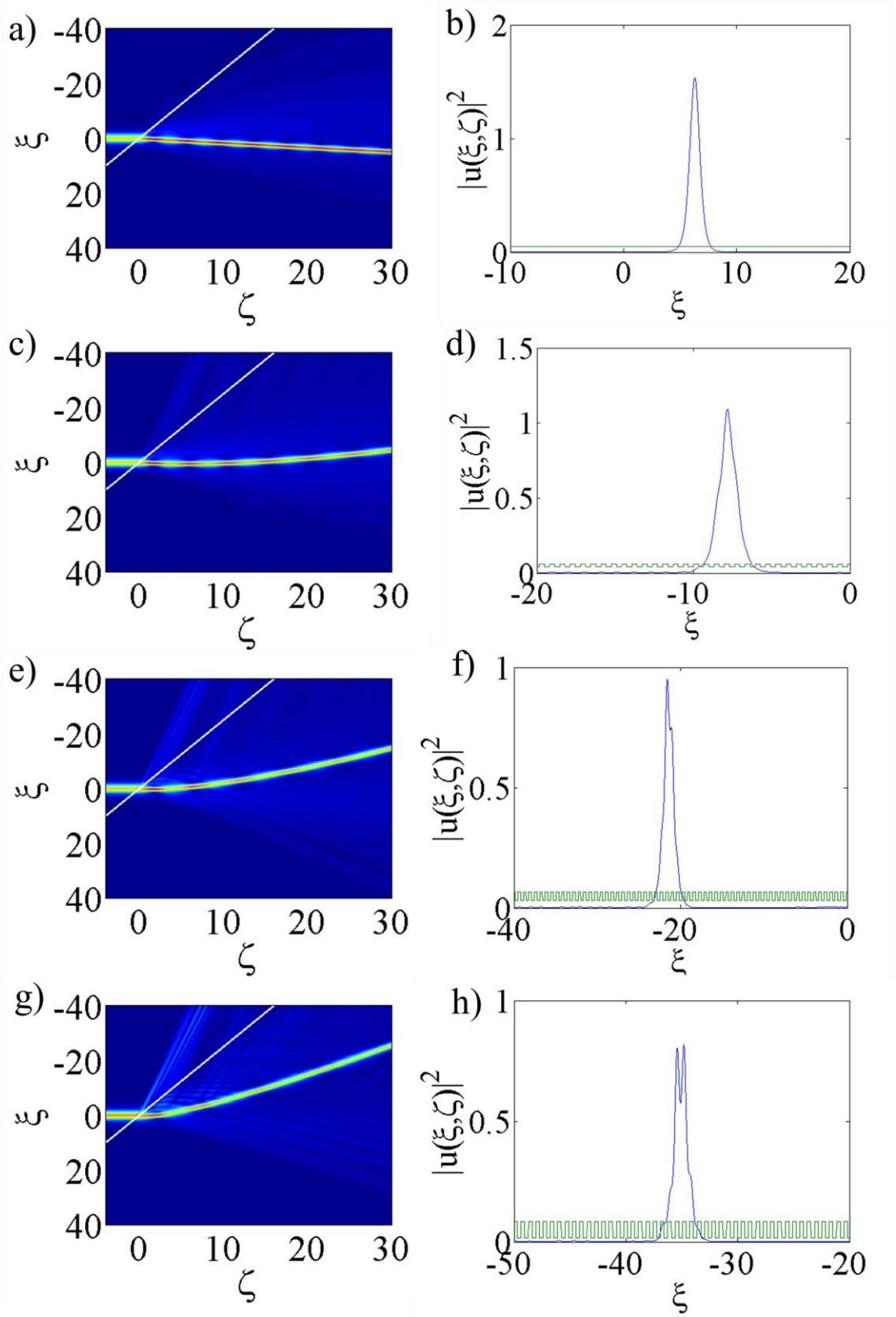

Figure 99 Showing the results for beam propagation in coupled waveguide arrays, where $\kappa = 2.5\times10^{-3}$, $\Delta = 0$, $\alpha = 2.0$, $\theta = 10°$ and a) and b) have $\sigma = 0$, c) and d) $\sigma = 0.0175$, e) and f) $\sigma = 0.035$ and g) and h) $\sigma = 0.07$. The green lines on these plots are a representation of the linear refractive index.

5.7 Conclusions

A Helmholtz governing equation has been derived to fully describe the beam propagation from a Kerr medium to a coupled waveguide array. Although this is not the first time Helmholtz spatial solitons have been investigated in CWAs, see reference [4], the independent work done here has been the most extensive study into Helmholtz solitons in CWAs to date. Moreover, unlike in reference [4], detailed results have been shown, and a variety of qualitative effects uncovered.

The results give detailed information highlighting the beam profiles whilst propagating in the CWA, the detail of which is of importance because studies of discrete solitons in CWAs are not able to fully describe the soliton solutions.

One of the main aims of the study was to investigate further the effect that the depth of the modulation has on the propagation of the beam. This idea was first broached in [12], where the transverse velocity of the beam in a waveguide array was shown to be different from that in its continuum counterpart (with no interface). Not only is this shown here, but also that as the depth of the modulations is increased from 0 (Kerr material) through 0.0175, 0.035 to 0.07, the results can be seen to change qualitatively as the size of the modulations increases. This finding is of particular importance when trying to predict the critical angle for an incident beam. When results are shown in near critical-angle regimes (where $\theta_{(incidence)}$ is set as the $\theta_{crit(theoretical)}$ for a Kerr interface), the qualitative difference is significant. The beam can change from reflecting, to propagating along the interface, to refracting, simply by changing the depth of the modulation in the CWA. This kind of detailed scrutiny of the ramifications of manipulating modulation depth has not been carried out previously.

Though this has been a comprehensive study of beam behaviour in CWAs, there remains much scope for further research. Firstly, finding exact soliton solutions for these beams would add value to the work, since this would lead to a generalised Snell's law and a prediction of the critical angle relating to the CWA, and not just Kerr materials (as have been considered here). Moreover, there is scope to extend the near critical-angle regime results shown in section 5.6.3 to make them as painstakingly thorough as those in chapter 3. In the current chapter, the Helmholtz governing equation was derived with the idea that the periodically patterned refractive index is directly related to the linear aspect of the

refractive index. Further investigations could examine the effect of having periodic patterning in the nonlinear part of the refractive index.

5.8 References

1. D. Mandelik, H.S. Eisenberg, Y. Silberberg, R. Morandotti, and J.S. Aitchison *Band-Gap Sturucture of Waveguide Arrays and Excitation of Floquet-Bloch Solitons*. Physical Review Letters, 2003. **90**, DOI: 053902.
2. D. Mandelik, R. Morandotti, J.S. Aitchison, and Y. Silberberg *Gap Solitons in Waveguide Arrays*. Physical Review Letters, 2004. **92**, DOI: 093904.
3. A.A. Sukhorukov, D. Neshev, W. Krolikowski, and Y.S. Kivshar *Nonlinear Bloch-Wave Interaction and Bragg Scattering in Optically Induced Lattices*. Physical Review Letters, 2004. **92**, DOI: 093901.
4. Z. Shi, Q. Guo, and H. Li *Transmission of nonparaxial nonlocal lattice solitons at nonlinear interfaces*. Europhysics Letters, 2014. **106**, DOI: 44002.
5. J.W. Fleischer, M. Sergev, N.K. Efremidis, and D.N. Christodoulides, *Observation of two-dimensional discrete solitons in optically induced nonlinear photonic lattices.* Nature, 2003. **422**(1): p. 147-150.
6. A. Vergara-Betancourt, E. Martí-Panameño, A. Luis-Ramos, and R. Parada-Alfonso *Formation of discrete solitons as a function of waveguide array geometry under the well-confined mode condition*. Journal of Optics, 2013. **15**, DOI: 105202.
7. F. Lederer, G.I. Stegeman, D.N. Christodoulides, G. Assanto, M. Segev, and Y. Silberberg, *Discrete solitons in optics.* Physics Reports, 2008. **463**(1-3): p. 1-126.
8. H.S. Eisenberg, R. Morandotti, Y. Silberberg, J.M. Arnold, G. Pennelli, and J.S. Aitchison, *Optical discrete solitons in waveguide arrays. I. Soliton formation.* Journal of the Optical Society of America B, 2002. **19**(12): p. 2938-2944.
9. M.J. Ablowitz, Z.H. Musslimani, and G. Biondini *Methods for discrete solitons in nonlinear lattices*. Physical Review E, 2002. **65**, DOI: 026602.
10. A.V. Yulin, D.V. Skryabin, and A.G. Vladimirov, *Modulational instability of discrete solitons in coupled waveguides with group velocity dispersion.* Optics Express, 2006. **14**(25): p. 12347-12352.
11. A.B. Aceves, *Optical gap solitons: Past, present, and future; theory and experiments.* Chaos: An Interdisciplinary Journal of Nonlinear Science, 2000. **10**(3): p. 584-589.
12. D. Mandelik, H.S. Eisenberg, Y. Silberberg, R. Morandotti, and J.S. Aitchison, *Band-Gap Structure of Waveguide Arrays and Excitation of Floquet-Bloch Solitons.* Physical Review Letters, 2003. **90**(053902).
13. M.J. Ablowitz and Z.H. Musslimani, *Discrete spatial solitons in a diffraction-managed nonlinear waveguide array: a unified approach.* Physica D, 2003. **184**(2003): p. 276-303.
14. D.N. Christodoulides and R.I. Joseph, *Discrete self-focusing in nonlinear arrays of coupled waveguides.* Optics Letters, 1988. **13**(9): p. 794-796.
15. J. Sánchez-Curto, P. Chamorro-Posada, and G.S. McDonald, *Helmholtz solitons at nonlinear interfaces.* Optics Letters, 2007. **32**(9): p. 1126-1128.

6. Thesis conclusion and future research

6.1 Summary of main findings

This is the first time that soliton beams at material interfaces have been presented in this kind of detail. The use of Helmholtz soliton theory has been justified by its ability to facilitate the investigation of beams propagating at arbitrary angles, meaning that a full description of the behaviour of these beams has been provided. The alternative, paraxial, approach to studying solitons at interfaces, no matter how ground breaking, can only ever scratch the surface in terms of providing a full description of beam behaviour at material boundaries.

The contributions of this study to our understanding of the properties of bright solitons will be revisited and brought together in what follows. For single interface investigations, which have been the main focus of this thesis and have also been a subject of particular interest for paraxial studies [1, 2], the work is novel in three fundamental aspects:

i. its basis in Helmholtz soliton theory - opening up the investigation to previously unscrutinised regimes (i.e. any angles above ~2°)

ii. the reporting of backwards, as well as the more traditional forwards, propagation of the beam

iii. the sheer volume of computational results - the presented research has been both timely and comprehensive. This has allowed for qualitative analysis to supplement the more usual quantitative analyses, giving rise to the drawing out of finer-grained differences in soliton behaviour.

Whilst the novelties listed above also apply to multi-interface work, there is less relevant literature against which to compare findings. The work presented in this thesis, therefore, acts as a strong foundation to any further research in this arena.

For cubic quintic interfaces, a generalised Snell's law was derived and tested, across a wide range of system parameters. A full explanation of its validity has been given. Chapter 3 then sees an expansion of this key result into an investigation of near critical angle regimes. Here Goos-Hänchen shifts larger than any previously seen in the literature were presented, and other effects seen in these particular angle regimes such as beam splitting. An in-depth discussion was also provided about the applicability of predicting

critical angles at nonlinear interfaces. It is important to note here, that despite considerable searching, no published works (paraxial or nonparaxial) concerning soliton refraction contexts with the type of system nonlinearity featured in chapters 2 and 3 have been found.

Also scrutinised were power-law interfaces, where the stability of the beams was predicted and tested, and it was shown how to determine if a surface wave will be stable from its initial parameters. It was seen that these predictions are reliable. The stability of these solutions was tested further still by analysing the behaviour after a collision with a soliton. Once again, this investigation provided novelty.

For coupled waveguide arrays, a model equation was derived, and this was used to run investigative simulations to show the propagation of the incident soliton. It was shown that as the depth of the modulations was varied, significant qualitative differences could be seen in the behaviour of the beam. This work only scratches the surface of what can be done, and should be used as a starting point for other research (suggestions for the direction this may take are given in section 6.3).

6.2 Applications of these findings

The potential applications of these findings include providing other researchers with the opportunity to perform experimental versions of the problems studied here. Although this is less applicable to multi-interfaces, where experimental literature has proliferated [3-5], experimental works at single interfaces are disproportionately lacking. This thesis, then, provides a good 'jumping–off point' for those wishing to take up the baton in carrying experiments with solitons at single interfaces.

As has been mentioned previously, spatial solitons can be used to transfer bits of optical data. This means that the beams could be exploited in the areas of data storage and information processing. After understanding the fundamentals of how a spatial solitons propagates in a nonlinear medium, the next most important aspect to appreciate is how the beam will behave at the boundary of two materials, in order to anticipate manufacturing limitations and restrictions (this will help in the design and manufacture of optical devices). If a beam has to propagate from a start point to an end point to carry the information successfully, then it is important to know what effect (if any) a possible interface will have on the propagation of the beam.

Multi interface work has its applications in still further areas. All-optical switching devices (where fully controlled switching of optical signals between the input and output ports is the ultimate goal [6]) are a highly relevant area of research. Literature shows that waveguides are a prime material for realising this type of technology [7], so the results presented in chapter 5, especially those at near-critical angle regimes, are likely to be of importance to the future development of these technologies.

6.3 Limitations and suggestions of future work

One of the obvious limitations of using Helmholtz soliton theory over the nonlinear Schrödinger equation is its increased mathematical and computational complexity. The extra term which is found in the nonlinear Helmholtz equation means that a completely different and more involved numerical approach has had to be deployed [8].

As with many research projects, the biggest limitation has been time. This has left the door open to work which may be studied in the future. Further research into critical angles at nonlinear interfaces (i.e. better ways to predict them on the basis of input variables) would be of much interest. Also the work presented in the CWA chapter is only the *beginning* of Helmholtz solitons in CWAs; this could be expanded upon by considering different ways to exploit the periodic patterning of the CWA. Also looking into more nonlinearities, power-law (what happens for $q \neq 2$) and cubic-quintic to name two, is an obviously necessary avenue of future research.

Lastly, an investigation into surface waves at cubic-quintic interfaces would be an important extension of single-inteface analyses, and may be considered a complementary aspect to this programme of research.

6.4 References

1. A.B. Aceves, J.V. Moloney, and A.C. Newell, *Theory of light-beam propagation at nonlinear interfaces. I. Equivalent-particle theory for a single interface.* Physical Review A, 1989. **39**(4): p. 1809-1827.
2. A.B. Aceves, J.V. Moloney, and A.C. Newell, *Theory of light-beam propagation at nonlinear interfaces. II. Multiple-particle and multiple-interface extensions.* Physical Review A, 1989. **39**(4): p. 1828-1840.
3. D. Mandelik, H.S. Eisenberg, Y. Silberberg, R. Morandotti, and J.S. Aitchison *Band-Gap Sturucture of Waveguide Arrays and Excitation of Floquet-Bloch Solitons*. Physical Review Letters, 2003. **90**, DOI: 053902.
4. D. Mandelik, R. Morandotti, J.S. Aitchison, and Y. Silberberg *Gap Solitons in Waveguide Arrays*. Physical Review Letters, 2004. **92**, DOI: 093904.
5. A.A. Sukhorukov, D. Neshev, W. Krolikowski, and Y.S. Kivshar *Nonlinear Bloch-Wave Interaction and Bragg Scattering in Optically Induced Lattices*. Physical Review Letters, 2004. **92**, DOI: 093901.
6. W. Krolikowski and Y.S. Kivshar, *Soliton-based optical switching in waveguide arrays.* Journal of the Optical Society of America B, 1996. **13**(5): p. 876-887.
7. G.I. Stegeman, E.M. Wright, N. Finlayson, R. Zanoni, and C.T. Seaton, *Third order nonlinear integrated optics.* Journal of Lightwave Technology, 1998. **6**(6): p. 953-970.
8. P. Chamorro-Posada, G.S. McDonald, and G.H.C. New, *Non-paraxial beam propagation methods.* Optics Communications, 2001. **192**(1–2): p. 1-12.

Appendix A

A.1 List of publications

JM Christian, J Sanchez-Curto, P Chamorro-Posada, GS McDonald and EA McCoy, Refraction of power-law spatial solitons - the Helmholtz-Snell law, IEEE Abstract, 5th International Conference on Advanced Optoelectronics & Lasers, CAOL 2010, Sevastopol, Crimea, Ukraine, 10-14 Sept 2010

JM Christian, EA McCoy, GS McDonald, J Sanchez-Curto and P Chamorro-Posada, Helmholtz bright spatial solitons and surface waves at power-law optical interfaces, JOURNAL OF ATOMIC, MOLECULAR AND OPTICAL PHYSICS, v2012, art no 137967, 2012

EA McCoy, JM Christian, GS McDonald, J Sanchez-Curto and P Chamorro-Posada, Refraction and scattering of Helmholtz bright spatial optical solitons at cubic-quintic material interfaces -- to be submitted

A.1 Conference contributions

1. J Sanchez-Curto, P Chamorro-Posada, JM Christian, GS McDonald and EA McCoy, Universal Snell's law & bright spatial soliton refraction, National Photonics Conference, Photon 10, Southampton, UK, 23-26 Aug 2010

2. JM Christian, J Sanchez-Curto, P Chamorro-Posada, GS McDonald and EA McCoy, Refraction of power-law spatial solitons - the Helmholtz-Snell law, IEEE Abstract, 5th International Conference on Advanced Optoelectronics & Lasers, CAOL 2010, Sevastopol, Crimea, Ukraine, 10-14 Sept 2010

3. EA McCoy, JM Christian, GS McDonald, J Sanchez-Curto and P Chamorro-Posada, Refraction law for self-collimated light beams at material interfaces, 1st CSE Doctoral School Postgraduate Research Conference, University of Salford, 17 Nov 2010

4. EA McCoy, JM Christian and GS McDonald, Spatial Soliton Refraction at Cubic-Quintic Material Interfaces, SPARC 11 conference, University of Salford, UK, 08-09 June 2011

5. EA McCoy, JM Christian and GS McDonald, Arbitrary-angle Scattering of Spatial Solitons from Dielectric Optical Interfaces, College Research Showcase Day, University of Salford, 16 June, UK, 2011

6. JM Christian, GS McDonald, C Bostock, EA McCoy, J Sanchez-Curto and P Chamorro-Posada, A Universal Nonparaxial Refraction Law for Spatial Solitons, Waves 2011 - 10th International Conference on Mathematical and Numerical Aspects of Waves, 25-29 July, Vancouver, Canada, 2011

7. EA McCoy, JM Christian and GS McDonald, Scattering of Helmholtz spatial optical solitons at material interfaces, First Annual Student Conference on Complexity Science, Winchester University, UK, 4-7 Aug, 2011

8. EA McCoy, JM Christian and GS McDonald, Nonlinear wave phenomena at optical boundaries: spatial soliton refraction, Proceedings of the 2nd CSE Postgraduate Research Doctoral School Conference, University of Salford, UK, ISBN: 978-1-907842-23-8, 33-35, 2011

9. EA McCoy, JM Christian and GS McDonald, Arbitrary-angle interaction of spatial solitons with layered photonic structures, SPARC 12 conference, University of Salford, UK, 30-31 May, 2012

10. EA McCoy, JM Christian & GS McDonald, Spatial solitons at interfaces: nonparaxial refraction & giant Goos-Hanchen shifts, Science & Technology College Research Showcase Day, University of Salford, UK, 20 June, 2012.

11. EA McCoy, JM Christian & GS McDonald, Spatial solitons at optical interfaces: new angles, paradigms & horizons, Proceedings of the 3rd CSE Postgraduate Research Doctoral School Conference, University of Salford, UK, ISBN: 978-1-907842-38-2, 10-13, 2012.

12. EA McCoy, JM Christian and GS McDonald, Propagation properties of Helmholtz power-law nonlinear surface waves, Second Annual Student Conference on Complexity Science, Oxstalls Campus, University of Gloucestershire, Gloucester, UK, 9-12 Aug, 2012

13. EA McCoy, JM Christian and GS McDonald, Nonparaxial refraction and giant Goos-Hanchen shifts at nonlinear optical interfaces, Second Annual Student

Conference on Complexity Science, Oxstalls Campus, University of Gloucestershire, Gloucester, UK, 9-12 Aug, 2012

14. JM Christian, EA McCoy, GS McDonald, J Sanchez-Curto and P Chamorro-Posada, Helmholtz spatial solitons and oblique propagation in coupled-waveguide arrays, National Photonics Conference, Photon 12, Durham, UK, 3-6 Sept, 2012

15. EA McCoy, JM Christian, GS McDonald, J Sanchez-Curto and P Chamorro-Posada, Nonparaxial refraction laws for spatial solitons at cubic-quintic material interfaces, National Photonics Conference, Photon 12, Durham, UK, 3-6 Sept, 2012

16. JM Christian, GS McDonald, EA McCoy, J Sanchez-Curto and P Chamorro-Posada, Nonparaxial refraction laws in optics: from non-Kerr interfaces to waveguide arrays, European Optical Society Annual Meeting, EOSAM 2012, Aberdeen, UK, 25-28 Sept, 2012

17. JM Christian, EA McCoy, GS McDonald, J Sanchez-Curto and P. Chamorro-Posada, Nonparaxial Soliton Refraction at Optical Interfaces with $\chi^{(3)}$and $\chi^{(5)}$Susceptibilities, CLEO Europe & IQEC 2013, Conference on Lasers and Electro-optics, International Quantum Electronics Conference (IQEC), Munich, Germany, 12-16 May, 2013

18. EA McCoy, JM Christian and GS McDonald, Helmholtz Surface Wave Propagation Along Nonlinear Interfaces, SPARC 2013 conference, University of Salford, UK, 5-6 June, 2013

19. EA McCoy, JM Christian and GS McDonald, Giant Goos-Hanchen Shifts and Soliton Refraction in Systems With χ^5Susceptibility, SPARC 2013 conference, University of Salford, UK, 5-6 June, 2013

20. RF Yates, JM Christian, EA McCoy and GS McDonald, Algebraic Soliton Refraction: New Wave Contexts for Nonlinear Snell's Law, Science & Technology College Research Showcase Day, Proceedings ISBN 978-1-907842-41-2, University of Salford, UK, 19 June, 2013

21. JM Christian, EA McCoy and GS McDonald, Coupled-Waveguide Arrays: Oblique Injection & Soliton Propagation, Science & Technology College Research

Showcase Day, Proceedings ISBN 978-1-907842-41-2, University of Salford, UK, 19 June, 2013

22. EA McCoy, JM Christian and GS McDonald, Refraction at Interfaces with $\chi^{(5)}$Nonlinearity: Snell's Law & Goos-Hanchen Shifts, Science & Technology College Research Showcase Day, Proceedings ISBN 978-1-907842-41-2, University of Salford, UK, 19 June, 2013

23. EA McCoy, JM Christian, GS McDonald, J Sanchez-Curto and P. Chamorro-Posada, Refraction and Goos-Hanchen Shifts of Spatial Solitons at Cubic-Quintic Interfaces, Optical Society of America, Nonlinear Optics 2013, Hawaii, USA, 21-26 July, 2013

24. EA McCoy, JM Christian and GS McDonald, Optical Soliton Refraction & Goos-Hanchen Shifts at Interfaces with $\chi^{(5)}$Susceptibility, Third Annual Student Conference on Complexity Sciences (SCCS), Oxford Brookes, UK, 14-17 Aug, 2013

25. EA McCoy, JM Christian and GS McDonald, Oblique Propagation of Spatial Solitons in Patterned Optical Structures, Third Annual Student Conference on Complexity Sciences (SCCS), Oxford Brookes, UK, 14-17 Aug, 2013

A.3 Published Paper

Hindawi Publishing Corporation
Journal of Atomic, Molecular, and Optical Physics
Volume 2012, Article ID 137967, 21 pages
doi:10.1155/2012/137967

Research Article

Helmholtz Bright Spatial Solitons and Surface Waves at Power-Law Optical Interfaces

J. M. Christian,[1,2] E. A. McCoy,[1] G. S. McDonald,[1] J. Sánchez-Curto,[2] and P. Chamorro-Posada[2]

[1] *Joule Physics Laboratory, School of Computing, Science and Engineering, Materials & Physics Research Centre, University of Salford, Greater Manchester M5 4WT, UK*
[2] *Departamento de Teoría de la Señal y Comunicaciones e Ingeniería Telemática, Universidad de Valladolid, ETSI Telecomunicación, Campus Miguel Delibes Paseo Belén 15, E-47011 Valladolid, Spain*

Correspondence should be addressed to J. M. Christian, j.christian@salford.ac.uk

Received 24 April 2012; Accepted 31 May 2012

Academic Editor: Alan Migdall

We consider arbitrary angle interactions between spatial solitons and the planar boundary between two optical materials with a single power-law nonlinear refractive index. Extensive analysis has uncovered a wide range of new qualitative phenomena in non-Kerr regimes. A universal Helmholtz-Snell law describing soliton refraction is derived using exact solutions to the governing equation as a nonlinear basis. New predictions are tested through exhaustive computations, which have uncovered substantially enhanced Goos-Hänchen shifts at some non-Kerr interfaces. Helmholtz nonlinear surface waves are analyzed theoretically, and their stability properties are investigated numerically for the first time. Interactions between surface waves and obliquely incident solitons are also considered. Novel solution behaviours have been uncovered, which depend upon a complex interplay between incidence angle, medium mismatch parameters, and the power-law nonlinearity exponent.

1. Introduction

A light beam impinging on the interface between two dissimilar dielectric materials is a fundamental optical geometry [1–12]. After all, the single-interface configuration is an elemental structure that facilitates more sophisticated device designs and architectures for a diverse range of photonic applications. The seminal work of Aceves et al. [6, 7] some two decades ago considered perhaps the simplest scenario, where a spatial soliton (i.e., a self-trapped and self-stabilizing optical beam) is incident on the boundary between two different Kerr-type materials. Their intuitive approach reduced the full complexity of the electromagnetic interface problem to something far more tractable, namely, the solution a scalar equation of the inhomogeneous nonlinear Schrödinger (NLS) type. The development of an equivalent-particle theory [3–6] provided an enormous level of insight into the behaviour of scalar solitons at material boundaries. The adiabatic perturbation technique developed by Aliev et al. [13, 14] provides another toolbox for analyzing interface phenomena (e.g., light incident on the boundary between a linear and a nonlinear medium). Photorefractive [15] and quadratic [16] materials have also been considered.

A recurrent feature of the *waves at interfaces* literature is the appearance of the paraxial approximation, which combines the assumptions of broad (predominantly transverse-polarized) beams and slowly varying envelopes [1–16]. The adoption of this ubiquitous mathematical device can impose some strong physical constraints that should be borne in mind when modelling precisely these types of angular geometries. Indeed, the class of problem at hand is inherently nonparaxial since impinging beams may be arbitrarily oblique with respect to the interface. External refraction (where the refracted beam deviates *away from* the interface) provides a specific context where beam refraction cannot be described using conventional approaches. Paraxial

wave optics must be applied with care since, in potentially off-axis regimes, it holds true only where angles (in the laboratory frame) of incidence, reflection, and refraction with respect to the reference direction are negligibly (or near-negligibly) small.

Recently, we proposed the first scalar model of spatial solitons at interfaces that is valid across the entire angular range [17, 18]. By respecting the essential role played by Helmholtz diffraction [19–24], the angular restriction was lifted while retaining an intuitive and manageable envelope equation. Preliminary analyses considered bright [17, 18] and dark [25, 26] spatial solitons incident on the boundary between dissimilar Kerr-type materials. They focused on establishing and developing the *propagation* aspects of our Helmholtz interfaces approach. By enforcing appropriate continuity conditions at the interface, a Snell's law for Kerr spatial solitons was derived whose validity was tested and confirmed by extensive numerical computations. Here, we take the first steps in a systematic study of the *materials* aspects of nonlinear beam-interface interactions. The simplest non-Kerr system one might consider is a class of host media whose refractive index $n_{\mathrm{NL}}(E)$ has a generic power-law dependence on the (complex) electric field amplitude E [27–29]:

$$n_{\mathrm{NL}}(E) = \frac{\alpha}{2n_0}|E|^q, \tag{1}$$

where α is a positive coefficient, n_0 is the linear index (at the optical frequency), and the exponent q lies within the range $0 < q < 4$. Typically, the nonlinear response of the medium is assumed to be weak so that $\alpha E_0^q/n_0 \ll O(1)$, where E_0 is the peak field amplitude.

Power-law models have played a key role in the theory of nonlinear waves for the past three decades [30, 31]. Indeed, [32] provides an excellent review of the fundamental importance of model (1) in photonics contexts. Materials that fall into this broad category include some semiconductors (e.g., InSb [33] and GaAs/GaAlAs [34]), doped filter glasses (e.g., CsS_xSe_{x-2} [35, 36]), and liquid crystals [32]. One expects non-Kerr regimes (where q deviates from the value of 2) to give rise to a diverse range of new quantitative and qualitative phenomena. The physical basis for this expectation lies in the idealized nature of the Kerr response. In a range of materials, one can often find higher-order nonlinear effects coming into play. Perhaps the most obvious example of the breakdown of Kerr-type behaviour is optical saturation, where the refractive index change becomes bleached in the presence of sufficiently high-intensity illumination. In such cases, model (1) with $q < 1$ can be used to describe generic leading-order corrections from a saturable (dispersive) nonlinearity [35, 36].

In this paper, a detailed account is presented of arbitrary-angle refraction of spatial solitons at the interface between dissimilar power-law materials. Also of intrinsic interest are nonlinear surface waves (i.e., localized modes that travel along the boundary). This fundamental class of excitation has been the subject of previous power-law studies involving a single interface [35–39] and guided waves in multilayer structures (e.g., slab waveguides) [40–43]. Stability characteristics have been inferred from inspection of *power-propagation constant* solution branches. However, to the best of our knowledge, direct verification of such predictions [37–43] (e.g., through numerical solution of the underlying nonlinear Helmholtz equation) has been absent from the literature to date. Rather, computational studies of surface waves tend to have been in the limit of slowly varying envelopes and nonlinear Schrödinger-type models, typically of the diffusive-Kerr [44, 45], thermal [46], or saturable [47] type. Here, we investigate the stability of exact analytical Helmholtz surface waves through direct numerical calculations. As a fairly stringent test of solution robustness, we also report on some key findings concerning arbitrary-angle interactions between surface waves and solitons. In beam-refraction and surface-wave contexts, simulations have uncovered strikingly distinct behaviours as the exponent q is varied and across a range of quasi-paraxial and fully nonparaxial angular regimes.

The layout of this paper is as follows. In **Section 2**, we propose a governing equation for scalar optical fields in two adjoining power-law materials with dissimilar medium coefficients. Exact analytical bright solitons are presented for both media, and these solutions are used as a nonlinear basis to derive a generalized *Helmholtz-Snell law*. In **Section 3**, extensive computations test predictions of the new refraction law over a range of system parameters. We also extend our first calculations of the Goos-Hänchen (GH) shifts [48] in the Helmholtz angular regime [49] with power-law nonlinearities. Nonlinear surface waves are derived in **Section 4**, and simulations provide what appears to be the first full investigation of the stability properties of this new class of Helmholtz solution. We conclude, in **Section 5**, with some comments about the impact of our results.

2. Helmholtz Model for Scalar Soliton Refraction

The formalism of Helmholtz soliton theory [23, 24] is now deployed to develop a framework for describing refraction phenomena in wider classes of nonlinear optical materials. This type of modelling approach is valid when the beam waist w_0 is much broader than its free-space carrier wavelength λ, such that $\varepsilon \equiv \lambda/w_0 \ll O(1)$. Ultranarrow beam corrections to the governing equation, typically obtained from single-parameter (i.e., ε-based) order-of-magnitude analyses of fully-nonlinear Maxwell equations [50–55], are unnecessary in such regimes.

2.1. Governing Equation. Within the scalar approximation [19–24], we consider an electric field of the form

$$E(x,z,t) = E(x,z)\exp(-\mathrm{i}\omega t) + E^*(x,z)\exp(+\mathrm{i}\omega t), \tag{2}$$

which is time harmonic with angular frequency ω. The laboratory space and time coordinates are (x,z) and t, respectively. In medium j (where $j = 1$ and 2), it is well

known that the complex spatial field $E(x,z)$ satisfies the Helmholtz equation

$$\frac{\partial^2 E}{\partial z^2}+\frac{\partial^2 E}{\partial x^2}+\frac{\omega^2}{c^2}n_j^2(E)E=0, \tag{3}$$

where c is the vacuum speed of light. The refractive index distribution $n_j(E)$ on either side of the boundary is introduced through $n_j^2(E) \equiv n_{0j}^2+\alpha_j|E|^q$, where n_{0j} is the linear index at frequency ω and α_j is a nonlinearity coefficient. To facilitate comparison with our earlier work [17, 18, 25, 26], we look for travelling-wave solutions to (3) of the form $E(x,z)=E_0u(x,z)\exp(\mathrm{i}k_1z)$. Here, E_0 is a (real) scale factor determining electric-field units, $u(x,z)$ is the dimensionless envelope, and $\exp(\mathrm{i}k_1z)$ biases the solution in the forward longitudinal direction (taken to be z), where $k_1 \equiv n_{01}\omega/c$ is the (linear) propagation constant of the carrier wave in medium 1. It then follows that u satisfies the inhomogeneous equation

$$\begin{aligned}&\frac{\partial^2 u}{\partial z^2}+\mathrm{i}2k_1\frac{\partial u}{\partial z}+\frac{\partial^2 u}{\partial x^2}+\frac{\omega^2}{c^2}\alpha_1E_0^q|u|^qu\\&=\left[k_1^2\left(1-\frac{n_{02}^2}{n_{01}^2}\right)+\frac{\omega^2}{c^2}\alpha_1E_0^q\left(1-\frac{\alpha_2}{\alpha_1}\right)|u|^q\right]h(x,z)u,\end{aligned} \tag{4}$$

where $h(x,z)$ is a Heaviside function that is equal to zero (unity) in the domain of medium 1 (medium 2). Equation (4) may be normalized with respect to the parameters in medium 1, in which case the following governing equation may be derived without further approximation [17, 18, 56, 57]:

$$\kappa\frac{\partial^2 u}{\partial\zeta^2}+\mathrm{i}\frac{\partial u}{\partial\zeta}+\frac{1}{2}\frac{\partial^2 u}{\partial\xi^2}+|u|^qu=\left[\frac{\Delta}{4\kappa}+(1-\alpha)|u|^q\right]h(\xi,\zeta)u. \tag{5}$$

The dimensionless longitudinal and transverse coordinates are $\zeta = z/L_D$ and $\xi = 2^{1/2}x/w_0$, respectively, where $L_D = k_1w_0^2/2$ is the diffraction length of a reference (paraxial) Gaussian beam. The inverse beam width is quantified by $\kappa = 1/(k_1w_0)^2 = \varepsilon^2/4\pi^2n_{01}^2 \ll O(1)$, where $\varepsilon \equiv \lambda/w_0$, and the field amplitude scales with $E_0 = (2n_{01}^2/\alpha_1k_1L_D)^{1/q}$. Model (5) is supplemented by the mismatch parameters [17, 18, 25, 26]

$$\Delta \equiv 1-\frac{n_{02}^2}{n_{01}^2}, \tag{6a}$$

$$\alpha \equiv \frac{\alpha_2}{\alpha_1}, \tag{6b}$$

which determine how the linear and nonlinear refractive properties of the system change as one traverses the boundary.

Equation (5) allows one access to material scenarios where $\Delta < 0$ (i.e., configurations with $n_{02} > n_{01}$) [17, 18, 25, 26]. By contrast, the scalings deployed in classic paraxial theory [8, 9] restrict those models to consideration of regimes with $\Delta > 0$. It is also apparent that setting $\kappa \approx 0$ in an attempt to recover the paraxial model is going to lead to complications when handling the linear mismatch term $\Delta/4\kappa$. The physical and mathematical difficulties of interpreting the paraxial approximation as the single-parameter limit $\kappa \approx 0$ have been discussed at length elsewhere [23, 24]; it is particularly well illustrated by interface geometries.

2.2. Solitons as a Nonlinear Basis. When investigating the refraction of nonlinear light beams at material boundaries, it is essential to have an appropriate set of basis functions with which to formulate the problem. Such a basis is provided by the underlying exact analytical Helmholtz solitons [56]. In the following analysis, we align the interface along the z axis so that it is located at transverse position $x = 0$. Medium 1 (the domain of the incident beam, where $h = 0$) is taken to occupy the half-plane $-\infty \le x < 0$, while medium 2 (the domain of the refracted beam, where $h = +1$), occupies $0 \le x \le +\infty$.

In medium 1, the governing equation (5) becomes

$$\kappa\frac{\partial^2 u}{\partial\zeta^2}+\mathrm{i}\frac{\partial u}{\partial\zeta}+\frac{1}{2}\frac{\partial^2 u}{\partial\xi^2}+|u|^qu=0. \tag{7}$$

Sufficiently far from the interface, (7) admits exact analytical solitons of the form [56]

$$\begin{aligned}u(\xi,\zeta)=\eta_0\mathrm{sech}^{2/q}&\left(a\frac{\xi-V_{\mathrm{inc}}\zeta}{\sqrt{1+2\kappa V_{\mathrm{inc}}^2}}\right)\\&\times\exp\left[\pm\mathrm{i}\sqrt{\frac{1+4\kappa\beta_0}{1+2\kappa V_{\mathrm{inc}}^2}}\left(V_{\mathrm{inc}}\xi+\frac{\zeta}{2\kappa}\right)\right]\\&\times\exp\left(-\mathrm{i}\frac{\zeta}{2\kappa}\right),\end{aligned} \tag{8a}$$

where η_0 is the peak amplitude of the beam, $a = q[\eta_0^q/(2+q)]^{1/2}$ determines the (inverse) solution width, and

$$\beta_0 = 2\frac{\eta_0^q}{2+q} \tag{8b}$$

quantifies nonlinear phase shift through the (typically small) quantity $4\kappa\beta_0$. The $\pm$ sign flags evolution in the forward/backward longitudinal direction. The propagation angle of the beam in the laboratory (i.e., the (x,z)) frame, denoted by θ_{inc} and measured with respect to the z axis, is related to the transverse velocity parameter V_{inc} through $\tan\theta_{\mathrm{inc}} = (2\kappa)^{1/2}V_{\mathrm{inc}}$ [23, 24]. In medium 2, u satisfies

$$\kappa\frac{\partial^2 u}{\partial\zeta^2}+\mathrm{i}\frac{\partial u}{\partial\zeta}+\frac{1}{2}\frac{\partial^2 u}{\partial\xi^2}-\frac{\Delta}{4\kappa}u+\alpha|u|^qu=0, \tag{9}$$

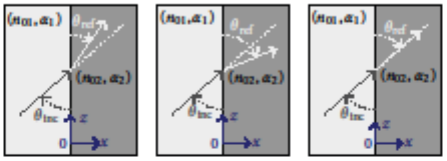

Figure 1: Schematic diagram illustrating (a) internal ($\theta_{ref} < \theta_{inc}$) and (b) external ($\theta_{ref} > \theta_{inc}$) refraction in the laboratory frame. The transparency condition ($\theta_{ref} = \theta_{inc}$) is shown in part (c). External refraction regimes tend to be highly angular and cannot be adequately described by the paraxial approximation.

and one may derive similar families of solitons,

$$u(\xi,\zeta) = \eta_0 \operatorname{sech}^{2/q}\left(a\sqrt{\alpha}\frac{\xi - V_{ref}\zeta}{\sqrt{1+2\kappa V_{ref}^2}}\right) \times \exp\left[\pm i\sqrt{\frac{1-\Delta+4\kappa\beta_0\alpha}{1+2\kappa V_{ref}^2}}\left(V_{ref}\xi + \frac{\zeta}{2\kappa}\right)\right] \times \exp\left(-i\frac{\zeta}{2\kappa}\right). \quad (10)$$

Note that the connection between transverse velocity V_{ref} and propagation angle θ_{ref}, that is, $\tan\theta_{ref} = (2\kappa)^{1/2}V_{ref}$, is unaffected by the (additional, linear) term $\Delta/4\kappa$ in (9) or by the nonlinear coefficient α. The geometry of these solitons, and their inherent stability against perturbations to the local beam shape, was explored in detail in [56].

2.3. Phase Continuity and Refraction. In recent analyses, we have shown that arbitrary-angle refraction is well described by anticipating that the phase distribution of the light be continuous across the interface [17, 18, 25, 26]. Matching the phases of solutions (8a) and (10) at $x = 0$ leads to the requirement that

$$\pm\sqrt{\frac{1+4\kappa\beta_0}{1+2\kappa V_{inc}^2}} = \pm\sqrt{\frac{1-\Delta+4\kappa\beta_0\alpha}{1+2\kappa V_{ref}^2}}. \quad (11)$$

Hence, continuity is possible if and only if the incident and refracted solitons share a common longitudinal sense (i.e., both must be in either the forward or backward directions). By rearranging (11), one can show that V_{ref} is related to V_{inc} through

$$V_{ref}^2 = V_{inc}^2 - \frac{1}{2\kappa}\left(\frac{1+2\kappa V_{inc}^2}{1+4\kappa\beta_0}\right)[\Delta + 4\kappa\beta_0(1-\alpha)]. \quad (12)$$

Expressed in this way, (12) provides a helpful form "$V_{ref}^2 = V_{inc}^2$ + *deviation*," where the sign of the *deviation* can be analysed separately. It is then instructive to define a net mismatch parameter δ as [17, 18]

$$\delta \equiv \Delta + 4\kappa\beta_0(1-\alpha). \quad (13)$$

This parameter can be interpreted as the sum of linear and nonlinear mismatches in material parameters. Its sign fully characterizes beam refraction. When $\delta > 0$, one has that $V_{ref}^2 < V_{inc}^2$, which is equivalent to $\theta_{ref} < \theta_{inc}$. This regime is referred to as *internal refraction*, and it corresponds to the situation where the beam in medium 2 is deviated toward the interface (see Figure 1(a)). Conversely, $\delta < 0$ implies that $V_{ref}^2 > V_{inc}^2$ or, equivalently, $\theta_{ref} > \theta_{inc}$. This *external refraction* regime corresponds to the beam in medium 2 being bent away from the interface (see Figure 1(b)). The special case of $\delta = 0$ is the transparency condition, where linear and nonlinear index mismatches oppose each other exactly so that $V_{ref}^2 = V_{inc}^2$ (or $\theta_{ref} = \theta_{inc}$). The interface is thus essentially transparent to the incident beam (see Figure 1(c)), which experiences no net change in dielectric properties as it crosses the boundary. It is interesting to note that the absence of an interface provides a parameter subset (i.e., $\Delta = 0$ and $\alpha = 1$) that satisfies the transparency condition identically.

2.4. The Helmholtz-Snell Law for Spatial Solitons. By recognizing the rotational symmetry inherent to Helmholtz spatial solitons [23, 24, 56], it becomes clear that "forward" and "backward" designations are arbitrary. The only physical distinction between the two families is the propagation direction relative to the observer. By deploying trigonometric identities to eliminate velocities V_{inc} and V_{ref}, the forward and backward solutions in each medium may be written as

$$u(\xi,\zeta) = \eta_0 \operatorname{sech}^{2/q}\left[a\left(\xi\cos\theta_{inc} - \frac{\zeta}{\sqrt{2\kappa}}\sin\theta_{inc}\right)\right] \times \exp\left[i\sqrt{\frac{1+4\kappa\beta_0}{2\kappa}}\left(\xi\sin\theta_{inc} + \frac{\zeta}{\sqrt{2\kappa}}\cos\theta_{inc}\right)\right] \times \exp\left(-i\frac{\zeta}{2\kappa}\right), \quad (14a)$$

and

$$u(\xi,\zeta) = \eta_0 \operatorname{sech}^{2/q}\left[a\sqrt{\alpha}\left(\xi\cos\theta_{ref} - \frac{\zeta}{\sqrt{2\kappa}}\sin\theta_{ref}\right)\right] \times \exp\left[i\sqrt{\frac{1-\Delta+4\kappa\beta_0\alpha}{2\kappa}}\right.$$

$$\times\left(\xi\sin\theta_{\text{ref}}+\frac{\zeta}{\sqrt{2\kappa}}\cos\theta_{\text{ref}}\right)\Bigg]$$
$$\times\exp\left(-\mathrm{i}\frac{\zeta}{2\kappa}\right). \tag{14b}$$

In this representation, the angles are bounded by $-180^\circ < \theta_{\text{inc, ref}} \leq +180^\circ$ with respect to the z-axis. By matching the solution phase at $\xi = 0$, one can obtain a compact Helmholtz-Snell refraction law involving laboratory-frame angles:

$$\gamma n_{01}\cos\theta_{\text{inc}} = n_{02}\cos\theta_{\text{ref}}, \tag{15a}$$

where

$$\gamma \equiv \left[\frac{1+4\kappa\beta_0}{1+4\kappa\beta_0\alpha(1-\Delta)^{-1}}\right]^{1/2}. \tag{15b}$$

It is worthwhile noting that (15a) has a form which is almost exactly identical to that encountered when studying the classic electromagnetic problem of *plane wave* refraction at the boundary between different *linear* dielectrics. Thus, the single correction factor γ captures the interplay between finite-waist beams (through the appearance of κ) and discontinuities in both the linear *and nonlinear* properties of the adjoining media. The exponent q appears implicitly through β_0.

When a beam encounters the boundary with a rarer medium, there is little penetration of light across that boundary until the incidence angle exceeds a critical value, denoted by θ_{crit}. At criticality, where $\theta_{\text{inc}} = \theta_{\text{crit}}$, the trajectory of the incident beam is deviated so that, in principle, the outgoing beam travels along the interface (i.e., $\theta_{\text{ref}} = 0$). Applying this condition to law (15a) and (15b) leads to an analytical prediction for θ_{crit} in terms of the mismatch parameters Δ and α and also the solution parameter $4\kappa\beta_0$:

$$\tan\theta_{\text{crit}} = \left[\frac{\Delta+4\kappa\beta_0(1-\alpha)}{1-\Delta+4\kappa\beta_0\alpha}\right]^{1/2}. \tag{16}$$

In practice, one rarely finds the refracted soliton travelling along the interface boundary since other effects tend to appear (we will return to this point later).

2.5. Universal versus Specific Representations. There is clearly a universal flavour about (12), (13), (15a), (15b) and (16). For instance, there is no explicit mention of the system nonlinearity so that refraction is fully described by the mismatch parameters Δ and α and the beam parameter $4\kappa\beta_0$. These equations are, in fact, more general than they first appear; for instance, laws of exactly the same structure govern the refraction of plane waves in power-law materials: a wave with real amplitude u_0 has $\beta_0 \equiv u_0^q$ (it is noteworthy that the refraction analysis for plane waves does not capture the modulational instability of such solutions in the single power-law context [58]).

The power-law nature of the problem becomes apparent after one substitutes for β_0 from (8b). The γ factor (c.f. (15b)) then becomes

$$\gamma = \left[\frac{1+8\kappa\eta_0^q(2+q)^{-1}}{1+8\kappa\eta_0^q\alpha(2+q)^{-1}(1-\Delta)^{-1}}\right]^{1/2}, \tag{17a}$$

while the relation for the critical angle (c.f. (16)) is given by

$$\tan\theta_{\text{crit}} = \left[\frac{\Delta+8\kappa\eta_0^q(2+q)^{-1}(1-\alpha)}{1-\Delta+8\kappa\eta_0^q\alpha(2+q)^{-1}}\right]^{1/2}, \tag{17b}$$

and the net mismatch parameter (c.f. (13)) is $\delta = \Delta + 8\kappa\eta_0^q(1-\alpha)/(2+q)$.

3. Simulations of Solitons at Power-Law Interfaces

The Helmholtz type of off-axis nonparaxiality demands that the inequalities $\kappa \ll O(1)$ and $4\kappa\beta_0 \ll O(1)$ are always met, which is equivalent to the *simultaneous* requirements of broad beams with moderate intensities, respectively [23, 24, 56]. Here, attention is restricted to configurations where the mismatch parameters are relatively small, typically $\alpha = O(1)$ and $|\Delta| \ll O(1)$. We now proceed with a three-stage analysis. The simplest case to consider first is that of linear interfaces. We then move on to investigate nonlinear interfaces and conclude by noting the dependence of GH shifts [48, 49] on the nonlinearity exponent q. Stable solitons of the homogeneous power-law Helmholtz model tend to exist in the continuous interval $0 < q < 4$ [27, 56]. For definiteness, we consider here only three discrete values: $q = 1$ (sub-Kerr), 2 (Kerr), and 3 (super-Kerr).

3.1. Solitons at Linear Interfaces. From (13), linear interfaces are defined by the inequality $4\kappa\beta_0|1-\alpha| \ll |\Delta|$. To isolate the effects of a linear-index change alone, we set $\alpha = 1.0$ so that $\delta = \Delta$. One therefore finds the existence of a critical angle in regimes where $\Delta > 0$ (since $n_{02} < n_{01}$). The following simulations consider $q = 1$. Figure 2 shows generally good agreement between theoretical predictions and full numerical calculations when $\kappa = 2.5\times10^{-3}$; the level of agreement is improved even further when $\kappa = 1.0\times10^{-4}$.

The fact that smaller values of κ give rise to better theory-numerics agreement, despite the increased magnitude of the linear-interface perturbation term at $\Delta/4\kappa$, invites comment. We suspect that one possible explanation may lie in the origin of the Helmholtz-Snell law, whereby one matches solution phase (but not amplitude) at the boundary: the matching condition thus takes no account of amplitude curvature. In the laboratory frame, broader beams (i.e., those characterized by smaller κ values) tend to have lower amplitude curvature, and the corresponding spatial solitons (which play the role of nonlinear basis functions) thus map much more consistently onto the inherent assumptions of the analytical approach.

Upon crossing the interface, the refracted soliton may suffer small oscillations (in its amplitude, width, and area)

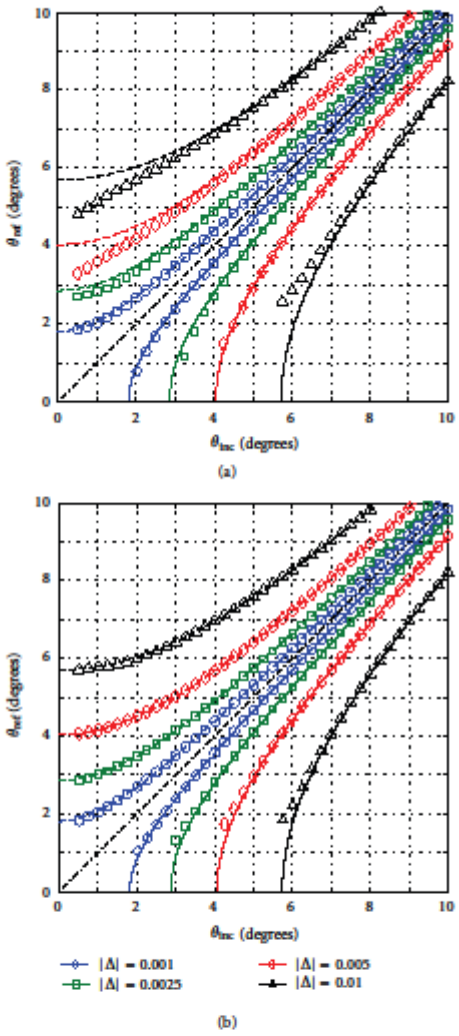

FIGURE 2: Comparison of the theoretical Snell's law given by (15a) and (15b) (lines) against full numerical computations (points) for a unit-amplitude ($\eta_0 = 1.0$) spatial soliton at a linear interface ($\alpha = 1.0$) with $q = 1$ and when (a) $\kappa = 2.5 \times 10^{-3}$ and (b) $\kappa = 1.0 \times 10^{-4}$. Curves below (above) the $\theta_{ref} = \theta_{inc}$ line have $\Delta > 0$ ($\Delta < 0$), so that the refraction is internal (external).

reminiscent of those reported in previous studies [56], and be accompanied by a radiation pattern. Computations [59] have verified the effective independence of the refraction angle θ_{ref} with respect to the incident amplitude η_0. Accordingly, the curves in Figure 2 are essentially insensitive to q; they are quantitatively very similar to those obtained for $q = 2$ [10] and (when θ_{inc} is sufficiently above θ_{crit} in internal-refraction regimes) for $q = 3$.

Any interaction between a spatial soliton and an interface generally involves three distinct components: a reflected beam, a refracted beam (sometimes more than one), and radiation. The way in which the incident energy is distributed amongst these components depends on a complicated interplay between the interface and beam parameters, and also the incidence angle. At very small angles (e.g., $\theta_{inc} < 1^\circ$), the interaction can be highly inelastic and nonadiabatic (especially in external refraction regimes). Crucially, the single refracted soliton (as predicted in Section 2) dominates as θ_{inc} approaches even modest nonparaxial angles, with reflected and radiation components hardly excited at all. The Helmholtz-Snell law embodied by (15a) and (15b) is, of course, most valid in such regimes.

3.2. Solitons at Nonlinear Interfaces. Nonlinear interface effects dominate beam refraction when $4\kappa\beta_0|1 - \alpha| \gg |\Delta|$. Without loss of generality, we isolate such effects by setting $\Delta = 0$ so that the net mismatch parameter is given by $\delta = 4\kappa\beta_0(1 - \alpha) = 8\kappa\eta_0^q(1 - \alpha)/(2 + q)$. Refraction thus becomes far more sensitive to κ in nonlinear regimes (compare this to linear regimes, where $\delta = \Delta$ is independent of κ). Theoretical predictions are shown in Figure 3. While there is generally good agreement with numerics for both $\kappa = 2.5 \times 10^{-3}$ and $\kappa = 1.0 \times 10^{-4}$ when $\alpha \approx 1.0$, the fit becomes less reliable for $\alpha = 2.0$ and $\alpha = 0.3$. For such parameters, the nonlinear refractive index change across the boundary is no longer small: one cannot expect to find such a close match because of strong nonlinear effects (e.g., beam splitting and radiation phenomena). While the fit is clearly better for broader beams ($\kappa = 1.0 \times 10^{-4}$), the Helmholtz-Snell predictions for narrower beams ($\kappa = 2.5 \times 10^{-3}$) are still in good qualitative agreement.

Detailed attention is first paid to regimes with $\alpha > 1$ (external refraction, since $\delta < 0$), where the nonlinearity is stronger in the second medium. Since the width of the refracted soliton is proportional to $\alpha^{-1/2}$, it follows that the beam must become narrower as it crosses the interface. In this type of material regime, the incident soliton always has sufficient energy flow to excite a self-trapped soliton-like state in medium 2.

Simulations have shown that nonlinear external refraction tends to induce stronger oscillations in the parameters (amplitude, width, and area = amplitude × width) of the outgoing beam than in the linear case. Such oscillations are not captured by the adiabatic analysis in Section 2 (which anticipates a stationary state), but one expects their appearance intuitively. Qualitatively different effects can appear at quasi-paraxial incidence angles as the exponent q is varied; an illustrative example is shown in Figure 4 for $\theta_{inc} = 3^\circ$ when $\alpha = 2.0$. A unit-amplitude soliton exhibits a pronounced splitting phenomenon when $q = 1$ (see Figure 4(b)), whereby the field distribution in the second medium is shared between a dominant externally refracted beam (as predicted by analysis) and a weaker internally refracted component (there is also a low-amplitude reflected

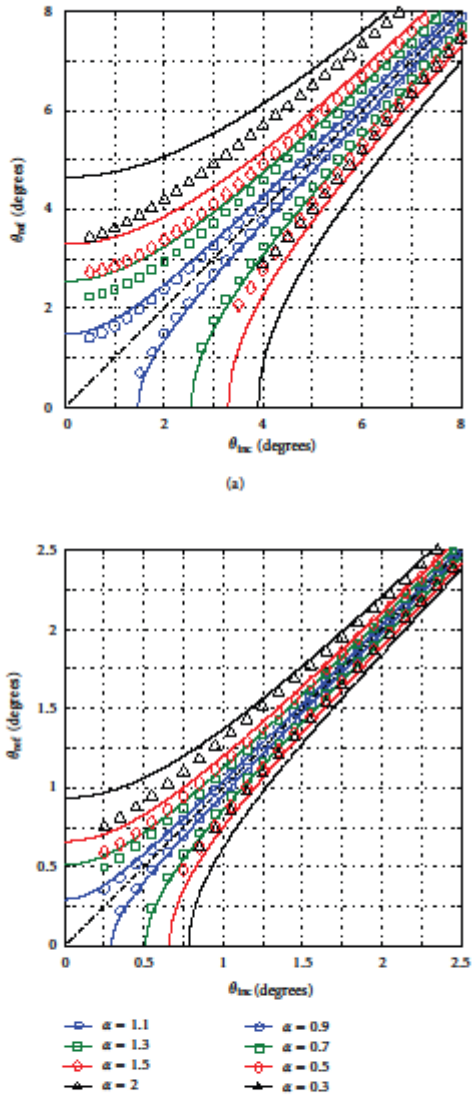

FIGURE 3: Comparison of the theoretical Snell's law given by (15a) and (15b) (lines) against full numerical computations (points) for a unit-amplitude ($\eta_0 = 1.0$) spatial soliton at a nonlinear interface ($\Delta = 0$) with $q = 1$ and when (a) $\kappa = 2.5 \times 10^{-3}$ and (b) $\kappa = 1.0 \times 10^{-4}$. Curves below (above) the $\theta_{ref} = \theta_{inc}$ line are labelled by the right-hand (left-hand) legend and have $\alpha < 1$ ($\alpha > 1$) so that refraction is internal (external). Note that the numerical datapoints for $\alpha = 0.3$ and $\alpha = 0.5$ are very close together in both panes.

component in the form of radiation modes). Since the internally refracted beam carries away some of the momentum of the incident beam, it follows that the dominant refracted beam travels at a smaller angle than that predicted by (15a) and (15b). This type of splitting is not present for unit-amplitude solitons with $q = 2$ (see Figure 4(b)), though it may appear for incident solitons with higher peak intensities [60]. In such cases, the properties of the daughter solitons may be quantified with recourse to inverse scattering techniques. Splitting is also absent at $q = 3$ (see Figure 4(c)), though one finds quite a complicated radiation ripple pattern in the second medium.

Refraction in nonparaxial regimes tends to be a much cleaner process, with little radiation generated by the beam-interface interaction in comparison with quasi-paraxial regimes. Even at modest angles (e.g., $\theta_{inc} = 30^{\circ}$), where the interface perturbation is distributed over a relatively short interaction length, the quantitative characteristics of the outgoing beam depend crucially on the power-law exponent. Both the depth of modulation and (longitudinal spatial) frequency of the oscillations tend to increase with q, as shown in Figure 5(a). When $q = 2$, the oscillations tend to vanish in ζ; for $q = 1$ and 3, they survive in the long-term evolution (this is also true for the oscillations shown in Figure 4(a)). A more detailed comparison of how the q affects beam refraction is presented in Figures 5(b)–5(d).

For material combinations with $\alpha < 1$ (internal refraction, since $\delta > 0$), the nonlinearity is weaker in the second medium. In that case, one should expect a critical angle to exist (in accordance with (17b)). If the incident soliton survives the interaction with the interface, then the refracted beam may be expected to undergo self-reshaping oscillations in its parameters, with the overall trend being toward an increase in solution width. Simulations have confirmed this to be the case, with diffractive broadening generally accompanied by a reduction in peak amplitude (see Figure 6(a))—these oscillations are reminiscent of those uncovered previously for perturbed initial-value problems [56].

Computations have uncovered a range of q-dependent effects, an illustrative sample of which is shown in Figure 6 for beams with $\kappa = 2.5 \times 10^{-3}$, a nonparaxial incidence angle $\theta_{inc} = 30^{\circ}$, and a nonlinear mismatch of $\alpha = 0.5$. The (longitudinal spatial) frequency of the reshaping oscillations tends to decrease with increasing q (c.f., the *increase* with q when $\alpha > 1$). Also at higher q values (e.g., for $q = 3$), a threshold phenomenon can appear whereby the energy-flow [56] of the incident soliton may not be great enough to excite a refracted beam (if the energy flows associated with solutions (8a) and (10) are denoted by W_{inc} and W_{ref}, respectively, then it can be shown that $W_{ref} \approx W_{inc}/\alpha^{1/2}$). This instability is shown in Figure 6(d): upon colliding with the interface, the beam breaks up into radiation (this scenario is also present at quasi-paraxial incidence angles above the critical angle θ_{crit}).

3.3. *Snaking at Nonparaxial Angles.* Equations (15a) and (15b) show that, at nonlinear interfaces, the refraction

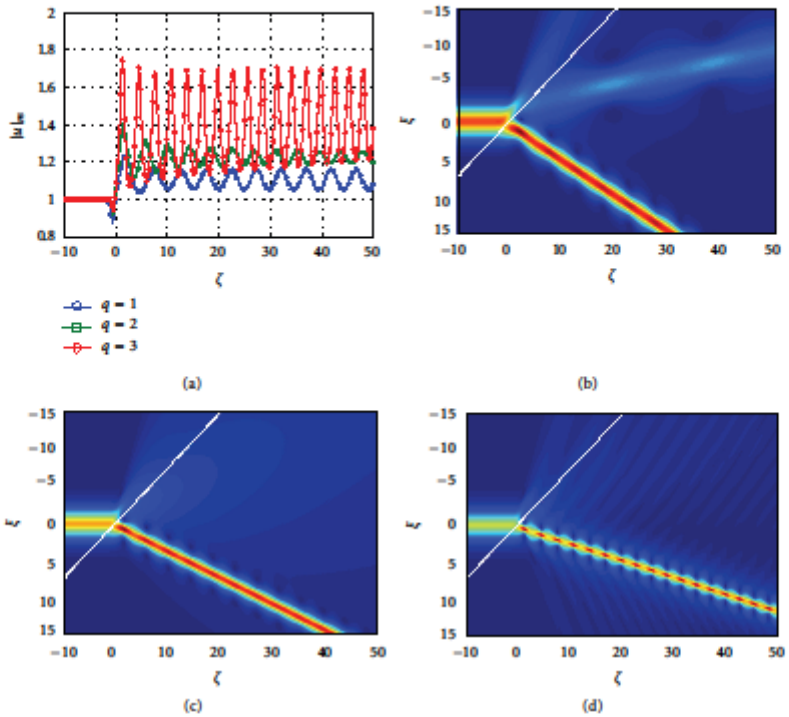

Figure 4: External refraction of a unit-amplitude ($\eta_0 = 1.0$) spatial soliton at a nonlinear interface with $\alpha = 2.0$ and a quasi-paraxial incidence angle $\theta_{inc} = 3°$ when $\kappa = 2.5 \times 10^{-3}$. (a) Evolution in ζ of the peak amplitude $|u|_m$ of the beam. (b), (c), and (d) show the full numerical solution $|u(\xi, \zeta)|$ of (5) when the nonlinearity exponent is $q = 1$, 2, and 3, respectively.

angle must depend on q (a prediction supported by simple inspection of Figures 4, 5, and 6). At this point, it also becomes instructive to consider the trajectory of refracted beams more carefully. Detailed numerical calculations reveal that at quasi-paraxial incidence angles, the beam in the second medium tends to follow a straightline path. Such a simple notion of refraction, founded upon intuition from plane wave theory, is illustrated in Figure 7(a) for a nonlinear interface with $\alpha = 2.0$ and a beam with $\theta_{inc} = 3°$ and $\kappa = 2.5 \times 10^{-3}$. However, if the incidence angle is increased into the nonparaxial domain (e.g., $\theta_{inc} = 30°$), a qualitatively different picture emerges. Now, the straightline path $\xi - V_{ref}\zeta = 0$ predicted by solution (10) defines an average trajectory about which the refracted beam "snakes." Figure 7(b) quantifies this snaking effect for the external refraction simulations shown in Figures 5(b)–5(d). Snaking is more apparent with sub-Kerr nonlinearities (i.e., where $q < 2$), and it increases for narrower beams (i.e., larger values of κ) at a fixed amplitude (see Figure 8(a), where $\eta_0 = 1.0$). Beams with larger amplitudes also exhibit snaking, but oscillations tend to be more rapid in the longitudinal direction (see Figure 8(b)).

The snaking phenomenon is most pronounced in regimes with $\alpha > 1$, where the nonlinearity is stronger in the second medium. There is also an intrinsic dependence on θ_{inc} that can be seen in Figure 7. For small angles of incidence, the incoming soliton experiences an interface perturbation that is distributed over a relatively long distance. The refracting beam is able to accommodate the inhomogeneity in the system since changes in focusing properties of the host medium occur gradually in the longitudinal direction. For larger-incidence angles, the effective beam-interface interaction length may be much shorter. Solitons impinging on the boundary then exhibit a sharp (rather than a gradual) perturbation whose action is to induce sustained oscillations.

3.4. Goos-Hänchen Shifts at Power-Law Interfaces. Recently, GH shifts [48] have been investigated within the context of Helmholtz spatial solitons at Kerr-type material interfaces [49]. These shifts describe the translation in the trajectory

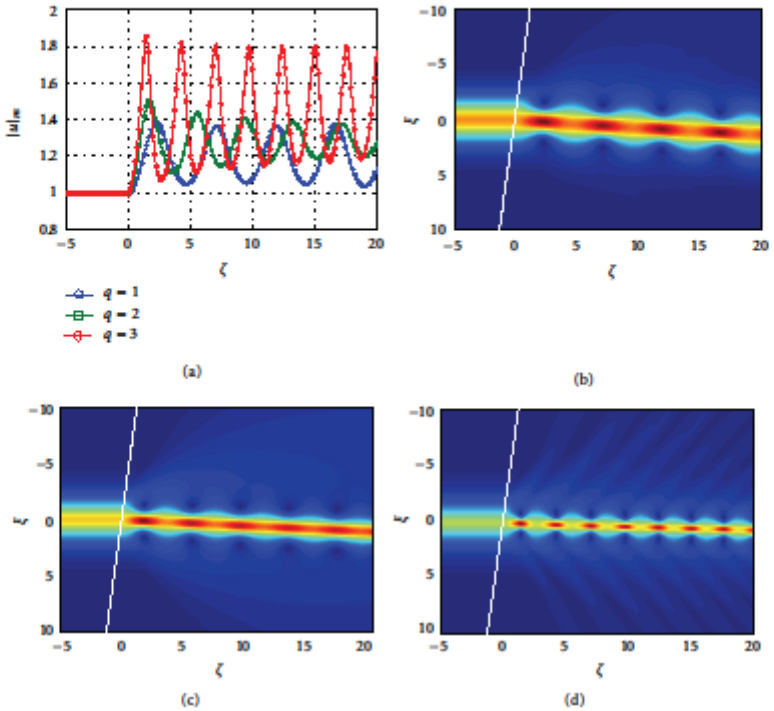

FIGURE 5: External refraction of a unit-amplitude ($\eta_0 = 1.0$) spatial soliton at a nonlinear interface with $\alpha = 2.0$ and a nonparaxial incidence angle $\theta_{inc} = 30°$ when $\kappa = 2.5 \times 10^{-3}$. (a) Evolution in ζ of the peak amplitude $|u|_m$ of the beam. (b), (c), and (d) show the full numerical solution $|u(\xi, \zeta)|$ of (5) when the nonlinearity exponent is $q = 1$, 2, and 3, respectively.

of a reflected beam relative to its position as predicted by geometrical optics. Extensive numerical investigations considered the interplay between incidence angle θ_{inc}, material mismatches (Δ, α), and the nonparaxial parameter κ. Radiation-induced trapping was found to play a key role in determining the magnitude of the shift. Also uncovered were giant *external* GH shifts (in regimes with $\delta > 0$ but where the second medium has a *weaker* nonlinearity (i.e., $\alpha < 1$)). While a similar investigation of GH shifts in the power-law context is certainly outside our current scope, a small selection of results will now be presented to illustrate how they depend upon the nonlinearity exponent q.

We begin by considering linear interfaces and unit-amplitude incident solitons with $\kappa = 2.5 \times 10^{-3}$. According to (16), interfaces with $\Delta = 0.0025$ have a theoretical critical angle of $\theta_{crit} \approx 2.86°$ (this value depends only very weakly on q). Figure 9(a) gives a representative set of results. Inspection shows that, for any θ_{inc}, the magnitude of the shift is generally greater for systems with $q = 1$ than for $q = 2$ or $q = 3$. The true critical angle (which can only be found through full simulations) is also slightly greater than that predicted by theory (for $q = 1$ and $q = 2$, $\theta_{crit} \approx 3.016°$ and $\theta_{crit} \approx 3.030°$; both angles exceed their theoretical values of $\theta_{crit} \approx 2.857°$ and $\theta_{crit} \approx 2.859°$, respectively). While the qualitative behaviour of systems with $q = 1$ and $q = 2$ is largely very similar, strong qualitative differences have been uncovered in the case of $q = 3$. As θ_{inc} approaches the theoretical critical angle, the incident soliton often becomes unstable against the interface perturbation. Large amounts of radiation tend to be generated by the interaction (c.f. Figure 9(d)), so that there is essentially no reflected or refracted beam and a GH shift is thus not easily quantifiable (or even meaningful). However, when θ_{inc} is sufficiently above θ_{crit}, the refraction angle is still well described by theory.

GH shifts at nonlinear interfaces have also been analyzed; results are presented in Figure 10 for $\alpha = 0.7$ and where system nonlinearity has been augmented by considering incident solitons with $\eta_0 = 2.0$. Regimes with $\Delta = -0.001$ and $\Delta = -0.0025$ are associated with linear *external* refraction, while (13) shows that $\delta > 0$ (i.e., for these parameter sets, net refraction is *internal* so that a critical angle should still exist). One general trend to emerge is that the true critical angle is slightly less than the theoretical value (c.f. linear interfaces of Figure 9, where

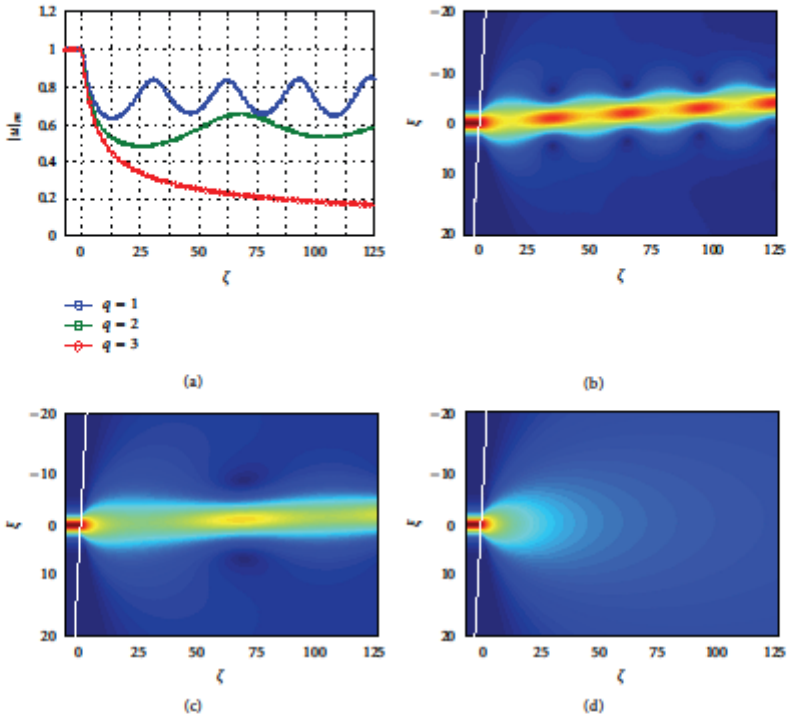

FIGURE 6: Internal refraction of a unit-amplitude ($\eta_0 = 1.0$) spatial soliton at a nonlinear interface with $\alpha = 0.5$ and a nonparaxial incidence angle $\theta_{inc} = 30^\circ$ when $\kappa = 2.5 \times 10^{-3}$. (a) Evolution in ζ of the peak amplitude $|u|_m$ of the beam. (b), (c), and (d) show the full numerical solution $|u(\xi, \zeta)|$ of (5) when the nonlinearity exponent is $q = 1$, 2, and 3, respectively.

the true critical angle slightly exceeds theory). However, it is worth noting that the qualitative behaviour predicted by (16), namely that θ_{crit} increases with q, is supported by numerics. Close to the (true) critical angle, simulations show that there is a strong divergence in the GH shift (which becomes highly sensitive to θ_{inc}). Two other general trends are that (i) GH shifts are larger (sometimes notably) for $q = 1$ than for $q = 3$; (ii) in nonlinear regimes, the GH shifts depend more strongly on q than for the case of linear interfaces (compare Figure 10 to Figure 9(a)).

Figure 10(b) reveals new types of behaviour at power-law interfaces when $q \neq 2$. In particular, for $q = 3$ one enters a regime wherein the GH shift no longer increases monotonically with θ_{inc}; instead, there is a marked decrease in the shift before the divergence at $\theta_{inc} \approx \theta_{crit}$ sets in. These results provide clear evidence that one can, quite reasonably, expect to find new qualitative phenomena in material regimes that deviate from the idealized Kerr-type response.

4. Helmholtz Nonlinear Surface Waves

Surface waves are well known in nonlinear photonics, being stationary localized light states that travel along the interface between different media. The transverse mode profiles are typically asymmetric due to the differences in dielectric properties defining the interface. We now derive the surface modes of model (5) using solitons (8a) and (10) as a nonlinear basis. These new solutions are most conveniently parameterized by β, which is related to the propagation constant in paraxial theory [27, 56].

4.1. Exact Analytical Solutions. To proceed, one seeks solutions to (5) of the form $u(\xi, \zeta) = F(\xi - \xi_J) \exp(ik_\zeta \zeta) \exp(-i\zeta/2\kappa)$, where k_ζ is the propagation constant and $F(\xi - \xi_J)$ is the (real) envelope profile that is centred on ξ_J. After substituting for u and defining $\kappa k_\zeta^2 - 1/4\kappa \equiv \beta$, it can be shown that in medium 1

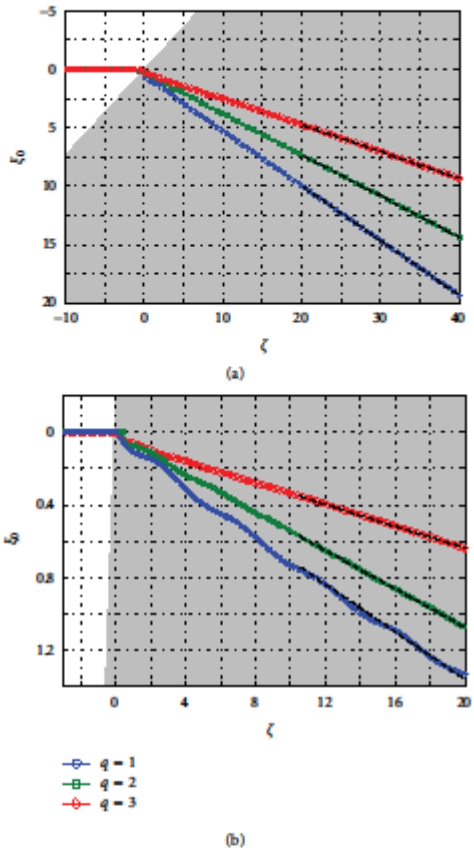

Figure 7: External refraction of a unit-amplitude ($\eta_0 = 1.0$) spatial soliton at a nonlinear interface with $\alpha = 2.0$ when the incidence angle is (a) quasi-paraxial ($\theta_{inc} = 3^\circ$) and (b) nonparaxial ($\theta_{inc} = 30^\circ$) for $\kappa = 2.5 \times 10^{-3}$. In (a), the trajectory of the beam in the second medium is essentially a straight line. In (b), the trajectory oscillates ("snakes") around the straight-line path predicted by the analysis in Section 2. Calculations of the beam centre ξ_0 were obtained by fitting the numerical solution at each longitudinal position to a trial function of the form $u_{fit}(\xi) = \eta(\zeta)\mathrm{sech}^{2/q}\{a(\zeta)[\xi - \xi_0(\zeta)]\}$. Black dashed lines: best-fit trajectory.

$$u(\xi,\zeta) = \left(\frac{2+q}{2}\beta\right)^{1/q}\mathrm{sech}^{2/q}\left[\frac{q}{\sqrt{2}}\beta^{1/2}(\xi-\xi_1)\right] \times \exp\left(\pm i\sqrt{1+4\kappa\beta}\frac{\zeta}{2\kappa}\right)\exp\left(-i\frac{\zeta}{2\kappa}\right), \quad (18a)$$

while in medium 2

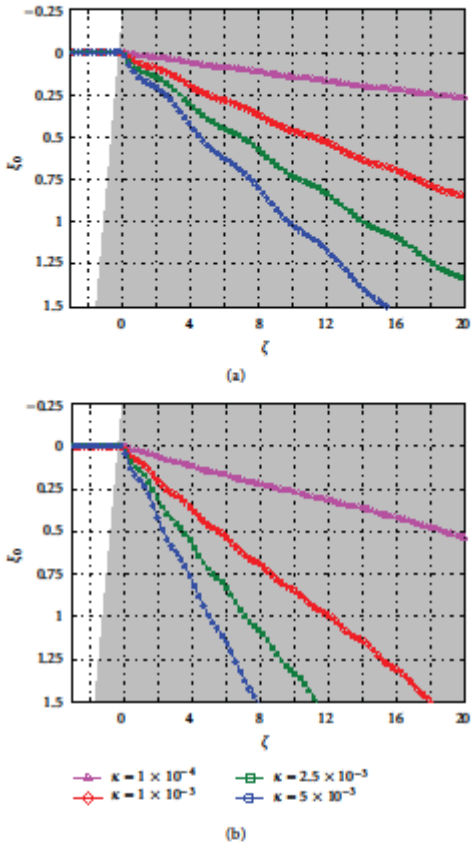

Figure 8: External refraction of spatial solitons at a nonlinear interface with $\alpha = 2.0$ for a nonparaxial angle $\theta_{inc} = 30^\circ$ for $q = 1$ and different values of κ. The peak amplitude of the incident beam in each case is (a) $\eta_0 = 1.0$ and (b) $\eta_0 = 2.0$.

$$u(\xi,\zeta) = \left[\left(\frac{2+q}{2}\beta\right)\left(\frac{1}{\alpha}\right)\left(1+\frac{\Delta}{4\kappa\beta}\right)\right]^{1/q} \times \mathrm{sech}^{2/q}\left[\frac{q}{\sqrt{2}}\beta^{1/2}\left(1+\frac{\Delta}{4\kappa\beta}\right)^{1/2}(\xi-\xi_2)\right] \times \exp\left(\pm i\sqrt{1+4\kappa\beta}\frac{\zeta}{2\kappa}\right)\exp\left(-i\frac{\zeta}{2\kappa}\right). \quad (18b)$$

For a nonlinearity exponent q, the surface waves associated with any given interface are parameterized solely by β. The displacements ξ_1 and ξ_2, as yet undetermined, can be found by considering the auxiliary equations that arise from respecting continuity of u and its normal derivative (here

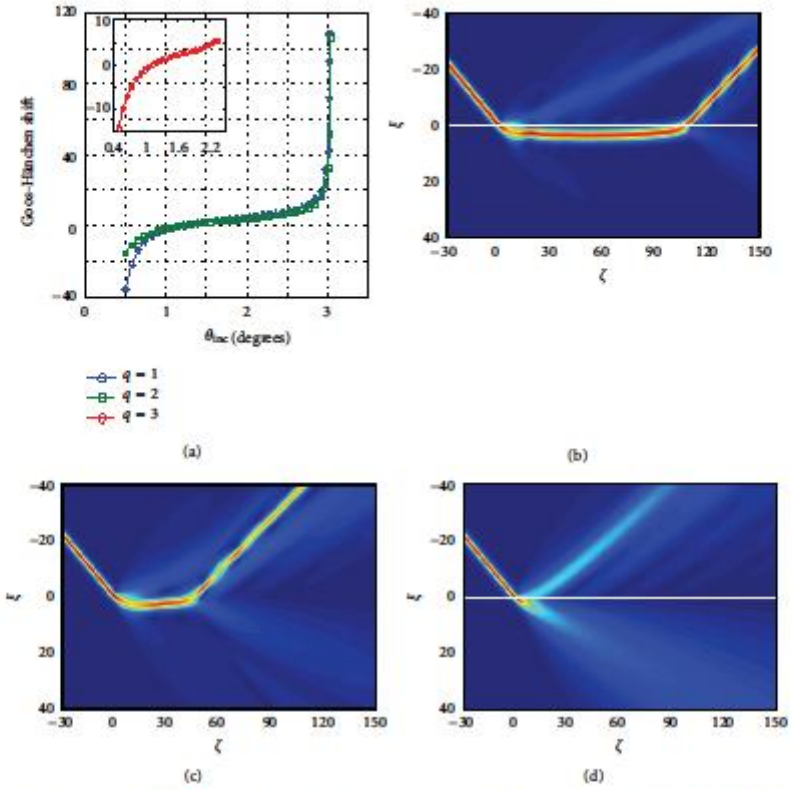

Figure 9: Demonstration of the GH shift for a unit-amplitude ($\eta_0 = 1.0$) spatial soliton at a linear interface with $\Delta = 0.0025$ and when $\kappa = 2.5 \times 10^{-3}$. (a) Variation of the GH shift with changing nonlinearity exponent q (the $q = 3$ results (inset) closely follow those for $q = 2$ until radiation effects come into play more strongly). (b), (c), and (d) show the full numerical solution $|u(\xi, \zeta)|$ of (5) when $q = 1$, 2 and 3, respectively (note that, over longer propagation lengths, the solution in (d) breaks up into radiation). The incidence angle in (b), (c), and (d) is $\theta_{inc} = 3.016°$, which exceeds the (almost q-independent) critical angle $\theta_{crit} \approx 2.86°$.

$\partial u/\partial\xi$ or, equivalently, $dF/d\xi$) across the interface. These conditions lead to

$$\operatorname{sech}^{2/q}\left(\frac{q}{\sqrt{2}}\beta^{1/2}\xi_1\right) = \left[\frac{1}{\alpha}\left(1+\frac{\Delta}{4\kappa\beta}\right)\right]^{1/q} \times \operatorname{sech}^{2/q}\left[\frac{q}{\sqrt{2}}\beta^{1/2}\left(1+\frac{\Delta}{4\kappa\beta}\right)^{1/2}\xi_2\right], \tag{19a}$$

$$\tanh\left(\frac{q}{\sqrt{2}}\beta^{1/2}\xi_1\right) = \left(1+\frac{\Delta}{4\kappa\beta}\right)^{1/2} \times \tanh\left[\frac{q}{\sqrt{2}}\beta^{1/2}\left(1+\frac{\Delta}{4\kappa\beta}\right)^{1/2}\xi_2\right], \tag{19b}$$

respectively. After some algebraic manipulation of (19a) and (19b), one finds that

$$\xi_1 = \frac{\sqrt{2}}{q}\beta^{-1/2}\ln\left(\frac{1\pm\sqrt{1-\delta^2}}{\delta}\right) \tag{20a}$$

$$\xi_2 = \frac{\sqrt{2}}{q}\beta^{-1/2}\left(1+\frac{\Delta}{4\kappa\beta}\right)^{-1/2}\ln\left(\frac{1\pm\sqrt{1-\mu^2}}{\mu}\right), \tag{20b}$$

where the parameters δ and μ are given by $\delta \equiv [\Delta/4\kappa\beta(\alpha - 1)]^{1/2}$ and $\mu \equiv [(\Delta/4\kappa\beta)(1 + \Delta/4\kappa\beta)^{-1}(1 - 1/\alpha)^{-1}]^{1/2}$.

4.2. Surface Wave Existence Criterion. For displacements ξ_1 and ξ_2 to be real, it must be that $0 < \delta^2 < 1$ and $0 < \mu^2 < 1$. These two simultaneous requirements lead to a third

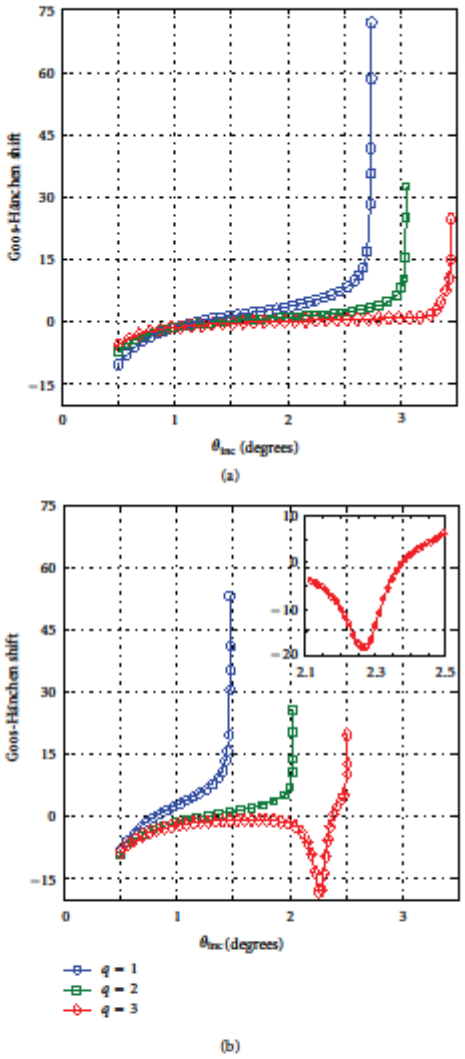

FIGURE 10: Numerical calculation of the GH shift for incident spatial solitons with $\eta_0 = 2.0$ at a nonlinear interface with $\alpha = 0.7$, (a) $\Delta = -0.001$, and (b) $\Delta = -0.0025$ when $\kappa = 2.5 \times 10^{-3}$ (inset shows the behaviour of the shift for $q = 3$ around the minimum).

inequality placed on the product $4\kappa\beta$, namely, $4\kappa\beta > 4\kappa\beta_{min}$, where

$$4\kappa\beta_{min} = \frac{\Delta}{\alpha - 1} \tag{21}$$

(it is interesting to note that $4\kappa\beta_{min}$ is independent of q). Thus, existence criterion (21) for Helmholtz surface waves explicitly involves the (inverse) beam size through the appearance of κ. Since $4\kappa\beta$ must remain positive, it follows that surface modes are supported in two distinct parameter regimes: (i) regime 1: $\Delta > 0$ and $\alpha > 1$ (i.e., $n_{02}^2 < n_{01}^2$ and $\alpha_2 > \alpha_1$) and (ii) regime 2: $\Delta < 0$ and $0 < \alpha < 1$, (i.e., $n_{02} > n_{01}, \alpha_2 < \alpha_1$). We mention, in passing, that (21) is reminiscent of the existence criterion derived by Aceves et al. [8]; it differs through the explicit appearance of κ. Typical surface wave profiles are shown in Figure 11.

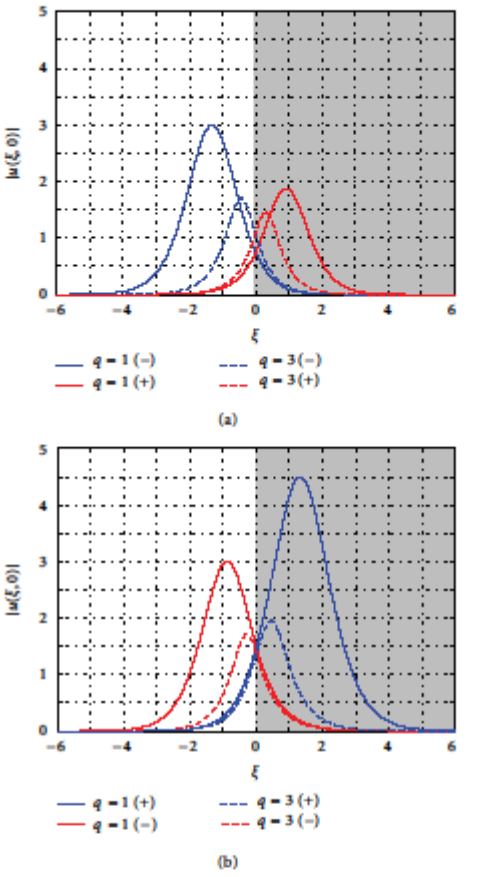

FIGURE 11: Nonlinear surface wave profiles for $\kappa = 2.5 \times 10^{-3}$ in (a) regime 1 (with $\Delta = 0.005$ and $\alpha = 2.0$) and (b) regime 2 (with $\Delta = -0.005$ and $\alpha = 0.5$). From (21), one has that $4\kappa\beta_{min} = 0.005$ and hence $\beta_{min} = 0.5$ for the solutions in (a), while $4\kappa\beta_{min} = 0.01$ and hence $\beta_{min} = 1.0$ in (b). In these profiles, $\beta = 2.0$ so that $\beta > \beta_{min}$ in each case. The + and − signs in the legends refer to the choice of sign solution in (20a) and (20b).

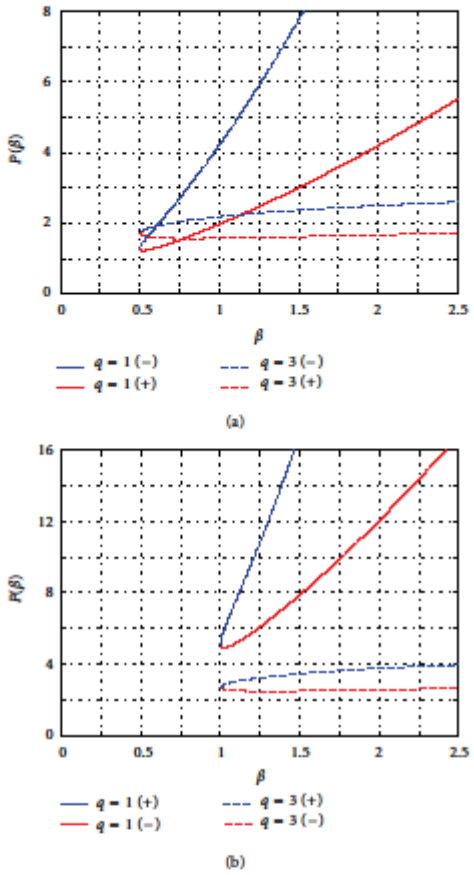

FIGURE 12: Power curves as a function of the propagation constant β, obtained from (22) with $\kappa = 2.5 \times 10^{-3}$. (a) Regime 1 with $\Delta = 0.005$ and $\alpha = 2.0$ and (b) regime 2 with $\Delta = -0.005$ and $\alpha = 0.5$. The + and − signs in the legends refer to the choice of solution in (20a) and (20b). Lower (upper) solution branches appear as red (blue) lines, and each branch generally satisfies the VK stability criterion [61].

4.3. Solution Families and Wave Power. For both forward- and backward-propagating surface waves, there exist two solution families. The origin of this duality lies in solving simultaneous equations (19a) and (19b), where one is eventually obliged to find the roots of quadratic equations. Figure 11 reveals that, for fixed (Δ, α, β), the profile depends strongly on the nonlinearity exponent q. That is, the peak amplitude, width, and area all decrease with increasing q. The difference between the two peak amplitudes and the distance of each solution peak from the interface also decrease with increasing nonlinearity exponent.

Since the surface wave profiles differ, it is plausible that the two families will not share the same stability properties. We begin an analysis of Helmholtz solutions (18a) and (18b) by considering the power P, where

$$P(\beta; q) \equiv \int_{-\infty}^{+\infty} d\xi \, |u(\xi, \zeta)|^2, \tag{22}$$

as a function of the free parameter β for different values of the nonlinearity exponent q. The energy-flow invariant W [56] is related to P through $W(\beta) = \pm(1 + 4\kappa\beta)^{1/2} P(\beta)$, where the $\pm$ sign here corresponds to forward- or backward-propagating envelopes (being distinct from the sign choice in (20a) and (20b)). A representative set of curves is shown in Figure 12, where it can be seen that $P(\beta)$ comprises two branches. In regime 1 (where $\Delta > 0$ and $\alpha > 1$), the lower (upper) branch corresponds to the $-(+)$ sign in (20a) and (20b). This situation is reversed for regime 2 (where $\Delta < 0, 0 < \alpha < 1$), in which the lower (upper) branch corresponds to the $+(-)$ sign (see Figure 11). We note that for lower-branch solutions, the peak of the surface wave always resides in whichever medium has the lower linear refractive index.

Global trends in the parameter dependence of the modes profiles can be readily identified and discussed in the context of the two solution branches. For instance, one might fix Δ, β, and κ and consider the effect of varying α. In regime 1, one finds that upon increasing α, the upper-branch solutions tend to retain their shape while the lower-branch solutions experience a decrease in amplitude, width, and area. The separation between the pair of solutions also becomes greater, with each localized wave moving *away from* the interface. As α is increased in regime 2, the lower-branch solutions tend to retain their shape while the upper-branch solution exhibits decreases in amplitude, width, and area. Also, the separation between the solutions tends to decrease with increasing α (so that the solutions move *toward* the boundary).

4.4. Surface Wave Stability. Except near the intersection point (where $\beta \approx \beta_{\text{min}}$), both $P(\beta)$ branches satisfy the classic Vakhitov-Kolokolov (VK) criterion for stability; namely, $dP/d\beta > 0$ [61]. Extensive simulations have revealed that lower-branch solutions always tend to remain self-trapped within the vicinity of the interface (so long as $dP/d\beta > 0$) evolving with a stationary profile over arbitrarily long distances.

Upper-branch solutions tend to display a spontaneous instability in finite ζ. A set of typical results is shown in Figure 13 for regime 1 with $\Delta = 0.005$ and $\alpha = 2.0$, where the input wave is localized predominantly in medium 1 (compare with Figure 11(a)). The initial stages of evolution appear to be stationary, but instability sets in after a finite propagation length. The unstable solution deviates spontaneously into medium 2, crossing the boundary and shedding radiation in the process. The beam in medium 2 undergoes narrowing since $\alpha > 1$. For fixed interface and solution parameters, the instability growth rate clearly increases with q. However, the angular deviation of the

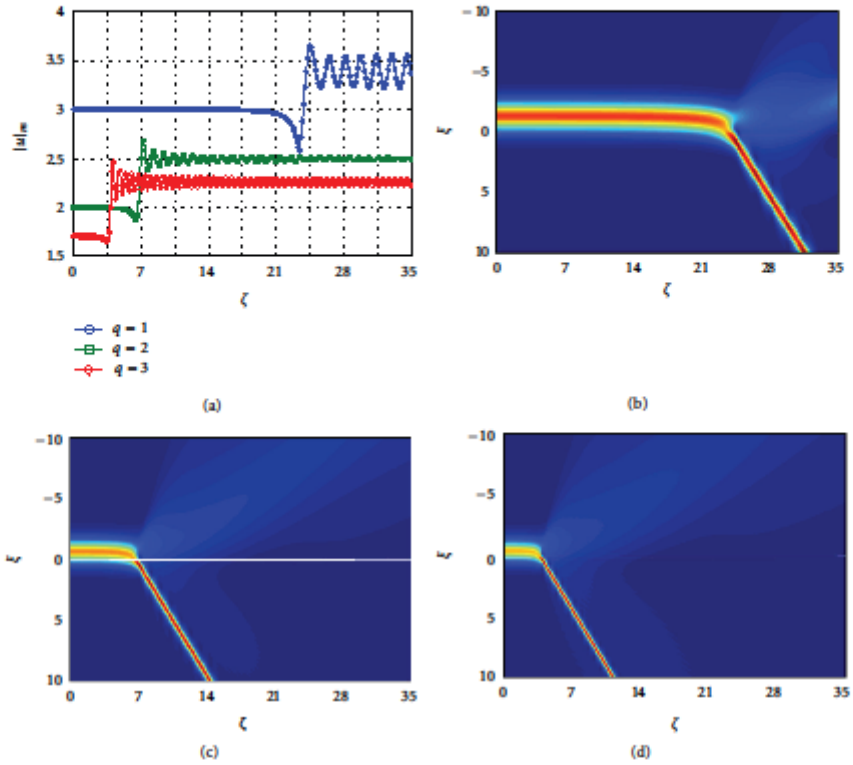

FIGURE 13: Spontaneous instability of nonlinear surface waves lying on the upper solution branch of Figure 12(a), where $\kappa = 2.5 \times 10^{-3}$ and $\beta = 2.0$ (interface mismatch parameters are $\Delta = 0.005$ and $\alpha = 2.0$). (a) Evolution in ζ of the peak amplitude $|u|_m$ of the beam. (b), (c), and (d) show the full numerical solution $|u(\xi, \zeta)|$ of (5) when the nonlinearity exponent is $q = 1$, 2, and 3, respectively. Note that the profiles of the input waves in (b) and (d) correspond to the upper-branch solutions shown in Figure 11(a).

(reshaping) daughter beam relative to the interface is largely insensitive to q.

Qualitatively different effects appear in regime 2 with $\Delta = -0.005$ and $\alpha = 0.5$; this time, the input wave is localized predominantly in medium 2 (compare with Figure 11(b)). After a finite propagation length, the surface wave bends smoothly away from the interface and is deflected deeper into medium 2. There is relatively little radiation shed in this process, and the localized wave suffers only a very small change to its shape (largely because the beam remains always on the same side of the interface, so does not encounter changes in refractive index). In common with regime 1, the instability growth rate increases with q.

4.5. Interactions between Solitons and Surface Waves. The stability of lower-branch surface waves is now investigated by considering their resilience against interactions with spatial solitons. Only a brief summary is presented here since the primary motivation is to uncover qualitatively new effects that depend upon the exponent q (detailed quantitative analyses are reserved for future works). For definiteness, we present simulation results for collisions between a unit-amplitude ($\eta_0 = 1.0$) soliton and surface waves in regimes 1 ($\Delta = 0.005, \alpha = 2.0$) and 2 ($\Delta = -0.005, \alpha = 0.5$) with $\beta = 2.0$ and $\kappa = 2.5 \times 10^{-3}$.

Regime 1 is considered first for a quasi-paraxial incidence angle of $\theta_{\text{inc}} = 3°$ (see Figure 14). When $q = 1$, the two distinct beams persist after the interaction. The path of the outgoing soliton has been deflected relative to its ingoing trajectory. The surface wave, on the other hand, survives as a localized spatial structure but can no longer be interpreted as a "surface wave" per se since it travels obliquely to (not along) the interface. This picture is qualitatively different for $q = 2$ and 3; there, the interaction results in the coalescence

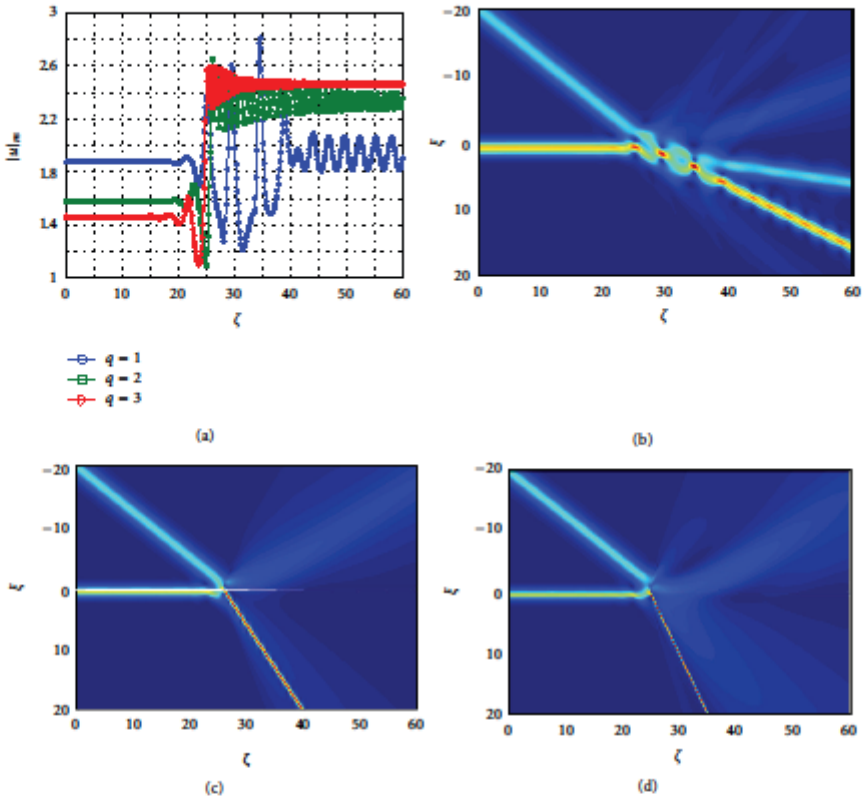

FIGURE 14: Quasi-paraxial interaction ($\theta_{inc} = 3^{\circ}$) between a lower-branch nonlinear surface wave (with $\beta = 2.0$) and a unit-amplitude ($\eta_0 = 1$) soliton in regime 1 (mismatch parameters $\Delta = 0.005$ and $\alpha = 2.0$) with $\kappa = 2.5 \times 10^{-3}$. (a) Evolution in ζ of the peak amplitude $|u|_m$ of the solution. Parts (b), (c), and (d) show the full numerical solution $|u(\xi, \zeta)|$ of (5) when the nonlinearity exponent is $q = 1$, 2 and 3, respectively.

of the soliton and surface wave, producing a single higher-intensity narrow filament travelling obliquely to the interface (narrowing is to be expected for medium combinations with $\alpha > 1$). It is noteworthy that the propagation angle of the filament, relative to the interface, increases with q. Also, as one might expect, nonlinear beams interacting at quasi-paraxial angles tend to shed a large amount of radiation.

The qualitative behaviour can change dramatically at nonparaxial angles; a representative set of simulations for $\theta_{inc} = 30^{\circ}$ is shown Figure 15. We have not observed coalescence phenomena; instead of this, individual beams retain their separate identities and can be clearly resolved. While the soliton often survives intact (and experiences a narrowing effect due to $\alpha > 1$), the evolution of the surface wave depends strongly on the nonlinearity exponent: (i) for $q = 1$, it acquires slow modulations in its shape but remains localized within the vicinity of the interface (i.e., it remains essentially a surface wave after the interaction); (ii) for $q = 2$, its path is deviated by the interaction so that it no longer travels along the interface (this obliquely-evolving self-trapped structure is, by definition, not a surface wave); (iii) for $q = 3$, the collision destroys it completely. It is interesting to note the general trend that larger-interaction angles generate far less radiation than their paraxial counterparts [62].

We now turn our attention to similar interaction scenarios in regime 2. For a quasi-paraxial incidence angle of 3°, the behaviour is strikingly different from that uncovered for the same angle in regime 1 (compare Figures 16 and 14, respectively). When $q = 1$, the soliton survives the interaction and the surface wave remains quasi-bound to the interface (but exhibiting a longitudinal "skimming" effect).

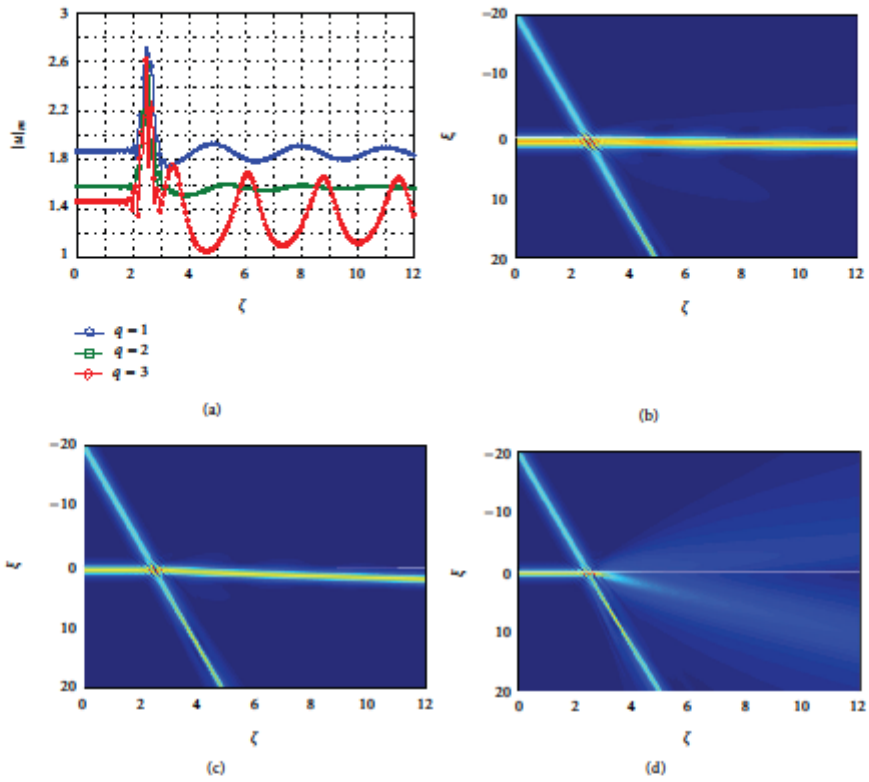

FIGURE 15: Nonparaxial interaction ($\theta_{inc} = 30^\circ$) between a lower-branch nonlinear surface wave (with $\beta = 2.0$) and a unit-amplitude ($\eta_0 = 1$) soliton in regime 1 (mismatch parameters $\Delta = 0.005$ and $\alpha = 2.0$) with $\kappa = 2.5 \times 10^{-3}$. (a) Evolution in ζ of the peak amplitude $|u|_m$ of the solution. (b), (c), and (d) show the full numerical solution $|u(\xi, \zeta)|$ of (5) when the nonlinearity exponent is $q = 1$ (surface wave follows interface), 2 (surface wave deflected), and 3 (surface wave destroyed), respectively.

For $q = 2$ and 3, the interaction deflects the surface wave away from the boundary (i.e., the surface wave becomes an obliquely-evolving beam). However, the behaviour of the soliton is different for $q = 2$ and 3: it survives intact in the former case and breaks up into radiation in the latter (this effect is related to the threshold phenomenon discussed in Section 3.2 and is not a consequence of the interaction with the surface wave).

5. Conclusion

We have presented, to the best of our knowledge, the first investigation of the way spatial solitons behave at the planar interface between dissimilar materials whose refractive index has a power-law dependence on the electric field amplitude. This analysis has thus extended arbitrary angle refraction considerations beyond the ubiquitous Kerr-type case [17, 18, 25, 26]. Exact analytical solitons have been deployed as a nonlinear basis [56], permitting the derivation of a generalized Helmholtz-Snell law. Extensive numerical computations have tested its predictions, which are most accurate in regimes where only the linear refractive index changes across the boundary.

A range of new quantitative *and qualitative* effects that depend strongly upon the exponent q has been identified. For example, simulations have found that, at linear interfaces with $\Delta > 0$ and where $q = 1$ or 2, there is generally a well-defined transition (as θ_{inc} increases) from soliton reflection, through GH shifting, to soliton refraction. In contrast, systems with $q = 3$ are often far more complex: the reflection-to-refraction transition is generally obscured by radiation effects over a finite band of incidence angles around the (theoretical) critical angle: solitons interacting with

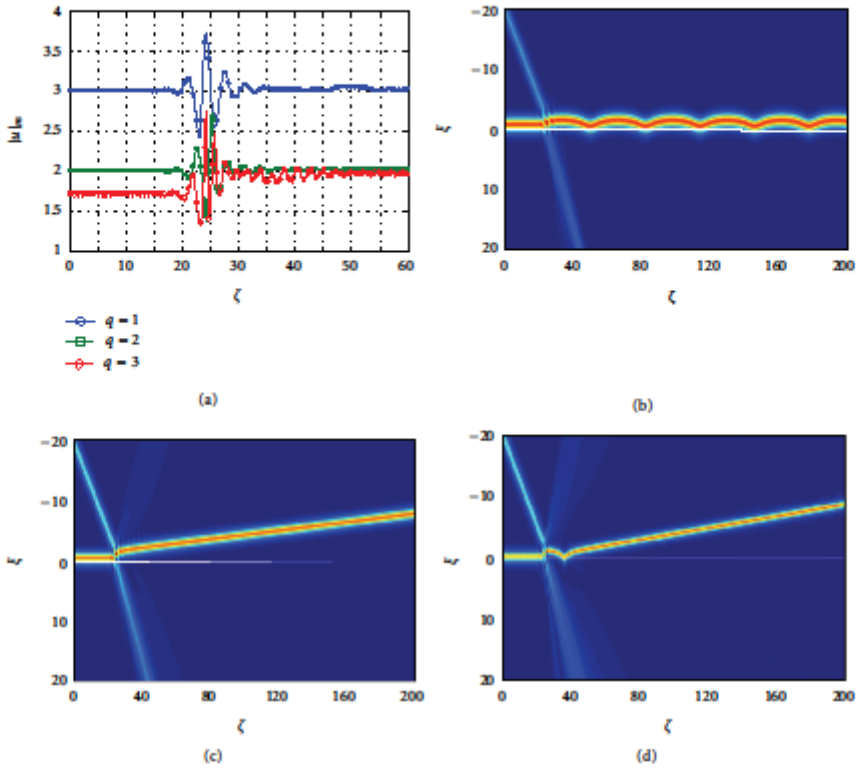

FIGURE 16: Quasi-paraxial interaction ($\theta_{inc} = 3^{\circ}$) between a lower-branch nonlinear surface wave (with $\beta = 2.0$) and a unit-amplitude ($\eta_0 = 1$) soliton in regime 2 (mismatch parameters $\Delta = -0.005$ and $\alpha = 0.5$) with $\kappa = 2.5 \times 10^{-3}$. (a) Evolution in ζ of the peak amplitude $|u|_m$ of the solution. (b), (c), and (d) show the full numerical solution $|u(\xi, \zeta)|$ of (5) when the nonlinearity exponent is $q = 1$ (surface wave "skimming"), 2 (deflection of the surface wave), and 3 (deflection of the surface wave and breakup of the soliton into radiation), respectively.

the interface may collapse into low-amplitude diffracting waves, with GH shifts becoming difficult to interpret or quantify in the absence of a well-defined reflected beam. However, strong supporting evidence has been obtained to confirm the validity of our Helmholtz-Snell modelling in arbitrary-angle non-Kerr regimes. In this way, the first steps have been taken towards understanding how (fully 2D) diffraction/nonlinearity interplays govern spatial soliton refraction in a much wider class of systems.

Nonlinear surface waves of model (5) have been derived, and we have performed the first numerical analysis of these types of solutions. Simulations have addressed the stability properties of the new surface waves, which tend to lie on one of two possible branches of the classic (β, P) curves. Solutions lying on the lower branch are predicted to behave as stable robust entities, while solutions on the upper branch are inherently unstable. Extensive computations have lent direct numerical support for this stability prediction in the more general Helmholtz context, and the growth rate of the upper-branch instability has been found to increase with q.

The stability properties of lower-branch Helmholtz surface waves have been further investigated by considering collisions with obliquely incident spatial solitons. A rich variety of behaviours, which depend crucially on both the nonlinearity exponent and the interaction angle, has been discovered. Finding analytical descriptions (e.g., through a perturbation theory [62]) of these phenomena seems a remote possibility since much of the behaviour is clearly non-adiabatic. Hence, computer simulations play a fundamental role in investigating solitons, surface waves, and their interactions in non-Kerr regimes.

The research presented in this paper provides a clear indication that deviating from the ideal Kerr-type nonlinearity ($q = 2$) can give rise to novel, interesting, and

potentially exploitable phenomena. Each component of this paper (testing the Helmholtz-Snell law, calculating GH shifts, analyzing surface wave stability, and studying soliton-surface wave interactions) is a problem for detailed investigation in its own right. Our findings unpin analyses of other types of optical (and nonoptical) contexts involving solitons and surface waves where the power-law type of nonlinearity takes centre stage. One can expect other distinct classes of surface wave to exist when the interface comprises combinations of focusing/defocusing power-law nonlinearities [42, 43, 63]; the stability properties of these waves can, quite reasonably, be expected to differ from those reported here. Furthermore, the validity of our Helmholtz-Snell modelling in power-law regimes suggests that it may also be applicable to other material configurations, for example, to single- and multi-interface problems with cubic-quintic [64–67] and saturable [68–70] nonlinearities. Research is currently underway that investigates the generality of our findings in these other contexts, and preliminary results do suggest wider applicability.

Acknowledgment

This work was supported by the Engineering and Physical Sciences Research Council (EPSRC), grant number EP/H011595/1.

References

[1] P. W. Smith and W. J. Tomlinson, "Nonlinear optical interfaces: switching behaviour," *IEEE Journal of Quantum Electronics*, vol. 20, no. 1, pp. 30–36, 1984.

[2] W. J. Tomlinson, J. P. Gordon, P. W. Smith, and A. E. Kaplan, "Reflection of a Gaussian beam at nonlinear interface," *Applied Optics*, vol. 21, no. 11, pp. 2041–2051, 1982.

[3] P. W. Smith, J. P. Hermann, W. J. Tomlinson, and P. J. Maloney, "Optical bistability at a nonlinear interface," *Applied Physics Letters*, vol. 35, no. 11, pp. 846–848, 1979.

[4] A. E. Kaplan, "Theory of hysteresis reflection and refraction of light by a boundary of a nonlinear medium," *Soviet Physics Journal of Experimental and Theoretical Physics*, vol. 45, no. 1, pp. 896–905.

[5] A. E. Kaplan, "Hysteresis reflection and refraction by nonlinear boundary: a new class of effects in nonlinear optics," *Journal of Experimental and Theoretical Physics Letters*, vol. 24, no. 1, pp. 115–119, 1976.

[6] A. B. Aceves, J. V. Moloney, and A. C. Newell, "Reflection and transmission of self-focused channels at nonlinear dielectric interfaces," *Optics Letters*, vol. 13, no. 11, pp. 1002–1004, 1988.

[7] A. B. Aceves, J. V. Moloney, and A. C. Newell, "Snell's laws at the interface between nonlinear dielectrics," *Physics Letters A*, vol. 129, no. 4, pp. 231–235, 1988.

[8] A. B. Aceves, J. V. Moloney, and A. C. Newell, "Theory of light-beam propagation at nonlinear interfaces. I. Equivalent-particle theory for a single interface," *Physical Review A*, vol. 39, no. 4, pp. 1809–1827, 1989.

[9] A. B. Aceves, J. V. Moloney, and A. C. Newell, "Theory of light-beam propagation at nonlinear interfaces. II. Multiple-particle and multiple-interface extensions," *Physical Review A*, vol. 39, no. 4, pp. 1828–1840, 1989.

[10] A. B. Aceves, P. Varatharajah, A. C. Newell et al., "Particles aspects of collimated light channel propagation at nonlinear interfaces and waveguides," *Journal of the Optical Society of America B*, vol. 7, no. 6, pp. 963–974, 1990.

[11] P. Varatharajah, A. C. Newell, J. V. Moloney, and A. B. Aceves, "Transmission, reflection, and trapping of collimated light beams in diffusive Kerr-like nonlinear media," *Physical Review A*, vol. 42, no. 3, pp. 1767–1774, 1990.

[12] A. B. Aceves and J. V. Moloney, "Effect of two-photon absorption on bright spatial soliton switches," *Optics Letters*, vol. 17, no. 21, pp. 1488–1490, 1992.

[13] Y. M. Aliev, A. D. Boardman, A. I. Smirnov, K. Xie, and A. A. Zharov, "Spatial dynamics of solitonlike channels near interfaces between optically linear and nonlinear media," *Physical Review E*, vol. 53, no. 5, pp. 5409–5419, 1996.

[14] Y. M. Aliev, A. D. Boardman, K. Xie, and A. A. Zharov, "Conserved energy approximation to wave scattering by a nonlinear interface," *Physical Review E*, vol. 49, no. 2, pp. 1624–1633, 1994.

[15] A. D. Boardman, P. Bontemps, W. Ilecki, and A. A. Zharov, "Theoretical demonstration of beam scanning and switching using spatial solitons in a photorefractive crystal," *Journal of Modern Optics*, vol. 47, no. 11, pp. 1941–1957, 2000.

[16] I. V. Shadrivov and A. A. Zharov, "Dynamics of optical spatial solitons near the interface between two quadratically nonlinear media," *Journal of the Optical Society of America B*, vol. 19, no. 3, pp. 596–602, 2002.

[17] J. Sánchez-Curto, P. Chamorro-Posada, and G. S. McDonald, "Nonlinear interfaces: intrinsically nonparaxial regimes and effects," *Journal of Optics A*, vol. 11, no. 5, Article ID 054015, 2009.

[18] J. Sánchez-Curto, P. Chamorro-Posada, and G. S. McDonald, "Helmholtz solitons at nonlinear interfaces," *Optics Letters*, vol. 32, no. 9, pp. 1126–1128, 2007.

[19] T. A. Laine and A. T. Friberg, "Self-guided waves and exact solutions of the nonlinear Helmholtz equation," *Journal of the Optical Society of America B*, vol. 17, no. 5, pp. 751–757, 2000.

[20] S. Blair, "Nonparaxial one-dimensional spatial solitons," *Chaos*, vol. 10, no. 3, pp. 570–583, 2000.

[21] A. P. Sheppard and M. Haelterman, "Nonparaxiality stabilizes three-dimensional soliton beams in Kerr media," *Optics Letters*, vol. 23, no. 23, pp. 1820–1822, 1998.

[22] M. D. Feit and J. A. Fleck, "Beam nonparaxiality, filament formation, and beam breakup in the self-focusing of optical beams," *Journal of the Optical Society of America B*, vol. 5, no. 3, pp. 633–640, 1988.

[23] P. Chamorro-Posada, G. S. McDonald, and G. H. C. New, "Exact soliton solutions of the nonlinear Helmholtz equation: communication," *Journal of the Optical Society of America B*, vol. 19, no. 5, pp. 1216–1217, 2002.

[24] P. Chamorro-Posada, G. S. McDonald, and G. H. C. New, "Non-paraxial solitons," *Journal of Modern Optics*, vol. 45, no. 6, pp. 1111–1121, 1998.

[25] J. Sánchez-Curto, P. Chamorro-Posada, and G. S. McDonald, "Black and gray Helmholtz-Kerr soliton refraction," *Physical Review A*, vol. 83, no. 1, Article ID 013828, 2011.

[26] J. Sánchez-Curto, P. Chamorro-Posada, and G. S. McDonald, "Dark solitons at nonlinear interfaces," *Optics Letters*, vol. 35, no. 9, pp. 1347–1349, 2010.

[27] A. W. Snyder and D. J. Mitchell, "Spatial solitons of the power-law nonlinearity," *Optics Letters*, vol. 18, no. 2, pp. 101–103, 1993.

[28] A. Biswas, "Perturbation of solitons due to power law nonlinearity," *Chaos, Solitons and Fractals*, vol. 12, no. 3, pp. 579–588, 2001.

[29] S. Konar and A. Biswas, "Soliton-soliton interaction with power law nonlinearity," *Progress in Electromagnetics Research*, vol. 54, no. 1, pp. 95–108, 2005.

[30] E. W. Laedke and K. H. Spatschek, "Lifetime of spikons," *Physics Letters A*, vol. 74, no. 3-4, pp. 205–207, 1979.

[31] Y. V. Katyshev, N. V. Makhaldiani, and V. G. Makhankov, "On the stability of soliton solutions to the Schrödinger equation with nonlinear term of the form $\psi|\psi|^{\nu}$," *Physics Letters A*, vol. 66, no. 6, pp. 456–458, 1978.

[32] D. Mihalache, M. Bertolotti, and C. Sibilia, "Nonlinear wave propagation in planar structures," *Progress in Optics*, vol. 27, pp. 229–313, 1989.

[33] J. G. H. Mathew, A. K. Kar, N. R. Heckenberg, and I. Galbraith, "Time resolved self-defocusing in InSb at room temperature," *IEEE Journal of Quantum Electronics*, vol. 21, no. 1, pp. 94–99, 1985.

[34] D. S. Chemla, D. A. B. Miller, and P. W. Smith, "Nonlinear optical properties of GaAs/GaAlAs multiple quantum well material: Phenomena and applications," *Optical Engineering*, vol. 24, no. 4, pp. 556–564, 1985.

[35] R. K. Jain and R. C. Lind, "Degenerate four-wave mixing in semiconductor-doped glasses," *Journal of the Optical Society of America*, vol. 73, no. 5, pp. 647–653, 1983.

[36] S. S. Yao, C. Karaguleff, A. Gabel, R. Fortenberry, C. T. Seaton, and G. I. Stegeman, "Ultrafast carrier and grating lifetimes in semiconductor-doped glasses," *Applied Physics Letters*, vol. 46, no. 9, pp. 801–802, 1985.

[37] J. G. Ma, "Nonlinear surface waves on the interface of two non-Kerr-like nonlinear media," *IEEE Transactions on Microwave Theory and Techniques*, vol. 45, no. 6, pp. 924–930, 1997.

[38] A. W. Snyder and H. T. Tran, "Surface modes of power law nonlinearities," *Optics Communications*, vol. 98, no. 4–6, pp. 309–312, 1993.

[39] G. I. Stegeman, C. T. Seaton, J. Ariyasu, T. P. Shen, and J. V. Moloney, "Saturation and power law dependence of nonlinear waves guided by a single interface," *Optics Communications*, vol. 56, no. 5, pp. 365–368, 1986.

[40] L. Wu, "Examination of the core field uniformity for 3-layer power-law nonlinear slab waveguides," *Optics Communications*, vol. 224, no. 1–3, pp. 51–56, 2003.

[41] G. I. Stegeman, E. M. Wright, C. T. Seaton et al., "Nonlinear slab-guided waves in non-Kerr-like media," *IEEE Journal of Quantum Electronics*, vol. 22, no. 6, pp. 977–983, 1986.

[42] J. G. Ma and I. Wolff, "TE wave properties of slab dielectric guide bounded by nonlinear non-Kerr-like media," *IEEE Transactions on Microwave Theory and Techniques*, vol. 44, no. 5, pp. 730–738, 1996.

[43] J. G. Ma and I. Wolff, "Propagation characteristics of TE-waves guided by thin films bounded by nonlinear media," *IEEE Transactions on Microwave Theory and Techniques*, vol. 43, no. 4, pp. 790–795, 1995.

[44] P. Varatharajah, A. B. Aceves, J. V. Moloney, and E. M. Wright, "Stationary nonlinear surface waves and their stability in diffusive Kerr-like nonlinear media," *Journal of the Optical Society of America B*, vol. 7, no. 2, pp. 220–229, 1990.

[45] D. R. Andersen, "Surface-wave excitation at the interface between diffusive Kerr-like nonlinear and linear media," *Physical Review A*, vol. 37, no. 1, pp. 189–193, 1988.

[46] Y. V. Kartashov, F. Ye, V. A. Vysloukh, and L. Torner, "Surface waves in defocusing thermal media," *Optics Letters*, vol. 32, no. 15, pp. 2260–2262, 2007.

[47] P. J. Bradley and C. De Angelis, "Soliton dynamics and surface waves at the interface between saturable nonlinear dielectrics," *Optics Communications*, vol. 130, no. 1–3, pp. 205–218, 1996.

[48] F. Goos and H. Hänchen, "Ein neuer und fundamentaler Versuch zur Totalreflexion," *Annalyen Der Physik*, vol. 1, no. 1, pp. 333–346, 1947.

[49] J. Sánchez-Curto, P. Chamorro-Posada, and G. S. McDonald, "Giant Goos-Hänchen shifts and radiation-induced trapping of Helmholtz solitons at nonlinear interfaces," *Optics Letters*, vol. 36, no. 18, pp. 3605–3607, 2011.

[50] S. Chi and Q. Guo, "Vector theory of self-focusing of an optical beam in Kerr media," *Optics Letters*, vol. 20, no. 15, pp. 1598–1600, 1996.

[51] M. Lax, W. H. Louisell, and W. B. McKnight, "From Maxwell to paraxial wave optics," *Physical Review A*, vol. 11, no. 4, pp. 1365–1370, 1975.

[52] A. Ciattoni, B. Crosignani, S. Mookherjea, and A. Yariv, "Nonparaxial dark solitons in optical Kerr media," *Optics Letters*, vol. 30, no. 5, pp. 516–518, 2005.

[53] B. Crosignani, A. Yariv, and S. Mookherjea, "Nonparaxial spatial solitons and propagation-invariant pattern solutions in optical Kerr media," *Optics Letters*, vol. 29, no. 11, pp. 1254–1256, 2004.

[54] A. Ciattoni, P. Di Porto, B. Crosignani, and A. Yariv, "Vectorial nonparaxial propagation equation in the presence of a tensorial refractive-index perturbation," *Journal of the Optical Society of America B*, vol. 17, no. 5, pp. 809–819, 2000.

[55] B. Crosignani, P. Di Porto, and A. Yariv, "Nonparaxial equation for linear and nonlinear optical propagation," *Optics Letters*, vol. 22, no. 11, pp. 778–780, 1997.

[56] J. M. Christian, G. S. McDonald, R. J. Potton, and P. Chamorro-Posada, "Helmholtz solitons in power-law optical materials," *Physical Review A*, vol. 76, no. 3, Article ID 033834, 2007.

[57] J. M. Christian, G. S. McDonald, R. J. Potton, and P. Chamorro-Posada, "Erratum: Helmholtz solitons in power-law optical materials (Physical Review A (2007) 76 (033834))," *Physical Review A*, vol. 76, no. 4, Article ID 049905, 2007.

[58] J. M. Christian, G. S. McDonald, and P. Chamorro-Posada, "Helmholtz bright and boundary solitons," *Journal of Physics A*, vol. 40, no. 7, pp. 1545–1560, 2007.

[59] P. Chamorro-Posada, G. S. McDonald, and G. H. C. New, "Non-paraxial beam propagation methods," *Optics Communications*, vol. 192, no. 1-2, pp. 1–12, 2001.

[60] J. Sánchez-Curto, P. Chamorro-Posada, and G. S. McDonald, "Helmholtz bright and black soliton splitting at nonlinear interfaces," *Physical Review A*, vol. 85, no. 1, Article ID 013836, 2012.

[61] N. G. Vakhitov and A. A. Kolokolov, "Stationary solutions of the wave equation in a medium with nonlinearity saturation," *Radiophysics and Quantum Electronics*, vol. 16, no. 7, pp. 783–789, 1975.

[62] P. Chamorro-Posada and G. S. McDonald, "Spatial Kerr soliton collisions at arbitrary angles," *Physical Review E*, vol. 74, no. 3, Article ID 036609, 2006.

[63] Y. Chen, "Bright and dark surface waves at a nonlinear interface," *Physical Review A*, vol. 45, no. 7, pp. 4974–4978, 1992.

[64] J. M. Christian, G. S. McDonald, and P. Chamorro-Posada, "Bistable Helmholtz solitons in cubic-quintic materials," *Physical Review A*, vol. 76, no. 3, Article ID 033833, 2007.

[65] D. Mihalache, D. Mazilu, M. Bertolotti, and C. Sibilia, "Exact solutions for nonlinear thin-film guided waves in higher-order nonlinear media," *Journal of the Optical Society of America B*, vol. 5, no. 2, pp. 565–570, 1988.

[66] D. Mihalache and D. Mazilu, "Stability and instability of nonlinear guided waves in saturable media," *Solid State Communications*, vol. 63, no. 3, pp. 215–217, 1987.

[67] K. I. Pushkarov, D. I. Pushkarov, and I. V. Tomov, "Self-action of light beams in nonlinear media: soliton solutions," *Optical and Quantum Electronics*, vol. 11, no. 6, pp. 471–478, 1979.

[68] J. M. Christian, G. S. McDonald, and P. Chamorro-Posada, "Bistable Helmholtz bright solitons in saturable materials," *Journal of the Optical Society of America B*, vol. 26, no. 12, pp. 2323–2330, 2009.

[69] D. Mihalache and D. Mazilu, "Stability of nonlinear stationary slab-guided waves in saturable media: a numerical analysis," *Physics Letters A*, vol. 122, no. 6-7, pp. 381–384, 1987.

[70] D. Mihalache and D. Mazilu, "TM-polarized nonlinear slab-guided waves in saturable media," *Solid State Communications*, vol. 60, no. 4, pp. 397–399, 1986.

Appendix B

B.1 Derivation of Model Equation

From Maxwell's equations:

$$\frac{\partial^2 E}{\partial z^2}+\frac{\partial^2 E}{\partial x^2}+\frac{\omega^2 n^2}{c^2}E=0 \tag{5.7}$$

For dissimilar cubic-quintic materials:

$$n_1^2=n_{01}^2+\alpha_1\left|E\right|^2+\nu_1\left|E\right|^4 \tag{5.8}$$

$$n_2^2=n_{02}^2+\alpha_2\left|E\right|^2+\nu_2\left|E\right|^4 \tag{5.9}$$

Medium 1 (where $x < 0$)

$$\frac{\partial^2 E}{\partial z^2}+\frac{\partial^2 E}{\partial x^2}+\frac{\omega^2}{c^2}n_{01}^2E+\frac{\omega^2}{c^2}\alpha_1\left|E\right|^2E+\frac{\omega^2}{c^2}\nu_1\left|E\right|^4E=0 \tag{5.10}$$

Transform to forward reference frame (substitute $E(x,z)=E_0u(x,z)\exp(ik_1z)$)

$$\frac{\partial^2 u}{\partial z^2}+i2k_1\frac{\partial u}{\partial z}-k_1^2u+\frac{\partial^2 u}{\partial x^2}+\frac{\omega^2}{c^2}n_{01}^2u+\frac{\omega^2}{c^2}\alpha_1E_0^2\left|u\right|^2u+\frac{\omega^2}{c^2}\nu_1E_0^4\left|u\right|^4u=0 \tag{5.11}$$

But:

$$k_1^2=\frac{\omega^2}{c^2}n_{01}^2=k_0^2n_{01}^2$$

$$\frac{\partial^2 u}{\partial z^2}+i2k_1\frac{\partial u}{\partial z}-\frac{\omega^2}{c^2}n_{01}^2u+\frac{\partial^2 u}{\partial x^2}+\frac{\omega^2}{c^2}n_{01}^2u+\frac{\omega^2}{c^2}\alpha_1E_0^2\left|u\right|^2u+\frac{\omega^2}{c^2}\nu_1E_0^4\left|u\right|^4u=0 \tag{5.12}$$

$$\frac{\partial^2 u}{\partial z^2}+i2k_1\frac{\partial u}{\partial z}+\frac{\partial^2 u}{\partial x^2}+\frac{\omega^2}{c^2}\alpha_1E_0^2\left|u\right|^2u+\frac{\omega^2}{c^2}\nu_1E_0^4\left|u\right|^4u=0 \tag{5.13}$$

Rescale using:

$\xi=\frac{\sqrt{2}}{w_0}x$	$\zeta=\frac{z}{L_{D1}}$
$\frac{\partial}{\partial x}=\frac{\sqrt{2}}{w_0}\frac{\partial}{\partial \xi}$	$\frac{\partial}{\partial z}=\frac{1}{L_{D1}}\frac{\partial}{\partial \zeta}$

$$\left(\frac{1}{L_{D1}}\right)^2 \frac{\partial^2 u}{\partial \zeta^2} + i2k_1 \frac{1}{L_{D1}} \frac{\partial u}{\partial \zeta} + \frac{2}{w_0^2} \frac{\partial^2 u}{\partial \xi^2} + \frac{\omega^2}{c^2} \alpha_1 E_0^2 |u|^2 u + \frac{\omega^2}{c^2} \nu_1 E_0^4 |u|^4 u = 0 \tag{5.14}$$

Multiply by $\frac{L_{D1}}{2k_1}$

$$\frac{1}{L_{D1} 2k_1} \frac{\partial^2 u}{\partial \zeta^2} + i \frac{\partial u}{\partial \zeta} + \frac{L_{D1}}{k_1 w_0^2} \frac{\partial^2 u}{\partial \xi^2} + \frac{\omega^2}{c^2} \frac{L_{D1}}{2k_1} \alpha_1 E_0^2 |u|^2 u + \frac{\omega^2}{c^2} \frac{L_{D1}}{2k_1} \nu_1 E_0^4 |u|^4 u = 0 \tag{5.15}$$

$$\kappa = \frac{1}{L_{D1} 2k_1}, \quad L_{D1} = \frac{k_1^2 w_0^2}{2}, \quad \frac{L_{D1}}{2k_1^2} \frac{2}{w_0^2} = \frac{1}{2}$$

$$\kappa \frac{\partial^2 u}{\partial \zeta^2} + i \frac{\partial u}{\partial \zeta} + \frac{1}{2} \frac{\partial^2 u}{\partial \xi^2} + \frac{\omega^2}{c^2} \frac{L_{D1}}{2k_1} \alpha_1 E_0^2 |u|^2 u + \frac{\omega^2}{c^2} \frac{L_{D1}}{2k_1} \nu_1 E_0^4 |u|^4 u = 0 \tag{5.16}$$

Need to choose units for the electric field:

$$\frac{\omega^2}{c^2} \frac{L_{D1}}{2k_1} \alpha_1 E_0^2 \equiv 1 \tag{5.17}$$

$$\frac{L_{D1}}{2k_1} \frac{k_1^2}{n_{01}^2} \alpha_1 E_0^2 = \frac{L_{D1} k_1 \alpha_1}{2n_{01}^2} E_0^2 = 1$$

Units of electric field:

$$E_0 = \left(\frac{2n_{01}^2}{L_{D1} k_1 \alpha_1} \right)^{1/2} \tag{5.18}$$

$$\frac{L_{D1}}{2k_1} \frac{\omega^2}{c^2} \nu_1 E_0^4 = \frac{\nu_1 E_0^4}{\alpha_1 E_0^2} = \frac{\nu_1 E_0^2}{\alpha_1} \equiv \sigma_1 \tag{5.19}$$

Where δ_1 is the ratio of linear and nonlinear phase shifts.

For medium 1:

$$\kappa \frac{\partial^2 u}{\partial \zeta^2} + i \frac{\partial u}{\partial \zeta} + \frac{1}{2} \frac{\partial^2 u}{\partial \xi^2} + |u|^2 u + \sigma_1 |u|^4 u = 0 . \tag{5.20}$$

Medium 2 (where $x > 0$)

$$\frac{\partial^2 E}{\partial z^2}+\frac{\partial^2 E}{\partial x^2}+\frac{\omega^2}{c^2}n_{02}^2 E+\frac{\omega^2}{c^2}\alpha_2\left|E\right|^2 E+\frac{\omega^2}{c^2}\nu_1\left|E\right|^4 E=0 \tag{5.21}$$

Transform to the forward reference frame:

$$\frac{\partial^2 u}{\partial z^2}+i2k_1\frac{\partial u}{\partial z}-k_1^2 u+\frac{\partial^2 u}{\partial x^2}+\frac{\omega^2}{c^2}n_{02}^2 u+\frac{\omega^2}{c^2}\alpha_2 E_0^2\left|u\right|^2 u+\frac{\omega^2}{c^2}\nu_1 E_0^4\left|u\right|^4 u=0 \tag{5.22}$$

$$k_1^2=\frac{\omega^2}{c^2}n_{02}^2$$

$$\frac{\partial^2 u}{\partial z^2}+i2k_1\frac{\partial u}{\partial z}-\frac{\omega^2}{c^2}n_{01}^2 u+\frac{\partial^2 u}{\partial x^2}+\frac{\omega^2}{c^2}n_{02}^2 u+\frac{\omega^2}{c^2}\alpha_2 E_0^2\left|u\right|^2 u+\frac{\omega^2}{c^2}\nu_2 E_0^4\left|u\right|^4 u=0 \tag{5.23}$$

$$\frac{\partial^2 u}{\partial z^2}+i2k_1\frac{\partial u}{\partial z}-\frac{\omega^2}{c^2}n_{01}^2\left(1-\frac{n_{02}^2}{n_{01}^2}\right)u+\frac{\partial^2 u}{\partial x^2}+\frac{\omega^2}{c^2}\alpha_2 E_0^2\left|u\right|^2 u+\frac{\omega^2}{c^2}\nu_2 E_0^4\left|u\right|^4 u=0 \tag{5.24}$$

$$\Delta\equiv 1-\left(\frac{n_{02}^2}{n_{01}^2}\right)$$

$$\frac{\partial^2 u}{\partial z^2}+i2k_1\frac{\partial u}{\partial z}-\frac{\omega^2}{c^2}n_{01}^2\Delta u+\frac{\partial^2 u}{\partial x^2}+\frac{\omega^2}{c^2}\alpha_2 E_0^2\left|u\right|^2 u+\frac{\omega^2}{c^2}\nu_2 E_0^4\left|u\right|^4 u=0 \tag{5.25}$$

Rescale using the table above:

$$\left(\frac{1}{L_{D1}}\right)^2\frac{\partial^2 u}{\partial\zeta^2}+i2k_1\frac{1}{L_{D1}}\frac{\partial u}{\partial\zeta}-\frac{\omega^2}{c^2}n_{01}^2\Delta u+\frac{2}{w_0^2}\frac{\partial^2 u}{\partial\xi^2}+\frac{\omega^2}{c^2}\alpha_2 E_0^2\left|u\right|^2 u+\frac{\omega^2}{c^2}\nu_2 E_0^4\left|u\right|^4 u=0 \tag{5.26}$$

Multiply by $\frac{L_{D1}}{2k_1}$

$$\frac{1}{2L_{D1}k_1}\frac{\partial^2 u}{\partial\zeta^2}+i\frac{\partial u}{\partial\zeta}-\frac{\omega^2}{c^2}n_{01}^2\Delta u\frac{L_{D1}}{2k_1}+\frac{1}{2}\frac{\partial^2 u}{\partial\xi^2}+\frac{\omega^2}{c^2}\frac{L_{D1}}{2k_1}\alpha_2 E_0^2\left|u\right|^2 u+\frac{\omega^2}{c^2}\frac{L_{D1}}{2k_1}\nu_2 E_0^4\left|u\right|^4 u=0 \tag{5.27}$$ $\kappa=\frac{1}{L_{D1}2k_1}$

$$\kappa\frac{\partial^2 u}{\partial\zeta^2}+i\frac{\partial u}{\partial\zeta}+\frac{1}{2}\frac{\partial^2 u}{\partial\xi^2}-\frac{\omega^2}{c^2}n_{01}^2\Delta u\frac{L_{D1}}{2k_1}+\frac{\omega^2}{c^2}\frac{L_{D1}}{2k_1}\alpha_2 E_0^2\left|u\right|^2 u+\frac{\omega^2}{c^2}\frac{L_{D1}}{2k_1}\nu_2 E_0^4\left|u\right|^4 u=0 \tag{5.28}$$

$$\frac{\omega^2}{c^2}n_{01}^2\frac{L_{D1}}{2k_1}=\frac{k_1 L_{D1}}{2k_1}=\frac{1}{2}k_\zeta L_{D1}=\frac{1}{4\kappa}$$

$$\kappa\frac{\partial^2 u}{\partial\zeta^2}+i\frac{\partial u}{\partial\zeta}+\frac{1}{2}\frac{\partial^2 u}{\partial\xi^2}-\frac{\Delta}{4\kappa}u+\frac{\omega^2}{c^2}\frac{L_{D1}}{2k_1}\alpha_1\left(\frac{\alpha_2}{\alpha_1}\right)E_0^2|u|^2u+\frac{\omega^2}{c^2}\frac{L_{D1}}{2k_1}\nu_1\left(\frac{\nu_2}{\nu_1}\right)E_0^4|u|^4u=0 \tag{5.29}$$

But

$$\frac{L_{D1}}{2k_1}\frac{\omega^2}{c^2}\alpha_1E_0^2\equiv 1,\frac{L_{D1}}{2k_1}\frac{\omega^2}{c^2}\nu_1E_0^4=\frac{\nu_1E_0^4}{\alpha_1E_0^2}=\frac{\nu_1E_0^2}{\alpha_1}\equiv\sigma_1$$

$$\kappa\frac{\partial^2 u}{\partial\zeta^2}+i\frac{\partial u}{\partial\zeta}+\frac{1}{2}\frac{\partial^2 u}{\partial\xi^2}-\frac{\Delta}{4\kappa}u+\left(\frac{\alpha_2}{\alpha_1}\right)|u|^2u+\sigma\left(\frac{\nu_2}{\nu_1}\right)|u|^4u=0 \tag{5.30}$$

$$\frac{\alpha_2}{\alpha_1}\equiv\alpha\,,\ \frac{\nu_2}{\nu_1}\equiv\nu$$

For medium 2:

$$\kappa\frac{\partial^2 u}{\partial\zeta^2}+i\frac{\partial u}{\partial\zeta}+\frac{1}{2}\frac{\partial^2 u}{\partial\xi^2}-\frac{\Delta}{4\kappa}u+\alpha|u|^2u+\sigma\nu|u|^4u=0 \tag{5.31}$$

Full model equation:

$$\kappa\frac{\partial^2 u}{\partial\zeta^2}+i\frac{\partial u}{\partial\zeta}+\frac{1}{2}\frac{\partial^2 u}{\partial\xi^2}+|u|^2u+\sigma|u|^4u=\left[\frac{\Delta}{4\kappa}+(1-\alpha)|u|^2+(1-\nu)\sigma|u|^4\right]H(\xi)u \tag{5.32}$$

B.2 Exact Soliton Solutions

Using the equation below:

$$\kappa\frac{\partial^2 u}{\partial\zeta^2}+i\frac{\partial u}{\partial\zeta}+\frac{1}{2}\frac{\partial^2 u}{\partial\xi^2}+|u|^2u+\sigma|u|^4u=\left[\frac{\Delta}{4\kappa}+(1-\alpha)|u|^2+(1-\nu)\sigma|u|^4\right]H(\xi)u \qquad (5.33)$$

need to find on-axis solution of the form:

$$u=A[1+B\cosh(C\xi)]^{-1/2}\exp(ik_\zeta\zeta), \qquad (5.34)$$

either side of the interface.

Medium 1

Substitute equation (5.34) into:

$$\kappa\frac{\partial^2 u}{\partial\zeta^2}+i\frac{\partial u}{\partial\zeta}+\frac{1}{2}\frac{\partial^2 u}{\partial\xi^2}+|u|^2u+\sigma_1|u|^4u=0 \qquad (5.35)$$

$$\frac{\partial u}{\partial\xi}=-\frac{1}{2}ABC\exp(ik_\zeta\zeta)\sinh(C\xi)\left[1+B\cosh(C\xi)\right]^{-3/2}$$

$$\frac{\partial^2 u}{\partial\xi^2}=-\frac{1}{2}ABC\exp(ik_\zeta\zeta)\left\{C\cosh(C\xi)[1+B\cosh(C\xi)]^{-3/2}-\tfrac{3}{2}BC\sinh^2(C\xi)[1+B\cosh(C\xi)]^{-5/2}\right\}$$

$$\frac{\partial u}{\partial\zeta}=ik_\zeta u$$

$$\frac{\partial^2 u}{\partial\zeta^2}=-k_\zeta^2u$$

Consider the first two terms of equation (5.35):

$$\kappa\frac{\partial^2 u}{\partial\zeta^2}+i\frac{\partial u}{\partial\zeta}$$

$$\kappa(-k_\zeta^2u)+i(ik_\zeta u)=-(\kappa k_\zeta^2+k_\zeta)u\equiv-\beta u$$

$$\kappa k_\zeta^2+k_\zeta=\beta$$

$$k_\zeta = \frac{-1 \pm \sqrt{1-4\kappa\beta}}{2\kappa}$$

So the propagation constant is:

$$k_\zeta = \frac{1}{2\kappa}\left[-1 \pm \sqrt{1+4\kappa\beta}\right]$$

Equation then becomes:

$$-\beta u + \frac{1}{2}\frac{\partial^2 u}{\partial \xi^2} + |u|^2 u + \sigma |u|^4 u = 0.$$

Substitute terms for u into the previous equation, and multiply by $\left[1 + B\cosh(C\xi)\right]^{-5/2}$:

$$\left[\cosh^2(C\xi)\right]\left[-\frac{2}{8}B^2C^2 + \frac{3}{8}B^2C^2 - \beta B^2\right] + \left[\cosh(C\xi)\right]\left[-\frac{BC^2}{4} + A^2B - 2\beta B\right]$$
$$+\left[-\frac{3}{8}B^2C^2 + A^2 + \sigma A^4 - \beta\right] = 0.$$

Equate the coefficients to zero:

$\left[\cosh^2(C\xi)\right] = 0$

$$-\beta + \frac{C^2}{8} = 0$$

$$C^2 = 8\beta$$

$$C = 2\sqrt{2\beta} \tag{5.36}$$

$\left[\cosh(C\xi)\right] = 0$

$$-\frac{C^2}{4} + A^2 - 2\beta = 0$$

$$A^2 = 4\beta \tag{5.37}$$

$\left[\cosh^0(C\xi)\right] = 0$

$$-\frac{3}{8}B^2C^2 + A^2 + \sigma A^4 - \beta = 0$$

but

$$\frac{A^2}{1+B} \equiv \rho_0$$

So

$$4\beta = \rho_0(1+B)$$

$$\beta = \frac{\rho_0}{4}(1+B) \tag{5.38}$$

$$-\frac{3}{\cancel{8}}B^2\cancel{8}\beta + \rho_0(1+B) + \sigma\rho_0^2(1+B)^2 - \beta = 0$$

$$-3B^2\frac{\cancel{\rho_0}}{4}(1+\cancel{B}) + \sigma\rho_0^{\cancel{2}}(1+B)^{\cancel{2}} - \frac{\cancel{\rho_0}}{4}(1+\cancel{B}) = 0$$

(5.39)

$$-\frac{3}{4}B^2 + \sigma\rho_0 + \sigma\rho_0 B + \frac{3}{4} = 0 \tag{5.40}$$

$$-\frac{3}{4}B^2 + \sigma\rho_0 B + \left(\sigma\rho_0 + \frac{3}{4}\right) = 0 \tag{5.41}$$

Solve the quadratic equation to find B.

$$B = \frac{2}{3}\sigma\rho_0 + \left(\frac{2}{3}\sigma\rho_0 + 1\right) \quad \text{or}$$

$$B = \frac{2}{3}\sigma\rho_0 - \left(\frac{2}{3}\sigma\rho_0 + 1\right)$$

$$B = \frac{4}{3}\sigma\rho_0 + 1 \quad \text{or} \quad B = -1$$

$$B = \frac{4}{3}\sigma\rho_0 + 1 \tag{5.42}$$

But

$$B = 1 + \frac{4}{3}\sigma\rho_0 \tag{5.43}$$

So

$$\beta = \frac{\rho_0}{2}\left(1 + \frac{2}{3}\sigma\rho_0\right) \tag{5.44}$$

Medium 2

$$\kappa\frac{\partial^2 u}{\partial\zeta^2} + i\frac{\partial u}{\partial\zeta} + \frac{1}{2}\frac{\partial^2 u}{\partial\xi^2} - \frac{\Delta}{4\kappa}u + \alpha|u|^2 u + \nu\sigma|u|^4 u = 0 \tag{5.45}$$

$$\frac{\partial u}{\partial\xi} = -\frac{1}{2}ABC\exp(ik_\zeta\zeta)\sinh(C\xi)\left[1 + B\cosh(C\xi)\right]^{-3/2} \tag{5.46}$$

$$\frac{\partial^2 u}{\partial\xi^2} = -\frac{1}{2}ABC\exp(ik_\zeta\zeta)\left\{C\cosh(C\xi)[1 + B\cosh(C\xi)]^{-3/2} - \tfrac{3}{2}BC\sinh^2(C\xi)[1 + B\cosh(C\xi)]^{-5/2}\right\} \tag{5.47}$$

$$\frac{\partial u}{\partial\zeta} = ik_\zeta u \tag{5.48}$$

$$\frac{\partial^2 u}{\partial\zeta^2} = -k_\zeta^2 u \tag{5.49}$$

$$-\beta u + \frac{1}{2}\frac{\partial^2 u}{\partial\xi^2} - \frac{\Delta}{4\kappa} + \alpha|u|^2 u + \nu\sigma|u|^4 u = 0. \tag{5.50}$$

$$\left[\cosh^2(C\xi)\right]\left[-\frac{2}{8}B^2C^2 + \frac{3}{8}B^2C^2 - \beta B^2 - \frac{\Delta}{4\kappa}\right] + \left[\cosh(C\xi)\right]\left[-\frac{BC^2}{4} + \alpha A^2 B - 2\beta B - 2\frac{\Delta}{4\kappa}B\right]$$
$$+\left[-\frac{3}{8}B^2C^2 + \alpha A^2 + \nu\sigma A^4 - \beta - \frac{\Delta}{4\kappa}\right] = 0. \tag{5.51}$$

$$\left[\cosh^2(C\xi)\right] = 0$$

$$-\frac{C^2}{4} - \frac{3}{8}C^2 - \beta - \frac{\Delta}{4\kappa} = 0. \tag{5.52}$$

$$\frac{C^2}{8} = \beta + \frac{\Delta}{4\kappa} \tag{5.53}$$

$$C = 2\sqrt{2\left(\beta + \frac{\Delta}{4\kappa}\right)} \tag{5.54}$$

$\left[\cosh(C\xi)\right] = 0$

$$-\frac{C^2}{4} - 2\beta - 2\frac{\Delta}{4\kappa} + \alpha A^2 = 0$$

$$-\frac{1}{4}8\left(\beta + \frac{\Delta}{4\kappa}\right) - 2\beta - 2\frac{\Delta}{4\kappa} = 0 \tag{5.55}$$

$$A^2 = \frac{4}{\alpha}\left(\beta + \frac{\Delta}{4\kappa}\right) \tag{5.56}$$

$\left[\cosh^0(C\xi)\right] = 0$

$$-\frac{3}{8}B^2C^2 - \left(\beta + \frac{\Delta}{4\kappa}\right) + \alpha A^2 + \nu\sigma A^4 = 0$$

$$-3B^2\left(\beta + \frac{\Delta}{4\kappa}\right) - \left(\beta + \frac{\Delta}{4\kappa}\right) + \alpha\rho_0(1+B) + \nu\sigma{\rho_0}^2(1+B)^2 = 0 \tag{5.57}$$

$A^2 = \frac{4}{\alpha}\left(\beta + \frac{\Delta}{4\kappa}\right)$

$\beta + \frac{\Delta}{4\kappa} = A^2\frac{\alpha}{4}$

$A^2 = \rho_0(1+B)$

$$\beta + \frac{\Delta}{4\kappa} = \rho_0(1+B)\frac{\alpha}{4} \tag{5.58}$$

$$-3B^2 + 4\frac{\nu\sigma\rho_0}{\alpha}B + \left(4\frac{\nu\sigma\rho_0}{\alpha} + 3\right) = 0. \tag{5.59}$$

Need to solve quadratic equation for *B*.

$$B = \frac{4}{3}\frac{\nu\sigma\rho_0}{\alpha} + 1 \tag{5.60}$$

Substitute into equation (5.58):

$$\beta = \frac{\alpha\rho_0}{4}\left(\frac{4}{3}\frac{\nu\sigma\rho_0}{\alpha} + 2\right) - \frac{\Delta}{4\kappa} \tag{5.61}$$

$$\beta = \frac{\rho_0}{2}\left(\alpha + \frac{2}{3}\nu\sigma\rho_0\right) - \frac{\Delta}{4\kappa} \tag{5.62}$$

Substitute into equation (5.54):

$$C = 2\left[\rho_0\left(\alpha + \frac{2}{3}\nu\sigma\rho_0\right)\right]^{1/2} \tag{5.63}$$

Also substitute equation (5.62) into (5.56):

$$A^2 = 2\rho_0\left(1 + \frac{2}{3}\frac{\nu\sigma\rho_0}{\alpha}\right) \tag{5.64}$$

Now need to apply the transformations in table 2 to find the off-axis solutions:

$$u(\xi,\zeta) = \left[\frac{4\beta}{1 + B\cosh\left(C\frac{\xi - V\zeta}{\sqrt{1+2\kappa V^2}}\right)}\right]^{1/2} \exp\left[i\sqrt{\frac{1+4\kappa\beta}{1+2\kappa V_{inc}{}^2}}\left(V_{inc}\xi + \frac{\zeta}{2\kappa}\right)\right]\exp\left(-i\frac{\zeta}{2\kappa}\right) \tag{5.65}$$

$$u(\xi,\zeta) = \left[\frac{4\beta}{1 + B\cosh\left(C\frac{\xi - V\zeta}{\sqrt{1+2\kappa V^2}}\right)}\right]^{1/2} \exp\left[i\sqrt{\frac{1+4\kappa\beta}{1+2\kappa V_{ref}{}^2}}\left(V_{ref}\xi + \frac{\zeta}{2\kappa}\right)\right]\exp\left(-i\frac{\zeta}{2\kappa}\right) \tag{5.66}$$

Where the constants remain unchanged after the transformation.

B.3 Derivation of Generalised Snell's Law for cubic-quintic interfaces

The phase of the solutions must be matched at the interface. The phase continuity condition is:

$$\frac{1+2\kappa\rho_0\left(1+\frac{2}{3}\sigma\rho_0\right)}{1+2\kappa V^2}=\frac{1-\Delta+2\kappa\rho_0\left(\alpha+\frac{2}{3}\nu\sigma\rho_0\right)}{1+2\kappa V'^2} \tag{5.67}$$

$$1+2\kappa V'^2=\left(\frac{1+2\kappa V^2}{1+2\kappa\rho_0\left(1+\frac{2}{3}\sigma\rho_0\right)}\right)\left[1-\Delta+2\kappa\rho_0\left(\alpha+\frac{2}{3}\nu\sigma\rho_0\right)\right] \tag{5.68}$$

$$2\kappa V'^2=\left(\frac{1+2\kappa V^2}{1+2\kappa\rho_0\left(1+\frac{2}{3}\sigma\rho_0\right)}\right)\left[1-\Delta+2\kappa\rho_0\left(\alpha+\frac{2}{3}\nu\sigma\rho_0\right)\right]-1 \tag{5.69}$$

$$2\kappa V'^2=\left(\frac{1+2\kappa V^2}{1+2\kappa\rho_0\left(1+\frac{2}{3}\sigma\rho_0\right)}\right)-1-\left(\frac{1+2\kappa V^2}{1+2\kappa\rho_0\left(1+\frac{2}{3}\sigma\rho_0\right)}\right)\left[\Delta-2\kappa\rho_0\left(\alpha+\frac{2}{3}\nu\sigma\rho_0\right)\right] \tag{5.70}$$

$$V'^2=\frac{1}{2\kappa}\left[\left(\frac{1+2\kappa V^2}{1+2\kappa\rho_0\left(1+\frac{2}{3}\sigma\rho_0\right)}\right)-1-\left(\frac{1+2\kappa V^2}{1+2\kappa\rho_0\left(1+\frac{2}{3}\sigma\rho_0\right)}\right)\left[\Delta-2\kappa\rho_0\left(\alpha+\frac{2}{3}\nu\sigma\rho_0\right)\right]\right] \tag{5.71}$$

$$V'^2=\frac{1}{\cancel{2\kappa}}\frac{\cancel{1}+\cancel{2\kappa}V^2-\cancel{1}+\cancel{2\kappa}\rho_0\left(1+\frac{2}{3}\sigma\rho_0\right)}{1+2\kappa\rho_0\left(1+\frac{2}{3}\sigma\rho_0\right)}-\frac{1}{2\kappa}\left(\frac{1+2\kappa V^2}{1+2\kappa\rho_0\left(1+\frac{2}{3}\sigma\rho_0\right)}\right)\left[\Delta-2\kappa\rho_0\left(\alpha+\frac{2}{3}\nu\sigma\rho_0\right)\right] \tag{5.72}$$

$$V'^2=\frac{V^2-\rho_0\left(1+\frac{2}{3}\sigma\rho_0\right)}{1+2\kappa\rho_0\left(1+\frac{2}{3}\sigma\rho_0\right)}-\frac{1}{2\kappa}\left(\frac{1+2\kappa V^2}{1+2\kappa\rho_0\left(1+\frac{2}{3}\sigma\rho_0\right)}\right)\left[\Delta-2\kappa\rho_0\left(\alpha+\frac{2}{3}\nu\sigma\rho_0\right)\right] \tag{5.73}$$

$$\frac{V^2-\rho_0\left(1+\frac{2}{3}\sigma\rho_0\right)}{1+2\kappa\rho_0\left(1+\frac{2}{3}\sigma\rho_0\right)}=V^2+\beta \tag{5.74}$$

$$\beta=\frac{V^2-\rho_0\left(1+\frac{2}{3}\sigma\rho_0\right)}{1+2\kappa\rho_0\left(1+\frac{2}{3}\sigma\rho_0\right)}-V^2 \tag{5.75}$$

$$=\frac{\cancel{V^2}-\rho_0\left(1+\frac{2}{3}\sigma\rho_0\right)-V^2\left[\cancel{1}+2\kappa\rho_0\left(1+\frac{2}{3}\sigma\rho_0\right)\right]}{1+2\kappa\rho_0\left(1+\frac{2}{3}\sigma\rho_0\right)} \tag{5.76}$$

$$\beta = \frac{-\rho_0\left(1+\frac{2}{3}\sigma\rho_0\right)\left(1+2\kappa V^2\right)}{1+2\kappa\rho_0\left(1+\frac{2}{3}\sigma\rho_0\right)} \tag{5.77}$$

$$V'^2 = V^2 - \rho_0\left(1+\tfrac{2}{3}\sigma\rho_0\right)\left(\frac{1+2\kappa V^2}{1+2\kappa\rho_0\left(1+\frac{2}{3}\sigma\rho_0\right)}\right) - \frac{1}{2\kappa}\left(\frac{1+2\kappa V^2}{1+2\kappa\rho_0\left(1+\frac{2}{3}\sigma\rho_0\right)}\right)\left[\Delta - 2\kappa\rho_0\left(\alpha+\tfrac{2}{3}\nu\sigma\rho_0\right)\right] \tag{5.78}$$

$$V'^2 = V^2 - 2\kappa\rho_0\left(1+\tfrac{2}{3}\sigma\rho_0\right)\left(\frac{1}{2\kappa}\right)\frac{1+2\kappa V^2}{1+2\kappa\rho_0\left(1+\frac{2}{3}\sigma\rho_0\right)} - \frac{1}{2\kappa}\left(\frac{1+2\kappa V^2}{1+2\kappa\rho_0\left(1+\frac{2}{3}\sigma\rho_0\right)}\right)\left[\Delta - 2\kappa\rho_0\left(\alpha+\tfrac{2}{3}\nu\sigma\rho_0\right)\right] \tag{5.79}$$

$$V'^2 = V^2 - \left(\frac{1}{2\kappa}\right)\frac{1+2\kappa V^2}{1+2\kappa\rho_0\left(1+\frac{2}{3}\sigma\rho_0\right)}\left[2\kappa\rho_0\left(1+\tfrac{2}{3}\sigma\rho_0\right) + \Delta - 2\kappa\rho_0\left(\alpha+\tfrac{2}{3}\nu\sigma\rho_0\right)\right] \tag{5.80}$$

$$V'^2 = V^2 - \left(\frac{1}{2\kappa}\right)\frac{1+2\kappa V^2}{1+2\kappa\rho_0\left(1+\frac{2}{3}\sigma\rho_0\right)}\left[\Delta + 2\kappa\rho_0\left(1+\tfrac{2}{3}\sigma\rho_0 - \alpha - \tfrac{2}{3}\nu\sigma\rho_0\right)\right] \tag{5.81}$$

$$V'^2 = V^2 - \left(\frac{1}{2\kappa}\right)\frac{1+2\kappa V^2}{1+2\kappa\rho_0\left(1+\frac{2}{3}\sigma\rho_0\right)}\left\{\Delta + 2\kappa\rho_0\left[\left(1-\alpha\right) + \tfrac{2}{3}\sigma\rho_0\left(1-\nu\right)\right]\right\} \tag{5.82}$$

The generalised Snell's law in terms of transverse velocities is:

$$V'^2 = V^2 - \left(\frac{1}{2\kappa}\right)\frac{1+2\kappa V^2}{1+2\kappa\rho_0\left(1+\frac{2}{3}\sigma\rho_0\right)}\delta \tag{5.83}$$

where:

$$\delta = \Delta + 2\kappa\rho_0\left[\left(1-\alpha\right) + \tfrac{2}{3}\sigma\rho_0\left(1-\nu\right)\right] \tag{5.84}$$

Generalised Snell's law in terms of angles

$$\frac{1}{1+2\kappa V^2} \equiv \cos^2\theta_i \qquad \text{and} \qquad \frac{1}{1+2\kappa V'^2} \equiv \cos^2\theta_t$$

$$\frac{1+2\kappa\rho_0\left(1+\frac{2}{3}\sigma\rho_0\right)}{1+2\kappa V^2} = \frac{1-\Delta+2\kappa\rho_0\left(\alpha+\frac{2}{3}\nu\sigma\rho_0\right)}{1+2\kappa V'^2} \tag{5.85}$$

$$\left[1+2\kappa\rho_0\left(1+\tfrac{2}{3}\sigma\rho_0\right)\right]\cos^2\theta_i = \left[1-\Delta+2\kappa\rho_0\left(\alpha+\tfrac{2}{3}\nu\sigma\rho_0\right)\right]\cos^2\theta_t \tag{5.86}$$

$$\left[1+2\kappa\rho_0\left(1+\tfrac{2}{3}\sigma\rho_0\right)\right]\cos^2\theta_i = (1-\Delta)\left[1+2\kappa\rho_0\left(\alpha+\tfrac{2}{3}\nu\sigma\rho_0\right)(1-\Delta)^{-1}\right]\cos^2\theta_t \tag{5.87}$$

$$\left[1+2\kappa\rho_0\left(1+\tfrac{2}{3}\sigma\rho_0\right)\right]\cos^2\theta_i = \left(\frac{n_{02}}{n_{01}}\right)^2\left[1+2\kappa\rho_0\left(\alpha+\tfrac{2}{3}\nu\sigma\rho_0\right)(1-\Delta)^{-1}\right]\cos^2\theta_t \tag{5.88}$$

$$\left[\frac{1+2\kappa\rho_0\left(1+\frac{2}{3}\sigma\rho_0\right)}{1+2\kappa\rho_0\left(\alpha+\frac{2}{3}\nu\sigma\rho_0\right)(1-\Delta)^{-1}}\right]^{1/2} n_{01}\cos\theta_i = n_{02}\cos\theta_t \tag{5.89}$$

Generalised Snell's law is:

$$\gamma n_{01}\cos\theta_i = n_{02}\cos\theta_t \tag{5.90}$$

where:

$$\gamma = \left[\frac{1+2\kappa\rho_0\left(1+\frac{2}{3}\sigma\rho_0\right)}{1+2\kappa\rho_0\left(\alpha+\frac{2}{3}\nu\sigma\rho_0\right)(1-\Delta)^{-1}}\right]^{1/2} \tag{5.91}$$

B.4 Critical Angle

$$\cos^2\theta_c = \frac{1}{\gamma^2}\left(\frac{n_{02}}{n_{01}}\right)^2 \tag{5.92}$$

$$\tan^2\theta + 1 = \frac{1}{\cos^2\theta_c} = \gamma^2\left(\frac{n_{01}}{n_{02}}\right)^2 \tag{5.93}$$

$$\tan^2\theta = \gamma^2\left(\frac{n_{01}}{n_{02}}\right)^2 - 1 \tag{5.94}$$

$$\left(\frac{n_{01}}{n_{02}}\right)^2 = \frac{1}{1-\Delta} = (1-\Delta)^{-1} \tag{5.95}$$

$$\tan^2\theta_c = \frac{1+2\kappa\rho_0\left(1+\tfrac{2}{3}\sigma\rho_0\right)}{1+2\kappa\rho_0\left(\alpha+\tfrac{2}{3}\nu\sigma\rho_0\right)(1-\Delta)^{-1}}(1-\Delta)^{-1} - 1$$

$$\tan^2\theta_c = \frac{(1-\Delta)^{-1}\left[1+2\kappa\rho_0\left(1+\tfrac{2}{3}\sigma\rho_0\right)\right] - \left[1+2\kappa\rho_0\left(\alpha+\tfrac{2}{3}\nu\sigma\rho_0\right)(1-\Delta)^{-1}\right]}{1+2\kappa\rho_0\left(\alpha+\tfrac{2}{3}\nu\sigma\rho_0\right)(1-\Delta)^{-1}}$$

$$\tan^2\theta_c = \frac{(1-\Delta)^{-1}\left[1+2\kappa\rho_0\left(1+\tfrac{2}{3}\sigma\rho_0\right)\right] - \left[1+2\kappa\rho_0\left(\alpha+\tfrac{2}{3}\nu\sigma\rho_0\right)(1-\Delta)^{-1}\right]}{1+2\kappa\rho_0\left(\alpha+\tfrac{2}{3}\nu\sigma\rho_0\right)(1-\Delta)^{-1}}\left(\frac{1-\Delta}{1-\Delta}\right)$$

$$\tan^2\theta_c = \frac{\cancel{1} + 2\kappa\rho_0\left(1+\tfrac{2}{3}\sigma\rho_0\right) - \cancel{1} - \Delta - 2\kappa\rho_0\left(\alpha+\tfrac{2}{3}\nu\sigma\rho_0\right)}{1-\Delta+2\kappa\rho_0\left(\alpha+\tfrac{2}{3}\nu\sigma\rho_0\right)}$$

$$\tan^2\theta_c = \frac{\Delta + 2\kappa\rho_0\left(1+\tfrac{2}{3}\sigma\rho_0\right) - 2\kappa\rho_0\left(\alpha+\tfrac{2}{3}\nu\sigma\rho_0\right)}{1-\Delta+2\kappa\rho_0\left(\alpha+\tfrac{2}{3}\nu\sigma\rho_0\right)}$$

$$\tan^2\theta_c = \frac{\Delta + 2\kappa\rho_0\left[\tfrac{2}{3}\sigma\rho_0(1-\nu) + (1-\alpha)\right]}{1-\Delta+2\kappa\rho_0\left(\alpha+\tfrac{2}{3}\nu\sigma\rho_0\right)}$$

$$\tan\theta_c = \left[\frac{\Delta + 2\kappa\rho_0\left[\tfrac{2}{3}\sigma\rho_0(1-\nu) + (1-\alpha)\right]}{1-\Delta+2\kappa\rho_0\left(\alpha+\tfrac{2}{3}\nu\sigma\rho_0\right)}\right]^{1/2} \tag{5.96}$$

B.5 Linear Interface Results

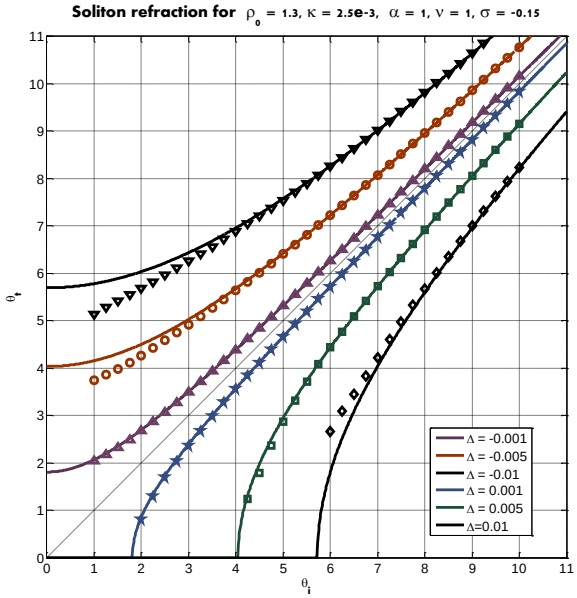

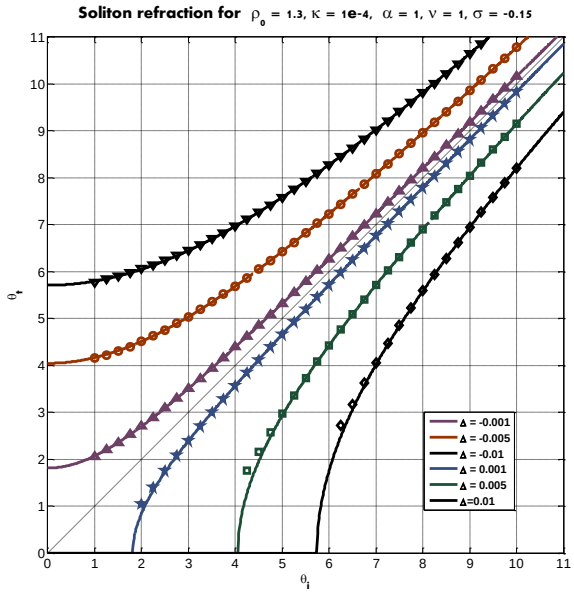

Snell's Law Plots for a linear interface with $\rho_0 = 1.3$

$\kappa = 2.5 \times 10^{-3}$ $\kappa = 1 \times 10^{-4}$

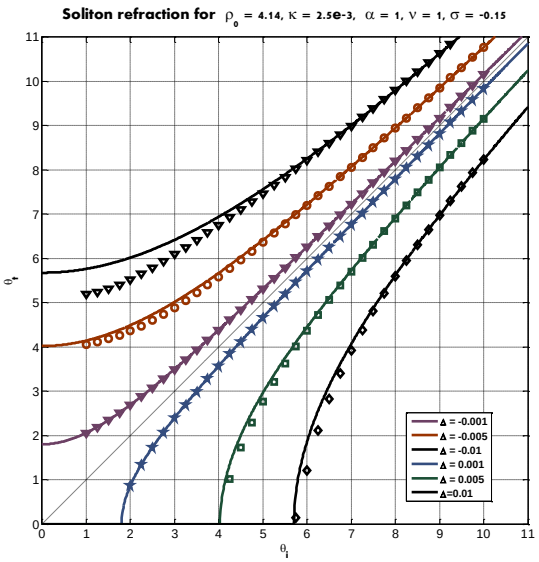

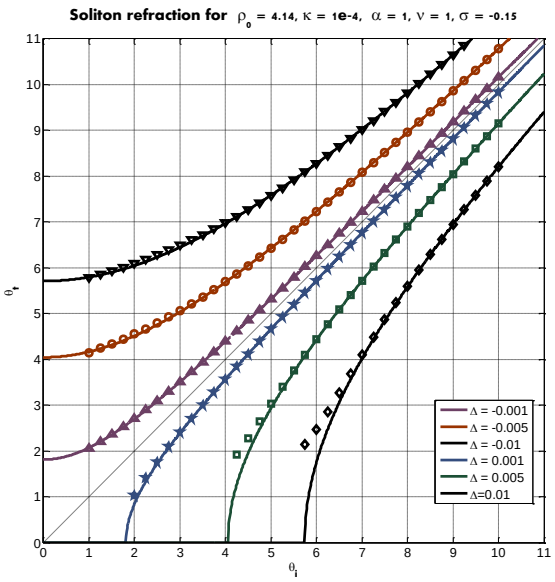

Snell's Law Plots for a linear interface with $\rho_0 = 4.14$

$\kappa = 2.5 \times 10^{-3}$ $\kappa = 1 \times 10^{-4}$

Mixed Interface Results – similar quintic coefficients (ν=1)

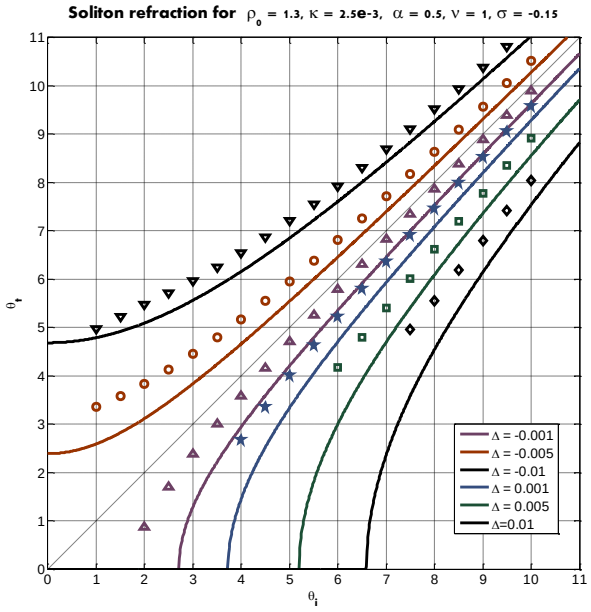

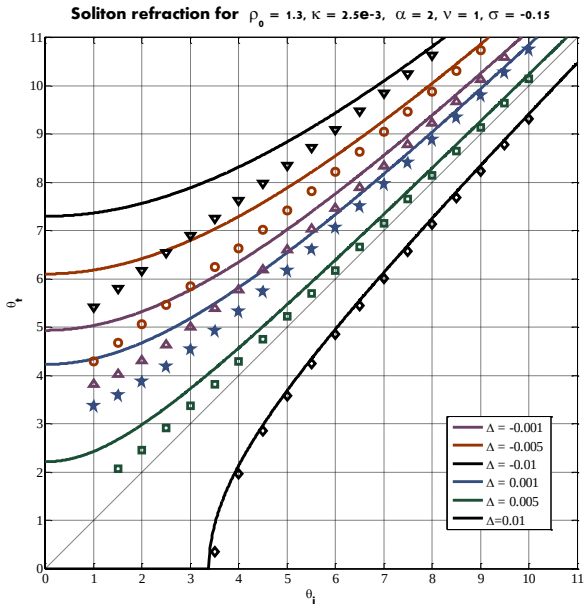

Snell's Law Plots for a mixed interface: $\rho_0 = 1.3$, $\nu = 1$ and $\kappa = 2.5 \times 10^{-3}$

$\alpha = 0.5$ $\alpha = 2.0$

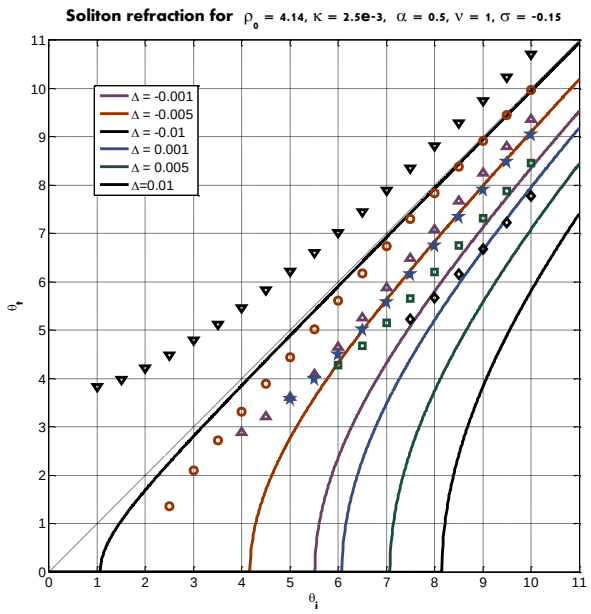

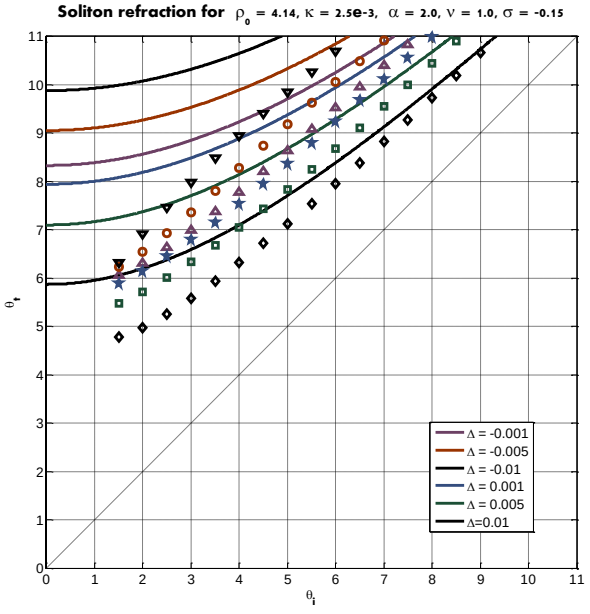

Snell's Law Plots for a mixed interface: $\rho_0 = 4.14$, $\nu = 1$ and $\kappa = 2.5 \times 10^{-3}$

$\alpha = 0.5$ $\alpha = 2.0$

Mixed Interface Results – similar cubic coefficient (α=1)

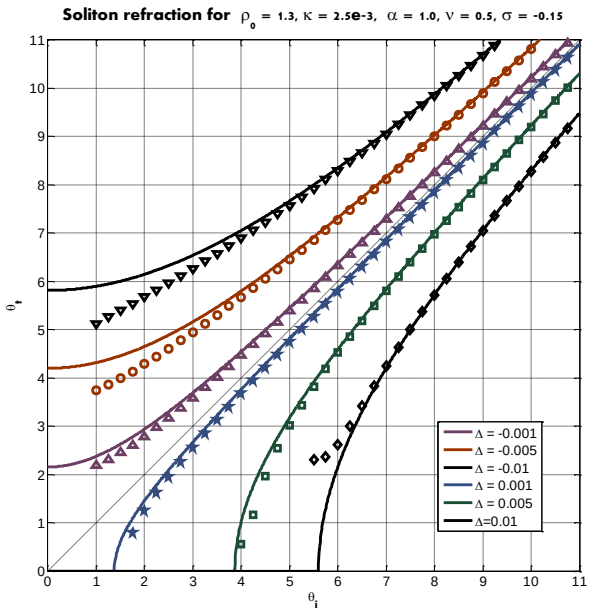

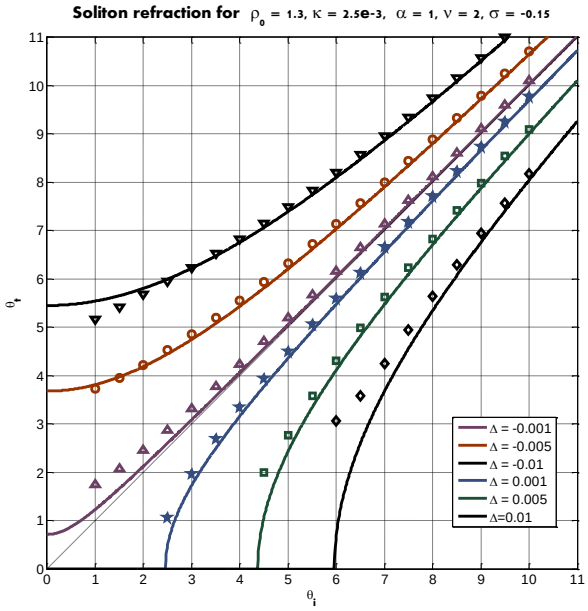

Snell's Law Plots for a mixed interface: $\rho_0 = 1.3$, $\alpha = 1$ and $\kappa = 2.5 \times 10^{-3}$

ν= 0.5 ν= 2.0

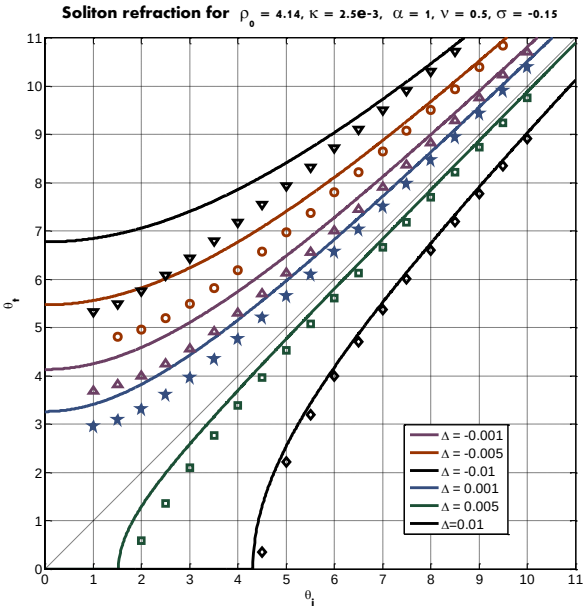

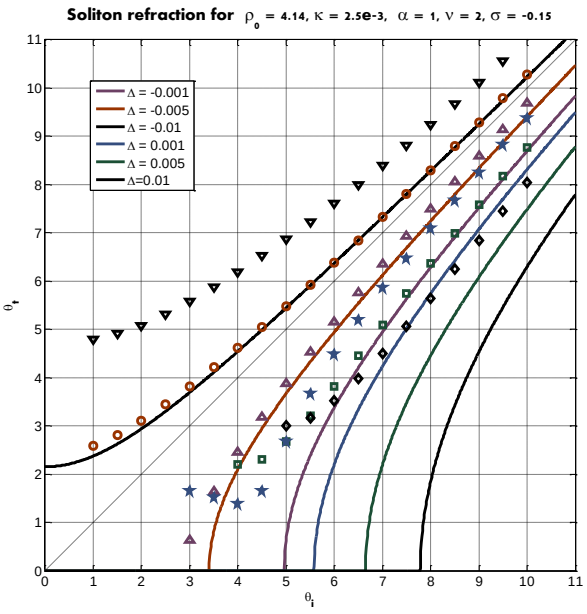

Snell's Law Plots for a mixed interface: $\rho_0 = 4.14$, $\alpha = 1$ and $\kappa = 2.5 \times 10^{-3}$

ν= 0.5 ν= 2.0

Mixed Interface Results – similar quintic coefficients (ν=1)

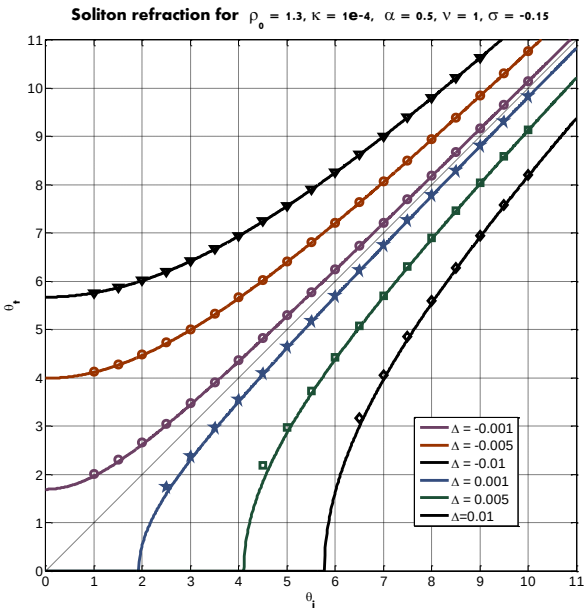

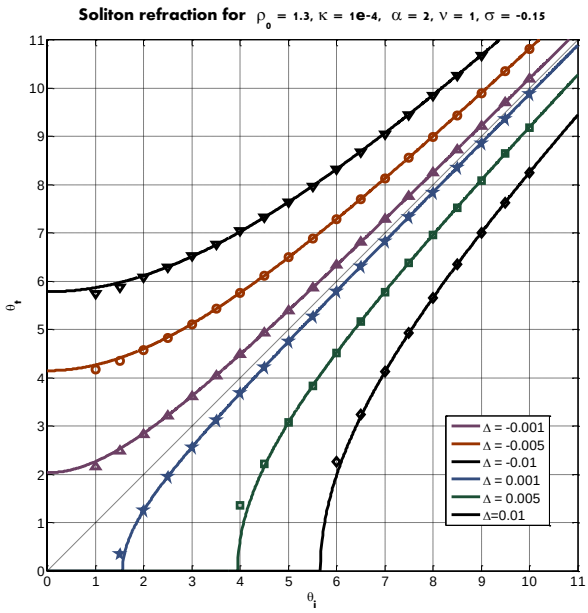

Snell's Law Plots for a mixed interface: $\rho_0 = 1.3$, $\nu = 1$ and $\kappa = 1 \times 10^{-4}$

$\alpha = 0.5$ $\alpha = 2.0$

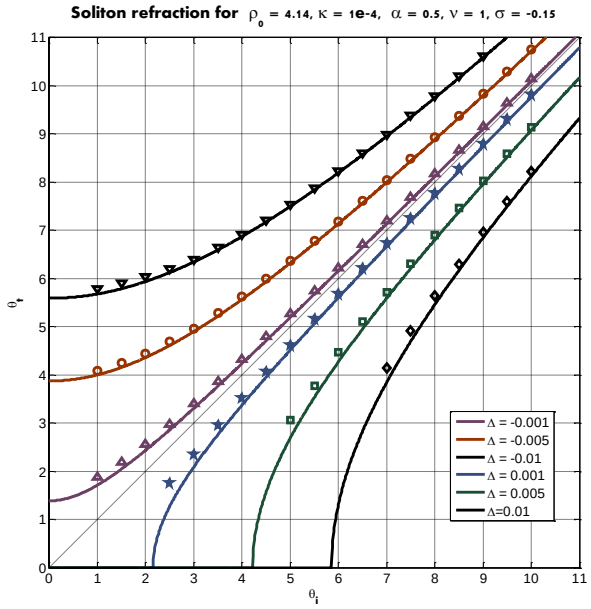

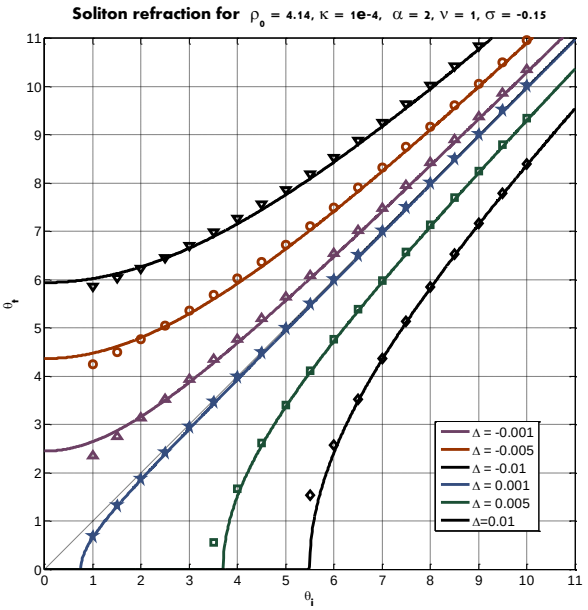

Snell's Law Plots for a mixed interface: $\rho_0 = 4.14$, $\nu = 1$ and $\kappa = 1 \times 10^{-4}$

$\alpha = 0.5$ $\alpha = 2.0$

Mixed Interface Results – similar cubic coefficient (α=1)

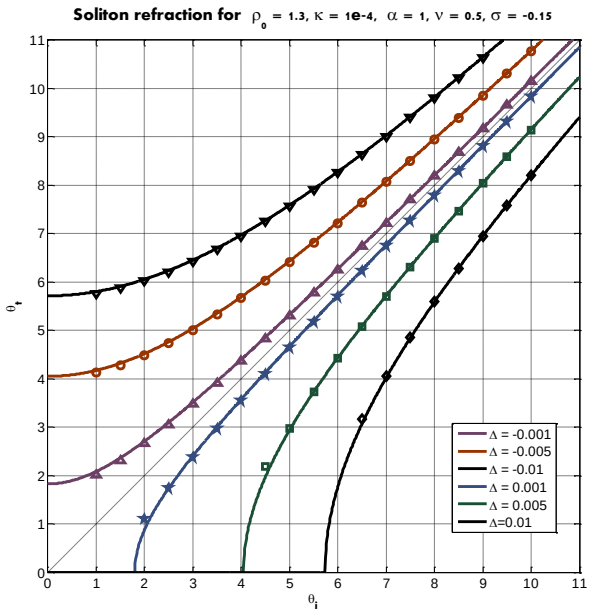

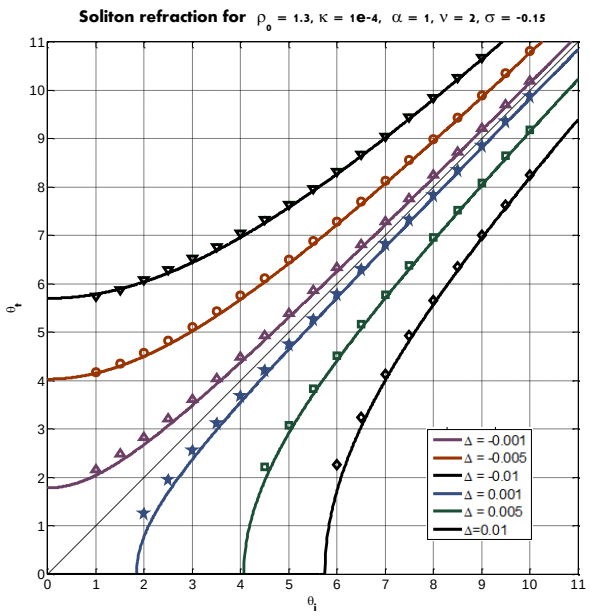

Snell's Law Plots for a mixed interface: $\rho_0 = 1.3$, $\alpha = 1$ and $\kappa = 1 \times 10^{-4}$

ν= 0.5 ν= 2.0

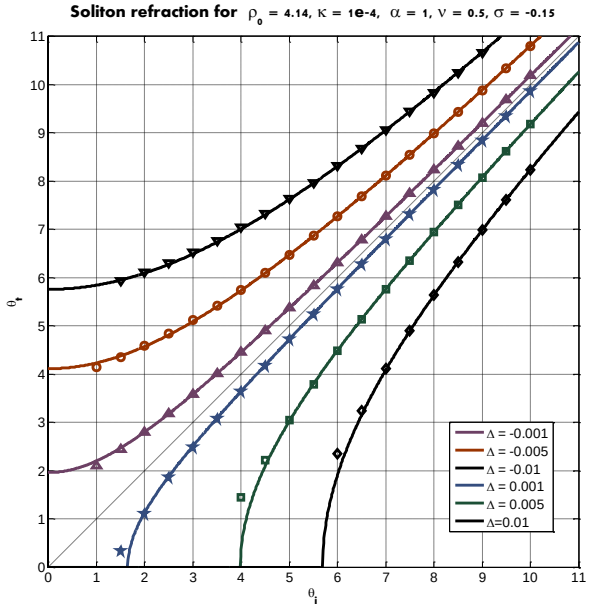

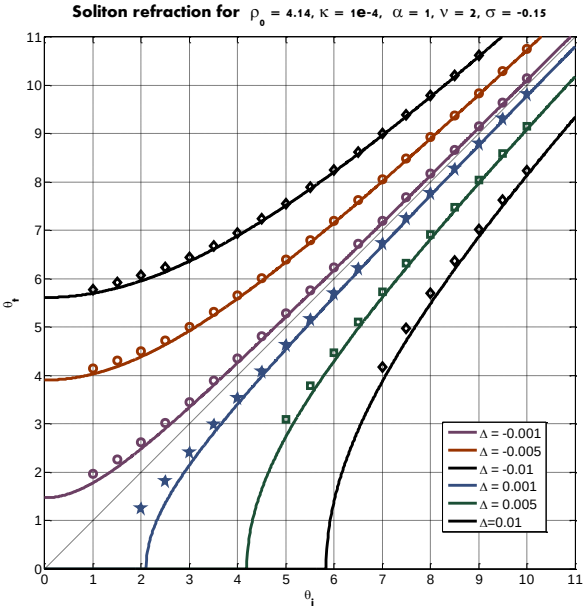

Snell's Law Plots for a mixed interface: $\rho_0 = 4.14$, $\alpha = 1$ and $\kappa = 1 \times 10^{-4}$

ν= 0.5 ν= 2.0

Nonlinear Interfaces - Δ=0

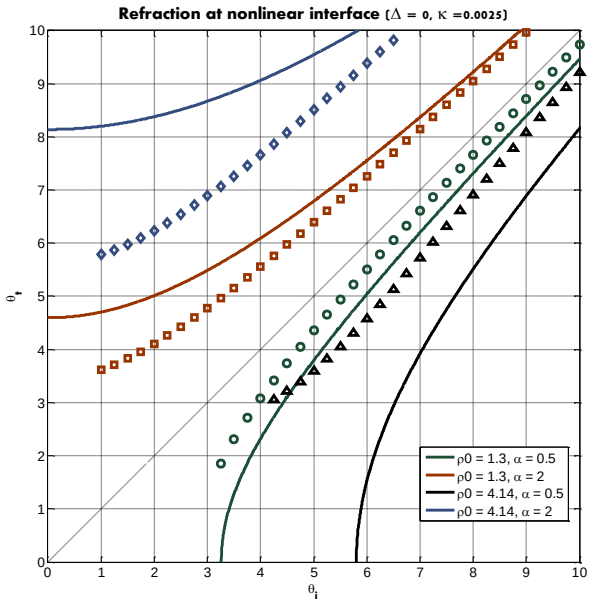

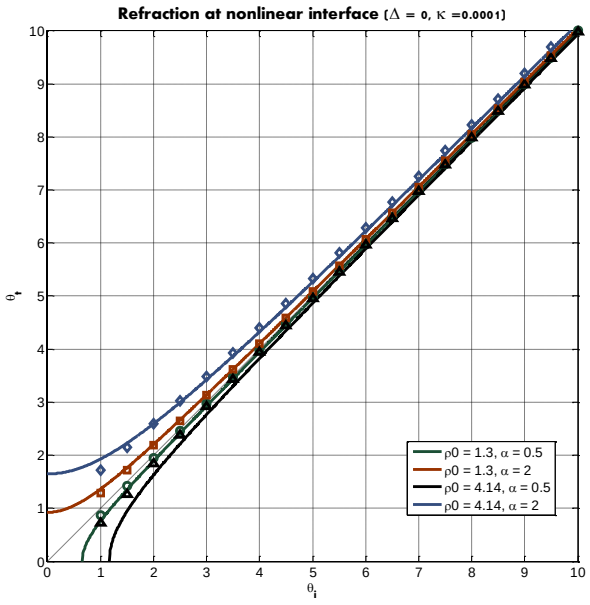

Snell's Law Plots for a nonlinear interface: $\Delta = 0$ and $\nu = 1$

$\kappa = 2.5 \times 10^{-3}$ $\kappa = 1 \times 10^{-4}$

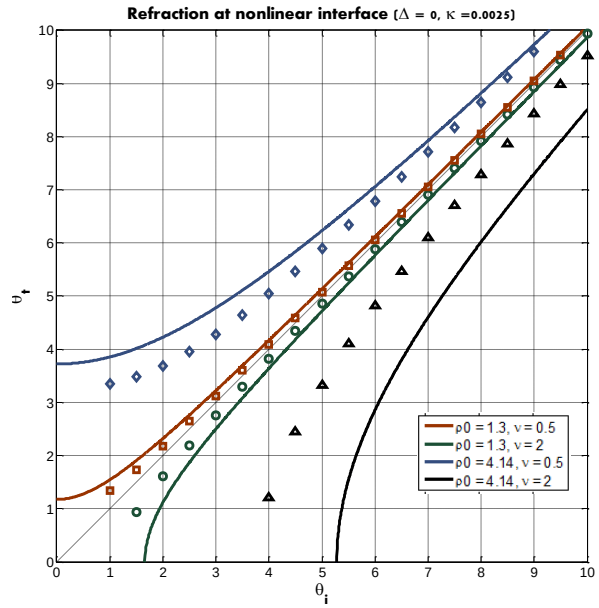

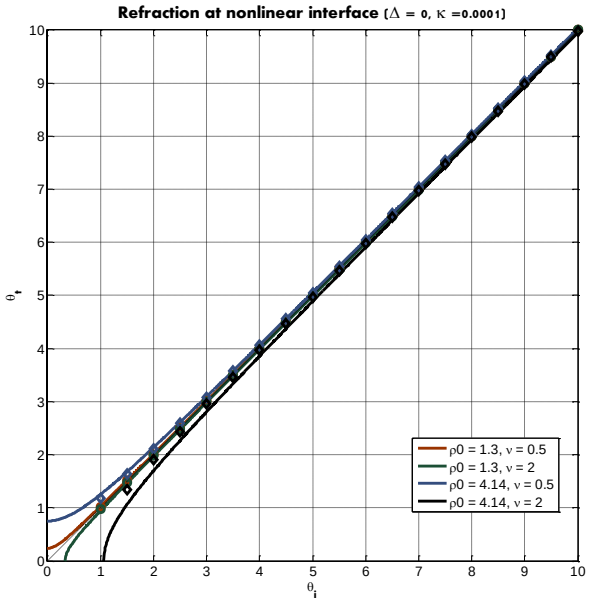

Snell's Law Plots for a nonlinear interface: $\Delta = 0$ and $\alpha = 1$

$\kappa = 2.5 \times 10^{-3}$ $\kappa = 1 \times 10^{-4}$

Linear Interface Results

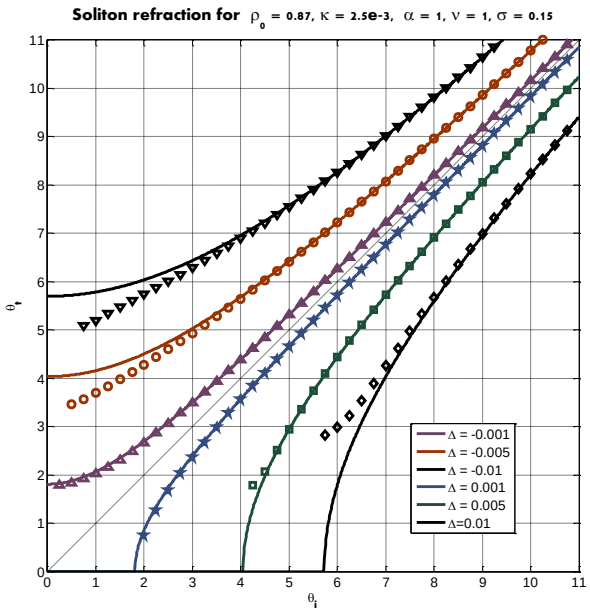

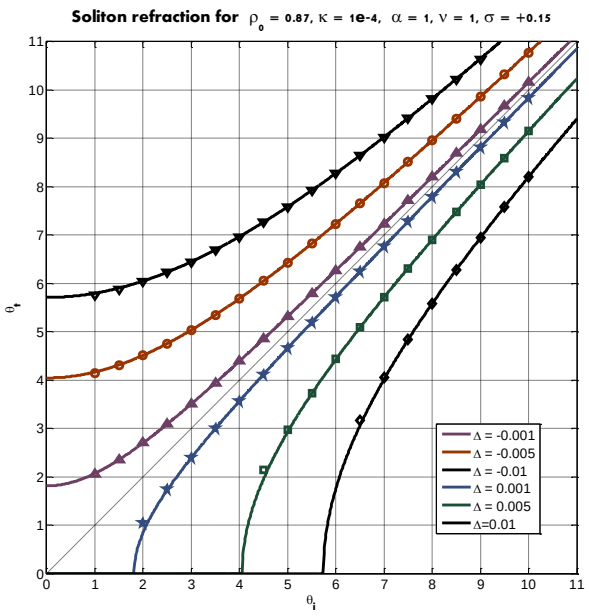

Snell's Law Plots for a linear interface with $\rho_0 = 0.87$

$\kappa = 2.5 \times 10^{-3}$ $\kappa = 1 \times 10^{-4}$

Mixed Interface Results – similar quintic coefficients (ν=1)

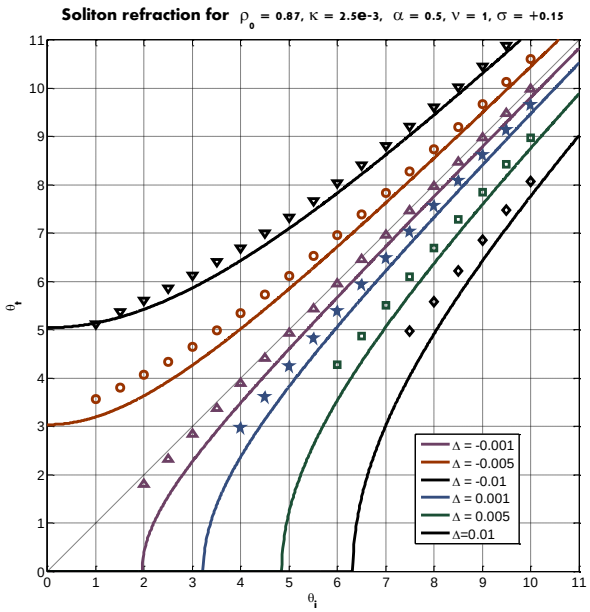

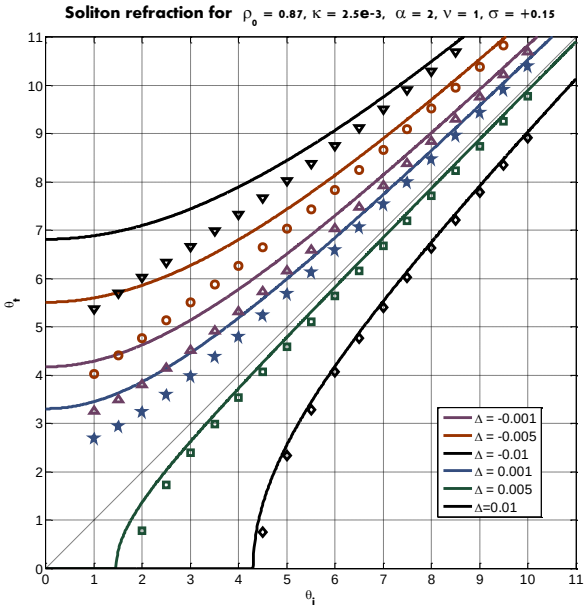

Snell's Law Plots for a mixed interface: $\rho_0 = 0.87$ $\nu = 1$ and $\kappa = 2.5 \times 10^{-3}$

$\alpha = 0.5$ $\alpha = 2.0$

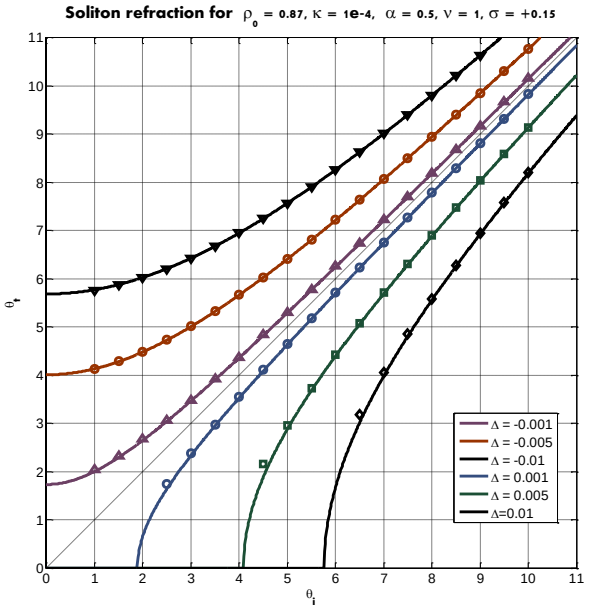

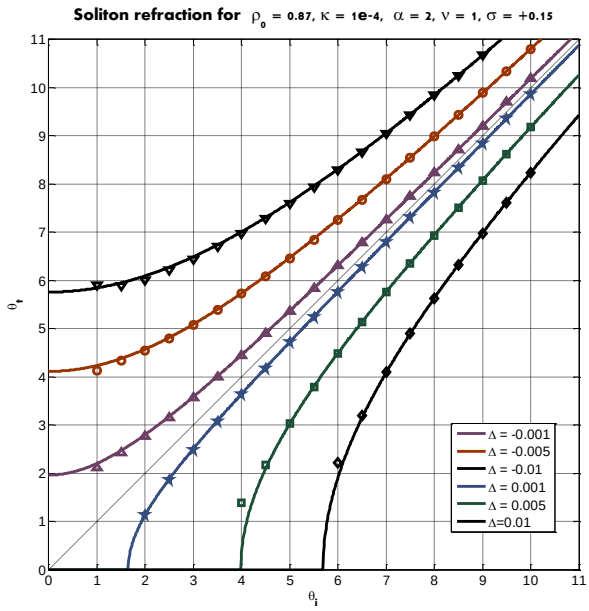

Snell's Law Plots for a mixed interface: $\rho_0 = 0.87$ $\nu = 1$ and $\kappa = 1 \times 10^{-4}$

$\alpha = 0.5$ $\alpha = 2.0$

Mixed Interface Results – similar cubic coefficient (α=1)

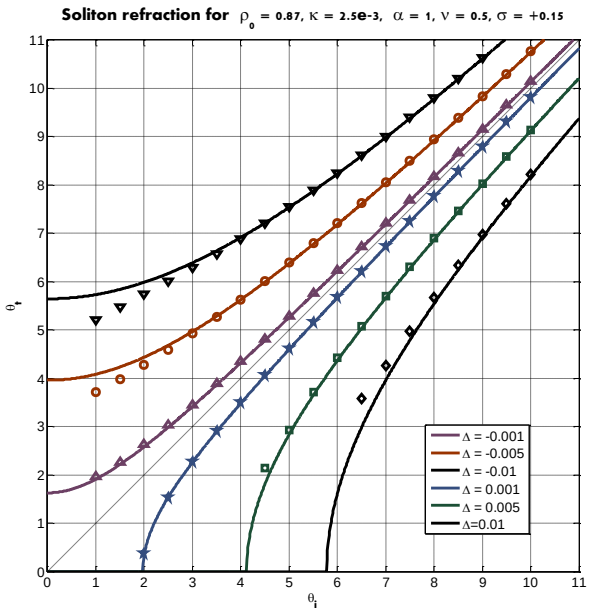

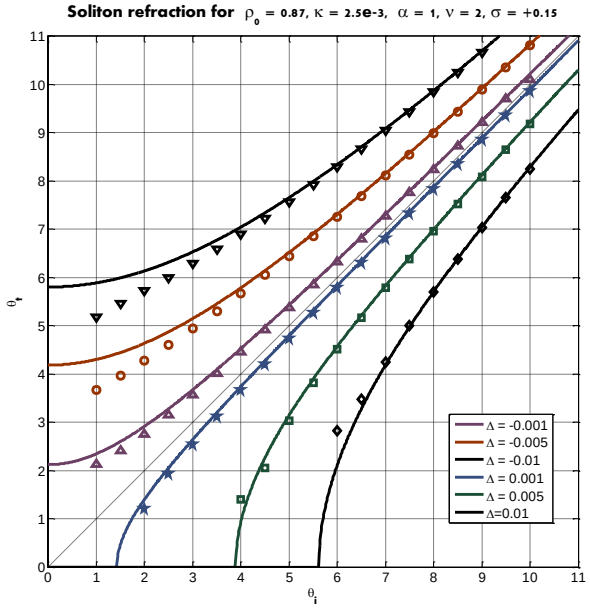

Snell's Law Plots for a mixed interface: $\rho_0 = 0.87$ $\alpha = 1$ and $\kappa = 2.5 \times 10^{-3}$

$\nu = 0.5$ $\nu = 2.0$

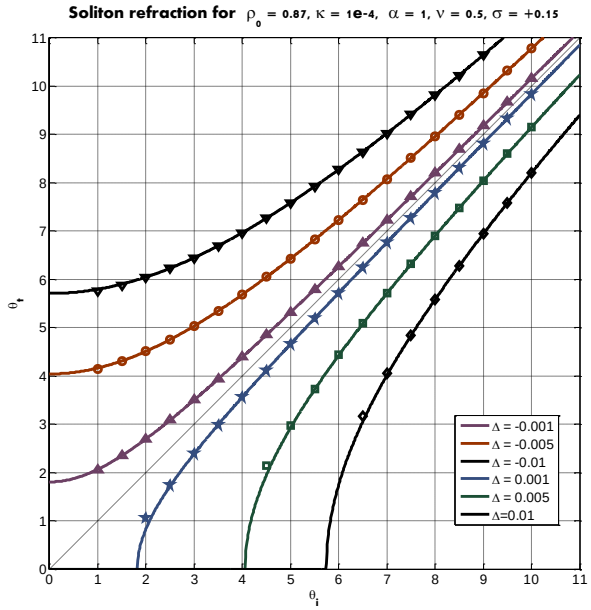

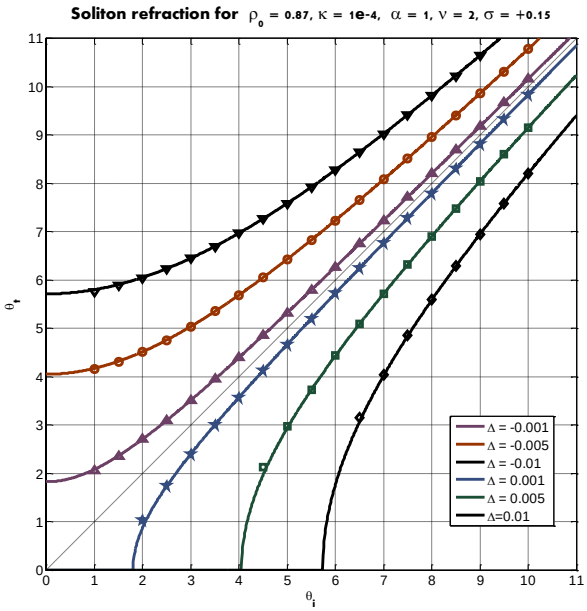

Snell's Law Plots for a mixed interface: $\rho_0 = 0.87$ $\alpha = 1$ and $\kappa = 1 \times 10^{-4}$

$\nu = 0.5$ $\nu = 2.0$

Nonlinear Interfaces - Δ=0

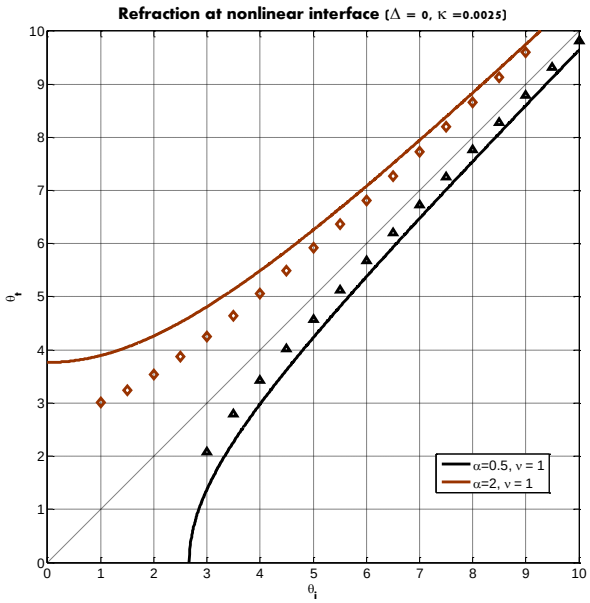

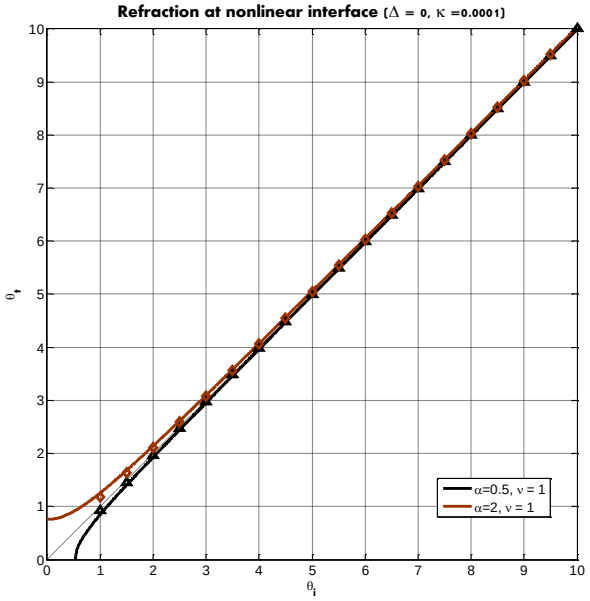

Snell's Law Plots for a nonlinear interface: $\Delta = 0$ and $\nu = 1$

$\kappa = 2.5 \times 10^{-3}$ $\kappa = 1 \times 10^{-4}$

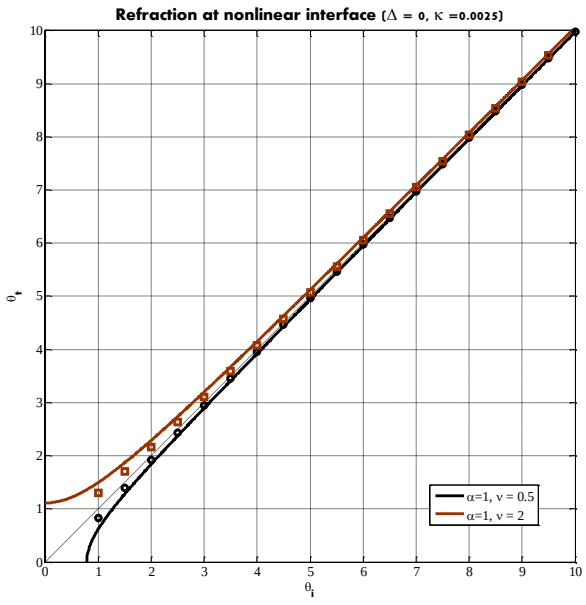

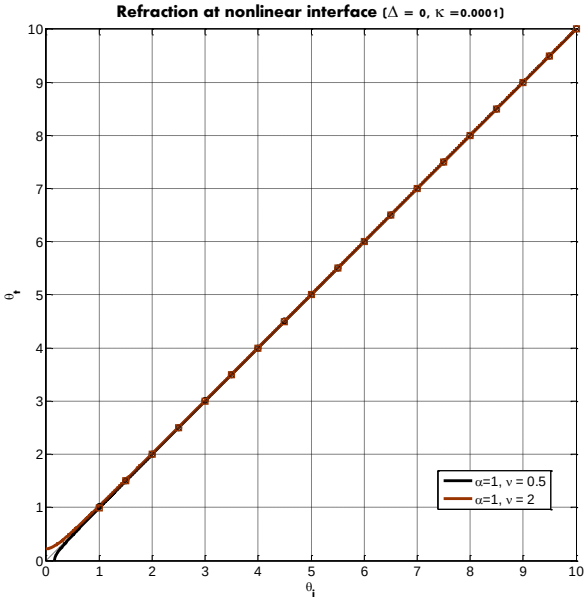

Snell's Law Plots for a nonlinear interface: $\Delta = 0$ and $\alpha = 1$

$\kappa = 2.5 \times 10^{-3}$ $\kappa = 1 \times 10^{-4}$

Appendix C

C.1 GHS Results Tables

Figure 25

$\rho_0 = 1.3,\ \kappa = 2.5 \times 10^{-3},\ \alpha = 1,\ \nu = 1,\ \sigma = -0.15$

Δ	$\theta_{c(theoretical)}$	$\theta_{c(actual)}$
0.001	1.8112	1.822
0.005	4.0447	3.582883
0.01	5.7106	5.463964

Figure 26

$\rho_0 = 1.3,\ \kappa = 1 \times 10^{-3},\ \alpha = 1,\ \nu = 1,\ \sigma = -0.15$

Δ	$\theta_{c(theoretical)}$	$\theta_{c(actual)}$
0.001	1.8112	1.886
0.005	4.0447	3.892405
0.01	5.7106	5.672973

Figure 27

$\rho_0 = 4.14,\ \kappa = 2.5 \times 10^{-3},\ \alpha = 1,\ \nu = 1,\ \sigma = -0.15$

Δ	$\theta_{c(theoretical)}$	$\theta_{c(actual)}$
0.001	1.8112	1.8024
0.005	4.0447	4.1137
0.01	5.7106	4.836937

Figure 32

$\rho_0 = 1.3,\ \kappa = 2.5 \times 10^{-3},\ \alpha = 0.5,\ \nu = 1,\ \sigma = -0.15$

Δ	$\theta_{c(theoretical)}$	$\theta_{c(actual)}$
0.001	3.7280	3.774
0.005	5.1926	6.672
0.01	6.5724	8.892

Figure 33

$\rho_0 = 4.14,\ \kappa = 2.5 \times 10^{-3},\ \alpha = 0.5,\ \nu = 1,\ \sigma = -0.15$

Δ	$\theta_{c(theoretical)}$	$\theta_{c(actual)}$
0.001	6.0790	5.045946
0.005	7.0703	6.672441
0.01	8.1355	8.892405

Figure 34

$\rho_0 = 4.14,\ \kappa = 2.5 \times 10^{-3},\ \alpha = 1,\ \nu = 2,\ \sigma = -0.15$

Δ	$\theta_{c(theoretical)}$	$\theta_{c(actual)}$
0.001	5.5809	3.06036
0.005	6.6474	4.185039
0.01	7.7714	5.308861

Figure 35

$\rho_0 = 1.3,\ \kappa = 2.5 \times 10^{-3},\ \alpha = 0.1,\ \nu = 2,\ \sigma = -0.15$

Δ	$\theta_{c(theoretical)}$	$\theta_{c(actual)}$
-0.001	3.9818	3.2342
-0.005	1.6423	None
-0.0055	1.0234	None

Figure 36

$\rho_0 = 0.87,\ \kappa = 2.5 \times 10^{-3},\ \alpha = 1,\ \nu = 0.1,\ \sigma = 0.15$

Δ	$\theta_{c(theoretical)}$	$\theta_{c(actual)}$
-0.0001	0.8859	0.14194
-0.00005	0.9741	0.6161
-0.00001	1.0393	0.7075

Figure 37

$\rho_0 = 4.14,\ \kappa = 2.5 \times 10^{-3},\ \alpha = 1,\ \nu = 2.5,\ \sigma = -0.15$

Δ	$\theta_{c(theoretical)}$	$\theta_{c(actual)}$
-0.001	6.2129	2.74
-0.0025	5.8040	2.643
-0.005	5.0471	None

Figure 38

$\rho_0 = 1.3, \Delta = 0, \sigma = -0.15$

κ	α	ν	$\theta_{c(theoretical)}$	$\theta_{c(actual)}$
1 x 10^{-3}	1	2	0.7097	1.0522
2.5 x 10^{-3}	1	2	1.1290	1.6611
1 x 10^{-3}	0.5	1	1.857	2.0639
2.5 x 10^{-3}	0.5	1	3.01	3.2589

Figure 39

$\rho_0 = 4.14, \Delta = 0, \sigma = -0.15$

κ	α	ν	$\theta_{c(theoretical)}$	$\theta_{c(actual)}$
1 x 10^{-3}	1	2	2.331	3.3484
2.5 x 10^{-3}	1	2	3.700	5.2796
1 x 10^{-3}	0.5	1	3.983	3.6802
2.5 x 10^{-3}	0.5	1	6.725	5.8039

Appendix D

D.1 Derivation of Governing Equation

From Maxwell's equations:

$$\frac{\partial^2 E}{\partial z^2}+\frac{\partial^2 E}{\partial x^2}+\frac{\omega^2 n^2}{c^2}E=0 \tag{5.97}$$

For dissimilar power-law materials:

$$n_1^2=n_{01}^2+\alpha_1\left|E\right|^q \tag{5.98}$$

$$n_2^2=n_{02}^2+\alpha_2\left|E\right|^q \tag{5.99}$$

Medium 1 (where $x < 0$)

$$\frac{\partial^2 E}{\partial z^2}+\frac{\partial^2 E}{\partial x^2}+\frac{\omega^2}{c^2}n_{01}^2E+\frac{\omega^2}{c^2}\alpha_1\left|E\right|^q E=0 \tag{5.100}$$

Transform to forward reference frame (substitute $E(x,z)=E_0u(x,z)\exp(ik_1z)$)

$$\frac{\partial^2 u}{\partial z^2}+i2k_1\frac{\partial u}{\partial z}-k_1^2u+\frac{\partial^2 u}{\partial x^2}+\frac{\omega^2}{c^2}n_{01}^2u+\frac{\omega^2}{c^2}\alpha_1E_0^q\left|u\right|^q u=0 \qquad (5.101)$$

But:

$$k_1^2=\frac{\omega^2}{c^2}n_{01}^2=k_0^2n_{01}^2$$

$$\frac{\partial^2 u}{\partial z^2}+i2k_1\frac{\partial u}{\partial z}-\frac{\omega^2}{c^2}n_{01}^2u+\frac{\partial^2 u}{\partial x^2}+\frac{\omega^2}{c^2}n_{01}^2u+\frac{\omega^2}{c^2}\alpha_1E_0^q\left|u\right|^q u=0 \tag{5.102}$$

$$\frac{\partial^2 u}{\partial z^2}+i2k_1\frac{\partial u}{\partial z}+\frac{\partial^2 u}{\partial x^2}+\frac{\omega^2}{c^2}\alpha_1E_0^q\left|u\right|^q u=0 \tag{5.103}$$

Rescale using:

$\xi=\frac{\sqrt{2}}{w_0}x$	$\zeta=\frac{z}{L_{D1}}$

$\frac{\partial}{\partial x} = \frac{\sqrt{2}}{w_0}\frac{\partial}{\partial \xi}$	$\frac{\partial}{\partial z} = \frac{1}{L_{D1}}\frac{\partial}{\partial \zeta}$

$$\left(\frac{1}{L_{D1}}\right)^2 \frac{\partial^2 u}{\partial \zeta^2} + i2k_1 \frac{1}{L_{D1}}\frac{\partial u}{\partial \zeta} + \frac{2}{w_0^2}\frac{\partial^2 u}{\partial \xi^2} + \frac{\omega^2}{c^2}\alpha_1 E_0^q |u|^q u = 0 \tag{5.104}$$

Multiply by $\frac{L_{D1}}{2k_1}$

$$\frac{1}{L_{D1}2k_1}\frac{\partial^2 u}{\partial \zeta^2} + i\frac{\partial u}{\partial \zeta} + \frac{L_{D1}}{k_1 w_0^2}\frac{\partial^2 u}{\partial \xi^2} + \frac{\omega^2}{c^2}\frac{L_{D1}}{2k_1}\alpha_1 E_0^q |u|^q u = 0 \tag{5.105}$$

$$\kappa = \frac{1}{L_{D1}2k_1}, \quad L_{D1} = \frac{k_1^2 w_0^2}{2}, \quad \frac{L_{D1}}{2k_1^2}\frac{2}{w_0^2} = \frac{1}{2}$$

$$\kappa\frac{\partial^2 u}{\partial \zeta^2} + i\frac{\partial u}{\partial \zeta} + \frac{1}{2}\frac{\partial^2 u}{\partial \xi^2} + \frac{\omega^2}{c^2}\frac{L_{D1}}{2k_1}\alpha_1 E_0^q |u|^q u = 0 \tag{5.106}$$

Need to choose units for the electric field:

$$\frac{\omega^2}{c^2}\frac{L_{D1}}{2k_1}\alpha_1 E_0^q \equiv 1 \tag{5.107}$$

$$\frac{L_{D1}}{2k_1}\frac{k_1^2}{n_{01}^2}\alpha_1 E_0^q = \frac{L_{D1}k_1\alpha_1}{2n_{01}^2}E_0^q = 1$$

Units of electric field:

$$E_0 = \left(\frac{2n_{01}^2}{L_{D1}k_1\alpha_1}\right)^{1/q} \tag{5.108}$$

For medium 1:

$$\kappa\frac{\partial^2 u}{\partial \zeta^2} + i\frac{\partial u}{\partial \zeta} + \frac{1}{2}\frac{\partial^2 u}{\partial \xi^2} + |u|^q u = 0\,. \tag{5.109}$$

Medium 2 (where $x > 0$)

$$\frac{\partial^2 E}{\partial z^2}+\frac{\partial^2 E}{\partial x^2}+\frac{\omega^2}{c^2}n_{02}^2 E+\frac{\omega^2}{c^2}\alpha_2\left|E\right|^q E=0 \tag{5.110}$$

Transform to the forward reference frame:

$$\frac{\partial^2 u}{\partial z^2}+i2k_1\frac{\partial u}{\partial z}-k_1^2 u+\frac{\partial^2 u}{\partial x^2}+\frac{\omega^2}{c^2}n_{02}^2 u+\frac{\omega^2}{c^2}\alpha_2 E_0^q\left|u\right|^q u=0 \tag{5.111}$$

$$k_1^2=\frac{\omega^2}{c^2}n_{01}^2$$

$$\frac{\partial^2 u}{\partial z^2}+i2k_1\frac{\partial u}{\partial z}-\frac{\omega^2}{c^2}n_{01}^2 u+\frac{\partial^2 u}{\partial x^2}+\frac{\omega^2}{c^2}n_{02}^2 u+\frac{\omega^2}{c^2}\alpha_2 E_0^q\left|u\right|^q u=0 \tag{5.112}$$

$$\frac{\partial^2 u}{\partial z^2}+i2k_1\frac{\partial u}{\partial z}-\frac{\omega^2}{c^2}n_{01}^2\left(1-\frac{n_{02}^2}{n_{01}^2}\right)u+\frac{\partial^2 u}{\partial x^2}+\frac{\omega^2}{c^2}\alpha_2 E_0^q\left|u\right|^q u=0 \tag{5.113}$$

$$\Delta\equiv 1-\left(\frac{n_{02}^2}{n_{01}^2}\right)$$

$$\frac{\partial^2 u}{\partial z^2}+i2k_1\frac{\partial u}{\partial z}-\frac{\omega^2}{c^2}n_{01}^2\Delta u+\frac{\partial^2 u}{\partial x^2}+\frac{\omega^2}{c^2}\alpha_2 E_0^q\left|u\right|^q u=0 \tag{5.114}$$

Rescale using the table above:

$$\left(\frac{1}{L_{D1}}\right)^2\frac{\partial^2 u}{\partial\zeta^2}+i2k_1\frac{1}{L_{D1}}\frac{\partial u}{\partial\zeta}-\frac{\omega^2}{c^2}n_{01}^2\Delta u+\frac{2}{w_0^2}\frac{\partial^2 u}{\partial\xi^2}+\frac{\omega^2}{c^2}\alpha_2 E_0^q\left|u\right|^q u=0 \tag{5.115}$$

Multiply by $\frac{L_{D1}}{2k_1}$

$$\frac{1}{2L_{D1}k_1}\frac{\partial^2 u}{\partial\zeta^2}+i\frac{\partial u}{\partial\zeta}-\frac{\omega^2}{c^2}n_{01}^2\Delta u\frac{L_{D1}}{2k_1}+\frac{1}{2}\frac{\partial^2 u}{\partial\xi^2}+\frac{\omega^2}{c^2}\frac{L_{D1}}{2k_1}\alpha_2 E_0^q\left|u\right|^q u=0 \tag{5.116}$$

$$\kappa=\frac{1}{L_{D1}2k_1}$$

$$\kappa\frac{\partial^2 u}{\partial\zeta^2}+i\frac{\partial u}{\partial\zeta}+\frac{1}{2}\frac{\partial^2 u}{\partial\xi^2}-\frac{\omega^2}{c^2}n_{01}^2\Delta u\frac{L_{D1}}{2k_1}+\frac{\omega^2}{c^2}\frac{L_{D1}}{2k_1}\alpha_2 E_0^q\left|u\right|^q u=0 \tag{5.117}$$

$$\frac{\omega^2}{c^2} n_{01}^2 \frac{L_{D1}}{2k_1} = \frac{k_1 L_{D1}}{2k_1} = \frac{1}{2} k_\zeta L_{D1} = \frac{1}{4\kappa}$$

$$\kappa \frac{\partial^2 u}{\partial \zeta^2} + i \frac{\partial u}{\partial \zeta} + \frac{1}{2} \frac{\partial^2 u}{\partial \xi^2} - \frac{\Delta}{4\kappa} u + \frac{\omega^2}{c^2} \frac{L_{D1}}{2k_1} \alpha_1 \left(\frac{\alpha_2}{\alpha_1} \right) E_0^q |u|^q u = 0 \tag{5.118}$$

But

$$\frac{L_{D1}}{2k_1} \frac{\omega^2}{c^2} \alpha_1 E_0^q \equiv 1$$

$$\kappa \frac{\partial^2 u}{\partial \zeta^2} + i \frac{\partial u}{\partial \zeta} + \frac{1}{2} \frac{\partial^2 u}{\partial \xi^2} - \frac{\Delta}{4\kappa} u + \left(\frac{\alpha_2}{\alpha_1} \right) |u|^q u = 0 \tag{5.119}$$

$$\frac{\alpha_2}{\alpha_1} \equiv \alpha$$

For medium 2:

$$\kappa \frac{\partial^2 u}{\partial \zeta^2} + i \frac{\partial u}{\partial \zeta} + \frac{1}{2} \frac{\partial^2 u}{\partial \xi^2} - \frac{\Delta}{4\kappa} u + \alpha |u|^q u = 0 \tag{5.120}$$

Full model equation:

$$\kappa \frac{\partial^2 u}{\partial \zeta^2} + i \frac{\partial u}{\partial \zeta} + \frac{1}{2} \frac{\partial^2 u}{\partial \xi^2} + |u|^q u = \left[\frac{\Delta}{4\kappa} + (1-\alpha) |u|^q \right] H(\xi) u \qquad (5.121)$$

D.2 Derivation of nonlinear Surface Waves

medium 1

$$\kappa \frac{\partial^2 u}{\partial \zeta^2} + i \frac{\partial u}{\partial \zeta} + \frac{1}{2} \frac{\partial^2 u}{\partial \xi^2} + |u|^q u = 0 \tag{5.122}$$

exact Surface wave solutions are sought using:

$$u(\xi, \zeta) = F\left(\xi - \xi_j\right) \exp\left(i k_\zeta \zeta\right) \exp\left(-i \frac{\zeta}{2\kappa}\right) \tag{5.123}$$

$$\frac{\partial u}{\partial \zeta} = i k_\zeta F \exp\left(i k_\zeta \zeta\right)$$

$$\frac{\partial^2 u}{\partial \zeta^2} = -k_\zeta^2 F \exp\left(i k_\zeta \zeta\right)$$

$$\frac{\partial^2 u}{\partial \xi^2} = \exp\left(i k_\zeta \zeta\right) \frac{\partial^2 F}{\partial \xi^2}$$

$$|u|^q u = F^{q+1} \exp\left(i k_\zeta \zeta\right)$$

$$\kappa\left(-k_\zeta^2 F e^{i k_\zeta \zeta}\right) + i\left(i - k_\zeta F e^{i k_\zeta \zeta}\right) + \frac{1}{2}\left(e^{i k_\zeta \zeta}\right) \frac{\partial^2 F}{\partial \xi^2} + F^{q+1} e^{i k_\zeta \zeta} = 0$$

$$\left(\kappa k_\zeta^2 + k_\zeta\right) F + \frac{1}{2} \frac{\partial^2 F}{\partial \xi^2} + F^{q+1} = 0$$

we know that $\kappa k_\zeta^2 + k_\zeta \equiv \beta$, so

$$\frac{1}{2} \frac{\partial^2 F}{\partial \xi^2} - \beta F + F^{q+1} = 0 \tag{5.124}$$

but $F\left(\xi\right) = \eta_1 \operatorname{sech}^p \theta_1$, where $\theta_1 = a_1\left(\xi - \xi_1\right)$, need to find $\frac{\partial^2 F}{\partial \xi^2}$:

first derivative of $\operatorname{sech}^p \theta_1$:

$u = \operatorname{sech} \theta_1$

$$y = u^p$$

$$\frac{du}{dx} = -\text{sech}\,\theta_1 \tan\theta_1(a_1)$$

$$\frac{dy}{du} = pu^{p-1}$$

$$\frac{dy}{dx} = -p\text{sech}^{p+1}\theta_1 \text{sech}\,\theta_1 \tan\theta_1(a_1) = -p\text{sech}^{p}\theta_1 \tanh\theta_1(a_1)$$

$$\frac{dF}{d\xi} = \eta_1\left[-p\text{sech}^{p}\theta_1 \tanh\theta_1(a_1)\right] = -pa_1 \tanh\theta_1 F$$

$$\frac{\partial^2 F}{\partial\xi^2} = u'v + v'u$$

$$u = -pa_1 \tanh\theta_1$$

$$u' = -pa_1^2 \text{sech}\,\theta_1$$

$$v = F$$

$$v' = -pa_1 \tanh\theta_1 F$$

$$\frac{\partial^2 F}{\partial\xi^2} = p^2 a_1^2\left(1 - \sec h^2\theta_1\right)F - pa_1^2 \sec h^2\theta_1 F$$

substitute into equation (5.124)

$$\frac{1}{2}\left[p^2 a_1^2\left(1-\text{sech}^2\theta_1\right) - pa_1^2\text{sech}^2\theta_1\right] - \beta + \eta_1^q \text{sech}^2\theta_1 = 0$$

by separating the coefficients to the constant and $\text{sech}^2\theta_1$ we are left with

constant:

$$a_1 = \sqrt{\frac{\beta}{2}}q$$

$\mathrm{sech}^2\theta_1$:

$$\eta_1 = \left(\frac{2+q}{2}\beta\right)^{1/q}$$

surface wave solution in medium 1:

$$u(\xi,\zeta) = \left(\frac{2+q}{2}\beta\right)^{1/q} \mathrm{sech}^{2/q}\left[q\left(\frac{\beta}{2}\right)^{1/2}\left(\xi-\xi_j\right)\right]\exp\left(\pm i\sqrt{1+4\kappa\beta}\,\frac{\zeta}{2\kappa}\right)\exp\left(-i\frac{\zeta}{2\kappa}\right) \quad (5.125)$$

<u>medium 2</u>

$$\kappa\frac{\partial^2 u}{\partial\zeta^2} + i\frac{\partial u}{\partial\zeta} + \frac{1}{2}\frac{\partial^2 u}{\partial\xi^2} - \frac{\Delta}{4\kappa} + \alpha|u|^q u = 0 \qquad (5.126)$$

exact Surface wave solutions are sought using:

$$u(\xi,\zeta) = F\left(\xi-\xi_j\right)\exp\left(ik_\zeta\zeta\right)\exp\left(-i\frac{\zeta}{2\kappa}\right) \qquad (5.127)$$

$$\frac{\partial u}{\partial\zeta} = ik_\zeta F\exp\left(ik_\zeta\zeta\right)$$

$$\frac{\partial^2 u}{\partial\zeta^2} = -k_\zeta^2 F\exp\left(ik_\zeta\zeta\right)$$

$$\frac{\partial^2 u}{\partial\xi^2} = \exp\left(ik_\zeta\zeta\right)\frac{\partial^2 F}{\partial\xi^2}$$

$$|u|^q u = F^{q+1}\exp\left(ik_\zeta\zeta\right)$$

$$\kappa\left(-k_\zeta^2 F e^{ik_\zeta\zeta}\right) + i\left(ik_\zeta F e^{ik_\zeta\zeta}\right) + \frac{1}{2}\left(e^{ik_\zeta\zeta}\right)\frac{\partial^2 F}{\partial\xi^2} - \frac{\Delta}{4\kappa}F e^{ik_\zeta\zeta} + \alpha F^{q+1}e^{ik_\zeta\zeta} = 0$$

$$-\left(\kappa k_\zeta^2 + k_\zeta\right)F + \frac{1}{2}\frac{\partial^2 F}{\partial\xi^2} - \frac{\Delta}{4\kappa}F + \alpha F^{q+1} = 0$$

we know that $\kappa k_\zeta^2 + k_\zeta \equiv \beta$, so

$$\frac{1}{2}\frac{\partial^2 F}{\partial \xi^2} - \left(\beta \frac{\Delta}{4\kappa}\right) F + \alpha F^{q+1} = 0 \tag{5.128}$$

but $F(\xi) = \eta_2 \operatorname{sech}^p \theta_2$, where $\theta_2 = a_2(\xi - \xi_2)$, need to find $\frac{\partial^2 F}{\partial \xi^2}$:

first derivative of $\operatorname{sech}^p \theta_2$:

$u = \operatorname{sech} \theta_2$

$y = u^p$

$\frac{du}{dx} = -\operatorname{sech} \theta_2 \tan \theta_2 (a_2)$

$\frac{dy}{du} = pu^{p-1}$

$\frac{dy}{dx} = -p\operatorname{sech}^{p+1} \theta_2 \operatorname{sech} \theta_2 \tan \theta_2 (a_2) = -p\operatorname{sech}^p \theta_2 \tanh \theta_2 (a_2)$

$$\frac{dF}{d\xi} = \eta_1 \left[-p\operatorname{sech}^p \theta_2 \tanh \theta_2 (a_2)\right] = -pa_2 \tanh \theta_2 F$$

$\frac{\partial^2 F}{\partial \xi^2} = u'v + v'u$

$u = -pa_2 \tanh \theta_2$

$u' = -pa_2^2 \operatorname{sech} \theta_2$

$v = F$

$v' = -pa_2 \tanh \theta_2 F$

$$\frac{\partial^2 F}{\partial \xi^2} = p^2 a_2^2 \left(1 - \operatorname{sec} h^2 \theta_2\right) F - pa_2^2 \operatorname{sec} h^2 \theta_2 F$$

substitute into equation (5.124)

$$\frac{a_2^2}{2}\left[\, p^2 - p\left(p+1\right)\mathrm{sech}^2\theta_2 \,\right] - \left(\beta\frac{\Delta}{4\kappa}\right) + \alpha\eta_2^q\mathrm{sech}^2\theta_2 = 0$$

by separating the coefficients to the constant and $\mathrm{sech}^2\theta_2$ we are left with

constant:

$$a_2 = \sqrt{\left(\beta + \frac{\Delta}{4\kappa}\right)}\frac{q}{2}$$

$\mathrm{sech}^2\theta_1$:

$$\eta_2 = \left[\left(\frac{1}{\alpha}\right)\left(\frac{2+q}{2}\right)\left(\beta + \frac{\Delta}{4\kappa}\right)\right]^{1/q}$$

surface wave solution in medium 2:

$$u(\xi,\zeta) = \left[\left(\frac{1}{\alpha}\right)\left(\frac{2+q}{2}\right)\left(\beta + \frac{\Delta}{4\kappa}\right)\right]^{1/q}\mathrm{sec}\,h^{2/q}\left[\frac{q}{\sqrt{2}}\left(\beta + \frac{\Delta}{4\kappa}\right)^{1/2}\left(\xi - \xi_2\right)\right]\exp\left(\pm i\sqrt{1+4\kappa\beta}\,\frac{\zeta}{2\kappa}\right)\exp\left(-i\frac{\zeta}{2\kappa}\right) \tag{5.129}$$

At the interface when ξ = 0 the field u and its normal derivative $\left(\frac{\partial u}{\partial \xi} = \frac{\partial F}{\partial \xi}\right)$ must be

continuous

continuity of u

$$\beta^{1/q}\mathrm{sech}^{2/q}\left[q\left(\frac{\beta}{2}\right)^{1/2}\right] = \left[\left(\frac{1}{\alpha}\right)\left(\beta + \frac{\Delta}{4\kappa}\right)\right]^{1/q}\mathrm{sech}^{2/q}\left[\frac{q}{\sqrt{2}}\left(\beta + \frac{\Delta}{4\kappa}\right)^{1/2}\xi_2\right] \tag{5.130}$$

continuity of du/dξ

$$\left(\frac{dF}{d\xi}\right)_0 = \sqrt{2\beta}\tanh\left[q\left(\frac{\beta}{2}\right)^{1/2}\xi_1\right]F(0) \tag{5.131}$$

$$\left(\frac{dF}{d\xi}\right)_0 = \sqrt{2}\left(\beta + \frac{\Delta}{4\kappa}\right)^{1/2}\tanh\left[\frac{q}{\sqrt{2}}\left(\beta + \frac{\Delta}{4\kappa}\right)^{1/2}\xi_2\right]F(0) \tag{5.132}$$

we now have two equation that we can use to find the remaining parameters. Solve the simultaneous equation to find:

$$\operatorname{sech}\theta_1 = \left[\frac{\Delta}{4\kappa\beta(\alpha-1)}\right]^{1/2} = \delta \tag{5.133}$$

$$\theta_1 = \left[q\left(\frac{\beta}{2}\right)^{1/2}\xi_1\right] = \ln\left(\frac{1\pm\sqrt{1-\delta^2}}{\delta}\right) \tag{5.134}$$

$$\xi_1 = \frac{1}{q}\left(\frac{2}{\beta}\right)^{1/2}\ln\left(\frac{1\pm\sqrt{1-\delta^2}}{\delta}\right) \tag{5.135}$$

$$\operatorname{sech}\theta_2 = \left[\frac{\Delta}{4\kappa}\left(\beta+\frac{\Delta}{4\kappa}\right)^{-1}\left(1-\frac{1}{\alpha}\right)^{-1}\right]^{1/2} = \mu \tag{5.136}$$

$$\theta_2 = \frac{q}{\sqrt{2}}\left(\beta+\frac{\Delta}{4\kappa}\right)^{1/2}\xi_2 = \ln\left(\frac{1\pm\sqrt{1-\mu^2}}{\mu}\right) \tag{5.137}$$

$$\xi_2 = \frac{2}{q}\left(\beta+\frac{\Delta}{4\kappa}\right)^{-1/2}\ln\left(\frac{1\pm\sqrt{1-\mu^2}}{\mu}\right) \tag{5.138}$$

D.3 Surface wave results

Lower Branch Regime 1

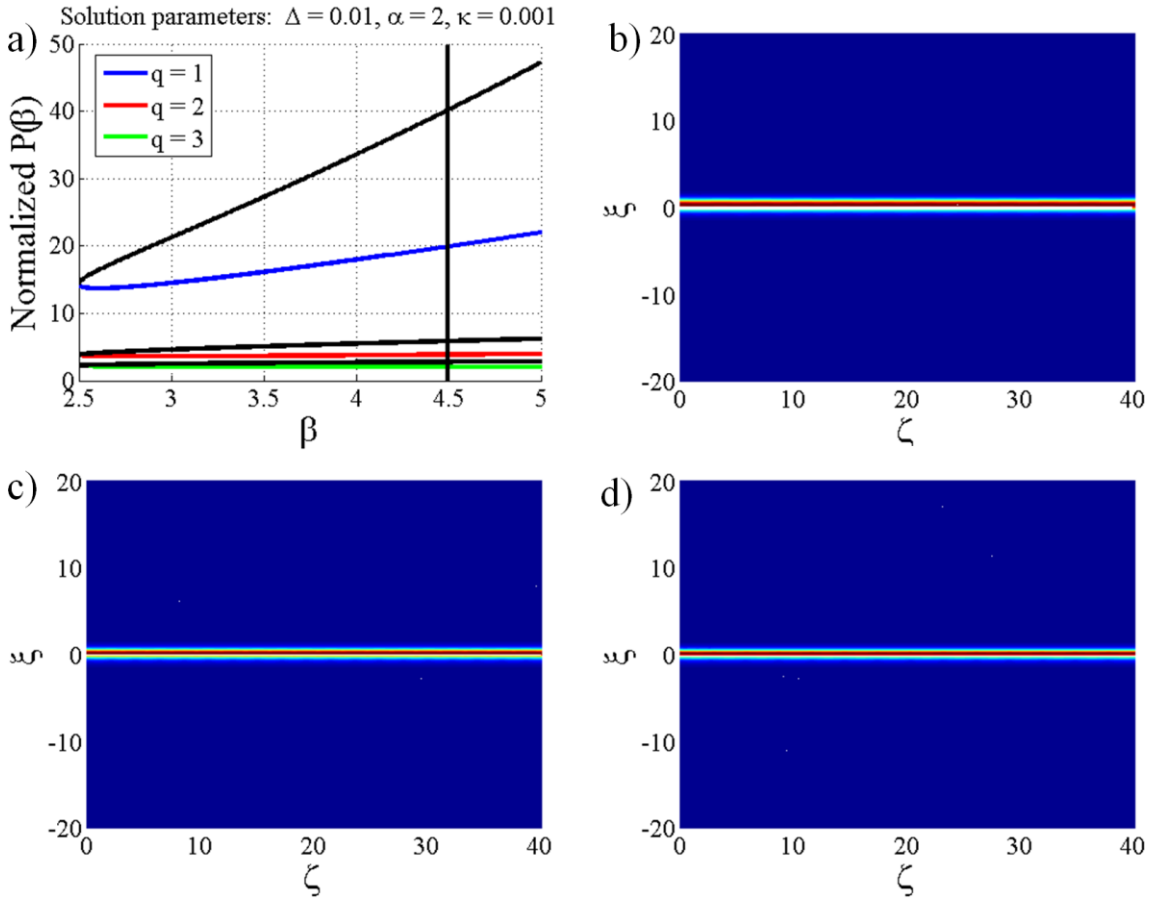

Figure 100 showing a) P(β) vs. β curves with the lower branches of the curves in colours representing q = 1, 2 or 3 and the upper branches shown in black (it is the lower branches that are now being considered). b), c) and d) show the surface wave solutions for q = 1, 2 and 3 respectively where, the interface is represented by a white line and β = 4.5 in all three cases.

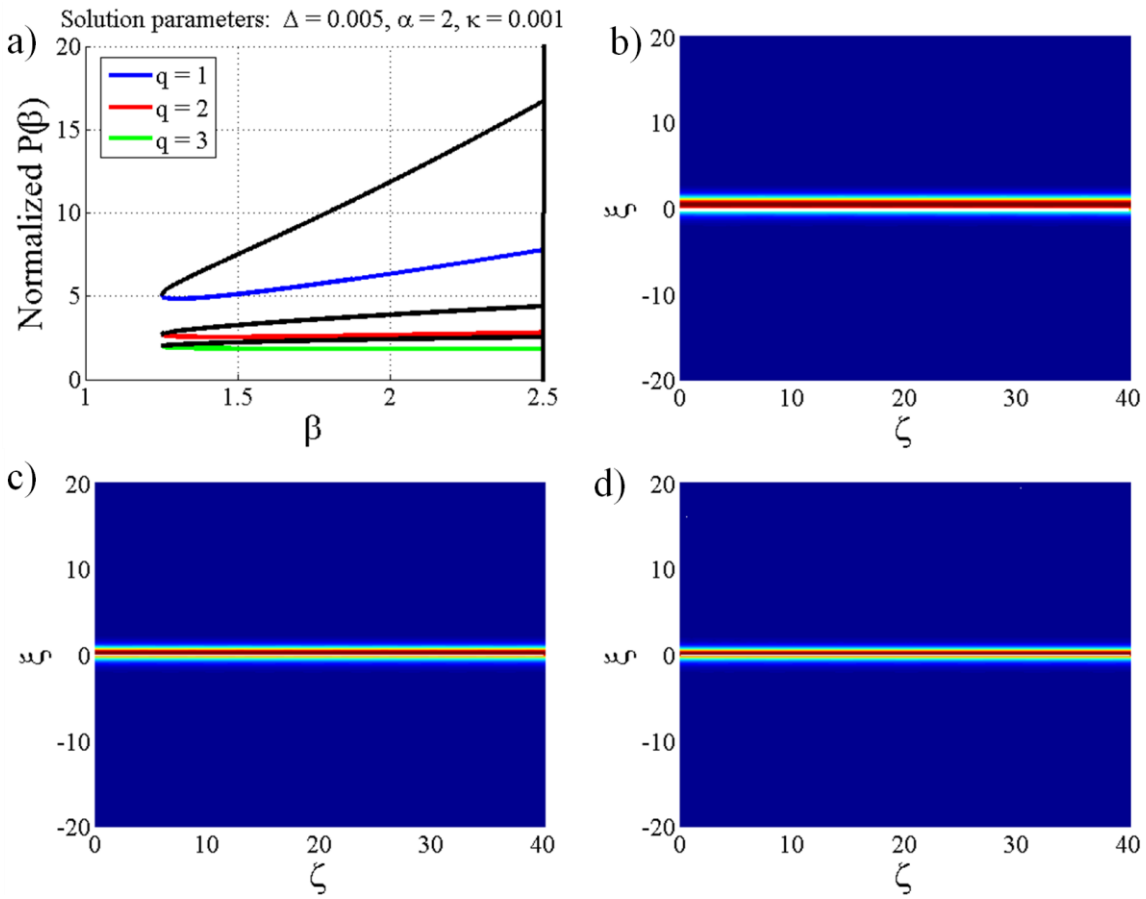

Figure 101 showing a) P(β) vs. β curves with the lower branches of the curves in colours representing q = 1, 2 or 3 and the upper branches shown in black (it is the lower branches that are now being considered). b), c) and d) show the surface wave solutions for q = 1, 2 and 3 respectively where, the interface is represented by a white line and β = 2.5 in all three cases.

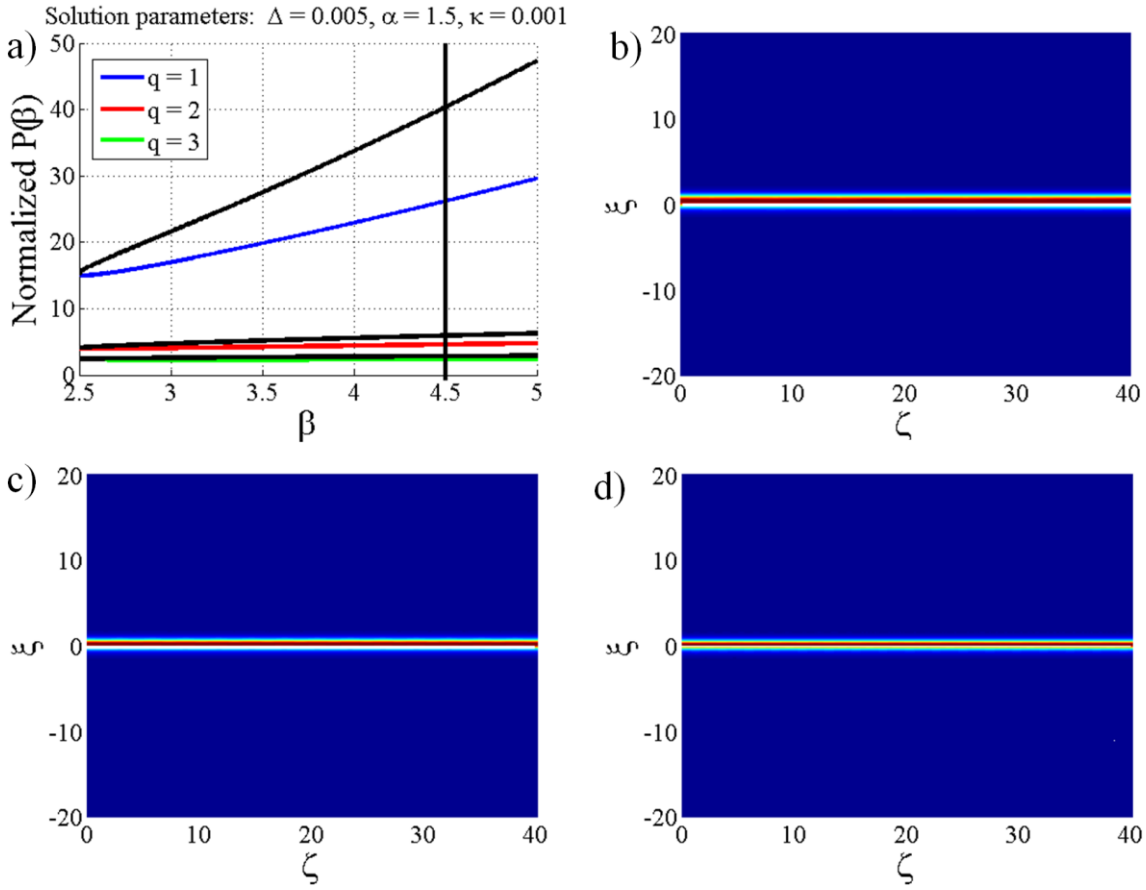

Figure 102 showing a) P(β) vs. β curves with the lower branches of the curves in colours representing q = 1, 2 or 3 and the upper branches shown in black (it is the lower branches that are now being considered). b), c) and d) show the surface wave solutions for q = 1, 2 and 3 respectively where, the interface is represented by a white line and β = 4.5 in all three cases.

Lower Branch Regime 2

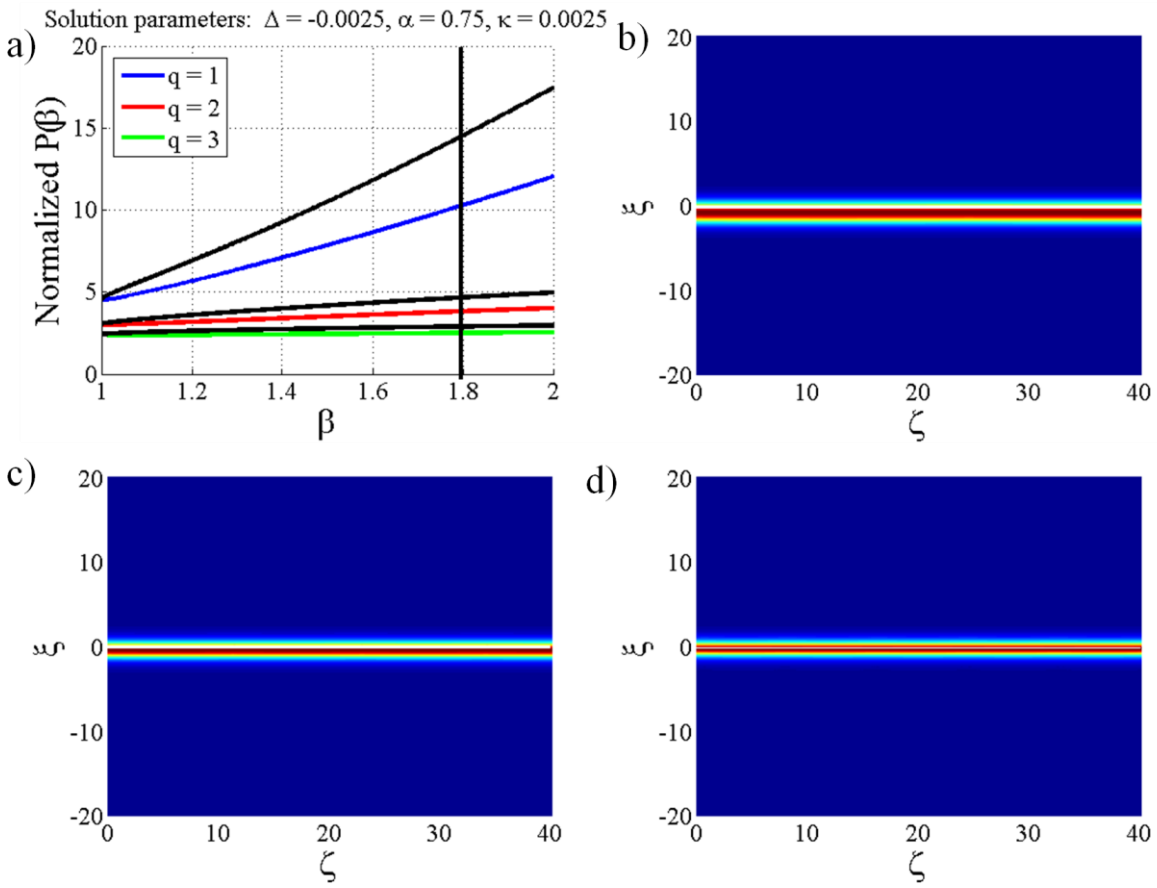

Figure 103 showing a) P(β) vs. β curves with the lower branches of the curves in colours representing q = 1, 2 or 3 and the upper branches shown in black (it is the lower branches that are now being considered). b), c) and d) show the surface wave solutions for q = 1, 2 and 3 respectively where, the interface is represented by a white line and β = 1.8 in all three cases.

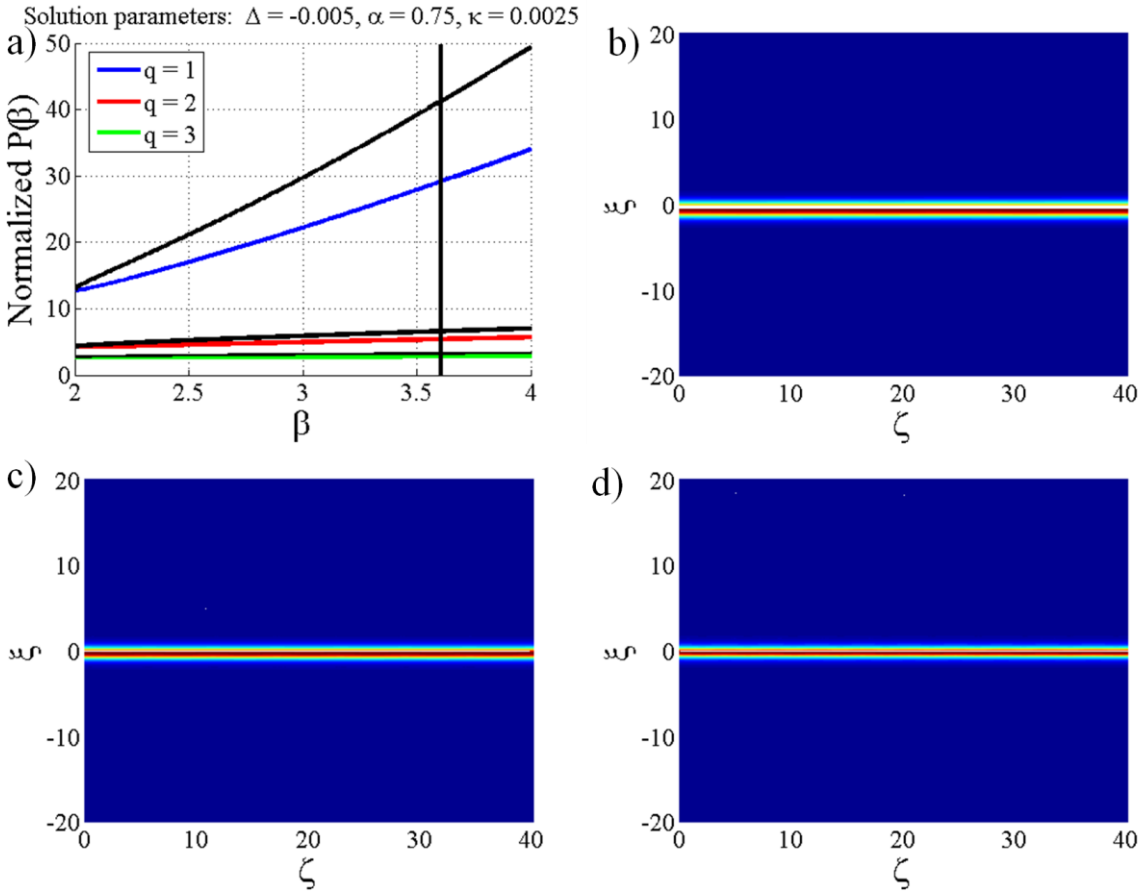

Figure 104 showing a) P(β) vs. β curves with the lower branches of the curves in colours representing q = 1, 2 or 3 and the upper branches shown in black (it is the lower branches that are now being considered). b), c) and d) show the surface wave solutions for q = 1, 2 and 3 respectively where, the interface is represented by a white line and β = 3.6 in all three cases.

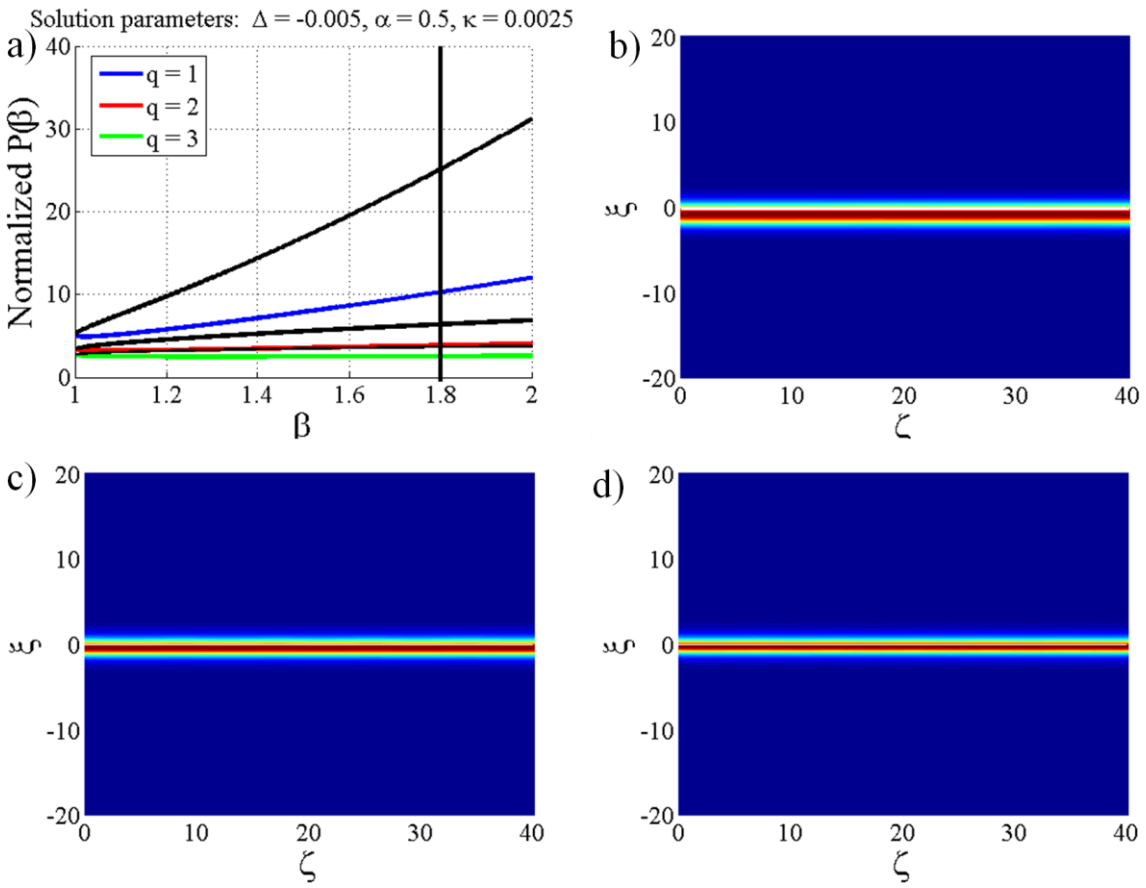

Figure 105 showing a) P(β) vs. β curves with the lower branches of the curves in colours representing q = 1, 2 or 3 and the upper branches shown in black (it is the lower branches that are now being considered). b), c) and d) show the surface wave solutions for q = 1, 2 and 3 respectively where, the interface is represented by a white line and β = 1.8 in all three cases.

Appendix E

E.1 Derivation of Governing Equation for CWA

From Maxwell's equations:

$$\frac{\partial^2 E}{\partial z^2}+\frac{\partial^2 E}{\partial x^2}+\frac{\omega^2}{c^2}\varepsilon_r E=0 \tag{5.139}$$

For dissimilar this model:

$$\varepsilon_{r(medium1)}=\varepsilon_{r1}+\alpha_1\left|E\right|^2 \tag{5.140}$$

$$\varepsilon_{r(medium2)}=\varepsilon_{r2}+\delta\frac{\varepsilon_{r2}}{2\varepsilon_{r2}}\sin\left(\frac{2\pi}{d}x\right)+\alpha_2\left|E\right|^2 \tag{5.141}$$

Medium 1 (where $x < 0$)

$$\frac{\partial^2 E}{\partial z^2}+\frac{\partial^2 E}{\partial x^2}+\frac{\omega^2}{c^2}\varepsilon_{r1}E+\frac{\omega^2}{c^2}\alpha_1\left|E\right|^2 E=0 \tag{5.142}$$

Transform to forward reference frame (substitute $E(x,z)=E_0 u(x,z)\exp(ik_1 z)$)

$$\frac{\partial^2 u}{\partial z^2}+i2k_1\frac{\partial u}{\partial z}-k_1^2 u+\frac{\partial^2 u}{\partial x^2}+\frac{\omega^2}{c^2}\varepsilon_{r1}u+\frac{\omega^2}{c^2}\alpha_1 E_0^2\left|u\right|^2 u=0 \qquad (5.143)$$

But:

$$k_1^2=\frac{\omega^2}{c^2}n_{01}^2=k_0^2 n_{01}^2$$

$$\frac{\partial^2 u}{\partial z^2}+i2k_1\frac{\partial u}{\partial z}-\frac{\omega^2}{c^2}\varepsilon_{r1}u+\frac{\partial^2 u}{\partial x^2}+\frac{\omega^2}{c^2}\varepsilon_{r1}u+\frac{\omega^2}{c^2}\alpha_1 E_0^2\left|u\right|^2 u=0 \tag{5.144}$$

$$\frac{\partial^2 u}{\partial z^2}+i2k_1\frac{\partial u}{\partial z}+\frac{\partial^2 u}{\partial x^2}+\frac{\omega^2}{c^2}\alpha_1 E_0^2\left|u\right|^2 u=0 \tag{5.145}$$

Rescale using:

$\xi=\frac{\sqrt{2}}{w_0}x$	$\zeta=\frac{z}{L_{D1}}$

$\frac{\partial}{\partial x} = \frac{\sqrt{2}}{w_0}\frac{\partial}{\partial \xi}$	$\frac{\partial}{\partial z} = \frac{1}{L_{D1}}\frac{\partial}{\partial \zeta}$

$$\left(\frac{1}{L_{D1}}\right)^2 \frac{\partial^2 u}{\partial \zeta^2} + i2k_1 \frac{1}{L_{D1}}\frac{\partial u}{\partial \zeta} + \frac{2}{w_0^2}\frac{\partial^2 u}{\partial \xi^2} + \frac{\omega^2}{c^2}\alpha_1 E_0^2 |u|^2 u = 0 \tag{5.146}$$

Multiply by $\frac{L_{D1}}{2k_1}$

$$\frac{1}{L_{D1}2k_1}\frac{\partial^2 u}{\partial \zeta^2} + i\frac{\partial u}{\partial \zeta} + \frac{L_{D1}}{k_1 w_0^2}\frac{\partial^2 u}{\partial \xi^2} + \frac{\omega^2}{c^2}\frac{L_{D1}}{2k_1}\alpha_1 E_0^2 |u|^2 u = 0 \tag{5.147}$$

$$\kappa = \frac{1}{L_{D1}2k_1}, \qquad L_{D1} = \frac{k_1^2 w_0^2}{2}, \qquad \frac{L_{D1}}{2k_1^2}\frac{2}{w_0^2} = \frac{1}{2}$$

$$\kappa\frac{\partial^2 u}{\partial \zeta^2} + i\frac{\partial u}{\partial \zeta} + \frac{1}{2}\frac{\partial^2 u}{\partial \xi^2} + \frac{\omega^2}{c^2}\frac{L_{D1}}{2k_1}\alpha_1 E_0^2 |u|^2 u = 0 \tag{5.148}$$

Need to choose units for the electric field:

$$\frac{\omega^2}{c^2}\frac{L_{D1}}{2k_1}\alpha_1 E_0^2 \equiv 1 \tag{5.149}$$

$$\frac{L_{D1}}{2k_1}\frac{k_1^2}{n_{01}^2}\alpha_1 E_0^2 = \frac{L_{D1}k_1\alpha_1}{2n_{01}^2}E_0^2 = 1$$

Units of electric field:

$$E_0 = \left(\frac{2n_{01}^2}{L_{D1}k_1\alpha_1}\right)^{1/2} \tag{5.150}$$

For medium 1:

$$\kappa\frac{\partial^2 u}{\partial \zeta^2} + i\frac{\partial u}{\partial \zeta} + \frac{1}{2}\frac{\partial^2 u}{\partial \xi^2} + |u|^2 u = 0\,. \tag{5.151}$$

Medium 2 (where $x > 0$)

$$\frac{\partial^2 E}{\partial z^2}+\frac{\partial^2 E}{\partial x^2}+\frac{\omega^2}{c^2}\varepsilon_{r2}\left[1+\frac{\delta\varepsilon_{r2}}{2\varepsilon_{r2}}\sin\left(\frac{2\pi}{d}x\right)\right]E+\frac{\omega^2}{c^2}\alpha_2\left|E\right|^2 E=0 \tag{5.152}$$

Transform to the forward reference frame:

$$\frac{\partial^2 u}{\partial z^2}+i2k_1\frac{\partial u}{\partial z}-k_1^2 u+\frac{\partial^2 u}{\partial x^2}+\frac{\omega^2}{c^2}\varepsilon_{r2}\left[1+\frac{\delta\varepsilon_{r2}}{2\varepsilon_{r2}}\sin\left(\frac{2\pi}{d}x\right)\right]u+\frac{\omega^2}{c^2}\alpha_2 E_0^2\left|u\right|^2 u=0 \tag{5.153}$$

$$k_1^2=\frac{\omega^2}{c^2}\varepsilon_{r1}$$

$$\frac{\partial^2 u}{\partial z^2}+i2k_1\frac{\partial u}{\partial z}-k_1^2+\frac{\partial^2 u}{\partial x^2}+\frac{\omega^2}{c^2}\varepsilon_{r2}\left[1+\frac{\delta\varepsilon_{r2}}{2\varepsilon_{r2}}\sin\left(\frac{2\pi}{d}x\right)\right]u+\frac{\omega^2}{c^2}\alpha_2 E_0^2\left|u\right|^2 u=0 \tag{5.154}$$

$$\frac{\partial^2 u}{\partial z^2}+i2k_1\frac{\partial u}{\partial z}-k_1^2\left(1-\frac{\varepsilon_{r2}}{\varepsilon_{r1}}\right)u+\frac{\partial^2 u}{\partial x^2}+k_1^2\left(\frac{\varepsilon_{r2}}{\varepsilon_{r1}}\right)\left[1+\frac{\delta\varepsilon_{r2}}{2\varepsilon_{r2}}\sin\left(\frac{2\pi}{d}x\right)\right]u+\frac{\omega^2}{c^2}\alpha_2 E_0^2\left|u\right|^2 u=0$$

(5.155)

$$\Delta\equiv 1-\left(\frac{\varepsilon_{r2}}{\varepsilon_{r1}}\right)$$

$$\frac{\partial^2 u}{\partial z^2}+i2k_1\frac{\partial u}{\partial z}-k_1^2\Delta u+\frac{\partial^2 u}{\partial x^2}+\frac{\omega^2}{c^2}\left[\frac{\delta}{2}\varepsilon_{r2}\sin\left(\frac{2\pi}{d}x\right)\right]u+\frac{\omega^2}{c^2}\alpha_2 E_0^2\left|u\right|^2 u=0 \tag{5.156}$$

Rescale using the table above:

$$\left(\frac{1}{L_{D1}}\right)^2\frac{\partial^2 u}{\partial\zeta^2}+i2k_1\frac{1}{L_{D1}}\frac{\partial u}{\partial\zeta}-k_1^2\Delta u+\frac{2}{w_0^2}\frac{\partial^2 u}{\partial\xi^2}+\frac{\omega^2}{c^2}\left[\frac{\delta}{2}\varepsilon_{r2}\sin\left(\frac{2\pi}{d}\frac{w_0}{\sqrt{2}}x\right)\right]u+\frac{\omega^2}{c^2}\alpha_2 E_0^2\left|u\right|^2 u=0$$

(5.157)

Multiply by $\frac{L_{D1}}{2k_1}$

$$\Lambda\equiv\sqrt{2}\frac{d}{w_0}$$

$$\frac{1}{2L_{D1}k_1}\frac{\partial^2 u}{\partial\zeta^2}+i\frac{\partial u}{\partial\zeta}-\frac{k_1}{2}\Delta u\frac{L_{D1}}{2k_1}+\frac{L_{D1}}{k_1 w_0}\frac{\partial^2 u}{\partial\xi^2}+\frac{\omega^2}{c^2}\frac{L_{D1}}{2k_1}\left(\frac{\delta}{2}\varepsilon_{r2}\right)\sin\left(\frac{2\pi}{\Lambda}\xi\right)u+\frac{\omega^2}{c^2}\frac{L_{D1}}{2k_1}\alpha_2 E_0^2\left|u\right|^2 u=0$$

(5.158)

$$\kappa = \frac{1}{L_{D1} 2k_1}$$

$$\frac{\omega^2}{c^2} n_{01}^2 \frac{L_{D1}}{2k_1} = \frac{k_1 L_{D1}}{2k_1} = \frac{1}{2} k_\zeta L_{D1} = \frac{1}{4\kappa}$$

$$\kappa \frac{\partial^2 u}{\partial \zeta^2} + i \frac{\partial u}{\partial \zeta} + \frac{1}{2} \frac{\partial^2 u}{\partial \xi^2} - \frac{\Delta}{4\kappa} u + \frac{\omega^2}{c^2} \frac{L_{D1}}{2k_1} \left(\frac{\delta}{2} \varepsilon_{r2} \right) \sin\left(\frac{2\pi}{\Lambda} \xi \right) u + \frac{\omega^2}{c^2} \frac{L_{D1}}{2k_1} \alpha_2 E_0^2 |u|^2 u = 0$$

(5.159)

But

$$\frac{L_{D1}}{2k_1} \frac{\omega^2}{c^2} \alpha_1 E_0^2 \equiv 1$$

$$\kappa \frac{\partial^2 u}{\partial \zeta^2} + i \frac{\partial u}{\partial \zeta} + \frac{1}{2} \frac{\partial^2 u}{\partial \xi^2} - \frac{\Delta}{4\kappa} u + \left(\frac{\alpha_2}{\alpha_1} \right) |u|^q u = 0 \qquad (5.160)$$

$$\frac{\alpha_2}{\alpha_1} \equiv \alpha$$

$$\sigma \equiv \delta \frac{\varepsilon_{r2}}{\varepsilon_{r1}}$$

For medium 2:

$$\kappa \frac{\partial^2 u}{\partial \zeta^2} + i \frac{\partial u}{\partial \zeta} + \frac{1}{2} \frac{\partial^2 u}{\partial \xi^2} - \frac{\Delta}{4\kappa} u + \frac{1-\Delta}{8\kappa} \sigma \sin\left(\frac{2\pi}{\Lambda} \xi \right) u + \alpha |u|^2 u = 0 \qquad (5.161)$$

Full model equation:

$$\kappa \frac{\partial^2 u}{\partial \zeta^2} + i \frac{\partial u}{\partial \zeta} + \frac{1}{2} \frac{\partial^2 u}{\partial \xi^2} + |u|^2 u = \left[\frac{\Delta}{4\kappa} - \frac{1-\Delta}{8\kappa} \delta \sin\left(\frac{2\pi}{\Lambda} \xi \right) + (1-\alpha) |u|^2 \right] H(\xi) u$$

(5.162)